UTS UNIVERSITY OF TECHNOLOGY SYDNEY

Modelling and Control of Continuum Robots with Variable Stiffness

by Yeman FAN

Thesis submitted in fulfilment of the requirements for the degree of

Doctor of Philosophy

under the supervision of D/Prof. Dikai Liu

EM/Prof. Gamini Dissanayake

University of Technology Sydney

Faculty of Engineering and Information Technology

December 2023

Certificate of Original Authorship

I, **Yeman Fan**, declare that this thesis is submitted in fulfilment of the requirements for the award of **Doctor of Philosophy**, in the Faculty of Engineering and Information Technology at the University of Technology Sydney.

This thesis is wholly my own work unless otherwise referenced or acknowledged. In addition, I certify that all information sources and literature used are indicated in the thesis.

This document has not been submitted for qualifications at any other academic institution.

This research is supported by the Australian Government Research Training Program.

Signature: Production Note:
Signature removed prior to publication.

Date: 30 December 2023

Modelling and Control of Continuum Robots with Variable Stiffness

by

Yeman FAN

A thesis submitted in fulfilment of the requirements for the degree of Doctor of Philosophy

Abstract

Continuum robots have significant potential in practical applications owing to their intrinsic compliance, dexterity, and adaptability. However, the mathematical modelling and real-time control of stiffness tuning in continuum robots represent a key research question that has not been thoroughly addressed. To address this research question, this thesis first proposes an innovative design for continuum robots by incorporating antagonism and layer jamming mechanisms to endow the robot with stiffness-tuning capability. A static deflection analysis method is developed, based on the Euler-Bernoulli beam theory, to examine robot stiffness under various conditions. An equivalent two section method is also proposed for analysing and calculating the workspace of multi-segment continuum robots. This research then develops a rigid-link dynamical model for analysing the stiffness-tuning capabilities of continuum robots equipped with antagonistic mechanisms. Based on this model, a novel passivity-based controller is designed for simultaneous control of robots' position and stiffness. This model is further developed for continuum robots with layer jamming as an additional stiffness tuning mechanism, allowing for theoretical analysis of shape locking and adjustable stiffness of continuum robots with layer jamming. Extensive simulations and experiments are conducted to validate the proposed robot design, modelling, and control methods.

Acknowledgements

I am immensely grateful for the successful completion of this PhD thesis, and I would like to extend my heartfelt appreciation to everyone who played a crucial role in reaching this significant milestone.

First and foremost, I express my deepest gratitude to my esteemed supervisor, Prof. Dikai Liu, whose unwavering guidance, encouragement, and wisdom have been the guiding light throughout my research journey. His expertise, patience, and dedication have inspired me to strive for excellence and have been instrumental in shaping the direction of my PhD research.

I am deeply thankful to Dr. Bowen Yi for his invaluable guidance and support throughout my research journey. His expertise and insights have played a pivotal role in shaping the theoretical aspects of Chapters 5 and 6 of this thesis. His willingness to share knowledge and kindness help have significantly enriched my learning experience.

I am indebted to all the members of my candidature assessment panel, Dr. Liang Zhao, Prof. Shoudong Huang, Prof. Jamie Valls Miro, Prof. Zhen Luo, Dr. Marc Carmichael, for their valuable insights and constructive feedback. Their thoughtful suggestions and rigorous evaluation have significantly strengthened the quality of this work.

My sincere thanks go to the Faculty, School, and Robotics Institute for providing an intellectually stimulating environment and access to invaluable resources. The academic atmosphere here has been instrumental in fostering my growth as a researcher. A special acknowledgment goes to my colleagues and fellow researchers, Mitchell C. Cullen, Zhehua Mao, Shilei Zhou, Qing Ni, Richardo Khonasty, Tharaka D. Dahanayaka, and Tiancheng Li, who have shared their knowledge and expertise, creating a supportive and collaborative research community. I am grateful for their camaraderie and the invaluable discussions, suggestions, support, and friendship they offered throughout this journey.

I am deeply thankful to the Australian Research Council (ARC) and the University of Technology Sydney (UTS), whose financial support made this research possible. The

funding not only eased the financial burden but also reaffirmed the importance of this research endeavour.

Finally, to my family and friends, I extend my heartfelt appreciation for their unwavering belief in me. Their love, encouragement, understanding, and support provided much-needed motivation during challenging times. I am grateful for their constant support and encouragement.

In conclusion, this research would not have been possible without the support and contributions of all those mentioned, as well as the countless others who have contributed in ways both big and small. I express my sincere gratitude to each and every one of them for being a part of this remarkable chapter in my life.

Contents

Declaration of Authorship i

Abstract iii

Acknowledgements v

Contents vii

List of Figures xi

List of Tables xv

List of Publications xvii

1 Introduction 1
- 1.1 Scope and overview . . . 1
- 1.2 Contributions . . . 2
- 1.3 Thesis structure . . . 3

2 Literature Review 5
- 2.1 Overview . . . 5
- 2.2 Stiffness tuning approaches . . . 10
  - 2.2.1 Antagonism . . . 10
  - 2.2.2 Thermally responsive materials . . . 16
  - 2.2.3 Jamming mechanism . . . 22
  - 2.2.4 Mechanical structure . . . 28
- 2.3 Comparisons and discussions . . . 31
- 2.4 Future perspectives . . . 35
  - 2.4.1 Multiple composite stiffening methodology . . . 36
  - 2.4.2 Novel materials . . . 37
  - 2.4.3 Advanced control models and algorithms . . . 37
- 2.5 Summary . . . 38

3 Design of a Continuum Robot with Jamming Mechanism 41
3.1 Introduction . . . 41
3.2 Robot design . . . 43
3.2.1 Overall design of the continuum robot . . . 43
3.2.2 Support spine and actuator . . . 44
3.2.3 Jamming sheath . . . 46
3.3 Approximate stiffness model . . . 50
3.3.1 Model description . . . 50
3.3.2 Model derivation . . . 52
3.4 Experiments and results . . . 56
3.4.1 Experiment setup . . . 56
3.4.2 Force-deflection results . . . 56
3.4.3 Stiffness variation results . . . 59
3.4.4 Actuation and gripping experiments . . . 61
3.5 Discussion . . . 62
3.6 Summary . . . 63

4 Robot Worksapce Analysis and Equivalent Two Section Method 65
4.1 Introduction . . . 66
4.2 Equivalent two section method . . . 67
4.2.1 Parameters of continuum robots . . . 67
4.2.2 Kinematic model . . . 68
4.2.3 True workspace estimation . . . 70
4.2.4 The equivalent two section method . . . 71
4.2.5 Workspace calculation algorithm . . . 74
4.3 Simulation experiments and results . . . 76
4.3.1 Simulation environment . . . 76
4.3.2 Workspace analysis . . . 76
4.3.3 Workspace area . . . 78
4.3.4 Workspace volume . . . 78
4.4 Discussion . . . 81
4.5 Summary . . . 82

5 Simultaneous Position and Stiffness Control 83
5.1 Introduction . . . 84
5.2 Model and problem set . . . 86
5.2.1 Modelling of a class of continuum robots . . . 86
5.2.2 Problem set . . . 93
5.3 Open-loop stiffening . . . 93
5.4 Control design . . . 97
5.4.1 Assignable equilibria . . . 98
5.4.2 Simultaneous position-and-stiffness control . . . 102
5.5 Discussions . . . 108
5.6 Experimental results . . . 109

5.6.1 Experimental setup . . . 109
5.6.2 Open-loop stiffening experiments . . . 112
5.6.3 Closed-loop experiments . . . 113
5.7 Summary . . . 120

6 Dynamic Model for Continuum Robots with Layer Jamming 125
6.1 Introduction . . . 125
6.2 Dynamic modelling . . . 127
6.2.1 Preliminary of jamming-free model . . . 127
6.2.2 Assumptions and frictional model with layer jamming . . . 128
6.2.3 Variable stiffness model using jamming layers . . . 132
6.3 Interpretation to key phenomena . . . 134
6.3.1 Shape locking . . . 134
6.3.2 Adjustable stiffness . . . 138
6.4 Experiments . . . 140
6.4.1 Shape locking . . . 140
6.4.2 Adjustable stiffness . . . 142
6.5 Discussions . . . 142
6.6 Summary . . . 145

7 Conclusions and Future Work 147
7.1 Conclusions . . . 147
7.2 Future work . . . 148

Bibliography 151

List of Figures

2.1 Classification diagram of variable stiffness continuum robots: the top shows the four main categories of stiffening approaches, and the bottom illustrates the five categories of actuation mechanisms. (a) a novel continuum robot using twin-pivot compliant joints [1]. (b) a spring-based continuum robot [2]. (c) a continuum microsurgical robot using nonuniform patterns on coaxial tubes [3]. (d) a MIS continuum robot with novel layer jamming mechanism [4]. (e) a cable-driven continuum robot with stiffening sheaths [5]. (f) a soft modular MIS manipulator [6]. (g) a pneumatically actuated soft manipulator with tendon-based stiffening [7]. (h) a SMA-driven soft robotic tentacle [8]. (i) a malleable continuum robot [9]. 7

2.2 Systematic literature review results. (a) selecting process of research studies from databases in PRISMA flowchart. (b) publication number of research articles on the stiffening approaches of continuum robots in the database (Web of Science and Scopus) and the number of studies included in this review. (c) the proportion of different stiffening mechanisms. (d) keywords about stiffness variation capability in continuum robots were used in research papers. 9

2.3 Diagram of the antagonistic forces and the antagonistic mechanisms. (a) three cases of tendon antagonism; note that the third case can be the tendon & fluidic antagonism if the origami or bellow structure is controlled by external airflow with high pressure. (b) two cases of fluidic antagonism. (c) two cases of tendon & fluidic antagonism. 11

2.4 Diagram of the TRMs used in continuum robots. (a) example relationship between temperature and the elastic modulus of LMPA. (b) diagram of the typical design structure of tendon-driven continuum robots with SMA spring spine. (c) diagram of the typical design structure of SMA-driven continuum robots. (d) diagram of the typical design structure of TRM applied in actuator-like fluidic-chamber-driven continuum robots. (e) diagram of the typical design structure of TRM applied in normal continuum robots. 17

2.5 Diagram of the jamming mechanism used in continuum robots. (a) illustration depicting the jamming phenomenon. (b) relationship between the elastic modulus and varying vacuum levels. (c) diagram of STIFF-FLOP [6]. (d) diagram of the typical design structure of FJ/GJ/LJ/HJ applied in actuator-like fluidic-chamber-driven continuum robots. (e) photo of the double-flap layer jamming pattern [10]. (f) diagram of the typical design structure of LJ applied in tendon-driven continuum robots [10]. (g) diagram of the typical robot body with FJ applied. (h) diagram of strings of beads type of GJ. (i) photos of the PJ [11]. 25
2.6 Diagrams of different mechanical structures for stiffness regulation in continuum robots. (a) lockable mechanism. (b) concentric anisotropic tube. (c) two types of variable stiffness ball joints. (d) friction change mechanism by SMA spring. (e) two types of constraint tubes, outer constraint and inner constraint. (f) active-braid element for fabricating the robot body. . . 29
2.7 Promising research topics on stiffening methods or mechanisms for continuum robots. 36

3.1 The continuum robot. (a) photo of the continuum robot. (b) a sectional view of the CAD model. (c) photo of the support spine of the robot. 43
3.2 A support spine segment. (a) assembly photo. (b) exploded-view drawing. . 45
3.3 Diagram of the actuator unit and drive mechanism. (a) diagram of the driving cable arrangement, A1-D1 are for controlling Section 1 (green), and A2-D2 are for controlling Section 2 (red). (b) photo of the actuator unit (motors labelled M1/M3 and M2/M4 were spaced 90° apart for controlling Section 1 and Section 2, respectively). (c) diagram of the spool mechanism. 46
3.4 Layer jamming in the double-side flap pattern with guide holes. 47
3.5 Jamming sheath. (a) diagram of the weaving method. (b) photo of the assembled layer jamming sheath that covers the support spine. 48
3.6 Diagram of equivalent beam and deflection cases. (a) diagram of the robot structure and equivalent beam. (b) four study cases of deflections of the continuum robot. *Case 1* straight beam under transverse load, *Case 2* straight beam under axial load, *Case 3* curved beam under transverse load, and *Case 4* curved beam under axial load. 51
3.7 Experiment setup. (a) robot at 0° bending. (b) robot at 90° bending. (c) robot at 180° bending. Note that A and T in the figure represent the axial and transverse directions, respectively. 56
3.8 Force-deflection plots of the robot under Transverse (T direction) loads: (a) at 0° bending, (b) at 90° bending, (c) at 180° bending; Force-deflection plots of the robot under axial (A direction) loads: (d) at 0° bending, (e) at 90° bending, (f) at 180° bending. 57
3.9 Average stiffness results. (a) transverse direction with $n = 3$. (b) axial direction with $n = 3$. (c) transverse direction with $n = 5$. (d) axial direction with $n = 5$. Note that the red dots denote the average stiffness, and the blue dots denote the stiffness before buckling. 61

3.10 Photos of the robot actuating and gripping experiments. (a)-(f) the robot is at different bending postures. (g) the robot is gripping a paper roll with a weight of 590g and a diameter of 145mm. (h) the robot is gripping an iron bucket with a weight of 1.2kg and a diameter of 180mm. (i)-(l) the robot is moving a piece of iron (511g) using its end-effector, (i)-(j) show a normal moving task, and (k)-(l) show the task with the obstacle. 62

4.1 Photos and diagram of the structure of continuum robots. (a) a novel extra slender continuum robot [12]. (b) a cable-driven manipulator [13]. (c) a snake-inspired layer-driven continuum robot [14]. (d) sectional view of a tendon-actuated continuum robot [5]. (e) a wire-driven continuum robot with six sub-sections [15]. (f) a diagram of general continuum robots. . . . 67
4.2 General robot kinematics. (a) the geometric relationship of a multi-segment continuum robot. (b) diagram of a constant curvature segment. 69
4.3 Diagram of the ETS method. 72
4.4 An example 2D workspace and boundary features of a continuum robot with $N = 3$, $L = 50$mm, $\theta_{\max} = 180°$. The green colour shows the true workspace area, and the blue colour shows the boundary generated by the ETS method. 73
4.5 Example boundary lines and boundary surfaces with $N = 3$, $D = 1°$, $L = 50$ mm, $\theta_{\max} = 180°$. (a) boundary line of the true workspace (Algorithm 4.1). (b) a quarter of the boundary surface of the true workspace (Algorithm 4.1). (c) boundary line from the ETS method (Algorithm 4.2). (d) a quarter of the boundary surface from the ETS method (Algorithm 4.2). 75
4.6 Workspace with different parameters. The green colour shows the true workspace area, and the blue lines show the boundary calculated by the ETS method. 77

5.1 Diagram of continuum robots. (a) a photo of the OctRobot-I robot. (b) mechanical structure of a class of continuum robots. 87
5.2 Diagram of the rigid-link approximate model of continuum robots. 89
5.3 Illustration of a continuum robot with two bending configurations [16]. . . . 92
5.4 Photo of the entire experimental platform. 110
5.5 The linearity between forces and lengths: the length L_1 vs the force u_1 of the right cable; and the length difference $\Delta L := L_1 - L_2$ vs the force difference $\tau_1 := u_1 - u_2$. ("×" represents test data, and the dash lines are the fitted functions.) 111
5.6 Experiments for open-loop stiffening. 112
5.7 Photo sequence of the position control with $\theta_\star = 10$ deg and $\gamma = 1, K_{\mathrm{d}} = 0.1$. 114
5.8 Position control performance for the desired configuration $\theta_\star = 5$ deg with $\gamma = 1$ and different K_{d}. 118
5.9 Position control performance for the desired configuration $\theta_\star = 5$ deg with $K_{\mathrm{d}} = 1$ and different γ. 119
5.10 Position control performance for the desired configurations $\theta_\star = 10$ deg and 15 deg with $K_{\mathtt{d}} = 1$ and $\gamma = 0.1$. 120
5.11 A large $\gamma = 10$ leads to unstable performance. 121

5.12 Stiffness regulation with the different configurations. 121
5.13 Experiments to evaluate the robustness of the closed-loop robotic system: (a) an external disturbance was added to the distal point of the robot. (b) the robot was controlled to encounter a semi-rigid foam obstruction. 121
5.14 Results of the robustness evaluation experiments: (Left) Applying external disturbances; (Right) Encountering a semi-rigid foam obstruction. 122

6.1 Schematic of a layer-jamming structure in continuum robots. 128
6.2 An illustration of the initial condition and the equilibria manifold $\mathcal{M}$. For a given initial condition $(\boldsymbol{q}(0), \mathbf{0}_3, \mathbf{0}_3)$, a larger $u_{\mathrm{p},1}$ implies a smaller distance from $\chi(0)$ to $\mathcal{M}$, thus $\chi(0)$ located in its domain of attraction; a smaller $u_{\mathrm{p},2}$ may cause the initial condition outside the domain of attraction, failing to achieve shape locking. 138
6.3 Photo sequence of the shape-locking experiments: (a) Phase 1: initial configuration without u; (b) Phase 2: drive to the bending configuration 60° via tendon force u; (c) Phase 3: vacuum to $u_{\mathrm{P}} = 30$ kPa with motor-driven retained; (d) Phase 4: vacuum retained and tendon released $u = 0$. (Photos were taken in the steady state of each phase.) 141
6.4 Trajectory of the tendon force u_1 in the shape-locking experiment. 141
6.5 Overlay photos of the shape-locking phenomenon. Left: displacement of 9.2 mm with $u_{\mathrm{p}} = 30$ kPa; Right: displacement of 3.8 mm with $u_{\mathrm{p}} = 80$ kPa. ("•" and "•" are used to mark a fixed point on the robot body; one-side contours are also highlighted in the figure.) 141
6.6 Experimental results showing the relationship between u_{p} and the transverse stiffness under jamming sheaths with different layers. ("×" shows the mean values; color band represents the ±1 standard deviation.) 142
6.7 Experimental results showing the relationship between pressure u_{p} and the steady-state input force u_1 ("×" shows the mean values; color band represents the ±1 standard deviation). 143

List of Tables

2.1 Classification of stiffness tuning approaches for continuum robots † 8
2.2 Summary of continuum robots with thermally responsive materials† 18
2.3 Summary of continuum robots with jamming mechanisms 24
2.4 Comparison of different stiffening approaches 33

3.1 Physical properties and performance of the continuum robot 44

4.1 Summary of parameters of example continuum robots 68
4.2 Summary of workspace area calculated by the ETS method 79
4.3 Summary of workspace volume calculated by the ETS method 80

5.1 The steady-state errors in the time interval $[4, 8]$s of different scenarios (Unit: deg) 116

6.1 List of coefficients in the LuGre model 131

List of Publications

1. Yeman Fan, Dikai Liu, Lin Ye, "A novel continuum robot with stiffness variation capability using layer jamming: design, modeling, and validation", *IEEE Access*, vol.10, pp.130253-130263, 2022.

2. Yeman Fan, Dikai Liu, "An equivalent two section method for calculating the workspace of multi-segment continuum robots", *2023 IEEE International Conference on Robotics and Automation (ICRA)*, London, United Kingdom, pp. 9658-9664, 2023.

3. Yeman Fan, Bowen Yi, Dikai Liu, "An overview of stiffening approaches for continuum robots", *Robotics and Computer-Integrated Manufacturing*, vol.90, pp.102811, 2024.

4. Bowen Yi†, Yeman Fan†, Dikai Liu, "A novel model of layer jamming-based continuum robots", *2024 IEEE International Conference on Robotics and Automation (ICRA)*, Yokohama, Japan, pp.12727-12733, 2024.

5. Bowen Yi†, Yeman Fan†, Dikai Liu, José Guadalupe Romero, "Simultaneous position-and-stiffness control of underactuated antagonistic tendon-driven continuum robots", *IEEE Transactions on Automation Science and Engineering*, pp.1-17, 2024, Early Access.

†Bowen Yi and Yeman Fan contributed equally to this work.

STATEMENT OF CONTRIBUTION OF AUTHORS:
In Publications 4 and 5 included in this thesis, Bowen Yi contributed to help develop models, controllers, and proofing the theories. In order to make this thesis self-contained and clearly present the entire research work, these collaborated works are included in this thesis and approved by Bowen Yi without interest of conflict. The author appreciates Bowen Yi for his help in completing this research work.

Chapter 1

Introduction

1.1 Scope and overview

A continuum robot is a type of robot or manipulator that draw inspiration from nature organisms, such as tentacles, snakes, and trunks. It has recently been a research focus due to its inherent characteristics, including compliance, flexibility, dexterity, and safety [17–19]. These advantages have facilitated the application of continuum robots in various domains, including living care service, medical surgery, unstructured environment exploration, and human-robot interaction [19–21]. Despite their increasing presence in real-world applications, continuum robots still face several technical challenges. Among them, a standing one is how to adjust or control the stiffness to meet different task requirements [19–23]. For example, in a minimally invasive surgery (MIS) or natural orifice transluminal endoscopic surgery (NOTES), a continuum robot needs to be in a low stiffness condition to minimise side effects to the patient when it is fed into the human body. On the other hand, when reaching to the target area, it may need to be shifted to a high stiffness level to transmit force and ensure motion accuracy for diminishing trauma [20, 24]. Therefore, the ability to dynamically adjust stiffness is essential for continuum robots.

The ability and methodology to adapt stiffness have been issues of fundamental importance for continuum robots. With the rapid development of bionics, design technology, and materials science, the continuum robotics community has reported momentous progress

on stiffening approaches in recent years [25–27]. However, several challenges have not been well addressed yet, e.g., dynamic stiffness control, large stiffness change ratios, fast response, compact and lightweight stiffness tuning devices, and versatile mechanisms.

In the meanwhile, despite many efforts that have been devoted to addressing the challenges of dynamical modelling [28–34] and real-time control for continuum robots [35–37], how to achieve simultaneous position-and-stiffness control for this type of robot is still an open area of research.

This thesis is devoted to addressing the research challenge of stiffness regulation in continuum robots by studies on robot design, workspace analysis, modelling, and control. Firstly, a continuum robot with a layer jamming technique was designed. To analyse the robot's effective stiffness and its changing tendency under varying conditions, a static deflection analysis method based on the Euler-Bernoulli beam theory was proposed. Subsequently, an equivalent two section method was developed for analysing the workspace of continuum robots based on forward kinematics and a piecewise constant curvature assumption. Furthermore, a rigid-link dynamical model was developed to analyse the robot's open-loop stiffening properties, and a new passivity-based controller that is capable of controlling the position and stiffness simultaneously was proposed. The rigid-link dynamical model was refined by integrating the layer jamming mechanism to elucidate two fundamental properties of continuum robots with layer jamming technique: shape locking and adjustable stiffness.

1.2 Contributions

The main contribution of this thesis is the modelling and control of a class of underactuated continuum robots to achieve variable stiffness. The specific contributions are as follows:

- Design of a layer jamming-based continuum robot with variable stiffness in both the transverse and axial directions (Chapter 3). The layer jamming sheath applied in this design was woven by a novel method that involves using restriction wires on the adjacent two layers to restrict the flaps to provide a larger relative movement capability. The robot's static deflections under different external forces were analysed,

and approximate stiffness models were also developed to analyse the robot's effective stiffness and its changing tendency.

- Introducing the equivalent two section (ETS) method (Chapter 4). The workspace feature of multi-segment continuum robots was analysed, and a preliminary threshold for the completed level of their workspace was identified. Based on these findings, the ETS method was proposed to provide an efficient and accurate means of calculating the workspace area and volume for multi-segment continuum robots.

- Establishing a rigid-link dynamical model for a class of underactuated antagonistic continuum robots (Chapter 5). This energy-based model has the ability to interpret the underlying mechanism for open-loop stiffening. Utilising this model, a novel potential energy-shaping controller was designed to achieve simultaneous position-and-stiffness control for underactuated continuum robots.

- Improving the proposed rigid-link dynamical model by incorporating the LuGre frictional model (Chapter 6). This integration allows the model has the ability to interpret the two fundamental properties of continuum robots with layer jamming techniques, i.e., shape locking and adjustable stiffness.

Additionally, this thesis also provides a comprehensive review of stiffness tuning approaches employed in continuum robots over the past two decades, which aims to elucidate the synergistic roles played by materials, actuators, mechanical configurations, and mechanisms in achieving controlled stiffness modulation.

1.3 Thesis structure

The remainder of this thesis is organised as follows:

Chapter 2 surveys related work within the realm of stiffness tuning approaches for continuum robots. It presents a comprehensive review of the state-of-the-art research on stiffness tuning techniques employed in continuum robots over the last two decades, and key techniques related to stiffness tunability mechanisms and stiffening methods are also analysed and categorised.

Chapter 3 presents the design and fabrication of the novel tendon-driven continuum robot (OctRobot-I). It illustrates the details of design of the robot's support spine, jamming sheaths, and actuator unit. This chapter also includes the analysis of the robot's static deflections and the development of approximate stiffness models to examine the robot's effective stiffness and its trend of changes. Furthermore, experimental results and real-world actuating and gripping performance of the robot are also demonstrated in this chapter.

Chapter 4 analyses the workspace features of multi-segment continuum robots and presents an efficient and accurate method to calculate their workspace area and volume. Additionally, simulations with several different configurations are included in this chapter to verify the proposed ETS method and identify a preliminary threshold of the completed level of their workspace.

Chapter 5 presents the modelling and control of a class of underactuated antagonistic continuum robots. It develops a rigid-link dynamical model for this type of robot and then establishes a port-Hamiltonian dynamical model to analyse its potential energy. Based on these, a novel potential energy-shaping controller is highlighted in this chapter to achieve simultaneous position-and-stiffness control. Furthermore, experiments and results under a series of control conditions to validate the proposed models and controller are also included.

Chapter 6 further improves the proposed rigid-link dynamical model by elegantly integrating the LuGre frictional model. It exhibits the abilities of the improved model to interpret the two fundamental properties of layer jamming-based continuum robots: shape locking and adjustable stiffness. Moreover, experiments to validate the model and the two phenomena are included in this chapter.

Chapter 7 concludes the thesis and discusses some potential avenues for future work.

Chapter 2

Literature Review

This chapter aims to present a comprehensive review and comparison of the state-of-the-art research on stiffening techniques for continuum robots over the last two decades. It explores the roles of materials, actuators, mechanical structures, and mechanisms for tuning stiffness and summarises the challenges that this field has encountered to provide an all-encompassing understanding of continuum robots. Through analysis and comparison, it aims to elucidate the synergistic roles played by materials, actuators, mechanical configurations, and mechanisms in achieving controlled stiffness modulation. By highlighting the challenges encountered along the way, it strives to offer a nuanced and complete perspective on the continuum robotics landscape. [1]

2.1 Overview

Tuning or controlling a continuum robot's stiffness to enhance its versatility and adaptability remains a significant challenge in the robotics community [18, 19, 23]. Stiffness, a fundamental property of materials, characterises their resistance to deformation under applied loads. It serves as a metric for measuring a material's ability to resist elastic deformation, typically quantified by parameters such as the modulus of elasticity or Young's

[1] The results presented in this chapter have previously appeared in the publication: Yeman Fan, Bowen Yi, Dikai Liu, "An overview of stiffening approaches for continuum robots", *Robotics and Computer-Integrated Manufacturing*, vol.90, pp.102811, 2024.

modulus. In the field of mechanics, stiffness is an important property for the design and analysis of structures and mechanical components. In robotics, stiffness refers to the ability of a robot's joints or links to resist changes in their shape or orientation when subjected to external forces or loads. Mathematically, stiffness can also be expressed as the ratio between the force/torque and the resulting change in its displacement or angle, respectively.

Compared to traditional rigid-link robots, continuum robots offer remarkable adaptability and maneuverability due to their characteristics of flexible and continuously bending bodies [17, 21]. There are several key points highlighting the flexibility of continuum robots, including enhanced maneuverability, versatility in movement, and safety and compliance. Their ability to adapt, manoeuvre, and safely interact with their environment sets them apart from traditional rigid-link robots, opening up new possibilities in robotics and automation. However, this greater flexibility and adaptability may sacrifice the stiffness of continuum robots, which, however, is a critical variable in characterising and controlling the behaviour of continuum robots, especially in tasks such as grasping, manipulating, and human–robot interaction [19, 23, 24]. In order to ensure continuum robots can be applied in various application scenarios, this type of robot is required to have the capability of adjustable stiffness. For example, a high stiffness level should be achieved to maintain its position and shape under extra loads, while low stiffness is preferred to allow the robot to adapt to changing or uncertain environments. Therefore, the ability to tune the robot's stiffness becomes vital for various purposes [25, 26]. The term *stiffening* refers to the process of modifying or adjusting robots' stiffness through internal or external factors, including antagonistic force, temperature, friction, pressure, structural switching, and active-braid element.

In recent years, significant interest has been focused on modulating stiffness for continuum robots to enhance their deformability, controllability, and stability [25–27]. This has led to the development of various types of stiffening approaches. This chapter aims to provide a systematic classification of these approaches, and primarily focuses on the technical routes that have been adopted for stiffness tuning in continuum robots. Hence, it leads to a broad classification: antagonism, thermally responsive materials, jamming mechanism, and mechanical structure. It is important to note that these stiffening approaches are closely

related to the actuation mechanisms adopted in robots, which have a significant impact on their application realms and stiffening performance. In this chapter, five categories of actuation mechanisms are considered, including tendon-driven, fluidic-driven, tendon & fluidic-driven, SMA-driven, and manual-driven. By considering the two perspectives, i.e., stiffening and actuation, the classification is further refined in Figure 2.1, and the details of relevant literature are summarised in Table 2.1.

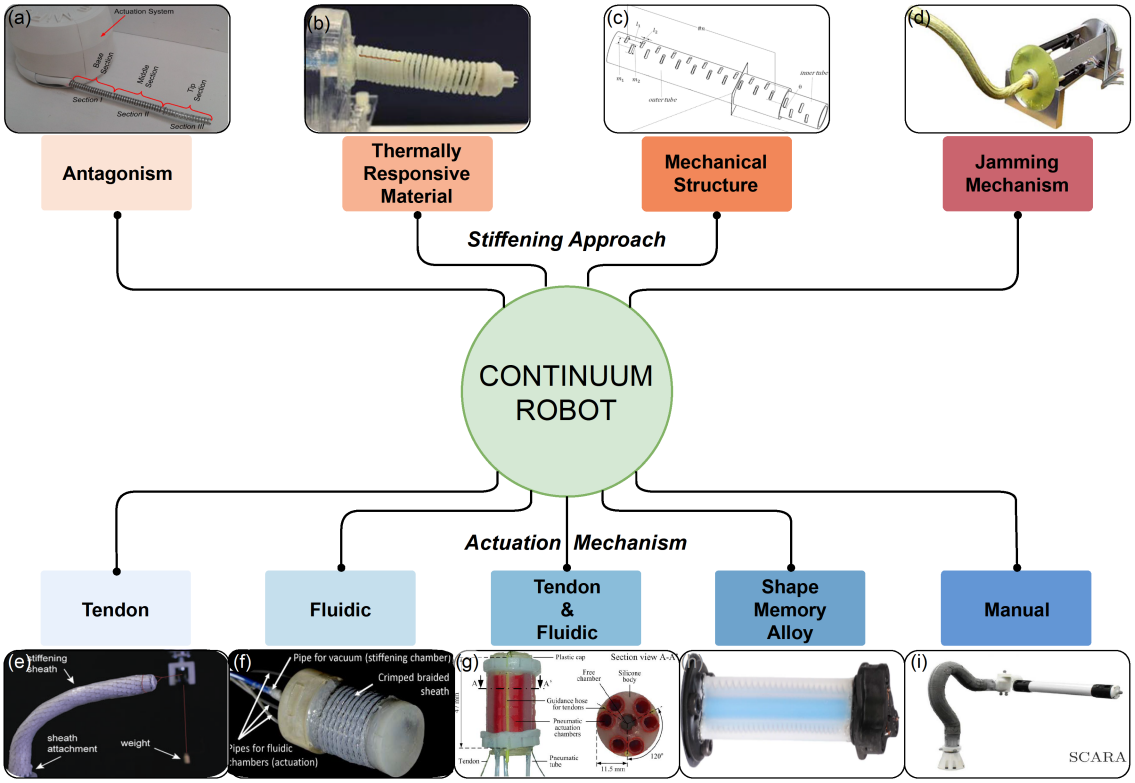

FIGURE 2.1: Classification diagram of variable stiffness continuum robots: the top shows the four main categories of stiffening approaches, and the bottom illustrates the five categories of actuation mechanisms. (a) a novel continuum robot using twin-pivot compliant joints [1]. (b) a spring-based continuum robot [2]. (c) a continuum microsurgical robot using nonuniform patterns on coaxial tubes [3]. (d) a MIS continuum robot with novel layer jamming mechanism [4]. (e) a cable-driven continuum robot with stiffening sheaths [5]. (f) a soft modular MIS manipulator [6]. (g) a pneumatically actuated soft manipulator with tendon-based stiffening [7]. (h) a SMA-driven soft robotic tentacle [8]. (i) a malleable continuum robot [9].

In order to demonstrate the existing research, quantitative data and the selection criteria for research papers on stiffening approaches for continuum robots are presented at the end of this section. A systematic literature search was conducted using the Web of Science and Scopus databases. The search terms "continuum robot", "soft robot", "variable stiffness",

TABLE 2.1: Classification of stiffness tuning approaches for continuum robots †

Classification			Actuation Mechanism		
			Tendon	Fluidic	Ten.&Fl., SMA
Stiffening approach	Antagonism		[1, 16, 38–53]	[54–62]	[7, 63–85] (Ten.&Fl.)
	Thermally responsive material	Shape Memory Alloy	[2, 86–91]	–	[8, 92–95] (SMA)
		Shape Memory Polymer	[96]	[97–101]	Manual
		Low Melting Point Alloy	[84, 102–106]	[107–113]	[114, 115]
		Thermoplastics	[116–121]	[122–125]	–
	Jamming mechanism	Fibre/filament	[126, 127]	[113, 128]	[129, 130]
		Granular/particle	[5, 131–139]	[6, 140–151]	[152–154]
		Layer/laminar	[4, 5, 10, 155–158]	[159, 160]	[9, 152, 153, 161]
		3D Printed Fabrics	–	[11, 162]	–
		Hybrid	[163]	[164]	[153]
	Mechanical structure	Lockable Mechanism	[165–167]	[168]	–
		Friction Change Mechanism	[169, 170]	–	–
		Variable Stiffness Ball Joint	–	[171]	[172, 173]
		Constraint Tube	[174–179]	[180]	–
		Concentric Anisotropic Tube	–	–	[3, 181, 182]
		Active-Braid Element	[183]	–	–

† "–" refers to no available work belonging to a specific category. Ten.&Fl. and SMA represent that continuum robots in these related works are actuated by Tendon & Fluidic and Shape Memory Alloy, respectively.

and "stiffening" were used in the article title, abstract, and keywords. The selection of papers for this chapter was conducted in accordance with PRISMA guidelines, as shown in Figure 2.2(a). After carefully assessing the main text for eligibility, 160 research papers highly related to this topic that have been published during the last two decades were found and included. As illustrated in the line chart of Figure 2.2(b), the number of research papers in the databases on this topic has significantly increased over the past two decades. This upward trend indicates that stiffening approaches in continuum robots represent a promising and rapidly growing area of research. The increasing number of publications underscores the importance and current interest in this innovative research direction. To clearly show the publication trend and paper distribution among publishing years, these studies were visualised in the bar chart of Figure 2.2(b). In the early stages, before 2014, the exploration of stiffening for continuum robots was in its infancy, with less than ten articles published annually and some years even lacking any contributions. However, a turning point occurred in 2016, marking the beginning of significant progress in this specific area. Notably, the year 2022 alone witnessed the indexing of more than 30 articles, demonstrating the continued growth and interest of the robotics community. Figure 2.2(c)

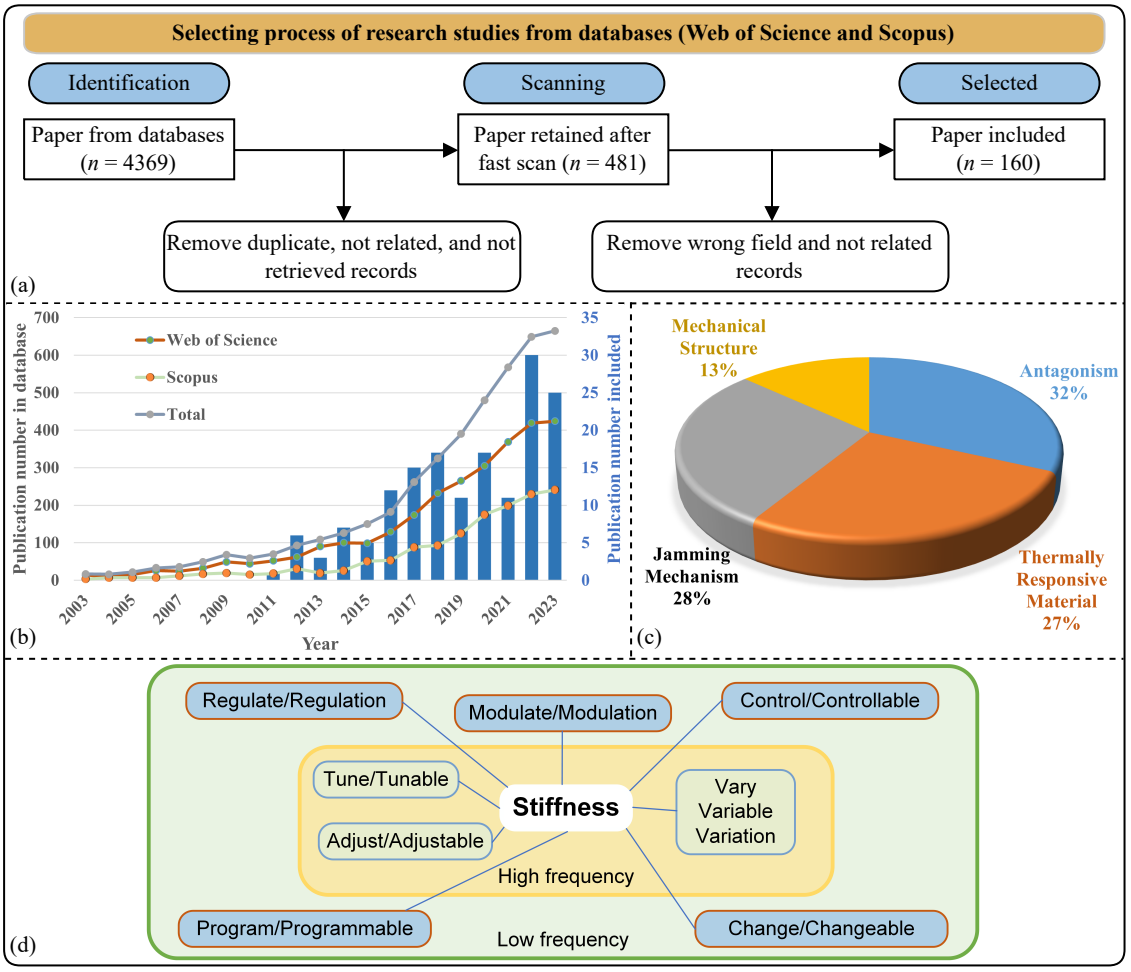

FIGURE 2.2: Systematic literature review results. (a) selecting process of research studies from databases in PRISMA flowchart. (b) publication number of research articles on the stiffening approaches of continuum robots in the database (Web of Science and Scopus) and the number of studies included in this review. (c) the proportion of different stiffening mechanisms. (d) keywords about stiffness variation capability in continuum robots were used in research papers.

illustrates the paper distribution of the four categories of stiffening approaches reviewed in this chapter. The keywords to describe stiffening phenomena in continuum robots are summarised in Figure 2.2(d) according to the frequency used in these papers.

In this chapter, the applications of continuum robots are broadly categorised into medical applications and general industrial applications. The medical applications encompass a range of procedures, including surgery, rehabilitation, endoscopy, guidance and navigation, and cardiac interventions. These utilisation scenarios demonstrate the potential of

continuum robots in performing minimally invasive procedures, enhancing surgical precision, and facilitating targeted interventions within the body. On the other hand, general industrial applications cover a variety of tasks, such as living assistance and elderly care, general grasping, pick-and-place operations, and actuation tasks. Continuum robots have the potential to be versatile and adaptive tools in these settings, offering gentle support for individuals with mobility challenges and providing flexible and adaptable manipulation capabilities.

2.2 Stiffness tuning approaches

The ability to achieve tunable stiffness is of utmost importance for continuum robots to effectively meet a wide range of application requirements. Stiffening approaches can be generally categorised into antagonism, thermally responsive materials, jamming mechanism, and mechanical structure. This section conducts an in-depth analysis of the detailed classification, working principles, and properties of these stiffness tuning methods, and then discusses their applications in continuum robots.

2.2.1 Antagonism

Antagonism-based techniques have been utilised to control the stiffness of continuum robots by leveraging opposing forces. It offers a simple and effective way to tune the stiffness without requiring additional structures or devices. The basic idea is to use a pair (or more) of antagonistic forces to manipulate the pressure, tension, or a combination of both within continuum robots. Figure 2.3 gives an intuitive illustration depicting the generation of a pair of antagonistic forces that are denoted as F and F' through the interaction between the robot body and the driven actuator. Due to their simplicity, antagonism mechanisms have gained popularity in tendon-driven, fluidic-driven, or tendon & fluidic-driven continuum robots. The antagonistic mechanism is applicable to various types of continuum robots in which a pair of antagonistic forces can be generated. Existing literature categorises the antagonisms used for stiffness tuning in continuum robots into three main types:

- Tendon Antagonism [1, 16, 38–53], see Figure 2.3(a)
- Fluidic Antagonism [54–62], see Figure 2.3(b)
- Tendon & Fluidic Antagonism (Ten.&Fl.) [7, 63–85], see Figure 2.3(a) and (c)

By employing these different antagonism mechanisms, continuum robots can effectively adapt to various tasks and environments. The choice of the specific antagonism technique depends on the robot's design, application requirements, and desired stiffness control capabilities.

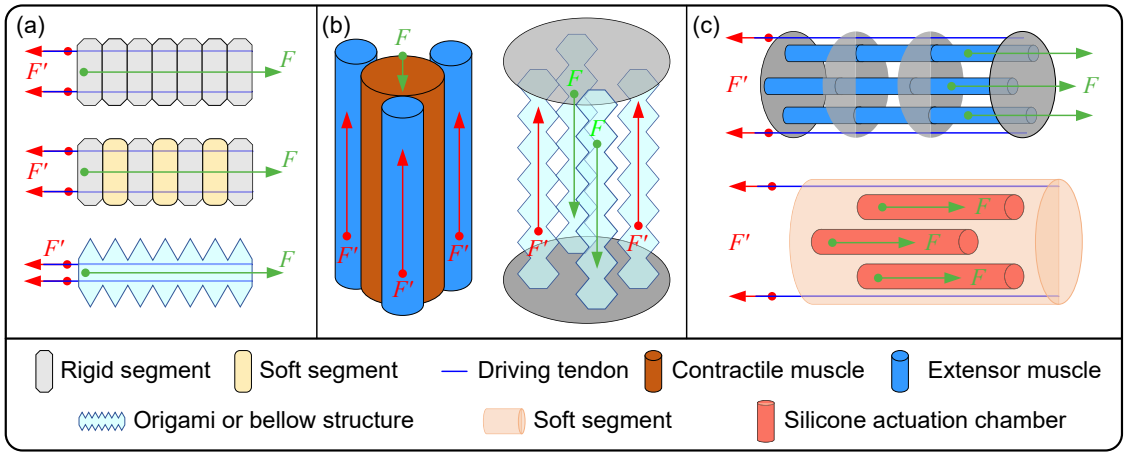

FIGURE 2.3: Diagram of the antagonistic forces and the antagonistic mechanisms. (a) three cases of tendon antagonism; note that the third case can be the tendon & fluidic antagonism if the origami or bellow structure is controlled by external airflow with high pressure. (b) two cases of fluidic antagonism. (c) two cases of tendon & fluidic antagonism.

2.2.1.1 Tendon antagonism

This type of antagonism relies on opposing tensions created by tension-driven mechanisms to achieve stiffness regulation [16]. This mechanism includes tendon-driven systems, where flexible cables or tendons are actuated to generate opposing forces that govern the robot's compliance. In the case of tendon actuation, the force F' is generated by driven cables. When a pair of cables are arranged on two sides of the robot, and tensions are increased simultaneously, the robot body undergoes compression, leading to a reaction to counteract the applied tensions. Hence, the elastic potential energy of the robot body increases – resulting in a higher stiffness. In this type of continuum robots, the behavior of the robot

body can be rigid [16, 38–41, 51, 52], rigid and soft [42–44], soft [45, 50], compliant origami [46, 53], compliant joint[1], or spring [47–49].

Many works have incorporated rigid bodies in continuum robots to enhance stiffness by tendon antagonism. For MIS, adjustable stiffness cable-driven manipulators with bendable hollow structures made of rigid links were developed, allowing continuous stiffness adjustment via cable tensions, even during motion [16, 38]. This approach also addressed stiffness issues of continuum robots used in NOTES [39]. A bio-inspired finger utilizing tension antagonism for stiffening was designed to mimic human finger movements [40, 50]. Additionally, Liu *et al.* [41] introduced a novel mechanism to improve stiffness and load capacity in cable-driven manipulators, ensuring dexterity and accuracy while allowing stiffness tuning for optimal performance in various scenarios.

In order to further improve stiffness variation capability, a combination of rigid and soft segments can be utilised. A robot tail with alternating rigid and soft segments was developed, allowing precise stiffness control through adjustable cable tensions [42]. Similarly, a variable stiffness mechanism for MIS needles, which alternates between rigid and compliant segments, regulates stiffness via driven cable tension [43]. Inspired by push puppet toys, Bern *et al.* developed a continuum arm that is based on rigid plastic and soft foam to realize stretch and stiffening capability [44].

A continuum robot with a soft body, compliant joint, origami body, or spring body enables easy stiffness control via cable tension by leveraging its compressibility. For instance, an octopus-like robot with an artificial muscular hydrostat made from silicone materials was developed in [45]. A programmable origami structure for dynamically dexterous robots uses flat sheet crease patterns to create adjustable stiffness through origami bellows [46, 53]. A novel continuum design with twin-pivot-compliant joints enhances stiffness and reduces parasitic twists [1]. Continuum mechanisms with cable-driven and spring bodies for stiffness variation were developed [47, 48], and an environmentally interactive manipulator capable of passing obstacles and adjusting stiffness via tendons was proposed [49].

In summary, tendon actuation proves to be a versatile approach for achieving variable stiffness in continuum robots. By manipulating cable tensions, these robots can exhibit a

wide range of stiffness tuning behaviours, presenting opportunities for developing precise and adaptable robotic systems.

2.2.1.2 Fluidic antagonism

In fluidic antagonism, stiffness control is achieved by manipulating fluid pressure within the robot's body. By regulating the flow or pressure of the fluid, it becomes possible to generate opposing forces, thus allowing for stiffness adjustments. Fluidic antagonism is often utilised in continuum robots that are driven by fluidic systems, such as pneumatic artificial muscles [54–58] and fluidic chambers [59–62]. These components enable the generation of a pair of antagonistic forces, i.e. F and F'. The actuators with antagonistic action, capable of extension and contraction, are responsible for producing these forces. As the robot undergoes this antagonistic action, the elastic potential energy within the system increases, thus leading to improved stiffness characteristics.

The continuum robots composed of artificial muscles typically follow a consistent structure, consisting of one extensor artificial muscle at the centre and surrounded by three contractile artificial muscles [54–57]. By combining contractile and extensor artificial muscles, the manipulator can independently adjust its stiffness regardless of the configuration. To further improve the working ability of the robot, a dual-segment continuum manipulator with independent stiffness and angular position was developed [56]. Furthermore, an improved structure was proposed in [58] to achieve greater flexibility in robot configurations, incorporating one extensor artificial muscle and six contractile artificial muscles arranged in three pairs. This novel robot arm design decouples end-effector positioning from stiffness by incorporating more contractile artificial muscles.

Fluidic chambers have also been utilised to implement the antagonism mechanism for stiffness control of continuum robots. It is worth noting that fluidic chambers generally have lower strength and force output compared to artificial muscles. While fluidic-driven systems can provide stiffness adjustability by manipulating fluid pressure or flow, they may have limitations in terms of the magnitude of generated forces. When the robot body consists of fluidic chambers, it can enable lightweight and compact designs while exhibiting antagonistic behaviours. A recent study [59] proposed a soft robotic joint featuring a

central vertebra and tilt-arranged pneumatic soft origami actuators, where the antagonism between actuators and the vertebra improved payload capacity and stiffness variability. Another design [61] introduced a soft joint with four parallel bellows-type actuators, using a "tune-down" method to reduce actuator stiffness via pneumatic pressure control. Babu *et al.* [60] developed variable stiffness elastomeric actuators with symmetric pneumatic chambers and an inextensible layer, enabling stiffness adjustment through pressure regulation.

Artificial muscles and fluidic chambers are two approaches widely used to realise antagonism for stiffness tuning in continuum robots. Artificial muscles are known for their high force output and precise control, allowing for robust and powerful stiffness adjustments. On the other hand, fluidic chambers provide lightweight and compact designs but typically have lower force output. The selection between these approaches depends on the specific application requirements, taking into account factors such as the desired force levels, precision, and desired extent of stiffness control.

2.2.1.3 Tendon & fluidic antagonism

Apart from the single antagonism by cables, artificial muscles or fluidic chambers, researchers have combined these approaches in designing continuum robots to achieve more versatile and flexible stiffness tuning ability. The combination of tension-based and fluidic-based methods is referred to as *tendon & fluidic antagonism* in this thesis. This approach is commonly employed in continuum robots requiring a higher degree of flexibility in stiffness adjustments, with each offering unique variations and capabilities, and can be further categorised into the following five representative subclasses:

1) Tendons with *artificial muscles* [63–66]. The combination of cables and artificial muscles in continuum robots ensures control accuracy and enhances payload capability. This approach has been used in the development of a shower arm for assisting with bathing tasks [63–65]. In this series of research, tendons and pneumatic muscles are arranged radially and alternatively to enable elongation, contraction, and omnidirectional bending of the robot. The coordinated activation of cables and tendons allows for stiffness modulation,

enhancing the robot's adaptability. Another study by Harsono *et al.* [66] presents a hybrid-driven continuum robot with a dual-plane backbone structure. The unique design of the robot allows decoupled stiffness regulation from its current configuration, which makes the design easily extendable to continuum robots with multiple sections, thus enabling more versatile and scalable applications.

2) Tendons with *inflatable sleeves* [67–70]. The solution of cables with inflatable sleeves makes it possible to realise stiffness regulation by a lightweight structure. Stiffness-controllable soft and inflatable manipulators based on a bio-inspired antagonistic actuation principle are introduced [67, 68]. The combination of the two actuation mechanisms in this antagonistic robot structure is inspired by the octopus, which uses its longitudinal and transversal muscles to steer, elongate, shrink and also stiffen its continuum arms. Similarly, a tendon-driven soft gripper with variable compliance can be found in [69]. This mechanism's variable compliance draws inspiration from the stiffening movement observed in hydrostatic skeletons. Additionally, Wang *et al.* reported a remarkable dexterous tip-extending robot that possesses the capability of changing its compliance through variable-length shape-locking [70].

3) Tendons with *origami chambers* [71, 72, 81, 84, 85]. Similar to the inflatable sleeves, origami chambers can also be combined with cables for continuum robots to achieve stiffening mechanisms. Hybrid-driven continuum robot inspired by the reconfigurable feature of origami structures was presented in [71, 81, 84, 85]. Combining tendon actuation and air pressure in origami chambers, these designs allow the robot to exhibit a high extension ratio, low input pressure, and no radial expansion. With the antagonistic actuation of tendon-pulling and air-pushing, the robot can perform three degrees of freedom motion with variable stiffness. A similar structure is investigated in [72], in which a robot is designed to assist the elderly and physically impaired individuals in performing daily life activities.

4) Tendons with *bellow actuators* [73–77]. Another approach to support continuum robots with lightweight body structures is bellow actuators combining with cables. The compliance of deformable hybrid serial-parallel manipulators was studied, revealing that pneumatic actuators work in extension while cables operate in compression, enhancing stiffness

through antagonistic actuation, especially in torsion [73]. A hybrid-antagonistic-pneumatic joint combining soft actuators and rigid structures was proposed for variable stiffness [74]. In [75], a bio-inspired soft hand with pneumatic bellows backbone and driving cables that enable antagonistic control was developed. Similarly, a soft continuum manipulator that adjusts length and stiffness by using air pressure and cables was implemented in [76]. A stiffness regulator with gasbags and flexible shells utilises combined cable and pneumatic pressure for stiffness modulation [77].

5) Tendons with *silicone actuation chambers* [7, 78–80, 82, 83]. The last is the cables with silicone actuation chambers. This method is mainly applied in soft continuum robots, which are easily realised with silicone materials. A continuum silicon-based manipulator with variable stiffness is designed in [7] for MIS by using a hybrid and inherently antagonistic actuation scheme. Similarly, a manipulator for flexible gastrointestinal endoscopy was developed in [83], soft pneumatic cylindrical modules made of fibre-reinforced polymer are described [78, 79], and a tendon-driven variable-stiffness pneumatic soft gripper was validated in [82]. By using air chambers and driving cables, an antagonistic mechanism can be realised to tune its stiffness. In addition, a novel soft actuator with the capability of bearing a load heavier than itself is proposed [80]. Its movement accuracy can be guaranteed due to its variable stiffness structure, even when working with heavy loads.

The above five combinations demonstrate various ways in which tension- and fluidic-based approaches can be combined to achieve more versatile stiffness tuning for continuum robots. These combinations provide benefits such as lightweight structures, improved control accuracy, increased payload capability, and versatile and flexible stiffness control, which enables the robot to adapt to different environments and interact with objects of varying compliance, allowing for a wide range of applications in different scenarios.

2.2.2 Thermally responsive materials

Thermally responsive materials (TRMs) are a class of materials that exhibit changes in their physical or chemical properties in response to temperature. As illustrated in Figure 2.4(a), when low melting point alloy (LMPA) materials are in a melting transition, they transform from a solid phase to a liquid phase, resulting in a substantial decrease

in stiffness from a high level to a low level. In the reverse process, it releases heat energy and transforms into a solid state, exhibiting high stiffness. This unique characteristic makes TRMs extremely attractive and suitable for continuum robots. By incorporating TRMs into continuum robots, their stiffness can be adjusted by altering the elastic modulus through controlled melting and solidification status at specific temperatures. Hence, this temperature-based regulation facilitates easy modulation of the robots' stiffness. Figure 2.4(a) and (b-e) show typical designs of TRMs employed as a method for tuning stiffness in continuum robots. However, this temperature-controlled method always results in relatively slow response speed and bulky temperature regulation devices, which needs to be addressed in future research.

TRMs represent a large range of materials that can be applied in continuum robots for stiffness adjustment. According to their distinct melting and solidification temperatures or transition features, they can be classified into five primary categories: shape memory alloy (SMA) [2, 86, 88–93], shape memory polymer (SMP) [96–101], LMPA [102–110, 114], and thermoplastics (TP) [116–124, 184]. In order to clearly show the difference and compare the existing continuum robots that used TRMs, a comprehensive summary of these works is provided in Table 2.2, outlining the diverse driving mechanisms and temperature control methods employed in each category.

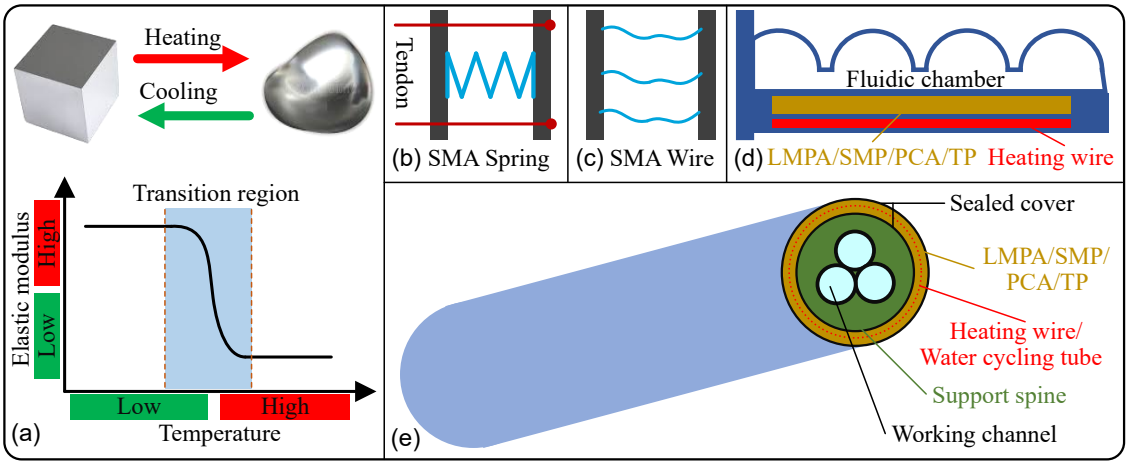

FIGURE 2.4: Diagram of the TRMs used in continuum robots. (a) example relationship between temperature and the elastic modulus of LMPA. (b) diagram of the typical design structure of tendon-driven continuum robots with SMA spring spine. (c) diagram of the typical design structure of SMA-driven continuum robots. (d) diagram of the typical design structure of TRM applied in actuator-like fluidic-chamber-driven continuum robots. (e) diagram of the typical design structure of TRM applied in normal continuum robots.

TABLE 2.2: Summary of continuum robots with thermally responsive materials†

MATERIALS	ACTUATION	TEMPERATURE CONTROL	APPLICATION	RELATED WORKS
SMA	SMA	DJ/A	Industrial (arm)	[8]
		DJ/P	Industrial (finger)	[94]
		DJ/W	Industrial (finger)	[95]
		DJ/P	Industrial (arm)	[92]
		DJ/A	Medical (MIS)	[93]
	Tendon	DJ/P	Industrial (arm)	[86, 87, 91]
		DJ/P	Medical (MIS)	[88, 89]
		EJ/P	Medical (surgery)	[90]
		DJ/W	Medical (surgery)	[2]
SMP	Tendon	EW/W	Medical (stenting)	[96]
	Fluidic	EJ/P	Industrial (arm)	[97]
		EJ/P	Industrial (finger)	[98, 99]
		EJ/A	Industrial (actuator)	[100]
		EW/W	Industrial (actuator)	[101]
LMPA	Tendon	EW/W	Medical (LESS)	[104]
		(EW+EJ)/W	Medical (LESS)	[105]
		EJ/W	Medical (colonoscopy)	[106]
		DJ/P	Medical (MIS)	[102]
		EW/W	Industrial (arm)	[103]
		EJ/P	Industrial (arm)	[84]
	Fluidic	EW/W	Industrial (arm)	[107]
		EJ/P	Industrial (actuator)	[108]
		(EW+EJ)/W	Industrial (actuator)	[109]
		EJ/P	Industrial (actuator)	[110]
		DJ/P	Industrial (actuator)	[111]
		EW/W	Industrial (arm)	[112]
	Manual	EW/P	Industrial (arm)	[114]
		EW/W	Industrial(stiffening tube)	[115]
TP	Magnetic	DJ/P	Medical (MIS)	[184]
	Tendon	EJ/A	Medical (endoscopy)	[116, 117]
		EJ/P	Industrial (arm)	[118]
		EW/W	Medical (endoscopy)	[119]
		EJ/W	Medical (NOTES)	[120] [121]
	Fluidic	EJ/(A/W)	Industrial (actuator)	[122, 123]
		EJ/P	Industrial (actuator)	[124]
		EJ/W	Industrial (actuator)	[125]

†**Acronyms in the table.** DJ/P: Direct Joule heating and passive cooling; DJ/A: Direct Joule heating and active air cooling; DJ/W: Direct Joule heating and active water cooling; EJ/P: External Joule heating and passive cooling; EW/W: External water heating and active water cooling; EJ/W: External Joule heating and active water cooling.

2.2.2.1 Shape memory alloy

SMA is a widely popular thermally responsive material in engineering, which enjoys the property of showing stiffness and flexibility in reaction to varying temperatures [185]. This property can change the internal elasticity of the module as temperature changes, thereby affecting the stiffness. However, SMA differs from other materials because it undergoes a solid-state phase transformation between austenite (high-temperature phase) and martensite (low-temperature phase), and can recover to its original shape upon heating, which makes it normally used as an actuation approach rather than a pure stiffening approach in continuum robots. The heating of SMA can be achieved through either external Joule heating methods [90] or direct Joule heating by passing an electrical current through the SMA wire [2, 86–89, 91–93].

Continuum robots with variable stiffness by SMA generally have two actuation mechanisms: SMA-driven [8, 92–95] and tendon-driven [2, 86–91]. The SMA-driven mechanism has been utilised in octopus-inspired robot arms or manipulators for manipulation tasks or MIS and exhibits remarkable capabilities such as elongation, contraction, bending in any direction, and adjustable stiffness [92, 93].

To enhance flexibility, the SMA wire/spring has been used in tendon-driven continuum robots for tuning stiffness. An octopus-inspired soft robot arm with SMA springs was developed in [86, 87], which has the ability to elongate the arm or increase its stiffness by the antagonism with the longitudinal driven cable. Cao *et al.* designed a flexible manipulator for MIS, whose variable stiffness is achieved by incorporating proactive deformation of SMA within each module [88]. Other similar designs are the SMA-based sheath used in a continuum manipulator for MIS [89], and the SMA spring applied in the wristed percutaneous robot for pericardiocentesis [90]. However, these robots lacked an active cooling system, resulting in extended transition times to a rigid state. To address such a cooling time issue, air cooling pumps were used in SMA-driven soft robotic tentacle [8], and water cooling systems were introduced in [2, 95].

2.2.2.2 Shape memory polymer

Similarly to SMA, SMP is used in continuum robots to attain variable stiffness capability. Notably, SMP has several advantages over SMA, including lower density ranging from 1.13 to 1.25 g/cm^3 and lower cost [97]. Additionally, SMP exhibits excellent suitability for processing complex 3D shapes, and it is compatible with 3D printing techniques. A continuum robot for gastrointestinal stenting made by 3D printable SMP tubes is presented in [96]. To trigger the phase transition by raising the temperature, a silicon tube that can circulate cold or warm water onto the SMP tube was integrated.

In the context of medical applications, SMP holds an exceptional advantage due to its biocompatibility. In [97], a pneumatic soft arm for MIS was developed by using spiral balloon weaving and an SMP backbone. The electric wire and cooling channels were applied to the SMP backbone, and this aims to achieve stiffness-changing ability. Similar designs also include SMP layers in SMP joints in air chamber-driven robotic fingers [98, 99], a soft pneumatic actuator [100], and an SMP and hydraulic temperature regulation system [101].

2.2.2.3 Low melting point alloy

LMPA provides another option for introducing variable stiffness capability in continuum robots because of its high strength and toughness. This material exhibits a state transition from solid to liquid and vice versa upon experiencing temperature variations. These alloys are composed of a mixture of elements with low melting temperature, such as bismuth (Bi), lead (Pb), tin (Sn), cadmium (Cd), gallium (Ga), and indium (In). When combined, these elements can form alloys with melting points even lower than those of the individual components [84, 103, 115]. The phase change temperature of the material can be precisely controlled by adjusting the composition of the alloy, and it has many advantages, including high energy density, environmental friendliness, and a long lifespan.

Sn-Bi alloy, whose melting point is around 50 °C and Young's modulus is about 1 GPa, was always chosen as the material to make the structure of continuum robots due to its good forming ability and small cooling shrinkage [103, 114]. In these two research studies, the

LMPA materials were fabricated as skeletons with multiple hollows for continuum robots to achieve lightweight and high rigidity. Similar materials like Ga-In alloy with a melting point of 29.78 °C [107] and Sn-In alloy with a melting point of 47 °C [110] were also used in continuum robots as a filling material. Apart from these simple alloys, many LMPAs with complex ingredients can be found in continuum robots to realise high stiffness when in a solid state, and they can be generally divided into eutectic alloys [108, 109, 111] and non-eutectic alloys [102, 106, 115]. For more details, the ingredients of LMPA used in continuum robots included the eutectic alloy (Roto144F, 32.5 % Bi, 51% In, and 16.5% Sn by weight) with a melting point of 62 °C [109], LMPA (Sn 8.3%, Bi 44.7%, Pb 22.6%, Cd 5.3%, and In 19.1% by weight) with a melting point of 47 °C [108], bismuth-base non-eutectic alloy (Cerrolow 117, Bi 45%, Pb 23%, In 19%, Sn 8%, and Cd 5% by weight) with a melting point of 47.2 °C [102, 115], nontoxic eutectic alloy (Bi 32.5%, In 51%, and Sn 16.5% by weight) with a melting point of 62 °C [106], and lightweight Field's metal (Bi, In, and Sn) [111].

These alloys used in continuum robots all have the attribute that their phase can be controlled effectively by direct Joule heating to switch between the rigid and flexible states. However, they may suffer from a low response speed to passively cooling down [84, 102, 108, 110]. To reduce the stiffness switching time, researchers have implemented active temperature control using cold and hot water circulation systems, where coiled tubes were used in the robot segment to enable effective heat and cool transmission for stiffness modulation [104, 105]. Some other efforts are being made to achieve faster variation in stiffness, such as using a special structure [103], active control of rigid and flexible states [107, 115], cooling tubes [106, 112], extra polyimide electric heating film [105], and active syringes [109]. The structure fabricated by this method demonstrates a large stiffness variation range and load capability, and the molds are low-cost and easy to assemble and disassemble with LPMA in it's liquid state.

2.2.2.4 Thermoplastics

TP constitutes another category of TRMs, encompassing a wide range of plastics or polymers and offering unique characteristics and applications. This type of material can

change its flexural modulus (Gpa) and strength (MPa) through the glass transition process [116]. Some notable examples used in continuum robots include graphene polylactic acid (GPLA) [184], resin material [125], polyethylene terephthalate (PET) [116, 117], polymorph [118], bioplastic [119], Conductive thermoplastic starch polymers (CTPSs) [123], thermoplastic starch (TPS) [124], polycaprolactone (PCL) [122], polyethylene terephthalate glycol (PETG) [120], and polyethylene glycol [121]. These diverse TP materials have varying properties and benefits, allowing their utilization in different applications within continuum robots.

In [184], a magnetically steerable manipulator with variable stiffness is introduced. The key component responsible for stiffness modulation in this manipulator is GPLA, which is a composite material comprising PLA and graphene. The stiffness variation is achieved through a phase transition by manipulating the temperature of the GPLA – when current is applied to the GPLA electrode, the temperature is increased by Joule heat. In [116, 117], Le *et al.* developed a PET tube in their tendon-driven continuum robots. The tube is constructed by placing a layer of PET over a flexible stainless steel sheath, which acts as the heating element when an electric current is applied. A similar design can be found in [118] by employing Nichrome wires and thermoplastics. On the other hand, the TP materials have been applied to continuum robots in different scenarios, such as variable stiffness endoscopic manipulators [119, 120], multijoint soft fingers [122, 123], bioinspired design of deep-sea glass sponges [124]. The work in [121] is underlined with a variable stiffness continuum over the tube. The over tube realises stiffness variation through the heating and cooling of filling materials, and polyethylene glycol has been found to be the best filling material.

2.2.3 Jamming mechanism

The jamming mechanism is a method used to alter the stiffness and shape of the body of continuum robots by controlling the internal friction between particles, fibres, or layers within a flexible medium. As shown in Figure 2.5(a), this is achieved by varying the pressure or vacuum within the medium, causing the particles, fibres, or layers to either lock together (jam/solid) or move freely (unjam/fluid) [186–188]. Sustaining a negative

pressure requires sealing the jamming structure within a vacuum envelope, typically described as a latex or rubber membrane in the relevant literature [10, 188]. Among existing stiffening techniques, the jamming mechanism is promising when applied to continuum robots due to their advantages of easy realisation, shape-locking capability, and relatively quick activation [186, 189].

According to the form of the filling materials used in continuum robots, the jamming mechanism can be generally divided into fibre/filament jamming (FJ) [126–130, 190], granular/particle jamming (GJ) [5, 6, 131–138, 140–150, 152, 153], layer/laminate jamming (LJ) [4, 5, 9, 10, 152, 153, 155–161], and 3D printed fabrics jamming (PJ) [11, 162]. In order to achieve more flexible stiffness tuning ability, researchers have combined the above single jamming mechanism in continuum robots, known as the hybrid jamming (HJ) [153, 163, 164, 191]. To clearly show the various jamming techniques employing different materials and drive mechanisms in the literature, an overview summary is provided in Table 2.3, and the typical designs of the jamming mechanism used as a stiffness-tuning approach in continuum robots in terms of filling materials are shown in Figure 2.5.

2.2.3.1 Fibre/filament jamming

In the FJ mechanism, the jamming materials are normally filled into continuum robots as the main bodies (Figure 2.5(g)). For example, the body of the continuum robot in [126, 127] is made up of identical and repeated interlocking fibres, and thus its effective stiffness can be controlled by changing the friction between fibres, which is achieved by evacuating air from the cover seal sheath. In [128], Hu *et al.* propose a novel jamming mechanism termed filament jamming that is used in a fluidic chamber-driven actuator-embedded robot. Similarly, stiffness-tunable soft bellows actuators utilising cross-fibre jamming were developed in [190]. Meanwhile, in many scenarios, there is an urgent need to improve the ability to jam in small and slender devices. To this end, [129] provides a design methodology for continuum robots with slender body and high flexural modulus based on the concept of fibre jamming. The proposed fibre jamming modules comprise axially packed fibres enclosed within an airtight envelope. These filling mediums exhibit a transition from a flexible to a rigid beam when a vacuum is generated inside the envelope.

TABLE 2.3: Summary of continuum robots with jamming mechanisms

TYPE	MATERIAL	ACTUATION	APPLICATION	RELATED WORKS
FJ	Aluminum Oxide 180 Grit/ VeroClear with texture/ VeroClear without texture	Manual	Industrial (arm)	[129]
	Polymer fibre	Tendon	Medical (nephrectomy)	[126]
	Nylon fibre	Fluidic	Industrial (actuator)	[128]
	Optical fibre	Tendon	Industrial (actuator)	[127]
	Mitchell abrasive fiber	Manual	Industrial (hapstick)	[130]
GJ	Matt surfaced glass	Manual	Industrial (arm)	[152, 153]
	Diameter polystyrene	Manual	Industrial (arm)	[153]
	Sucrose/Lactose/Ground coffee/Coarse magnesium/Collagen	Manual	Industrial (arm)	[5]
	Hollow glass bead/Coarse coffee/Fine coffee/Diatomaceous earth/Solid glass beads/Saw dust	Tendon	Industrial (arm)	[131]
	Ground coffee	Tendon	Industrial (arm)	[133]
		Tendon	Medical (nephrectomy)	[134]
		Fluidic	Medical (MIS)	[6, 140–145]
	Black pepper/Datura	Tendon	Industrial (arm)	[138]
	Glass bead	Tendon	Industrial (arm)	[135, 136]
	Saccharose/Refined sugar	Tendon	Medical (nephrectomy)	[132]
	PC-Max	Fluidic	Industrial (actuator)	[149]
	Corn	Fluidic	Industrial (actuator)	[147]
	Plastic/Desiccant/Corn	Fluidic	Industrial (actuator)	[137]
	Glass	Fluidic	Industrial (actuator)	[148]
	Small particle	Fluidic	Industrial (gripper)	[146, 150]
	Plastic spheres/Plastic cubes/Solid rubber cubes/Hollow rubber cubes/Solid rubber blocks/Composite cubes	Fluidic	Industrial (arm)	[151]
	Matte spherical/Smooth faceted/Matte cube/Smooth spherical	Manual	Industrial (arm)	[154]
LJ	Mylar film	Tendon	Medical (MIS)	[4, 156]
		Manual	Industrial (arm)	[9, 152, 153, 161]
	Synthetic fiber paper	Manual	Industrial (arm)	[5]
	Silicon carbide grit papers	Manual	Industrial (arm)	[158]
	Polyvinyl chloride film	Tendon	Industrial (arm)	[10]
	View foil/Projector transparencies	Tendon	Industrial (arm)	[155]
	Paper layer and spring steel sheet	Fluidic	Industrial (actuator)	[157]
	Spring steel sheet	Fluidic	Industrial (finger)	[159]
	Polyethylene	Fluidic	Industrial (finger)	[160]
PJ	Octahedron-octahedron (clear V4 resin)	Fluidic	Industrial (gripper)	[11]
	Octahedron-ring-octahedron	Fluidic	Industrial (arm)	[162]
HJ	Mylar film (LJ)+ Glass/Polystyrene (GJ)	Manual	Industrial (arm)	[153]
	Neobond layer (LJ) + Coffee/Collagen/Lactose/Sucrose (GJ)	Tendon	Medical (nephrectomy)	[163]
	Copy paper (LJ) + Glass (GJ)	Fluidic	Industrial (actuator)	[164]

Apart from manipulators, the FJ was also used in the Hapstick (a soft continuum body) to realise feedback stiffness adjustment for movement control of tendon-driven continuum robots.

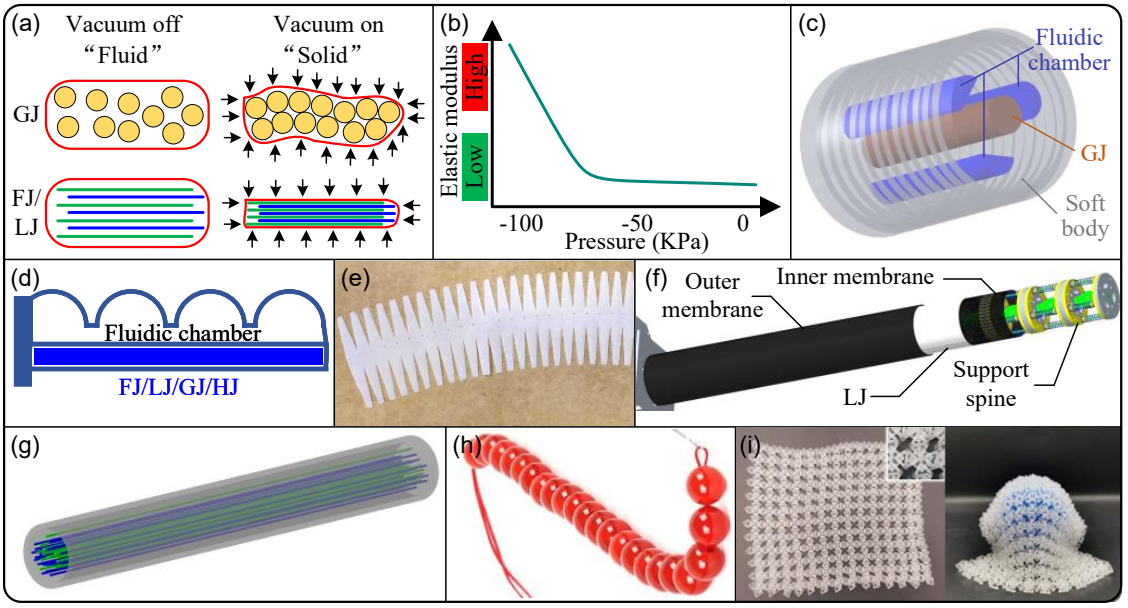

FIGURE 2.5: Diagram of the jamming mechanism used in continuum robots. (a) illustration depicting the jamming phenomenon. (b) relationship between the elastic modulus and varying vacuum levels. (c) diagram of STIFF-FLOP [6]. (d) diagram of the typical design structure of FJ/GJ/LJ/HJ applied in actuator-like fluidic-chamber-driven continuum robots. (e) photo of the double-flap layer jamming pattern [10]. (f) diagram of the typical design structure of LJ applied in tendon-driven continuum robots [10]. (g) diagram of the typical robot body with FJ applied. (h) diagram of strings of beads type of GJ. (i) photos of the PJ [11].

2.2.3.2 Granular/particle jamming

Similar to FJ, GJ is also utilised by filling materials into the body of continuum robots to allow variable stiffness capabilities. The particulate matter undergoes a transition between fluid-like and solid-like states caused by changes in particle packing [186, 187]. This transition creates jammed states with tightly packed particles that restrict their free movement, which results in a high stiffness. In order to realise this function, researchers have tried various filling materials in their robot design, such as matt surfaced glass beads (4 mm diameter) [152, 153], polystyrene packing beads (3 mm diameter) [153], and several different materials in one design for comparison purposes: sucrose, lactose, coarse magnesium, collagen, and ground coffee in [5]; plastic spheres, plastic cubes, solid rubber cubes, hollow rubber cubes, solid rubber blocks, and composite cubes in [151]; matte spherical, smooth faceted, matte cube, and smooth spherical in [154]; hollow glass bead, coarse coffee, fine coffee, diatomaceous earth, solid glass beads, and saw dust in [131].

The GJ can be easily embedded into tendon-driven continuum robots. It has been used in several continuum robots with multiple sections, such as two hyper-redundant manipulators [131], a two-segment variable stiffness manipulator for MIS [132], and three-segment robotic manipulators based on organic granular materials [133, 138]. In [134], it presents the initial investigations on the contour accuracy of one-segment manipulators utilising granular jamming for laparo-endoscopic single-site surgery (LESS). In [135], Zhou *et al.* developed a bioinspired soft wrist using a particle backbone to realise the tuning of the stiffness. In [136], pre-charged air chambers, particle jamming, and origami are combined to design a soft continuum robot that uses three air chambers to press the inside particle hamming chamber to realise stiffness tuning.

In contrast, GJ is more popular than other jamming methods in fluidic chamber-driven soft continuum robots because of its scalability and ease of fabrication. One highly prevalent example is the "STIFF-FLOP" robot [6, 140–145]. As shown in Figure 2.5(c), this robot is specifically designed for MIS and features a combination of three flexible fluidic actuators and a variable stiffness mechanism based on GJ. Fluidic actuators enable multidirectional bending and elongation, while the latter contributes to stiffness tuning. Additionally, as shown in Figure 2.5(d), integrating fluidic actuation and GJ has been used in several variable stiffness robotic grippers [137, 146–148]. In order to further improve the GJ's capability, a folded plate mechanism and a chain-like GJ are considered in [149, 150], respectively.

However, GJ may suffer from the challenge of poor restorability because the filling particles are difficult to flow out of the cavity due to the jamming effect and gravity. In order to address this, as shown in Figure 2.5(h), researchers used strings of beads instead of discrete particles to improve the restorability of the GJ used in continuum robots [192, 193].

2.2.3.3 Layer/laminar jamming

Different from GJ and FJ,LJ generally uses thin plastic or paper layers as its jamming flaps and can be easily applied to continuum robots as a reinforcing sheath, which results in the advantages of lighter weights and taking up less space of continuum robots [10, 155, 188]. For example, in [4, 156] layer jamming flaps were wrapped into a cylinder shape

to create a manipulator for MIS, while in [5, 9, 10, 152, 153, 161], manual robotic arms utilised a double-sided flap pattern with rounded jamming flaps on the support spine for stiffness tuning, as shown in Figure 2.5(e) and (f). Another example is using a particular structure to combine jamming layer strips and honeycomb cores to achieve stiffness tuning ability in [158], which is capable of achieving a rapid flexible-rigid state transition with biocompatibility.

For the finger-like robot actuated by an air chamber or tendon, the LJ can be applied on one side of the body and works as the support layer as well as affording the stiffness adjustable techniques, as shown in Figure 2.5(d). In [157], a tendon-driven griper was developed by embedding LJ inside the layer jamming cavity. Similarly, fluidic-driven actuator fingers were implemented and tested in [159, 160].

2.2.3.4 3D Printed Fabrics Jamming

The PJ was first systematically introduced in [194], as shown in Figure 2.5(i). It demonstrated structured fabrics with tunable bending modulus, which are made of three-dimensional particles arranged into layered chain mails. These chain mails can be flexible and conform to complex shapes, but the particles interlock and the chain mails jam when pressure (about 93 kilopascals) is applied at their boundaries, becoming over 25 times stiffer than in their relaxed state. By taking this advantage, a palm-shape variable-stiffness gripper was developed in [11]. The PJ pattern used in this research was the "octahedron-octahedron", which has a good stiffening ability but shows smaller extendable features. In order to achieve more flexible shape-changing capability, the "octahedron-ring-octahedron" pattern was developed for larger elongation (90%) with remaining stiffening function (15 times) in [162].

2.2.3.5 Hybrid jamming

Apart from the above single jamming mechanism, other mechanisms that combine FJ, LJ, and GJ are summarised as HJ. It has the advantage of achieving more flexible stiffness tuning ability due to combination [153, 163]. The design in [163] utilises LJ to cover the

manipulator segments, and GL is filled inside the backbone to realise the stiffness tuning ability with the advantages of being safe to use and showing high dynamic behaviour. This provides sufficient stiffening and is comparably cost-effective. In [164], it introduces a design of bioinspired soft robotic fingers based on the HJ principle that integrates layer jamming and particle jamming. This design takes advantage of the different characteristics of layer jamming and particle jamming, and the layer regions and particle regions are interlocked with each other to guarantee load transfer from the fixed finger end to the fingertip. A similar soft robotic finger was developed in [191] by integrating layer jamming and particle jamming in the same chamber. In [153], Clark *et al.* tried to combine two types of rigid granules and layer jamming in separate and single jamming volumes.

2.2.4 Mechanical structure

Mechanical structures play a vital role in the design of continuum robots, and they can also be used to achieve stiffness variation capability with various innovative approaches employed, including the lockable mechanism (LM) [165, 166, 168, 195, 196], friction change mechanism (FCM) [169, 170], variable stiffness ball joint (VSBJ) [171–173, 197], constraint tube (CT) [174–180], concentric anisotropic tube (CAT) [3, 181], and active-braid element (ABE) [183], as shown in Figure 2.6. These mechanical structures provide flexibility control for continuum robots, allowing them to adapt to different tasks and environments. The selection of a particular mechanical structure depends on the desired range of stiffness adjustments and the specific application requirements, thereby ensuring optimal performance and versatility in various robotic scenarios.

2.2.4.1 Lockable mechanism

By incorporating a LM, the stiffness of a continuum robot can be changed effectively. However, the lockable mechanism is limited to shift stiffness with two discrete states and cannot tune stiffness continuously. In [165], a modular lockable mechanism is designed such that it can be used to change the stiffness of tendon-driven surgical robots. Using the push-up module and the tooth module, locking and unlocking activities are actuated by pulling one tendon. By adopting elastic chambers in the flexible continuum joint, a

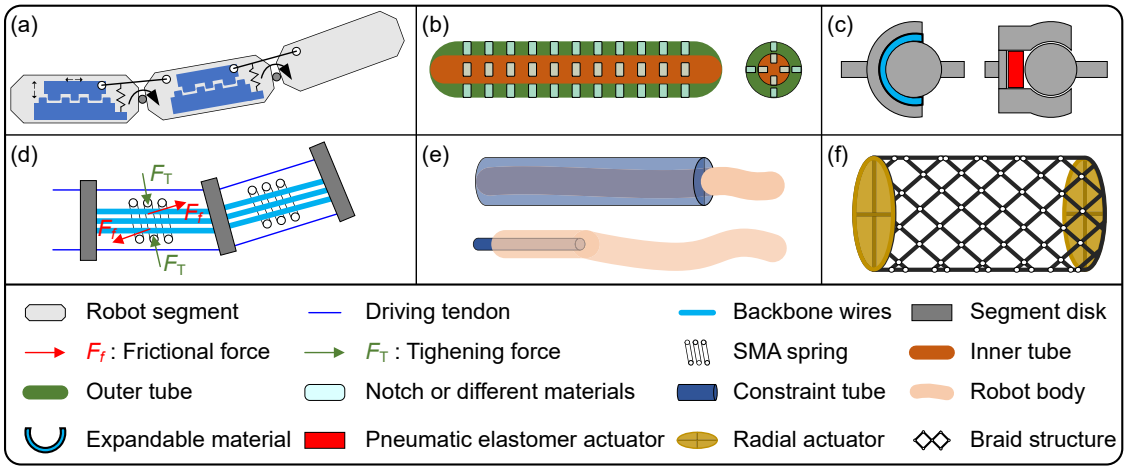

FIGURE 2.6: Diagrams of different mechanical structures for stiffness regulation in continuum robots. (a) lockable mechanism. (b) concentric anisotropic tube. (c) two types of variable stiffness ball joints. (d) friction change mechanism by SMA spring. (e) two types of constraint tubes, outer constraint and inner constraint. (f) active-braid element for fabricating the robot body.

robot arm is capable of switching between rigid and continuum [166], shows a flexible feature and becomes rigid when the joint is locked. In [168], the researchers propose a principle for stiffness variation based on fibre-reinforced structure matching (meshing), whose stiffness can be changed more easily compared to existing approaches. The basic principle is that two soft laminates made of fibrous composites have complementary shapes that can interlock with each other in a controlled way; the resulting structure will be soft when the two laminates separate, but rigid when the two laminates interlock with each other. Therefore, the stiffness of a structure can be adjusted by altering the separated and matched states. In addition, a novel variable stiffness mechanism powered by embedded SMA springs was presented in [91]. These SMA springs are capable of "locking" the drive rods onto the body structure with different configurations, resulting in variable stiffness effects. Similarly, a screw-locking method [196] and SMA clutches [167] were developed for rod-based locking of tendon-driven continuum robots.

2.2.4.2 Friction change mechanism

The FCM is applicable to the regulation of stiffness by changing the contact force, resulting in different friction forces. In [169, 170], the SMA spring is used to wind the ropes

to perform a variable stiffness or locking function by adjusting the friction between the ropes and the rods. The inner diameter of the SMA springs, which can be changed via temperature, creates a tightening force change that is applied to the backbone wires of the robot to adjust the overall stiffness. This simple structure is favourable for robot miniaturisation.

2.2.4.3 Variable stiffness ball joint

VSBJ is another mechanism to adjust stiffness by different damping levels of the joint. To achieve variable damping, the clearance between the ball and the socket is changed by external force or a soft pneumatic elastomer actuator, for example, [171–173, 197] with VSBJ used for the main backbone. The friction between the contact surfaces of the ball joint to control stiffness is investigated in [172, 173, 197]. When a force is used to close the clearance between the ball and the socket of a ball joint whose primary objective is to allow omnidirectional rotation, friction will be generated at the contact surfaces of the ball joint, and the greater the applied force, the greater the friction will be. To control clearance, a soft pneumatic elastomer actuator [172] or materials that can be expanded or deformed by pressure [173] can be applied.

2.2.4.4 Constraint Tube

A CT is a component used in continuum robots to control their stiffness or flexibility. It is typically a cylindrical structure made of flexible or rigid materials such as acrylonitrile butadiene styrene (ABS) [176], 3D printed plastic [180], translational tube [175], and steel tube [174, 177–179]. It can be inserted within the robot's body [174, 176–179] or an enclosure of the robot [175, 180]. The work [174] proposes a constrained wire-driven flexible mechanism and its key idea is to employ an active constraint to control the length of the bending section and use the wires to control the curvature of the bending section, and both the length and the curvature of the bending section are controllable. In [176], a 2-DOF soft robot with stiffness-changing capability is presented for tumour removal in neurosurgery under MRI guidance. A floating fixed-point approach is used to change the

physical length of the manipulator to decrease deflection and increase stiffness. In [177–179], a 2-segment continuum manipulator with adjustable stiffness based on continuously constrained bending curvature is investigated. It has tunable stiffness but does not affect the movement of the manipulator's end-effector. In addition, the stiffness of the manipulator is further improved through the redundant backbone arrangement using the concept of a dual continuum mechanism during the design phase.

2.2.4.5 Concentric anisotropic tube

Another approach is to apply CAT for stiffness tuning. The mechanism consists of multiple coaxial tubes, and each tube has an anisotropic distribution of flexural stiffness by different materials in its body [181], or non-uniform through-hole patterning [3, 182]. When relative rotation and translation are applied among the tubes, the overall stiffness can be easily controlled.

2.2.4.6 Active-braid element

The last is the ABE. In [183], a novel bioinspired continuum manipulator is presented with the ability to contract, extend, and bend in a three-dimensional space with varying stiffness. The manipulator utilises a flexible cross-link helical array structure as its main supporting body, which is deformed by using two radial actuators and a total of six longitudinal tendons. The helical array structure ensures that the manipulator behaves similarly to a constant volume structure (expanding while shortening and contracting while elongating). By shifting to a different braiding structure, its stiffness can be tuned.

2.3 Comparisons and discussions

The stiffening of continuum robots plays a crucial role in various fields, ranging from medical surgeries to industrial applications, which aims to address the inherent compliance and flexibility of continuum robots. It allows robots to exert greater force, achieve more precise positioning, and improve their stability during various tasks. By enhancing their

rigidity, continuum robots can achieve greater precision and control during complex tasks. As outlined in this survey, existing variable stiffness approaches in continuum robots can be achieved using antagonisms, thermally responsive materials, jamming mechanisms, and mechanical structure designs. The properties of each approach have been summarised in Section 2.2. To further illustrate these approaches, they are compared in terms of five factors in Table 2.4, including stiffening ratio, response speed, volume taking, mass, and safety level. In addition, potential risks are given for each approach. The table outlines the advantages and drawbacks of each approach, which may be helpful in identifying their suitability for specific applications for researchers and engineers.

Antagonism is a common method for stiffness adjustment in continuum robots, known for its simplicity but often suffering from low efficiency. It requires significant additional force or high muscle pressure, leading to heavy actuators with large driving motors or air pumps. Tendon antagonism offers rapid response and high safety but typically provides small stiffening ratios and may suffer from cable cracking under tension. Fluidic antagonism provides moderate stiffness and a relatively fast response but risks leaks or bursts from high-pressure fluid systems. A hybrid approach, combining tendon and fluidic antagonism, achieves a large stiffness-changing ratio but inherits the disadvantages of both methods.

Although TRMs used in continuum robots can achieve large stiffness tuning, they face several challenges, such as limited temperature ranges, low mechanical strength in liquid states, low thermal conductivity, and risks of heat damage or short circuits. TRMs can store and release heat energy, but they may result in slower phase change processes and reduced performance at specific temperatures. Additionally, addressing the risk of heat damage or potential short circuits and fires caused by electric heating coils is another crucial concern for continuum robots. Even with a water heating or cooling system to mitigate this risk, it requires a large volume and may lead to potential water leaks that could damage the robot's electric circuit system.

Jamming techniques have garnered significant attention in recent years, offering the advantage of providing large stiffness with varying response speeds and high safety levels. However, it is crucial to acknowledge the inherent risk of encountering positive or negative pressure, which could potentially lead to leaks, bursts, or raise safety concerns. Note that

Table 2.4: Comparison of different stiffening approaches

Stiffening Approaches		Stiffening Ratio	Response Speed	Volume	Mass	Safety Level	Potential issues
Antagonism	Tendon	Small	Very fast	Tiny	Negligible	High	Cable cracked
	Fluidic	Large	Fast	Medium	Medium	Low	Leak or burst
	Ten.&Fl.	Large	Fast	Medium	Medium	Low	Cable cracked, leak or burst
Thermally responsive material	SMA	Small	Slow	Small	Light	Low	Heat damage Electric heating: short circuit or fire Water heating or cooling: water leak
	SMP	Large	Slow	Medium	Light	Medium	
	LMPA	Very large	Slow	Medium	Medium	Medium	
	TP	Large	Slow	Medium	Light	Medium	
Jamming mechanism	FJ	Small	Medium	Medium	Medium	High	Positive pressure: leak or burst Negative pressure: hysteresis
	GJ	Large	Medium	Medium	Medium	High	
	LJ	Very large	Fast	Small	Light	High	
	PJ	Very large	Fast	Small	Light	High	
	HJ	Very large	Medium	Medium	Medium	High	
Mechanical structure	LM	Medium	Very fast	Small	Medium	High	Limited stiffening status, potential to be stuck
	FCM	Medium	Slow	Small	Medium	High	SMA actuation with heat damage, short circuit or fire
	VSBJ	Small	Fast	Medium	Medium	High	Leak or burst; Ball joint maybe stuck
	CT	Very large	Very fast	Medium	Heavy	Very high	Limited movement; Not flexible
	CAT	Small	Fast	Medium	Medium	Very high	Limited stiffness tuning behaviours
	ABE	Small	Medium	Large	Medium	Very high	Structure changes; Not flexible

†**Range of stiffening ratio.** Small: <5; Medium: 5 - 10; Large: 10 - 15; Vey large: >15.
Range of response speed. Very fast: 1s; Fast: 5 - 10s; Medium: 30s - 1min; Slow: >3min.
Range of volume and mass (proportion to robot). Tiny and Negligible: <1%; Samll and Light: 5 - 20%; Medium: 40 - 60%; Large and Heavy: >80%. The volume and mass of external devices for stiffness tuning are not included. For instance, the air pump, tendon driving motor, water flow device, and power supply.

it is essential to consider that jamming mechanisms require a significant volume of grains, fibres, or layered structures, posing challenges for miniaturisation efforts. Additionally, the process of exhausting air to achieve stable negative pressure is relatively complicated and hard to control.

The mechanical structure approaches vary significantly in both their structures and mechanisms. Lockable mechanisms provide very large stiffness adjustment with rapid response, but they are limited to binary stiffness states, allowing only a shift between high stiffness (locked) and low stiffness (unlocked). Friction change mechanisms, driven by SMA springs, offer a medium stiffness tuning ratio and a slow response speed but with high safety levels. Variable stiffness ball joints offer large stiffness with a medium response but risk leaks and mechanical sticking. Constraint tubes offer high stiffness adjustment with fast response, but they will limit the robots' movement and they lack flexibility. In contrast, concentric anisotropic tubes provide medium stiffness-changing ability with a fast response but exhibit limited stiffness-tuning behaviours. The active-braid element offers medium stiffness with a medium response speed and a very high safety level, but it may be large in volume and mass.

In practical applications, antagonism suits scenarios requiring rapid response and safety but may be limited by its lower stiffening ratios. For example, for the MIS or NOTES, continuum robots utilising antagonism could be safe for the patient. Similarly, it can also be used in the slender continuum robot for inspection or rescue in complex and narrow environments because there is plenty of space for the bulk driving device in these scenarios. TRMs are beneficial for applications needing temperature-driven stiffness changes, but their limited temperature ranges and mechanical strength can be constraints. This could be promising for industrial applications due to low response and the high and low-temperature switch requirements. Even though the LMPA could be used in medical manipulators, it still has a heating risk to patients because its melting point is generally around 50 °C. Jamming techniques are useful for achieving high stiffness with varying response speeds, but they are facing challenges of miniaturisation and pressure management. These unique features allow jamming to be used in both medical and industrial applications, such as grasping, manipulating, MIS, and NOTES. Mechanical structures could be used in any application due to their different structure design and actuation mechanisms.

A comprehensive review of four categories of prevalent stiffening approaches that have emerged in the last two decades has been conducted. Notably, there is a discernible trend toward employing *feedback control* to regulate the stiffness of continuum robots [198–202], though not discussed in this chapter. It has been applied in different types of continuum robots, including tendon-driven robots [200], concentric tube manipulator [203], tendon & fluidic driven robots [204], and pneumatic soft manipulators [205, 206]. It is widely known that control algorithms are applied to the problems of position regulation and tracking of robots; these algorithms, indeed, may change the stiffness of the closed-loop dynamics of a continuum robot. If the potential energy of a given robot is modelled as the function $U(q)$ with the configuration variable $q \in \mathbb{R}^n$, then the overall open-loop stiffness is given by $\nabla^2 U(q)$. When a position feedback controller is applied to the system and the desired potential function is assigned as $U_{\mathtt{d}}(q)$, the closed-loop stiffness would shift from $\nabla^2 U(q)$ to $\nabla^2 U_{\mathtt{d}}(q)$ [198, 200]. Therefore, the resulting stiffness is determined by the selection of a specific feedback law and gain parameters. However, it should be noted that the design of a controller to achieve the regulation of position and stiffness simultaneously is a challenging task, particularly for underactuated continuum robots, and there are still many open problems [201, 202]. For example, the stiffening ratio using purely control algorithms is relatively small [200], and it is promising to integrate control with other stiffening methods that have been reviewed in this chapter to improve stiffening performance.

2.4 Future perspectives

While the field of continuum robotics has achieved significant progress over the last two decades, many questions and technical challenges remain open. Therefore, some future perspectives related to stiffening approaches for continuum robots are presented in this section; see Figure 2.7 for an intuitive illustration. Advancements in the development of efficient and effective stiffening mechanisms for continuum robots are expected in the future. It would be focused on novel materials, actuation methods, and control strategies to increase stiffness while maintaining the robot's dexterity and flexibility. By optimising stiffness profiles and incorporating state-of-the-art control strategies, continuum robots

will gain the ability to adapt to diverse environments and tasks with improved precision and stability.

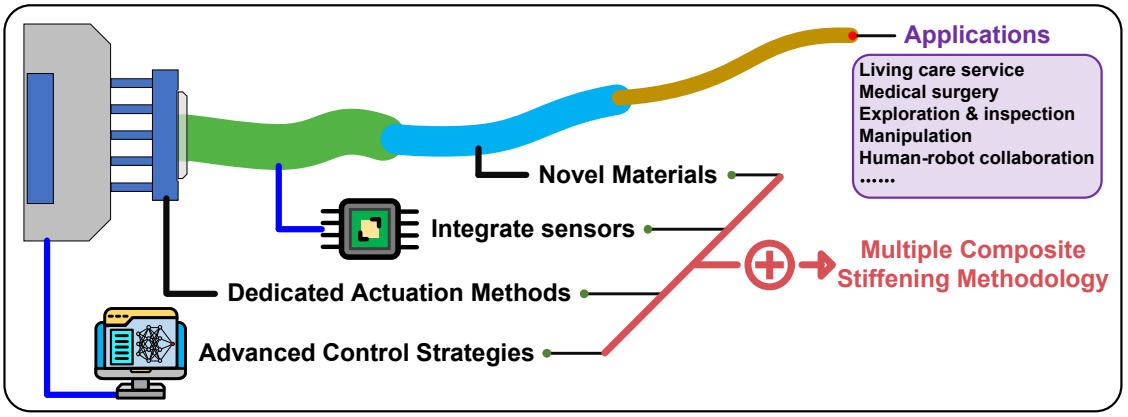

FIGURE 2.7: Promising research topics on stiffening methods or mechanisms for continuum robots.

2.4.1 Multiple composite stiffening methodology

Different stiffening approaches have unique characters and can be selected for continuum robots according to the task requirements. However, they can be combined to stiffen continuum robots for dedicated application scenarios. For instance, the tendon & fluidic antagonism and jamming mechanisms may be combined as a promising research direction for further improving the stiffening performance of continuum robots. This composite method is expected to take advantage of both the antagonism and jamming mechanisms to realise continuous real-time stiffness tuning. Indeed, several different stiffening approaches can be concurrently applied in one continuum robot to balance stiffness conditions and dexterity levels. For instance, the following combinations may be considered:

- jamming mechanism + lockable mechanism;
- jamming mechanism + tendon & fluidic antagonism

in order to achieve relatively fast stiffness regulation. Other examples are considered in the following cases:

- jamming mechanism + thermally responsive materials [113];

- jamming mechanism + tendon & fluidic antagonism + thermally responsive materials

to obtain large and flexible stiffness tuning performance. To the best of the authors' knowledge, there have been few designs utilising multiple composite methodologies for stiffness tuning in the field of continuum robots.

2.4.2 Novel materials

Balancing the need for increased stiffness while maintaining robot dexterity and adaptability requires innovative design approaches and advanced materials. For example, the current TRMs generally have a relatively high response temperature and slow response speed, and the transition range is relatively narrow for stiffness tuning, which limits the material's effectiveness in surgery robots. Additionally, biocompatible material is essential for the continuum robots that are applied to medical scenarios, such as targeted drug delivery, microsurgeries, and diagnostics. Integrating novel materials can further facilitate the integration of stiffening mechanisms into smaller-scale robots. One promising example is the hydrogel material, which offers significant advantages for robotics, including high flexibility and softness, biocompatibility, responsiveness to stimuli, self-healing properties, and tunable mechanical properties [207–209]. These advantages and properties make them promising for continuum robots even though they are currently rarely used.

In addition, materials with self-sensing functions are essential for continuum robots. It will further facilitate the control and actuation process and make it easier to mimic the properties of natural organs (trunk, tentacle, and tongue) if the robot body is made of materials that can sense itself. The development of materials that enable variable stiffness, self-sensing, and biocompatibility would allow continuum robots to adapt to various conditions and tasks in real-time, from medical interventions to environmental inspections.

2.4.3 Advanced control models and algorithms

The future of stiffening approaches for continuum robots lies in the integration of advanced sensing technologies, specific modelling, and artificial intelligence (AI) algorithms.

By equipping these robots with high-resolution sensors, such as force/torque sensors, vision systems, or tactile sensors, they can gather rich feedback data during operation. Therefore, by combining these data with advanced model-based controllers or AI control algorithms, the robot's stiffness can be enabled with real-time adaptation, which leads to more intelligent and autonomous behaviour. For instance, AI algorithms can use sensor data to predict and respond to changes in the robot's environment, allowing for dynamic adjustment of stiffness to optimise performance. In surgical applications, continuum robots equipped with tactile sensors can adjust their stiffness to navigate delicate tissues safely and minimise the risk of damage. Similarly, in industrial automation, force/torque sensors can help robots modulate their rigidity when handling objects of varying weights and fragilities, ensuring precise manipulation without compromising safety or efficiency.

Moreover, machine learning models trained on historical data can enable these robots to learn from past interactions, refining their stiffness control strategies over time. For example, in pipeline inspection, a robot would be capable of learning the optimal stiffness settings needed to navigate complex and variable terrains, improving its ability to perform inspections more efficiently and accurately.

By integrating these advanced control algorithms and sensing technologies, continuum robots will be able to optimise their stiffness based on detected task requirements, environmental conditions, and learned models from historical data. This integration will significantly enhance their performance and adaptability across a wide range of applications.

2.5 Summary

Stiffness tuning approaches hold great promise for improving structural integrity and expanding the capabilities of continuum robots. This chapter has reviewed four prevalent categories of tuning approaches that have been developed and applied in continuum robots. It has comprehensively summarised the key properties of these methodologies, discussed their application scenarios, and made comparisons among them. To address the technical

challenges, the exploration of multiple composite stiffening methodology and novel materials, along with advanced control models and algorithms, will enable continuum robots to achieve seamless transitions between soft and stiff configurations, expanding their range of applications.

Chapter 3

Design of a Continuum Robot with Jamming Mechanism

This chapter is to present the design and fabrication of a tendon-driven continuum robot with a jamming mechanism (OctRobot-I). This robot consists of an inner support spine and an outer layer jamming sheath, ensuring a flexible stiffness adjustment capability in both the transverse and axial directions. In order to analyse the robot's effective stiffness and its changing tendency under varying conditions, a static deflection analysis method based on the Euler-Bernoulli beam theory is developed, and experiments are conducted with two types of layer jamming sheaths and four different vacuum pressures at three different bending angles. The results validate the proposed method and show that the robot has a good stiffness variable capability. Additionally, the robot's performance in real-world applications, such as actuating and gripping, is also tested. [1]

3.1 Introduction

As partially described in Chapter 2, among the stiffness variable technologies, jamming mechanisms are promising when applied to continuum robots due to their advantages of

[1]The results presented in this chapter have previously appeared in the publication: Yeman Fan, Dikai Liu, Lin Ye, "A novel continuum robot with stiffness variation capability using layer jamming: design, modeling, and validation", *IEEE Access*, vol.10, pp.130253-130263, 2022.

easy realisation, shape-locking capability, and quick activation. From Chapter 2, it can be concluded that layer jamming is more effective than other jamming mechanisms when applied in continuum robots as a reinforcement sheath. This jamming mechanism uses thin plastic or paper layers as its jamming flaps [188, 210], which results in the advantages of lighter weights and taking up less space of continuum robots.

In [4], layer jamming flaps were wrapped into a cylinder shape to form a manipulator for MIS. A two-section prototype robot based on spring and layer jamming was designed in [155]. In [163], a flexible variable stiffness robot combined with layer jamming and backbone was developed for nephrectomy. However, these works are limited to small diameters and stiffness reinforcement ability [27]. Additionally, their actuator units were not compact and took up larger space than the robot body. In order to increase stiffness reinforcing ability, several robots with larger diameters were designed. In [153], six different continuum manipulator structures (diameters of 41-48 mm) utilising both granular and layer jamming mechanisms were implemented. In [9, 152], a malleable robot combining layer jamming with a flexible spine was developed. In [161], a stiffness-tuneable segment for continuum soft robots with vertebrae was presented. A revolute joint and stiffening sheaths based on layer jamming for continuum robots were developed in [211] and [5], respectively. These robots have improved with larger diameters; however, they were limited to shorter lengths, and there were no actuators.

In the above continuum robots, layer jamming was sewn along the guide holes and slots by an extra thread to form sheaths. Once the layer pattern was set, the sheaths' length-changing ability was mainly determined by the slot length, which was small (4 mm in [152]) and may affect the length change range. In addition, the design of previous research was focused on robots' performance in the transverse direction, and there was no testing conducted in the axial direction [4, 9, 152, 153, 163] to the best of the author's knowledge.

Furthermore, although some analytical models were researched for continuum robots under external loads, these models focused on the effect of the number of tendon or their displacement, and they were based on the cantilever beam model [212] or Euler-Lagrange equations [213], which indicates that there has seldom research work been related to approximate models of effective stiffness for continuum robots.

In this chapter, a novel continuum robot named OctRobot-I is presented. Layer jamming sheaths and a support spine are designed to achieve stiffness variation capability in both the transverse and axial directions. In order to evaluate the robot's performance, extensive force-deflection experiments are conducted in both directions. In addition, actuating and gripping capabilities are also validated and demonstrated.

3.2 Robot design

3.2.1 Overall design of the continuum robot

In nature, many organs have a continuum structure, such as elephant trunks, tentacles, and tongues. These organs are very flexible and also have excellent load capacity. One good example that inspired many researchers is the octopus tentacle [19]. Although octopus tentacles lack rigid structures, they have unique biomechanical capabilities that combine significant flexibility with the ability to change and control their stiffness. Therefore, by imitating an octopus tentacle's structure and motion mechanism, a novel continuum robot named OctRobot-I is designed, as shown in Figure 3.1.

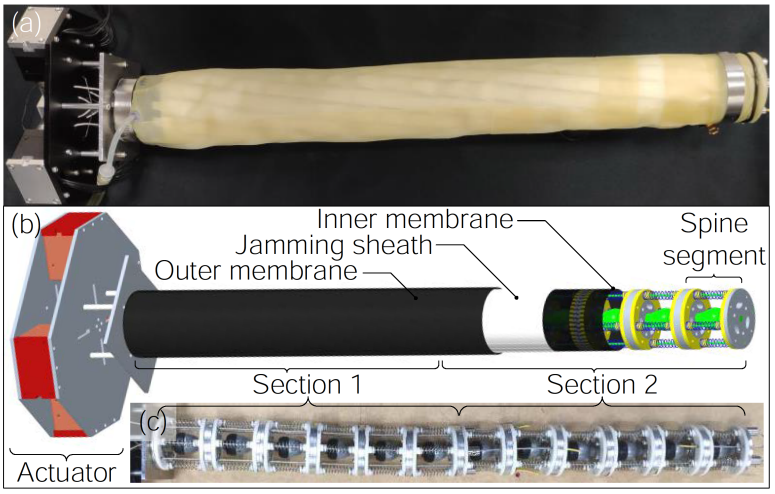

FIGURE 3.1: The continuum robot. (a) photo of the continuum robot. (b) a sectional view of the CAD model. (c) photo of the support spine of the robot.

The continuum robot consists of a support spine, inner membrane, jamming sheath, outer membrane, and actuator unit. The support spine uses ball joints to offer axial support

capability, and the jamming sheath is used to realise stiffness variation capabilities in both the transverse and axial directions when compressed. To compress the jamming sheath and activate its stiffening mechanism, two tubular latex membranes (thickness of 0.3 mm) are selected to seal the whole jamming sheath when evacuating the tubular volume between the two membranes [4, 152, 153]. The entire robot consists of two sections, and each section is controlled by two pairs of cables, providing the robot with four degrees of freedom in total. The continuum robot properties are summarised in Table 3.1.

TABLE 3.1: Physical properties and performance of the continuum robot

PROPERTIES	VALUE
Total robot length	572 mm
Actuator	68 mm
Robot body	504 mm
Total robot weight	1.7 kg
Actuator	0.8 kg
Robot body	0.9 kg
Robot outer diameter	~50 mm
The number of spine segments	12 (6/section)
Degrees of freedom	4 (2/section)
Maximum bending degree	180 °

3.2.2 Support spine and actuator

3.2.2.1 Spine segment

The whole support spine is made of 12 connected spine segments, as shown in Figure 3.1(c). A single segment is composed of two custom aluminium disc spacers, one pair of spring constraint discs, four helical compression springs, a ball joint (SQZ5-RS, China), and a grub screw, as shown in Figure 3.2.

In order to ensure that the spine segment can provide support in the axial direction, the ball joint (maximum tilt angle of 30°) is used in each segment to ensure it has both flexible bending ability and hard contact ability. Since ball joints lack self-recovery ability, four helical compression springs (measured spring constant of 493 N/m) are mounted around the ball joint to provide a particular force for the spine to recover to its original position. In addition, the aluminium disc spacer and spring constraint disc are used as support for

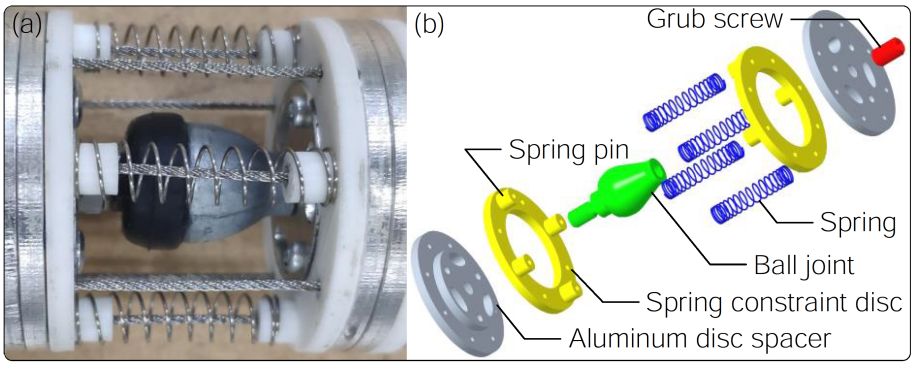

FIGURE 3.2: A support spine segment. (a) assembly photo. (b) exploded-view drawing.

the outside layer jamming. The spring constraint disc is 3D printed using polylactic acid (PLA) materials, and it has four small pins arranged at 90° to mount and constrain the springs. In order to connect the adjacent segments, three aluminium rivets ($\Phi 3.2 \times 12$ mm) are used and arranged at 120° intervals in the aluminium disc spacer.

3.2.2.2 Actuator unit

To actuate the cables for controlling the robot, an actuator unit is designed using servo motors and tailored aluminium spools. Unlike the robot actuated by ball screws [4] and worm gears [163], this design offers a compact, lightweight, low-volume actuator unit. Figure 3.3(a) shows the concept of four pairs of cables to actuate the whole continuum robot. The robot has two sections with each section driven by two pairs of cables. Stainless steel wire ropes with a diameter of 1.2 mm are selected. The rope is mounted in the spools, and its two ends go through its controlling section arranged at an interval of 180°. All the rope ends are fixed on the surface of the last aluminium disc spacer in each section.

Figure 3.3(b) and (c) show the design of the actuator unit and the spool mechanism employed in this continuum robot. The actuator unit is composed of four servo motors (XM430-W350, DYNAMIXEL), four tailored aluminium spools, four pairs of stainless-steel wire ropes, and support frames. In the spool mechanism, the cable goes through the lateral hole of the spool. The two ends of the cable are helically coiled on the spool in the clockwise and counterclockwise directions, respectively. Thus, the same cable length can be fed in and pulled out from both sides (End I and End II) by the rotation of the motor, which can maintain the cable tension at any configuration.

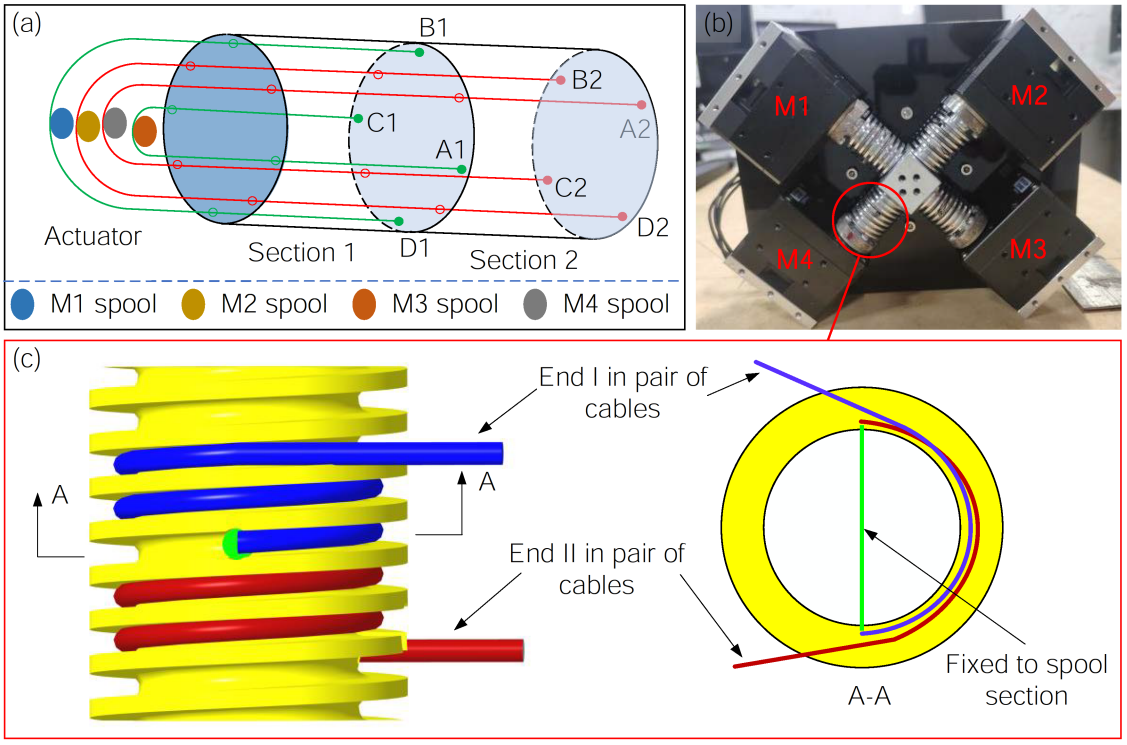

FIGURE 3.3: Diagram of the actuator unit and drive mechanism. (a) diagram of the driving cable arrangement, A1-D1 are for controlling Section 1 (green), and A2-D2 are for controlling Section 2 (red). (b) photo of the actuator unit (motors labelled M1/M3 and M2/M4 were spaced 90° apart for controlling Section 1 and Section 2, respectively). (c) diagram of the spool mechanism.

3.2.3 Jamming sheath

3.2.3.1 Jamming flap structure

The structure of the jamming layer for this continuum robot is based on the double-side flap pattern described in [4]. In order to suit a support spine of larger diameter (45 mm), the flap width W, middle strap length H, flap length L, and inclination angle φ are selected according to the requirements in this research and shown in Figure 3.4.

In order to make this double-side flap, the polyvinyl chloride (PVC) window film (Wf1224pf, Pillar, Australia) with a thickness of 0.18 mm is used and cut into a double-sided shape. The front and back sides of this film have different surface roughness, with each side contacting the opposite side when weaving into a sheath. The measured coefficient of friction is 0.5 between the two sides.

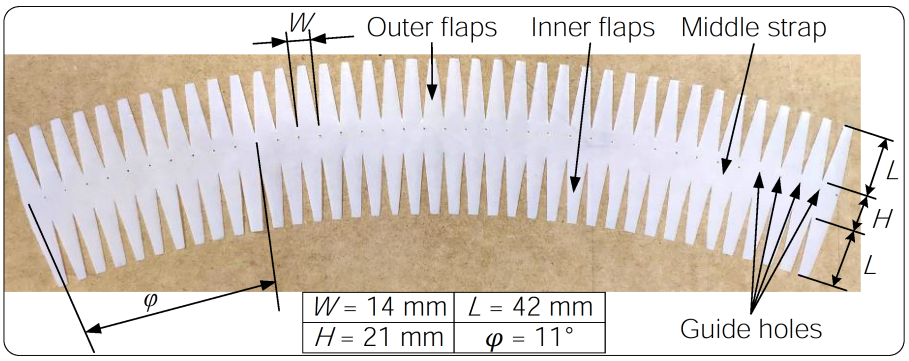

FIGURE 3.4: Layer jamming in the double-side flap pattern with guide holes.

3.2.3.2 Jamming sheath weaving method

When the continuum robot is bending, the layer jamming sheath is required to change its length correspondingly because the convex position will become longer while the concave position will be shorter. Therefore, the layer jamming sheath should have enough length-changing ability to ensure that the continuum robot can bend at enough angles to meet task requirements. For making the layer jamming sheath, researchers [4, 5, 9, 152, 161] used the guide hole and slot method. In that method, jamming flaps were restricted by a line going through the holes and slots, and the restriction line could shift in the slot. This provided the adjacent overlapping jamming flaps to move relative to each other, resulting in a length change of the whole sheath. However, that method had a limitation regarding the length-changing ability of the layer jamming sheaths due to the slot being too short (4 mm in [152]).

In order to improve the length-changing ability of the layer jamming sheath, a new weaving method is proposed to wind up the layer jamming into a tube sheath. To explain the weaving method, arbitrary adjacent three layers are selected. As shown in Figure 3.5(a), a nylon wire with a diameter of 0.6mm goes through the external side and internal side of all the jamming flaps alternately via the guide holes. The nylon line between the two guide holes is utilised for restricting the jamming flaps. The outer flaps and inner flaps of Layer (N) are inserted into the restriction nylon line on Layer ($N-1$) and Layer ($N+1$), respectively. Therefore, the outer flaps of the Layer (N) are confined by the line on the Layer ($N-1$), whereas the inner flaps of the Layer (N) are astricted by the line on the Layer ($N+1$). The two sectional view figures (A-A and B-B in Figure 3.5(a)) show the

insert position and restriction approach for the flaps. By this approach, the adjacent layers can be woven into a tube sheath and still have the capability to be bent, shrunk, and elongated arbitrarily. The completed layer jamming sheath is shown in Figure 3.5(b).

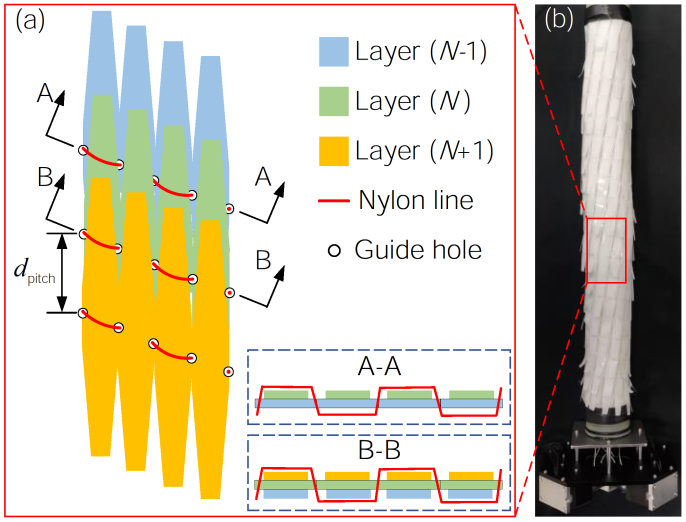

FIGURE 3.5: Jamming sheath. (a) diagram of the weaving method. (b) photo of the assembled layer jamming sheath that covers the support spine.

3.2.3.3 Length change evaluation of jamming sheaths

The stiffness reinforcement capability of a jamming sheath is determined by the force F_{J} required to detach the contact layers. According to the research in [4, 211], this force can be calculated as $F_{\mathrm{J}} = \mu n P S$, where μ is the coefficient of friction of the flaps, n is the layer overlap number, P is the applied pressure, and S is the overlap area which is determined by the overlap width and length of the flap. From this equation, two variables can be adjusted to vary stiffness once the flap pattern is set. The first one is the applied pressure P, which means different pressures would change the compression level of the jamming flaps. Then the cumulated friction results in a significant increase in rigidity. The second variable, the layer overlap numbers (n), can be used when winding up the layer jamming sheath to change its thickness. According to this jamming flap structure, the layer overlap numbers (n) can be achieved by applying different winding pitches (d_{pitch}) as

$$n = \frac{2L + H}{d_{\mathrm{pitch}}} \tag{3.1}$$

This is to ensure the inner and outer flaps are always moving relatively within the restriction nylon line and never out of the restriction. While ignoring the distortion of the flaps when weaving into a tube shape, the winding pitch range of this double-side flap is determined by

$$\frac{H}{2} < d_{\text{pitch}} < L + \frac{H}{2} \tag{3.2}$$

Because the layer jamming sheath is used to cover the support spine, its default length should be the same length as the support spine (l). When the robot is bending, adjacent jamming flaps will generate relative movement and then result in corresponding length changes of jamming sheaths as calculated by

$$\Delta l = \beta(\frac{l}{\beta} \pm 25) - l = \pm 25\beta \tag{3.3}$$

$$d_r = \frac{\Delta l d_{\text{pitch}}}{l} \tag{3.4}$$

where Δl is the length change of jamming sheaths and the plus and minus are the representation of the elongation (convex part) and contraction (concave part) of the jamming sheaths, respectively; β is the central angle of the robot when bending; d_r is the relative movement distance of adjacent jamming flaps.

In order to evaluate the designed jamming sheaths, the minimum and maximum length changes of jamming sheaths are calculated by

$$\Delta l_{\text{min}} = \frac{lH}{2d_{\text{pitch}}} - l \tag{3.5}$$

$$\Delta l_{\text{max}} = \frac{2lL + lH}{2d_{\text{pitch}}} - l \tag{3.6}$$

In this research, d_{pitch} = 35 mm and 21 mm are selected when weaving the layer jamming sheath on the support spine. Hence, the overlap layer numbers n = 3, and 5, respectively. Then the minimum and maximum length changes of jamming sheaths are Δl_{min} = -352.8 mm (n = 3), Δl_{max} = 252.0 mm (n = 3), Δl_{min} = -252.0 mm (n = 5), and Δl_{max} = 756.0 mm (n = 5), respectively. From these results, it can be seen that both two types of jamming sheaths can meet the length change requirements of Δl = ± 78.5 mm when the

robot is at the maximum designed bending angle of 180° with an outer diameter of 50 mm. The relative movement distance of adjacent jamming layer flaps are $d_r = \pm 5.5$ mm ($n = 3$) and $d_r = \pm 3.3$ mm ($n = 5$), respectively.

3.3 Approximate stiffness model

3.3.1 Model description

For analysing the stiffness and its changing tendency for the continuum robot under different conditions, stiffness models need to be developed. However, due to the complex structure and stiffness variability of the robot, it is hard to develop ideal beam models, and even finite element analysis has limitations because several parameters of the robot, including mechanical error, friction, and the jamming mechanism, are difficult to model. In order to define and qualitatively analyse the robot's effective stiffness and its changing tendency, an approximate stiffness model is developed based on the Euler-Bernoulli beam theory [214]. To represent the continuum robot with an equivalent beam model, the following assumptions are made [213, 215].

***Assumption* 3.1.** The continuum robot satisfies the properties:

(**a**) The deflection of the continuum robot is only caused by the position change of all movable parts of the robot and material strain is not considered;

(**b**) The analysis of continuum robot deflection is conducted in the horizontal plane, and gravity is not considered;

(**c**) The deflection of the continuum robot under external load has the same feature as a beam. ◁

When considering deflections of the continuum robot, it can be seen that deflections result from the structure shape change and material strain. The former is caused by the position change of all movable parts of the continuum robot, which is easier occurring compared to the latter because the material strain needs a greater force to generate a significant

deflection. Therefore, the Assumption 3.1**(a)** is made because the continuum robot has a flexible structure and the material strain is normally very small. Since stiffness analyses and experiments of the continuum robot are both conducted in the horizontal plane, considering that gravity does not have a significant effect on the stiffness in this static deflection analysis. Hence, the Assumption 3.1**(b)** is made. When the continuum robot is actuated by its actuator to the target shape, and then an external load is applied to its body, it is found that the whole robot body will correspondingly deflect, which has the same feature as a beam. Therefore, the Assumption 3.1**(c)** is made. Based on the above assumptions, the continuum robot can be treated as an equivalent cylindrical beam because it consists of two main cylindrical parts: a support spine and a jamming sheath, as shown in Figure 3.6(a).

In order to derive equations for analysing the effective stiffness and its changing tendency, the following assumptions are made for the equivalent beam [214, 216].

***Assumption* 3.2.** The equivalent beam satisfies the properties:

(**a**) The equivalent beam is homogeneous and obeys Hooke's law;

(**b**) Displacements of the equivalent beam are small compared to the length of the beam;

(**c**) The equivalent beam is in pure bending when it has deflections. ◁

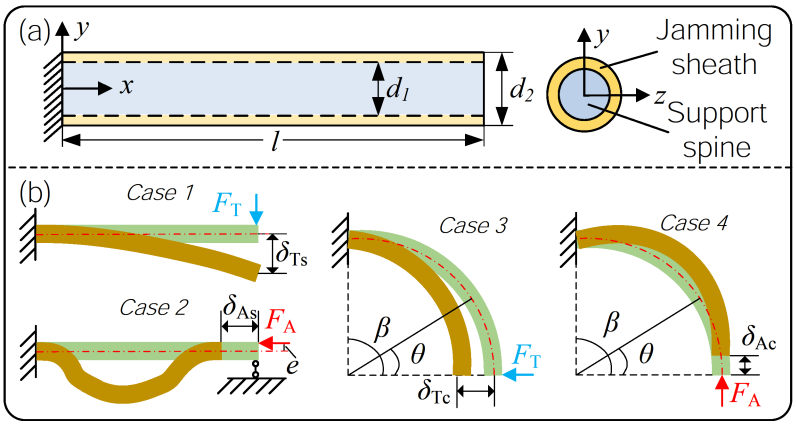

FIGURE 3.6: Diagram of equivalent beam and deflection cases. (a) diagram of the robot structure and equivalent beam. (b) four study cases of deflections of the continuum robot. *Case 1* straight beam under transverse load, *Case 2* straight beam under axial load, *Case 3* curved beam under transverse load, and *Case 4* curved beam under axial load.

When the continuum robot is in operation, external loads applying to the distal point of the continuum robot can be divided into transverse direction loads and axial direction loads. For the transverse direction loads, since the continuum robot has a cylinder shape and is symmetrical in circumference, the transverse direction loads at any point on the circumference should cause the same deflection. For the axial direction loads, only thrust loads are considered in this research because the support spine of the continuum robot is made of ball joints, and it's hard to generate significant deflection when drag loads apply. Therefore, only one type of transverse direction load and axial direction load are analysed for the continuum robot under different bending angles.

Once the continuum robot is represented by the equivalent beam, the stiffness of the robot can be analysed based on the Euler-Bernoulli beam theory. According to robot shapes and external loads, the equivalent beam can be a cantilever beam or fixed-fixed beam in form when analysing its deflections. Therefore, the equivalent beam is categorised into four types, as shown in Figure 3.6(b). When the robot is straight, its deflections can be analysed based on a cantilever beam model (*Case 1*) or fixed-fixed beam model (*Case 2*) depending on the directions of external loads [214]. When the robot is bent, its deflections can be analysed based on a cantilever beam model (*Case 3* and *Case 4*). In the four deflection cases, it's noted that the current effective stiffness only refers to the tip location. This focus is reasonable for continuum robots, as effective stiffness at the end-effector position is of greater interest and is easier to verify experimentally.

3.3.2 Model derivation

In this section, the robot's effective stiffnesses in the four cases are analysed. *Cases 1, 3* and *4* are solved based on the Maxwell-Mohr method [188], while *Case 2* is based on the integral method [214]. Based on the Maxwell-Mohr method, the deflection of a beam can be calculated as

$$\delta(x) = \int \frac{M(x)\overline{M}(x)}{D}\mathrm{d}x \tag{3.7}$$

where $\delta(x)$ is the deflection at x position, x is the analytical position on the beam and $x \in [0, l]$, $M(x)$ is the resultant moment at x position caused by an external load, $\overline{M}(x)$

is the moment at x position due to the unit load, D is flexural rigidity of the equivalent beam.

Case 1 Straight beam under transverse load:

When the continuum robot is straight, and the transverse load F_{T} is applied at the tip position, the resultant moment and unit moment at position x are

$$\begin{cases} M(x) = F_{\mathrm{T}} x \\ \overline{M}(x) = x \end{cases} \tag{3.8}$$

By substituting (3.8) into (3.7) and letting $x = l$, the effective stiffness in this case can be defined as

$$k_{\mathrm{TS}} = \frac{F_{\mathrm{T}}}{\delta_{\mathrm{TS}}} = \frac{F_{\mathrm{T}}}{\delta(x)\,|_{x=l}} = \frac{3D}{l^3} \tag{3.9}$$

where $\delta_{\mathrm{TS}} = \delta(x)\,|_{x=l}$ is the deflection at the tip position.

Case 2 Straight beam under axial load:

When the continuum robot is straight, and the external load F_{A} is applied on the robot's central axis, the stiffness of the robot in the axial direction should be infinite when ignoring the material strain. However, due to mechanical errors and assembly errors, the central lines of all movable parts cannot be kept in an exact line with the robot's central axis. Hence, infinite stiffness is only a theoretical stiffness under ideal conditions. In order to analyse the effective stiffness in the axial direction, a distance error (e) between the external load direction and the robot's central axis is assumed. In addition, a lateral force will be generated to restrict the robot's lateral motion when the axial load is applied to the robot. Hence, the robot deflection can be analysed based on the fixed-fixed model [214], and its governing equation and general solution are

$$\begin{cases} \dfrac{\mathrm{d}^4\delta(x)}{\mathrm{d}x^4} + a^2\dfrac{\mathrm{d}^2\delta(x)}{\mathrm{d}x^2} = 0, \quad a^2 = \dfrac{F_{\mathrm{A}}}{D} \\ \delta(x) = C_1\cos ax + C_2\sin ax + C_3 x + C_4 \end{cases} \tag{3.10}$$

where C_1, C_2, C_3, C_4 are some constants.

According to the Euler-Bernoulli beam theory, the boundary conditions for the fixed-fixed model are

$$\begin{cases} \delta(x)\,|_{x=0} = 0, & \delta(x)\,|_{x=l} = 0 \\ \delta''(x)\,|_{x=0} = 0, & \delta''(x)\,|_{x=l} = -\frac{F_{\mathrm{A}} e}{D} \end{cases} \tag{3.11}$$

Substituting boundary conditions (3.11) into (3.10), the explicit deflection solution is

$$\delta(x) = e(\frac{\sin ax}{\sin al} - \frac{x}{l}) \tag{3.12}$$

In (3.12), since $\sin al$ appears in the denominator, the deflection $\delta(x)$ will become infinite when $al = b\pi, (b \in \mathrm{Z})$. This phenomenon is called buckling, and the corresponding axial load is

$$F_{\mathrm{A}} = \frac{b^2\pi^2 D}{l^2} \tag{3.13}$$

When $b = 1, F_{\mathrm{cr}} = F_{\mathrm{A}}\,|_{b=1} = \frac{\pi^2 D}{l^2}$ is the critical load of buckling. Once the external load $F_{\mathrm{A}} \geq F_{\mathrm{cr}}$, the beam will buckle, and its stiffness will dramatically decrease. Since the tip deflection δ_{AS} is caused by the deflection $\delta(x)$ and both the two deflections are small, it assumes $\delta_{\mathrm{AS}} = \max[\delta(x)]$, then the effective stiffness in this case is

$$k_{\mathrm{AS}} = \frac{F_{\mathrm{T}}}{\delta_{\mathrm{AS}}} = \frac{F_{\mathrm{A}}}{\max[\delta(x)]}, \quad F_{\mathrm{A}} < F_{\mathrm{cr}} \tag{3.14}$$

Case 3 Curved beam under transverse load:

When the continuum robot is curved at a central angle $\beta \in (0, \pi]$, and the transverse load F_{T} is applied at the tip position, the resultant moment and unit moment at x position are

$$\begin{cases} M(\theta) = \dfrac{F_{\mathrm{T}} l \sin\theta}{\beta} \\ \overline{M}(\theta) = \dfrac{l \sin\theta}{\beta} \end{cases} \tag{3.15}$$

where $\theta = \frac{\beta(l-x)}{l}$ is the central angle between the x position and the tip position.

By substituting (3.15) into (3.7) and letting $x = l$, the effective stiffness in this case is defined as

$$k_{\mathrm{TC}} = \frac{F_{\mathrm{T}}}{\delta_{\mathrm{TC}}} = \frac{F_{\mathrm{T}}}{\delta(\theta)\,|_{x=l}} = \frac{4D\beta^3}{l^3(2\beta - \sin 2\beta)} \tag{3.16}$$

where $\delta_{\mathrm{TC}} = \delta(\theta)\,|_{x=l}$ is the deflection at the tip position.

Noted that $\frac{\beta^3}{2\beta - \sin 2\beta}$ in (3.16) is monotonically increasing about β. Hence, the effective stiffness k_{TC} will increase when increasing the robot's central angle β.

Case 4 Curved beam under axial load:

This case is the same as *Case 3* while the external load F_{A} is in the axial direction. When the axial load F_{A} is applied at the tip position, the resultant moment and unit moment at x position are

$$\begin{cases} M(\theta) = \dfrac{F_{\mathrm{A}} l(1 - \cos\theta)}{\beta} \\ \overline{M}(\theta) = \dfrac{l(1 - \cos\theta)}{\beta} \end{cases} \tag{3.17}$$

By substituting (3.17) in (3.7) and letting $x = l$, the effective stiffness in this case is defined as

$$k_{\mathrm{AC}} = \frac{F_{\mathrm{A}}}{\delta_{\mathrm{AC}}} = \frac{F_{\mathrm{A}}}{\delta(\theta)\,|_{x=l}} = \frac{4D\beta^3}{l^3(6\beta - 8\sin\beta + \sin 2\beta)} \tag{3.18}$$

where $\delta_{\mathrm{AC}} = \delta(\theta)\,|_{x=l}$ is the deflection at the tip position.

Noted that $\frac{\beta^3}{(6\beta - 8\sin\beta + \sin 2\beta)}$ in (3.18) is mainly monotonically decreasing about β. Hence, the effective stiffness k_{AC} will decrease when increasing the robot's central angle β.

When the robot is straight and horizontal, equation (3.9) shows that the effective stiffness k_{TS} is a constant with a specific flexural rigidity (D); equation (3.14) shows that the effective stiffness k_{AS} is divided into two levels by the critical load (F_{cr}): high stiffness before buckling and low stiffness after bucking. When the robot is bent, considering the monotonicity of equations (3.16) and (3.18), two specific curved angles ($\beta = 90°, 180°$) in the middle point and end point of the angle range ($\beta \in (0, \pi]$) are selected for the stiffness experiments because the effective stiffness k_{TC} and k_{AC} about the curved angle (β) are increasing and decreasing, respectively.

3.4 Experiments and results

3.4.1 Experiment setup

A test rig is built to test the robot's stiffness under different loading conditions. A linear actuator (L12-210-100-12I, Actuonix) is used to cause deflections, and an S-Beam load cell (JLBS-M2-10Kg) is used to collect resistance forces. In addition, a vacuum pump (KMDP-C1-12V) and a pressure sensor (DP-101A-E-P, Panasonic) are used to generate different vacuum pressures. To investigate the stiffness variation capability, the robot is tested at three different bending angles ($0°, 90°, 180°$) and four different vacuum pressures (0 kPa, 25 kPa, 50 kPa, 75 kPa). The tests are shown in Figure 3.7. In these experiments, the external load at the transverse and axial directions are applied separately.

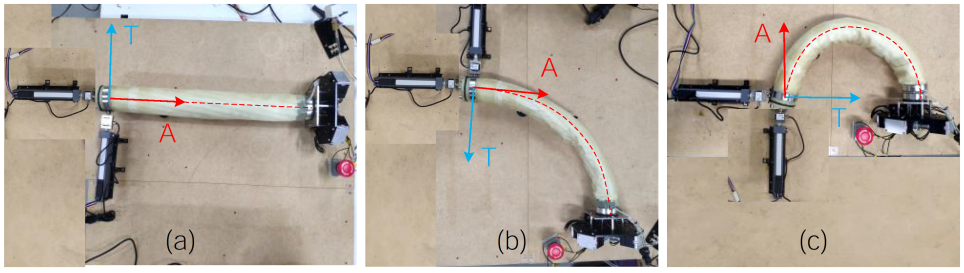

FIGURE 3.7: Experiment setup. (a) robot at 0° bending. (b) robot at 90° bending. (c) robot at 180° bending. Note that A and T in the figure represent the axial and transverse directions, respectively.

3.4.2 Force-deflection results

All the experimental data was collected and analysed using MATLAB™ software. Each experiment was repeatedly conducted five times under the same condition, and the mean value of the measured force in an experiment was calculated. Error bars shown in the plots are ±1 standard deviation for every 5mm deflection (transverse direction) and every 2 mm deflection (axial direction). The force-deflection results of the continuum robot are shown in Figure 3.8.

From Figure 3.8(a)-(c), it can be seen that both two types of jamming sheaths ($n = 3$ and 5) can enforce the resistance force in both the transverse and axial directions when

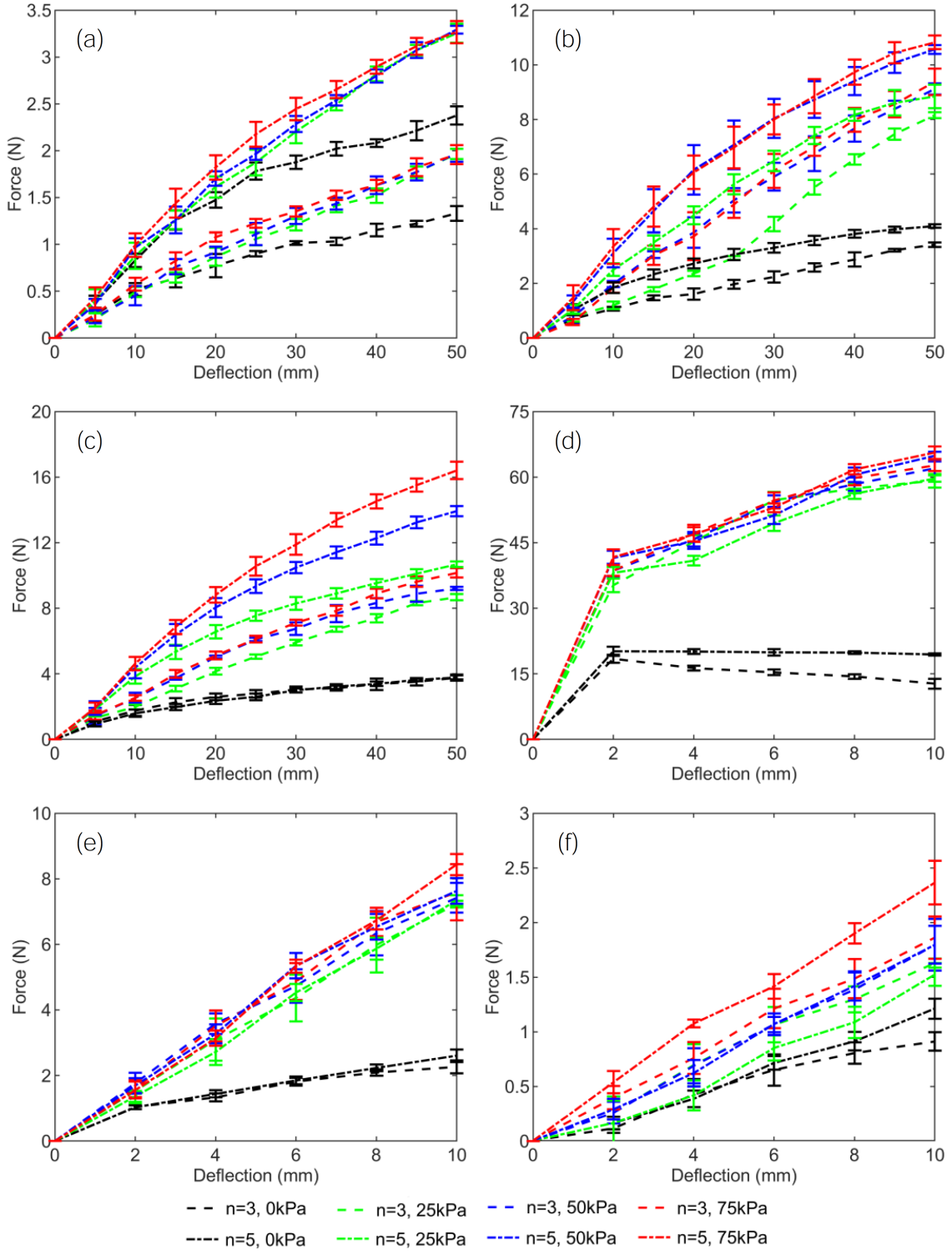

FIGURE 3.8: Force-deflection plots of the robot under Transverse (T direction) loads: (a) at 0° bending, (b) at 90° bending, (c) at 180° bending; Force-deflection plots of the robot under axial (A direction) loads: (d) at 0° bending, (e) at 90° bending, (f) at 180° bending.

vacuum pressures are applied, and the jamming sheath ($n = 5$) shows better ability than the jamming sheath ($n = 3$). When the bending angle is 0° (Figure 3.8(a)), because all jamming layers are tightly contacted, and there is no relative slip when vacuum pressure is applied, it shows the same stiffness tuning ability under different pressures [188]. Hence, the resisting forces are almost the same under the three vacuum pressures (25 kPa, 50 kPa, 75 kPa), with the maximum values of 2.0 N ($n = 3$) and 3.3 N ($n = 5$).

When the bending angle is 90° (Figure 3.8(b)), the overlap area of contacted jamming layers is changed, and it needs higher vacuum pressure to avoid relative slip. Hence, the resisting force of 25 kPa is lower than the force of 50 kPa and 75 kPa because slippage has occurred. The maximum resisting forces are 9.4 N ($n = 3$, 75 kPa) and 10.8 N (n= 5, 75 kPa). When the robot is bent by 180° (Figure 3.8(c)), in the convex part, as the jamming layer overlap area becomes much less, relative slip occurs at all the vacuum pressure conditions. After deflection of 15 mm, both types of jamming sheaths of $n = 3$ and 5 show contact layers slipping under all the vacuum pressures and resulting in different resisting forces. The maximum resisting forces in this situation are 10.2 N ($n = 3$, 75 kPa) and 16.4 N ($n = 5$, 75 kPa).

In the axial direction, Figure 3.8(d) and (e) show that the three different vacuum pressures (25 kPa, 50 kPa, 75 kPa) have a negligible effect on changing the resisting force. This is because the axial loads can hardly detach the contact jamming layers, and jamming sheaths always keep at the no-slip condition at all vacuum pressures. Therefore, higher vacuum pressure will not result in a better stiffening effect due to no relative slip occurring. When the bending angle is 0° (Figure 3.8(d)), the resistance forces are at the highest level and greater than in any other situation because ball joints on the support spine provides hard contact in the axial direction, and jamming sheaths cover the spine to restrict its tilt movement. The maximum resisting force is 62.6 N ($n = 3$) and 65.6 N ($n = 5$) under the vacuum pressure of 75 kPa. When the bending angle is 90° (Figure 3.8(e)), the robot shows almost the same resisting force under the vacuum pressure of 25 kPa, 50 kPa and 75 kPa, with a maximum value of 7.6 N ($n = 3$, 75 kPa) and 8.4 N ($n = 5$, 75 kPa). When the bending angle changes to 180° (Figure 3.8(f)), the contact layers are more likely to slip due to the change in the overlap area. Therefore, the resisting forces are different under

all the vacuum pressures and at the lowest level with the maximum values of 1.9 N (n = 3, 75 kPa) and 2.4 N (n = 5, 75 kPa).

3.4.3 Stiffness variation results

In order to reduce errors in comparing the stiffness under different conditions, average stiffness is calculated based on the force-deflection data presented in Figure 3.8.

1) Stiffness in the transverse direction

According to equations (3.9) and (3.16), the effective stiffness k_{TS} and k_{TC} should be constants with a specific flexural rigidity (D). However, the experimental data in Figure 3.8(a)-(c) are approximately linear. This error may result from the friction disturbance in the test rig, or the robot may not be perfectly represented by an equivalent beam model when it has deflections because of complex structures and mechanical errors of the robot. Therefore, to eliminate errors, the average stiffness of the robot is calculated by

$$S_{\mathrm{T}} = \frac{1}{10}\sum_{i=1}^{10}\frac{F_i}{\delta_i} \tag{3.19}$$

where S_{T} is the average transverse stiffness, F_i is the resisting force at point i, δ_i is the deflection at point i, i is the deflection point at Figure 3.8(a)-(c), starting at 5 mm and increasing 5 mm each time to 50 mm.

2) Stiffness in the axial direction

When the robot is straight, as analysed in *Case 2*, the effective stiffness keeps at a high level before critical load and will decrease to a low level once the robot buckles. In Figure 3.8(d), this phenomenon can be clearly seen. Before the 2 mm deflection, the robot shows high stiffness and then decreases to a low level with the deflection increasing, especially in no vacuum pressure conditions. Therefore, the robot stiffness should be divided into two

parts and calculated as

$$S_{\mathrm{AS}} = \begin{cases} \dfrac{F_{j=1}}{\delta_{j=1}}, \ (F_j < F_{\mathrm{cr}}) \\ \dfrac{1}{4}\displaystyle\sum_{j=2}^{5} \dfrac{F_j}{\delta_j}, \ (F_j \geq F_{\mathrm{cr}}) \end{cases} \tag{3.20}$$

where S_{AS} is the average axial stiffness when the robot is straight, F_j is the resisting force at point j, δ_j is the deflection at point j, j is the deflection point at Figure 3.8(d), starting at 2 mm and increasing 2 mm each time to 10 mm.

When the robot is bent, equation (3.18) shows that the effective stiffness k_{AC} is constant at a specific bending angle, and the experimental data in Figure 3.8(e) and (f) also show a linear relationship between force and deflection. Hence, the average stiffness is calculated as

$$S_{\mathrm{AC}} = \frac{1}{5}\sum_{j=1}^{5} \frac{F_j}{\delta_j} \tag{3.21}$$

As shown in Figure 3.9, the average stiffness results show that the vacuum pressure can change the robot stiffness at any condition, and the jamming sheath with a layer overlap number $n = 5$ has greater stiffness increasing ability compared to $n = 3$. The robot stiffness increases and decreases with the bending angle increasing in the transverse direction and axial direction, respectively. In the transverse direction, the robot is bent 0° with a vacuum pressure of 0 kPa has the minimum stiffness, i.e., 36.4 N/m ($n = 3$) and 65.7 N/m ($n = 5$), whereas the robot at the bending angle of 180° with a vacuum pressure of 75 kPa has the maximum stiffness of 241.7 N/m ($n = 3$) and 398.3 N/m ($n = 5$). At the bending angle of 90°, the stiffness is between that at bending 0° and 180° under each vacuum pressure.

In the axial direction, when the robot is straight and not buckling, the robot stiffness increases from 9.2×10^3 N/m to 19.3×10^3 N/m ($n = 3$) and 10.1×10^3 N/m to 20.8×10^3 N/m ($n = 5$) when the vacuum pressure changes from 0 kPa to 75 kPa. As presented before, this high stiffness is mainly a result of the mechanical stiffness of the support spine. After buckling, the maximum average stiffness decreases to 8.6×10^3 N/m ($n = 3$, 75 kPa) and 8.7×10^3 N/m ($n = 5$, 75 kPa). When the robot is at a bending of 180°, it has a minimum stiffness of 92.9 N/m ($n = 3$) and 106.7 N/m ($n = 5$) at the vacuum pressure

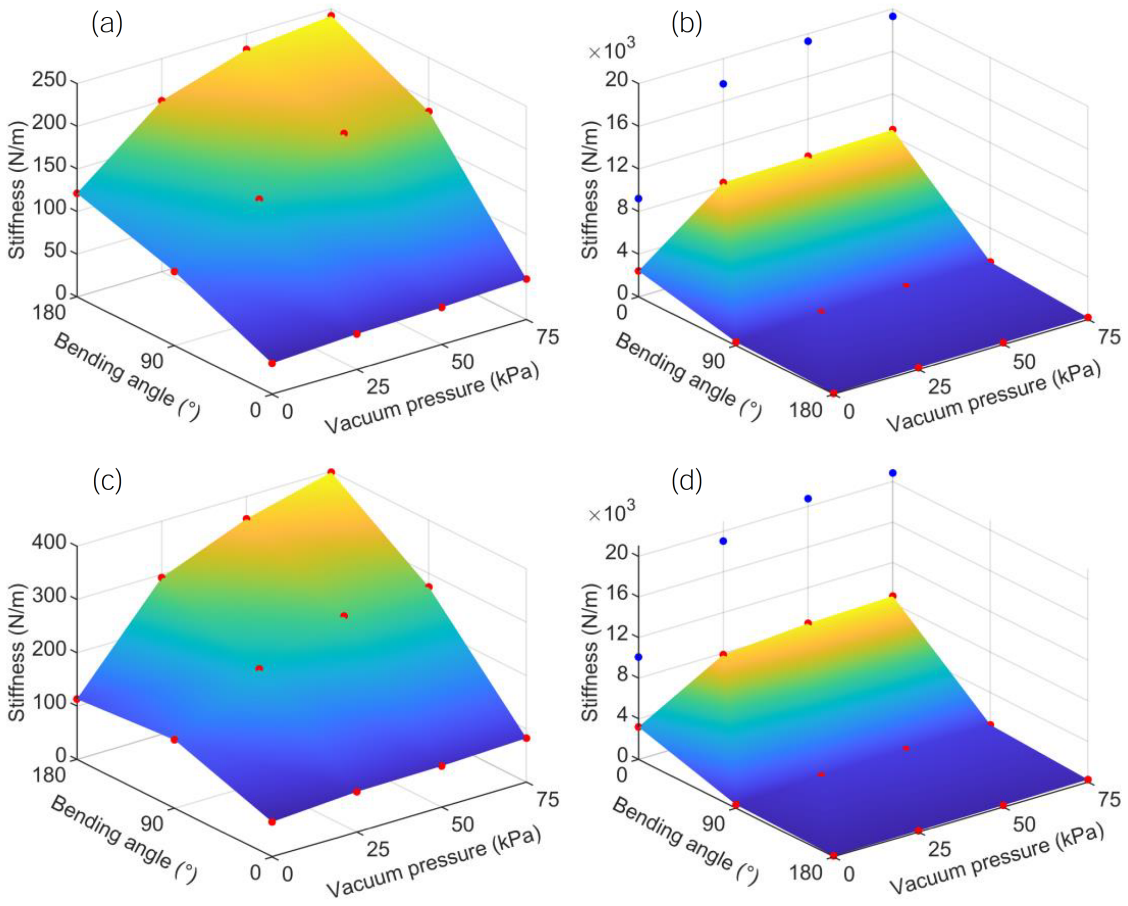

FIGURE 3.9: Average stiffness results. (a) transverse direction with $n = 3$. (b) axial direction with $n = 3$. (c) transverse direction with $n = 5$. (d) axial direction with $n = 5$. Note that the red dots denote the average stiffness, and the blue dots denote the stiffness before buckling.

of 0 kPa, and the stiffness increases to 192.4 N/m ($n = 3$) and 249.7 N/m ($n = 5$) when the vacuum pressure reached 75 kPa. Similarly, the stiffness has the same changing trend when the bending angle is 90°, from 328.6 N/m ($n = 3$, 0 kPa) and 344.5 N/m ($n = 5$, 0 kPa) rising to 816.6 N/m ($n = 3$, 75 kPa) and 827.1 N/m ($n = 5$, 75 kPa), respectively.

3.4.4 Actuation and gripping experiments

The designed prototype robot can be used as a manipulator for various tasks including gripping, moving, and inspection. Due to its inherent compliance and flexibility, this prototype robot can grasp or carry an object by its body or end-effector. Experiments about actuating and gripping are conducted. An electromagnet (GE-66-100-38, Magnetic

Sensor Systems, USA) is attached to the distal of the robot and works as an end-effector in moving tasks (e.g., a piece of iron). These experiments are shown in Figure 3.10.

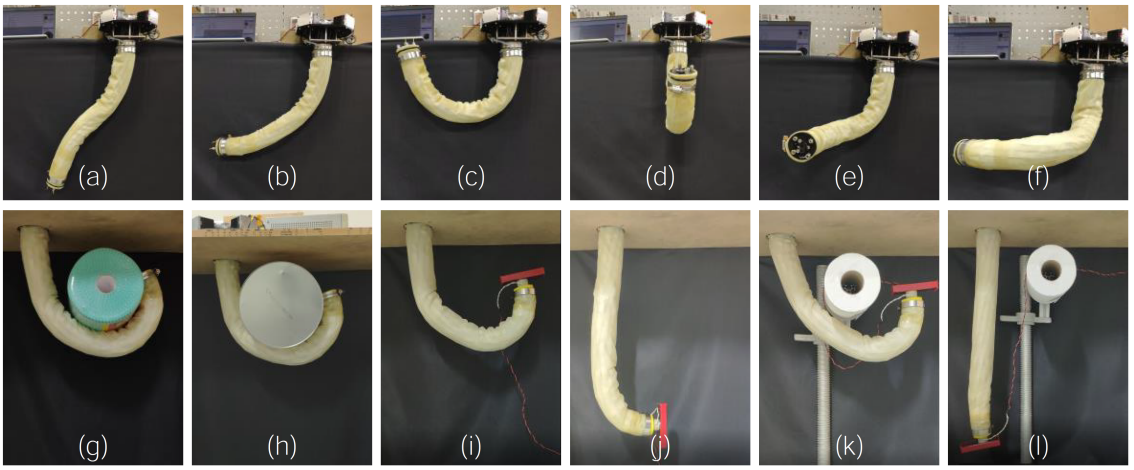

FIGURE 3.10: Photos of the robot actuating and gripping experiments. (a)-(f) the robot is at different bending postures. (g) the robot is gripping a paper roll with a weight of 590g and a diameter of 145mm. (h) the robot is gripping an iron bucket with a weight of 1.2kg and a diameter of 180mm. (i)-(l) the robot is moving a piece of iron (511g) using its end-effector, (i)-(j) show a normal moving task, and (k)-(l) show the task with the obstacle.

3.5 Discussion

The designed continuum robot uses ball joints to offer axial support. Its stiffness variation capabilities in both the transverse and axial directions are realised by using layer jamming. Compared to previous research, this design has the advantages of higher axial stiffness, and larger length changing ability of jamming sheaths. It has demonstrated that this robot can be used in different applications as a manipulator or end-effector.

In the four deflection cases, although the effective stiffness k_{TS}, k_{TC}, k_{AS}, and k_{AC} of the continuum robot cannot be numerically calculated due to the flexural rigidity (D) being hard to obtain because of the complex structure and stiffness variability of the robot, the stiffness changing tendency in the four cases can instead be analysed qualitatively. When the robot is straight, the effective stiffness k_{TS} is a constant with a specific flexural rigidity (D), and the effective stiffness k_{AS} is divided into two levels by the critical load (F_{cr}): high stiffness before buckling and low stiffness after bucking, and the critical load

(F_{cr}) is determined by the flexural rigidity (D). When the robot is bent, the effective stiffness k_{TC} will increase while the effective stiffness k_{AC} will decrease when the central angle of the continuum robot is increasing, respectively. In addition, the effective stiffness analysis in this work focuses solely on the tip location, as it is easier for experimental verification and aligns with current research. However, analysing stiffness along the entire continuum robot body and calculating flexural rigidity (D) could be explored as part of future work.

3.6 Summary

In this chapter, a novel continuum robot named OctRobot-I is presented. By designing support spine and layer jamming sheaths, the robot has stiffness variation capability in both transverse and axial directions. A new jamming sheath weaving method using a nylon line and adjacent layers to restrict jamming flaps is proposed, and its length changing ability is evaluated. Four deflection cases of the robot are analysed. Based on the Euler-Bernoulli beam theory and Maxwell-Mohr method, the robot's effective stiffnesses in the four cases are defined and derived.

Experiments are conducted with two types of layer jamming sheaths (overlap numbers n = 3, 5) and four different vacuum pressures (0 kPa, 25 kPa, 50 kPa, 75 kPa) at three different bending angles (0°, 90°, 180°). The results show that when the robot is fitted with the jamming sheath of $n = 3$, the stiffness ranges (ratios) are 36.4 to 241.7 N/m (6.6) and 92.9 to 19.3 $\times$ 10^3 N/m (207.8) in the transverse and axial directions, respectively. When fitted with the jamming sheath of $n = 5$, the stiffness ranges (ratios) are 65.7 to 398.3 N/m (6.1) and 106.7 to 20.8 $\times$ 10^3 N/m (194.9) in the transverse and axial directions, respectively. In addition, actuating and gripping experiments demonstrated the control and payload of the robot. Future work includes further improvement of the effectiveness of the stiffness model for numerical analysis of the stiffness variation capability, workspace analysis, real-time position and stiffness control.

Chapter 4

Robot Worksapce Analysis and Equivalent Two Section Method

The shape and size of a robot's workspace are essential for both design and control. However, determining the accurate workspace of a multi-segment continuum robot by graphic or analytical methods is a challenging task due to its inherent flexibility, complex structure, and high number of segments. This chapter will present an equivalent two section (ETS) method for calculating the workspace of multi-segment continuum robots. This method is based on the forward kinematics and a piecewise constant curvature (PCC) assumption to determine the boundaries of workspaces, and then calculate their size and volume. In order to verify the proposed method, simulation experiments are conducted using six different maximum bending angles and seven different number of segments. The results demonstrate that the ETS method is accurate and efficient. [1]

[1]The results presented in this chapter have previously appeared in the publication: Yeman Fan, Dikai Liu. "An equivalent two section method for calculating the workspace of multi-segment continuum robots." *2023 IEEE International Conference on Robotics and Automation (ICRA)*, London, United Kingdom, pp. 9658-9664, 2023.

4.1 Introduction

Continuum robots have many advantages when compared to traditional rigid robots, including inherent compliance, flexibility, and dexterity [19]. As partially described in Chapter 2, there are a lot of different types of continuum robots. However, obtaining their workspace remains a challenge due to their complex structure, infinite number of degrees of freedom, and high number of segments.

The workspace of a robot is defined as the set of positions that can be reached by its distal point. It is an important kinematic factor in measuring a robot's workability, and obtaining the shape and size of a robot's workspace is essential for its design, control, and planning [217, 218]. Generally, workspace calculation methods can be categorised into three types: graphic methods, analytical methods [219, 220], and numerical methods [221–224]. Analytical methods use multiple envelopes to determine the boundary of the workspace, which results in efficient calculation and high accuracy but with poor versatility and practicability [223]. Numerical methods calculate the distal point positions using extreme value theory, brute-force enumeration, or optimisation methods. They generate a workspace by calculating the feature points on the boundary of the workspace. A commonly used numerical method is the Monte Carlo method which uses the means of random sampling and is relatively simple to apply because it does not need inverse Jacobian calculation [222].

The brute-force Monte Carlo method needs to have sufficient sampling points to achieve reasonable precision, which has the shortcoming of low efficiency and large calculation errors [225]. A relatively more accurate workspace was calculated by combining the Beta distribution with the Monte Carlo method [221, 222]. By using the Gaussian growth method, an improved Monte Carlo method was proposed to attain higher workspace accuracy [225]. In [223], a Monte Carlo learning method based on boundary point densification was proposed. Although these methods improved the classical Monte Carlo method by taking advantage of the Beta distribution or Gaussian growth method to increase the density of boundary points, they need sufficient sampling points to obtain reasonable precision, which still has a high computational cost.

When the classical or improved Monte Carlo methods are applied to calculate the workspace of a multi-segment continuum robot, it can be found that most of the sample points overlap and are located in the high-probability regions of the workspace, which makes it difficult to characterise the true shape and size of the workspace of a continuum robot. This has been also observed in [221, 222, 225]. When a continuum robot has a large number of segments, these methods may not be able to find the complete workspace because the efficient of samples is extremely low. In order to address this problem, this chapter proposes the ETS method to calculate the workspace of continuum robots with multi-segments. The ETS method represents a multi-segment continuum robot with two equivalent sections and then utilises forward kinematics and a PCC assumption to generate the workspace boundary for calculating the workspace area and volume. To verify the proposed ETS method, simulation experiments are conducted using six different maximum bending angles and seven different number of segments. The results of the ETS method are compared to the true workspaces estimated by an exhaustive approach for validation.

4.2 Equivalent two section method

4.2.1 Parameters of continuum robots

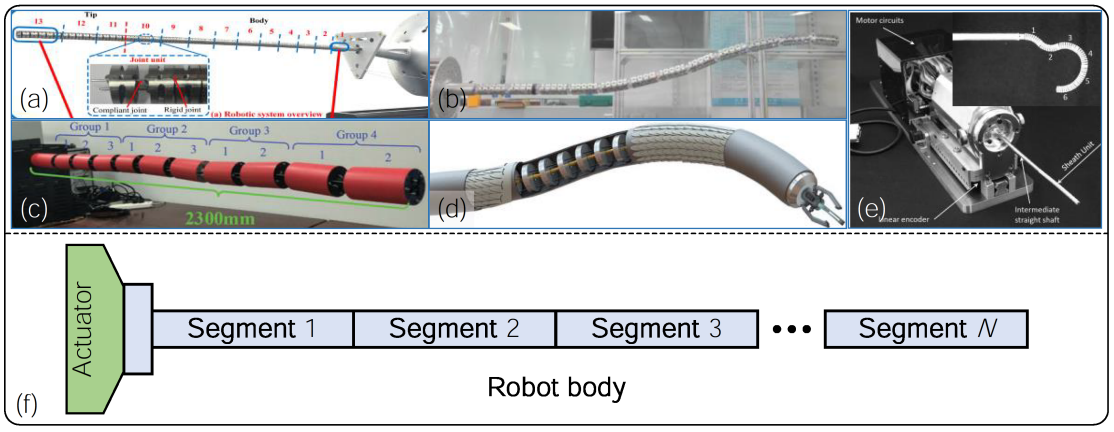

FIGURE 4.1: Photos and diagram of the structure of continuum robots. (a) a novel extra slender continuum robot [12]. (b) a cable-driven manipulator [13]. (c) a snake-inspired layer-driven continuum robot [14]. (d) sectional view of a tendon-actuated continuum robot [5]. (e) a wire-driven continuum robot with six sub-sections [15]. (f) a diagram of general continuum robots.

As shown in Figure 4.1, a continuum robot generally consists of an actuator unit and a flexible body. The robot body normally has many segments and each with bending capability. According to the existing design (Table 4.1), three common primary parameters of continuum robots are identified: the length of each segment, the number of segments, and the maximum bending angle of a segment. Clearly, the workspace size and shape of a continuum robot are mainly determined by these three parameters. Generally, all the segments in a continuum robot are identical. Therefore, this research focuses on continuum robots that consist of many identical segments, i.e., all the segments have the same length and same maximum bending angle.

TABLE 4.1: Summary of parameters of example continuum robots

NO.	ROBOT LENGTH (MM)	NUMBER OF SEGMENTS	BENDING ANGLE (°)	RELATED WORKS
1	550 165	10 (Body) 10 (Tip)	$-10 \sim +90$ $-90 \sim +90$	[12]
2	40	4	± 60	[165]
3	65	3	45	[2]
4	1800	12	45	[13]
5	4200	12	± 60	[226]
6	1500	6	20	[14]
7	2300 60	10 6	20 ± 90	[15]
8	630	3	60	[227]
9	210	3	36	[133]
10	831	3	90	[228]
11	560	4	± 45	[72]
12	165	3	83	[145]

4.2.2 Kinematic model

For calculating the distal position of a continuum robot, the PCC assumption is helpful for kinematic calculation [229–231]. The PCC assumption assumes that each segment has a constant curvature, which can change with different bending conditions. Figure 4.2 shows the geometric relationship of a multi-segment continuum robot based on the PCC assumption and an example constant curvature segment.

Based on the PCC assumption, the distal position can be calculated according to the robot kinematics. As shown in Figure 4.2(b), the curvature of a segment is determined by

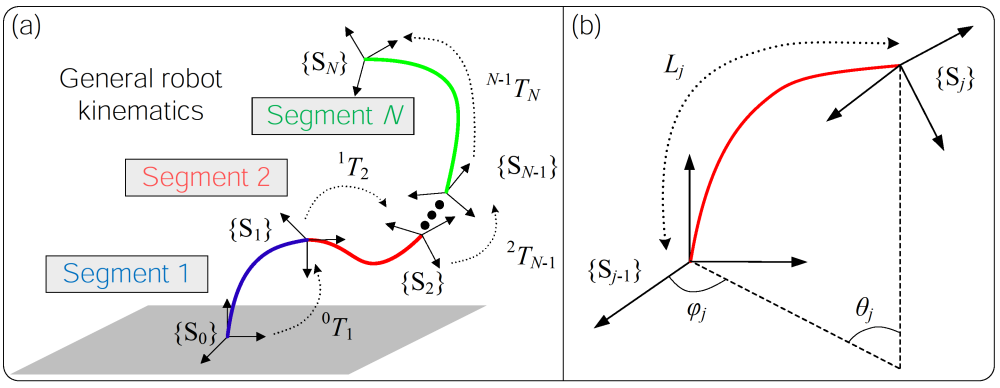

FIGURE 4.2: General robot kinematics. (a) the geometric relationship of a multi-segment continuum robot. (b) diagram of a constant curvature segment.

the segment length (L_j), bending angle (θ_j), and rotation angle (φ_j). Once the segment length is determined, according to the geometric relationship, the coordinate of a point on a continuum robot depends on the bending angle (θ_j), rotation angle (φ_j) and the reference coordinate system, which can be formulated by a 4×4 homogeneous transformation matrix (HTM)

$$ {}^{j-1}T_j = \begin{bmatrix} R_j & P_j \\ 0 & 1 \end{bmatrix} \tag{4.1} $$

$$ R_j = \begin{bmatrix} \mathrm{c}^2\varphi_j\mathrm{c}\theta_j + \mathrm{s}^2\varphi_j & \mathrm{c}\varphi_j\mathrm{s}\varphi_j\mathrm{c}\theta_j - \mathrm{c}\varphi_j\mathrm{s}\varphi_j & \mathrm{c}\varphi_j\mathrm{s}\theta_j \\ \mathrm{c}\varphi_j\mathrm{s}\varphi_j\mathrm{c}\theta_j - \mathrm{c}\varphi_j\mathrm{s}\varphi_j & \mathrm{s}^2\varphi_j\mathrm{c}\theta_j + \mathrm{c}^2\varphi_j & \mathrm{s}\varphi_j\mathrm{s}\theta_j \\ -\mathrm{c}\varphi_j\mathrm{s}\theta_j & -\mathrm{s}\varphi_j\mathrm{s}\theta_j & \mathrm{c}\theta_j \end{bmatrix} \tag{4.2} $$

$$ P_j = \begin{bmatrix} \frac{L_j}{\theta_j}\mathrm{c}\varphi_j(1-\mathrm{c}\theta_j) & \frac{L_j}{\theta_j}\mathrm{s}\varphi_j(1-\mathrm{c}\theta_j) & \frac{L_j}{\theta_j}\mathrm{s}\theta_j \end{bmatrix}^T \tag{4.3} $$

where j is the segment number. $\mathrm{s}\theta_j = \sin\theta_j$, $\mathrm{c}\theta_j = \cos\theta_j$, $\mathrm{s}\varphi_j = \sin\varphi_j$, $\mathrm{c}\varphi_j = \cos\varphi_j$, $\mathrm{s}^2\varphi_j = (\sin\varphi_j)^2$, $\mathrm{c}^2\varphi_j = (\cos\varphi_j)^2$, $\varphi_j \in [0, 2\pi]$.

In (4.3), there is a singularity when $\theta_j = 0$. Therefore, in this research, $\theta_{\min} = 0.0001$ is used to replace the singular point ($\theta_j = 0$) in the calculations. From kinematics, the coordinate system S_N relative to the base coordinate system S_0 can be expressed as

$$ {}^{0}T_N = {}^{0}T_1 {}^{1}T_N \cdots {}^{N-1}T_N = \begin{bmatrix} n_x & o_x & a_x & p_x \\ n_y & o_y & a_y & p_y \\ n_z & o_z & a_z & p_z \\ 0 & 0 & 0 & 1 \end{bmatrix} \tag{4.4} $$

4.2.3 True workspace estimation

From (4.4), all the feasible positions of the robot distal point can be calculated, and the true workspace can be obtained if the sample configurations are sufficient. As presented in Section 4.1, the true workspace of a continuum robot with a large number of segments is hard to obtain. Therefore, an exhaustive approach is used to estimate the workspace, which is considered as the approximation of the true workspace. Algorithm 4.1 presents the exhaustive approach to estimating the workspace area (A) or volume (V) of a continuum robot by exhaustively generating the configurations of each segment. For simplicity, the term "true workspace" used in this thesis means the workspace estimated by using the exhaustive approach. This workspace will be used to analyse the accuracy and efficiency of the proposed ETS method.

The exhaustive approach can only estimate the true workspace of a continuum robot with a small number of segments and intervals. With the increase in the number of segments, the sample configurations of the distal positions will increase exponentially. For example, if the number of segments is $N = 10$, the maximum bending angle $\theta_{\max} = 180°$ and the sampling interval $D = 2°$, the total number of total distal point positions to be calculated will be 181^{10}. The computational cost can be reduced by increasing the interval angle. For example, when the sampling interval is increased to $D = 180°$, the total number of distal positions to be calculated will decrease to 3^{10}. However, this large sampling interval will result in sparse distal point positions, and incomplete and inaccurate workspace.

Algorithm 4.1 Workspace calculation by an exhaustive approach

Input: Sampling interval value D;
Number of segments N;
Maximum bending angle $\theta_{\max}$;
Section length L.
Outputs: Workspace area (A) and volume (V).
Algorithm:
for $i \leftarrow 1$ to N **do**
  $\theta_i \leftarrow [\theta_{\min}, D, 2D, ..., \theta_{\max}]$
  $\theta_i \leftarrow [\theta_i * \cos(0), \theta_i * \cos(\pi)]$ ▷ Generate the bending angle matrix
end for
$J \leftarrow (2\theta_{\max}/D + 2)^N$ ▷ Calculate sample size
for $j \leftarrow 1$ to J **do**
  $[{}^0T_1, {}^1T_2, ..., {}^{N-1}T_N] \leftarrow f\{\theta_i, L, j\}$ ▷ Calculate the HTM, (4.1)-(4.3)
  ${}^0T_N \leftarrow {}^0T_1 * {}^1T_2 ... * {}^{N-1}T_N$
  $P[x, y] \leftarrow f\{{}^0T_N\}$ ▷ Calculate the distal position matrix, (4.4)
end for
$[BL, A] \leftarrow$ *find the boundary line (BL) and area (A) of P[x, z]*
$BS \leftarrow$ *rotate BL to generate the boundary surface (BS)*
$V \leftarrow$ *calculate the volume of (BS)*
return A, V

4.2.4 The equivalent two section method

In order to calculate the workspace of a continuum robot with multi-segments, the ETS method is proposed. When the maximum bending angle ($\theta_{\max}$) and the number of segments (N) are determined, the ETS method can be used for estimating the workspace, as shown in Figure 4.3. The ETS method utilises the *Equivalent Section 1* to represent the first several segments and the *Equivalent Section 2* to replace the remaining segments. In order to increase the accuracy, the *Equivalent Section 1* should have enough maximum bending angle to reach all the feasible workspace boundaries. The parameters of the ETS method can be derived as

$$
\begin{cases}
L_{\mathrm{E1}} = \begin{cases} L & (\theta_{\max} \geq \pi) \\ \pi L/\theta_{\max} & (\theta_{\max} < \pi) \end{cases} \\
L_{\mathrm{E2}} = NL - L_{\mathrm{E1}} \\
\theta_{\mathrm{E1\,max}} = \begin{cases} \pi & (\theta_{\max} \geq \pi) \vee (\pi/\theta_{\max} \leq N-1) \\ (N-1)\theta_{\max} & (\pi/\theta_{\max} > N-1) \end{cases} \\
\theta_{\mathrm{E2\,max}} = \begin{cases} \pi & (\theta_{\max} \geq \pi) \vee (N\theta_{\max} - \theta_{\mathrm{E1\,max}} \geq \pi) \\ N\theta_{\max} - \theta_{\mathrm{E1\,max}} & (N\theta_{\max} - \theta_{\mathrm{E1\,max}} < \pi) \end{cases}
\end{cases} \tag{4.5}
$$

where L is the segment length of a continuum robot, L_{E1} is the length of the first equivalent section of the ETS method, L_{E2} is the second equivalent section length, $\theta_{\mathrm{E1\,max}}$ is the maximum bending angle of the first equivalent section, $\theta_{\mathrm{E2\,max}}$ is the maximum bending angle of the second equivalent section.

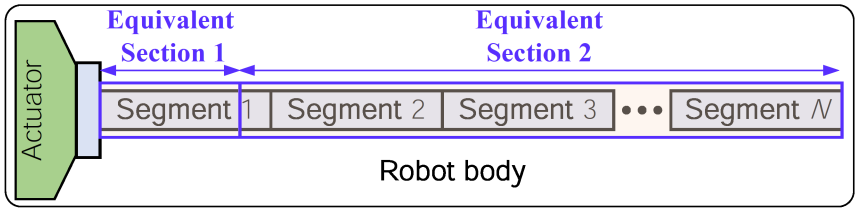

FIGURE 4.3: Diagram of the ETS method.

As shown in Figure 4.3, a multi-segment continuum robot can now be represented with an equivalent two section robot according to the ETS method. For example, when the robot parameters are $N = 3$, $\theta_{\max} = 180°$, and $L = 50$ mm, the parameters of the ETS model are $\theta_{\mathrm{E1\,max}} = \theta_{\mathrm{E2\,max}} = 180°$, $L_{\mathrm{E1}} = 50$ mm, and $L_{\mathrm{E2}} = 100$ mm; when the robot parameters are $N = 8$, $\theta_{\max} = 120°$, and $L = 50$ mm, the parameters of the ETS model are $\theta_{\mathrm{E1\,max}} = \theta_{\mathrm{E2\,max}} = 180°$, $L_{\mathrm{E1}} = 75$ mm, and $L_{\mathrm{E2}} = 325$ mm. Once the parameters $\theta_{\mathrm{E1\,max}}$, $\theta_{\mathrm{E2\,max}}$, L_{E1}, and L_{E2} are obtained, the ETS robot model can be used to calculate the workspace of a continuum robot. In order to demonstrate and verify the proposed ETS method, an example overlap 2D workspace is shown in Figure 4.4. The true workspace area [Green] is estimated by the exhaustive approach (Algorithm 4.1), and the workspace area calculated by the ETS method is the area covered by the boundary lines [Blue].

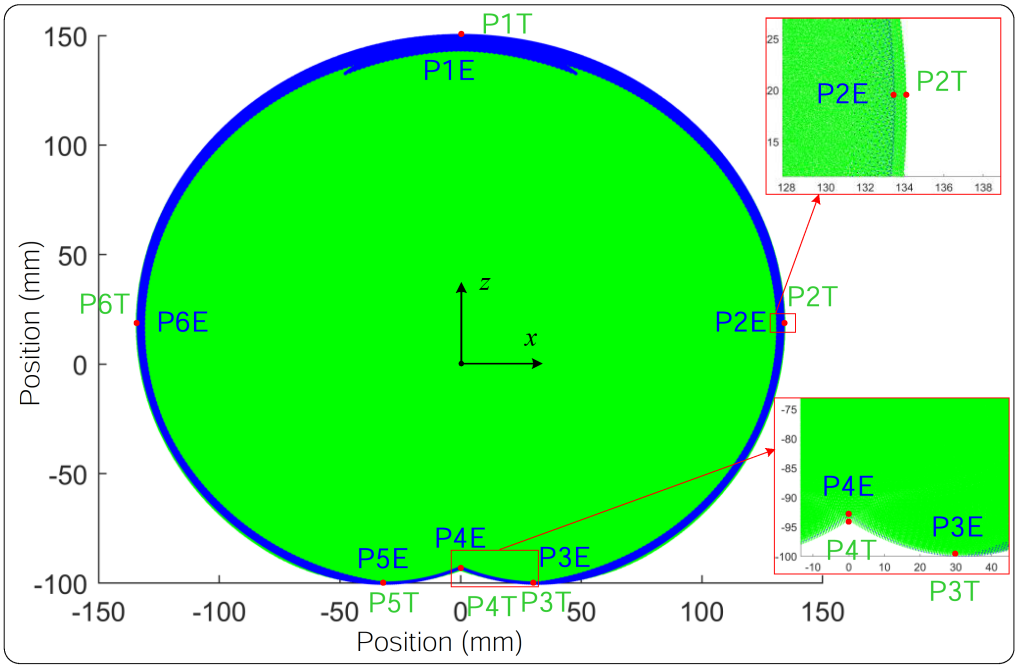

FIGURE 4.4: An example 2D workspace and boundary features of a continuum robot with $N = 3$, $L = 50$mm, $\theta_{\max} = 180°$. The green colour shows the true workspace area, and the blue colour shows the boundary generated by the ETS method.

Points P1T-P6T and P1E-P6E in Figure 4.4 are feature points of the true workspace and the boundary lines calculated by the ETS method, respectively. P1T and P1E are the points with maximum z position value on the true workspace and the boundary from the ETS method, respectively. P2T and P2E, and P6T and P6E are the points with maximum and minimum x position values on the true workspace and the boundary of the ETS method, respectively. P3T and P3E and P5T and P5E are the points with minimum z value on the true workspace and the boundary of the ETS method, respectively. P4T and P4E are the points with x= 0 on the true workspace and the boundary of the ETS method, respectively. It is found that P1T and P1E always overlap, and P2T and P6T, P2E and P6E, P3T and P4T, and P3E and P4E are symmetry about the z-axis, respectively. Their values can be calculated from (4.6).

$$
\begin{cases}
x_{\mathrm{P1T}} = p_x|_{\theta_{i=1,\ldots,N}=\theta_{\min},\varphi_{i=1,\ldots,N}=0} \approx 0 \\
z_{\mathrm{P1T}} = p_z|_{\theta_{i=1,\ldots,N}=\theta_{\min},\varphi_{i=1,\ldots,N}=0} \approx \sum_{i=1}^{N} L_i \\
x_{\mathrm{P1E}} = x_{\mathrm{E}}|_{\theta_{\mathrm{E1}}=\theta_{\mathrm{E2}}=\theta_{\min},\varphi_{\mathrm{E1}}=\varphi_{\mathrm{E2}}=0} \approx 0 \\
z_{\mathrm{P1E}} = z_{\mathrm{E}}|_{\theta_{\mathrm{E1}}=\theta_{\mathrm{E2}}=\theta_{\min},\varphi_{\mathrm{E1}}=\varphi_{\mathrm{E2}}=0} \approx L_{\mathrm{E1}} + L_{\mathrm{E2}} \\
x_{\mathrm{P2T}} = -x_{\mathrm{P6T}} = \max(p_x) \\
z_{\mathrm{P2T}} = z_{\mathrm{P6T}} = p_z|_{p_x=\max(p_x)} \\
x_{\mathrm{P2E}} = -x_{\mathrm{P6E}} = \max(x_{\mathrm{E}}) \\
z_{\mathrm{P2E}} = z_{\mathrm{P6E}} = z_{\mathrm{E}}|_{x_{\mathrm{E}}=\max(x_{\mathrm{E}})} \\
x_{\mathrm{P3T}} = -x_{\mathrm{P5T}} = p_x|_{p_z=\min(p_z)} \\
z_{\mathrm{P3T}} = z_{\mathrm{P5T}} = \min(p_z) \\
x_{\mathrm{P3E}} = -x_{\mathrm{P5E}} = x_{\mathrm{E}}|_{Z_{\mathrm{E}}=\min(z_{\mathrm{E}})} \\
z_{\mathrm{P3E}} = z_{\mathrm{P5E}} = \min(z_{\mathrm{E}}) \\
x_{\mathrm{P4T}} = x_{\mathrm{P4E}} = p_x = 0 \\
z_{\mathrm{P4T}} = p_z|_{p_x=0} \\
z_{\mathrm{P4E}} = z_E|_{x_E=0}
\end{cases}
\tag{4.6}
$$

4.2.5 Workspace calculation algorithm

Once the boundary shape is obtained by using the ETS method (e.g., the blue line in Figure 4.4), the workspace area can be calculated (e.g., using the Convhull function in MATLAB™). Then, the workspace volume can be calculated by rotating the workspace area around the z-axis. Figure 4.5 shows the example boundary lines and a quarter of the workspace volume generated by the exhaustive approach and the ETS method. The pseudocode of the ETS method is shown in Algorithm 4.2.

Algorithm 4.2 Workspace calculation by the ETS method

Input: Sampling interval value D;
Number of segments N;
Maximum bending angle $\theta_{\max}$;
Section length L.
Outputs: Workspace area (A) and volume (V).
Algorithm:
$[L_{\mathrm{E1}}, L_{\mathrm{E2}}, \theta_{\mathrm{E1\,max}}, \theta_{\mathrm{E2\,max}}] \leftarrow f\{D, N, \theta_{\max}, L\}$ ▷ Calculate ETS parameters, (4.5)
$\theta_{\mathrm{E1}} \leftarrow \{[\theta_{\min}, 1, 2, \ldots, \theta_{\mathrm{E1\,max}}] * \cos(0); [\theta_{\min}, 1, 2, \ldots, \theta_{\mathrm{E1\,max}}] * \cos(\pi)\}$
$\theta_{\mathrm{E2}} \leftarrow \{[\theta_{\min}, 1, 2, \ldots, \theta_{\mathrm{E2\,max}}] * \cos(0); [\theta_{\min}, 1, 2, \ldots, \theta_{\mathrm{E2\,max}}] * \cos(\pi)\}$ ▷ Generate the bending angle matrix
for $i \leftarrow 1$ to **size**(θ_{E1}) **do**
  $\theta_1 \leftarrow \theta_{\mathrm{E1}}(i))$
  for $j \leftarrow 1$ to **size**(θ_{E2}) **do**
    $\theta_2 \leftarrow \theta_{\mathrm{E2}}(j)$
    $[{}^0T_1, {}^1T_2] \leftarrow f\{L_{\mathrm{E1}}, L_{\mathrm{E2}}, \theta_{\mathrm{E1\,max}}, \theta_{\mathrm{E2\,max}}\}$ ▷ Calculate the HTM, (4.1)-(4.3)
    ${}^0T_2 \leftarrow {}^0T_1 * {}^1T_2$
    $P[x, y] \leftarrow f\{{}^0T_2\}$ ▷ Calculate the distal position matrix, (4.4)
  end for
end for
$[BL, A] \leftarrow$ *find the boundary line (BL) and area (A) of P[x, z]*
$BS \leftarrow$ *rotate BL to generate the boundary surface (BS)*
$V \leftarrow$ *calculate the volume of (BS)*
return A, V

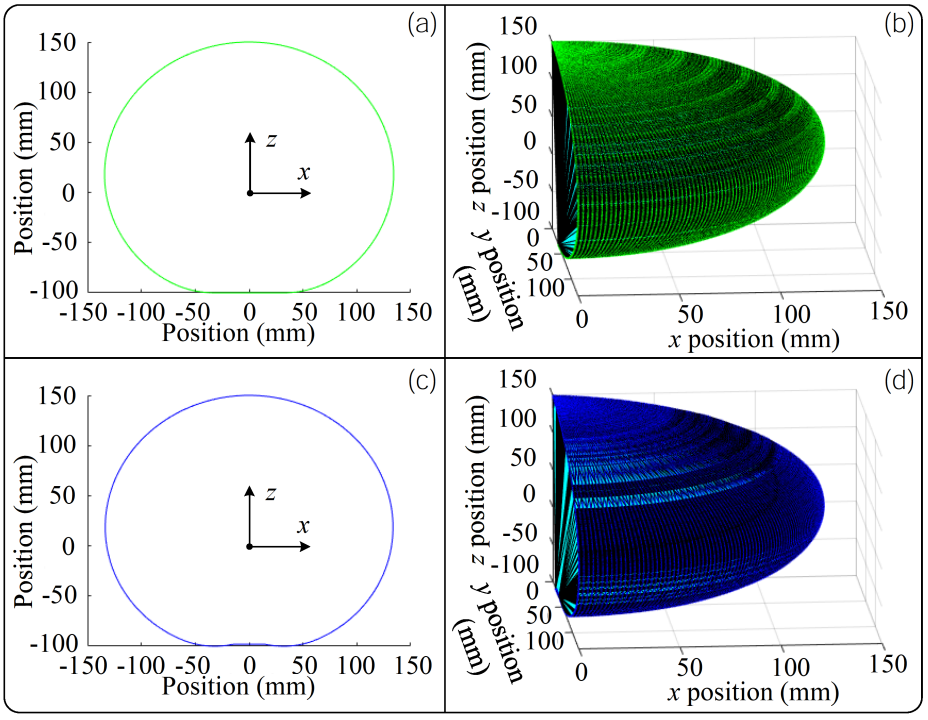

FIGURE 4.5: Example boundary lines and boundary surfaces with $N = 3$, $D = 1°$, $L = 50$ mm, $\theta_{\max} = 180°$. (a) boundary line of the true workspace (Algorithm 4.1). (b) a quarter of the boundary surface of the true workspace (Algorithm 4.1). (c) boundary line from the ETS method (Algorithm 4.2). (d) a quarter of the boundary surface from the ETS method (Algorithm 4.2).

4.3 Simulation experiments and results

4.3.1 Simulation environment

All simulations are run on MATLAB™ R2020a software in a high-performance computing cluster. The cluster's configurations are Intel(R) Xeon(R) Gold 6238R CPU @ 2.20GHz processors, 18GB System memory, and Quadro RTX 5000 GPU. Considering the computation time and memory consumption of the exhaustive approach (Algorithm 4.1), the maximum sample number of the distal point positions is set as 10^8. The interval of bending angle (D) is chosen as 1° if the total sample number is less than or equal to 10^8. With the increase of the number of segments of a continuum robot, if the total sample number may be greater than 10^8, the interval of bending angle (D) can be increased to limit the total sample distal point positions to less than 10^8.

4.3.2 Workspace analysis

The workspace of a continuum robot is determined mainly by the length of segments (L), the maximum bending angle ($\theta_{\max}$) of each segment and the number of segments (N). Figure 4.6 shows the results of workspace analyses with various maximum bending angles ($\theta_{\max}$) and different number of segments (N). It can be seen that, for a continuum robot with the number of segments (N) less than a certain threshold, its workspace is not a fully complete (or filled) area in 2D or volume in 3D (Figure 4.6(a)-(e)). The maximum bending angle ($\theta_{\max}$) of each segment has effects on the workspace as well. When the number of segments and the bending angle reaches a certain threshold, the workspace becomes a complete or fully filled area or volume (Figure 4.6(g)-(k)). Note that all the example configurations of the maximum bending angle $\theta_{\max} = 30^\circ$ have no completed workspace (Figure 4.6(f) and (i)). More details about the workspace are shown in Table 4.2 and Table 4.3.

For a continuum robot with incomplete workspaces (e.g., Figure 4.6(a)-(f) and (l)), the exhaustive search approach can be used to estimate its workspace. The computational cost can be handled in this case because both the number of segments (N) and the maximum

bending angle ($\theta_{\max}$) are small. Attention needs to be paid to the selection of the interval of bending angle (D) when generating the sample distal positions. When the number of segments (N) of a robot is increased to a certain threshold, the workspace becomes complete. The exhaustive approach is hardly used due to computational cost. Then the ETS method can be utilised for workspace calculation.

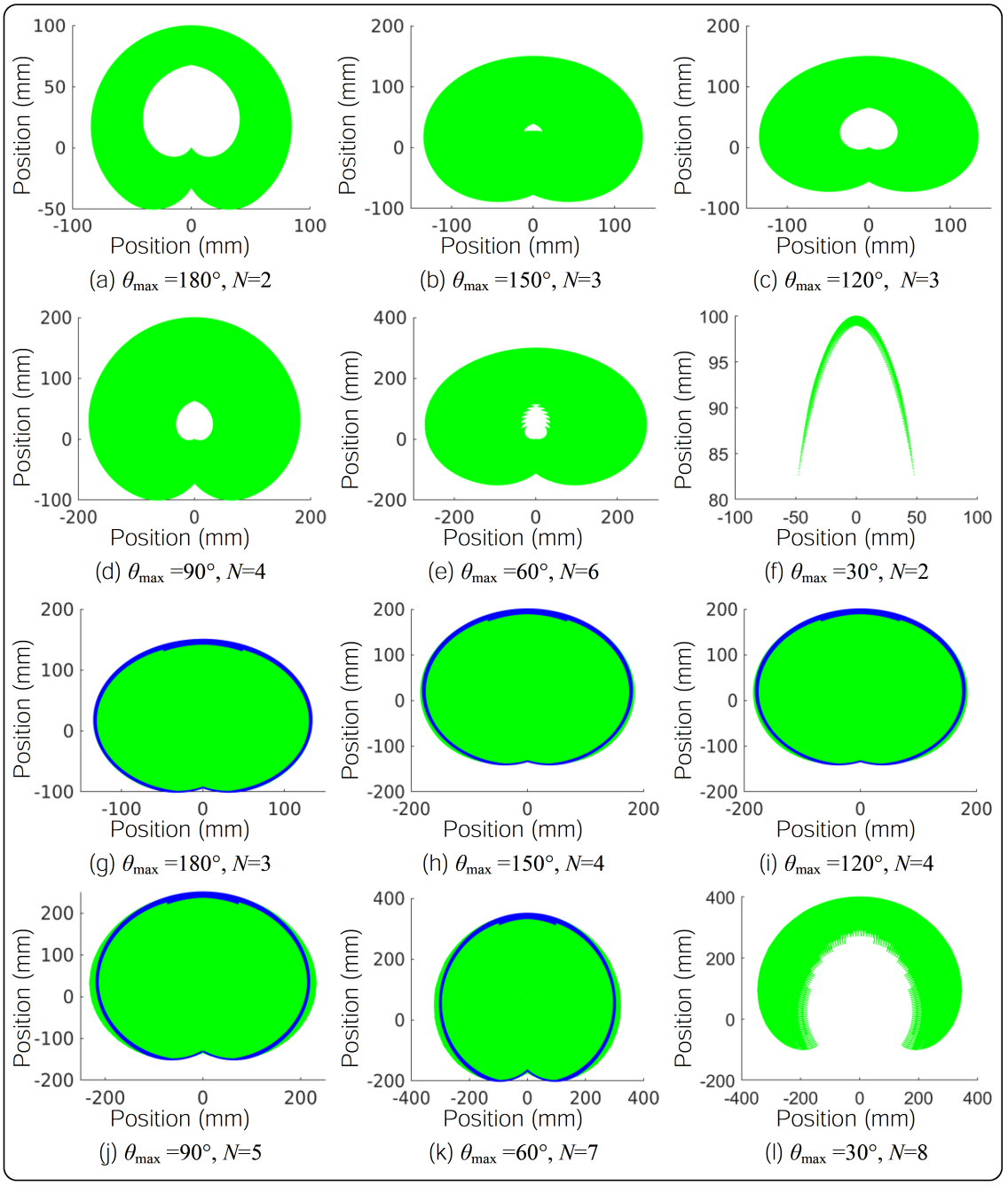

FIGURE 4.6: Workspace with different parameters. The green colour shows the true workspace area, and the blue lines show the boundary calculated by the ETS method.

4.3.3 Workspace area

This section analyses the workspace in 2D, which is defined as the maximum cross-sectional area of the workspace volume (named workspace area). For comparison, true workspace estimated by the exhaustive approach (Algorithm 4.1) is used in the analyses. Table 4.2 shows the results of the workspace area calculated by the ETS method for a continuum robot with various combinations of the number of segments (N) and the maximum bending angle ($\theta_{\max}$). The length of each segment is assumed to be 50 mm in the simulation. The results show that the maximum and minimum errors of workspace area calculated by the ETS method, compared to the true workspace area estimated by the exhaustive approach, are -5.58 % and -0.03 % when $N = 7$, $\theta_{\max} = 60°$ and $N = 3$, $\theta_{\max} = 180°$, respectively. When $N = 3$ and $\theta_{\max} = 180°$, the workspace from the ETS model is almost the same as the true workspace, hence it has the minimum error. With the increase of N and $\theta_{\max}$, the error decreases. However, once these two parameters are over a certain threshold (e.g., $N > 7$ and $\theta_{\max} = 120°$ or $150°$; $N > 4$ and $\theta_{\max} = 180°$), the errors become a positive value because the sample points of 10^8 of the exhaustive search approach are not enough to obtain the real completed workspace, and the ETS method shows better results (i.e., the workspace from the ETS method is greater and more complete than that of the exhaustive approach), which proves that the ETS method has better performance and more close to the real true workspace than the exhaustive approach when the computational resource is limited.

4.3.4 Workspace volume

Table 4.3 shows the results of workspace volume calculated by the ETS method for a continuum robot with various combinations of the number of segments (N) and the maximum bending angle ($\theta_{\max}$). The length of each segment is assumed to be 50 mm. The true workspace volumes calculated by the exhaustive approach (Algorithm 4.1) are included for comparison. The results show that the maximum and minimum errors of workspace volume estimated by the ETS method compared to the true workspace volume calculated by the exhaustive approach are -12.33 % and -1.62 % when $N = 7$, $\theta_{\max} = 60°$ and N=8,

TABLE 4.2: Summary of workspace area calculated by the ETS method

$\theta_{\max}$	N	2	3	4	5	6	7	8
30°	True (mm^2)	2.31×10^2	1.89×10^3	7.81×10^3	2.22×10^4	5.19×10^4	1.03×10^5	1.78×10^5
60°	True (mm^2)	1.20×10^3	1.09×10^4	4.24×10^4	1.04×10^5	1.91×10^5	2.83×10^5	3.83×10^5
	ETS (mm^2)	⋆	⋆	⋆	⋆	⋆	2.67×10^5	3.67×10^5
	ETS error (%)	⋆	⋆	⋆	⋆	⋆	-5.58	-4.35
90°	True (mm^2)	3.39×10^3	2.76×10^4	8.34×10^4	1.47×10^5	2.20×10^5	3.12×10^5	4.15×10^5
	ETS (mm^2)	⋆	⋆	⋆	1.40×10^5	2.14×10^5	3.04×10^5	4.09×10^5
	ETS error (%)	⋆	⋆	⋆	-4.83	-2.76	-2.77	-1.49
120°	True (mm^2)	6.85×10^3	4.42×10^4	9.50×10^4	1.57×10^5	2.34×10^5	3.25×10^5	4.30×10^5
	ETS (mm^2)	⋆	⋆	9.17×10^4	1.53×10^5	2.30×10^5	3.23×10^5	4.31×10^5
	ETS error (%)	⋆	⋆	-3.49	-2.73	-1.73	-0.80	0.28
150°	True (mm^2)	1.12×10^4	5.15×10^4	1.01×10^5	1.65×10^5	2.44×10^5	3.36×10^5	4.41×10^5
	ETS (mm^2)	⋆	⋆	9.80×10^4	1.61×10^5	2.40×10^5	3.34×10^5	4.44×10^5
	ETS error (%)	⋆	⋆	-2.77	-2.25	-1.56	-0.36	0.81
180°	True (mm^2)	1.55×10^4	5.35×10^4	1.02×10^5	1.65×10^5	2.44×10^5	3.37×10^5	4.41×10^5
	ETS (mm^2)	⋆	5.35×10^4	1.02×10^5	1.67×10^5	2.47×10^5	3.42×10^5	4.54×10^5
	ETS error (%)	⋆	-0.03	0.14	0.91	1.08	1.48	2.94

⋆ shows that the workspace is incomplete, in which case an exhaustive approach is suggested for use in calculating the workspace.

TABLE 4.3: Summary of workspace volume calculated by the ETS method

$\theta_{\max}$	N	2	3	4	5	6	7	8
30°	True (mm^3)	1.07×10^4	2.17×10^5	1.46×10^6	5.74×10^6	1.63×10^7	3.60×10^7	6.94×10^7
	t_{True} (s)	1	1	6	80	92	188	293
60°	True (mm^3)	1.42×10^5	2.32×10^6	1.18×10^7	3.33×10^7	6.86×10^7	1.22×10^8	1.92×10^8
	t_{True} (s)	1	2	67	86	121	183	315
	ETS (mm^3)	⋆	⋆	⋆	⋆	⋆	1.07×10^8	1.70×10^8
	ETS error (%)	⋆	⋆	⋆	⋆	⋆	-12.33	-11.36
90°	True (mm^3)	5.33×10^5	6.10×10^6	2.09×10^7	4.60×10^7	8.59×10^7	1.43×10^8	2.23×10^8
	t_{True} (s)	1	3	40	85	120	280	355
	ETS (mm^3)	⋆	⋆	⋆	4.05×10^7	7.61×10^7	1.28×10^8	1.98×10^8
	ETS error (%)	⋆	⋆	⋆	-11.95	-11.47	-10.95	-11.22
120°	True (mm^3)	1.12×10^6	8.59×10^6	2.35×10^7	5.04×10^7	9.26×10^7	1.53×10^8	2.35×10^8
	t_{True} (s)	2	6	41	72	120	216	266
	ETS (mm^3)	⋆	⋆	2.14×10^7	4.55×10^7	8.35×10^7	1.38×10^8	2.13×10^8
	ETS error (%)	⋆	⋆	-9.10	-9.64	-9.91	-9.41	-9.50
150°	True (mm^3)	1.70×10^6	9.43×10^6	2.52×10^7	5.20×10^7	9.30×10^7	1.48×10^8	2.29×10^8
	t_{True} (s)	2	11	38	74	197	186	393
	ETS (mm^3)	⋆	⋆	2.34×10^7	4.90×10^7	8.80×10^7	1.43×10^8	2.21×10^8
	ETS error (%)	⋆	⋆	-6.91	-5.81	-5.43	-3.40	-3.37
180°	True (mm^3)	2.08×10^6	9.77×10^6	2.55×10^7	5.26×10^7	9.32×10^7	1.51×10^8	2.31×10^8
	t_{True} (s)	2	17	39	76	153	200	343
	ETS (mm^3)	⋆	9.45×10^6	2.48×10^7	5.13×10^7	9.15×10^7	1.49×10^8	2.27×10^8
	ETS error (%)	⋆	-3.27	-2.88	-2.31	-1.84	-1.70	-1.62

⋆ shows that the workspace is incomplete, in which case an exhaustive approach is suggested for use in calculating the workspace.

$\theta_{\max} = 180°$, respectively. Similar to the workspace area results, with the increase of N and $\theta_{\max}$, the errors are decreased.

Additionally, the ETS method has a significantly better performance in computational efficiency. The robot configurations have no effect on the computational cost of the ETS method, and the ETS method takes almost the same time of 2 s for all the configurations. For example, the efficiency of the ETS method is 196 times better than the exhaustive approach when $N = 8$ and $\theta_{\max} = 150°$. The reason that the ETS method is compared with an exhaustive approach is that the exhaustive approach has an reasonable efficiency among numerical methods, and other methods, e.g., improved Monte Carlo method [223, 225], can hardly be applied to a continuum robot with multi-segment.

4.4 Discussion

This chapter proposed an ETS method for calculating the workspace of multi-segment continuum robots. The results show that the ETS method is efficient and accurate enough for workspace calculation. The accuracy increases with the increase in the number of segments (N) and the maximum being angle ($\theta_{\max}$). When applying the ETS method, the number of segments (N) and the maximum being angle ($\theta_{\max}$) need to be greater than certain thresholds, which is suggested in Tables 4.2 and 4.3. Because of the complex internal cavity of the workspace when the number of segments (N) and the maximum being angle ($\theta_{\max}$) are less than the thresholds, the current ETS method can not be used in several cases (marked with $\star$ in Tables 4.2 and 4.3). Therefore, further investigation can be conducted to determine the internal cavity and improve the accuracy of the threshold of the proposed ETS method. Additionally, all the segments are assumed to be identical in this research. For a continuum robot that has different lengths or different bending angles among its segments, this ETS method needs to be modified, which is also one of the future research tasks.

In this research, the ETS method relies on the PCC assumption, which generally holds for continuum robots under normal operating conditions. However, when the robot is subjected to external loads, its actual workspace may diverge from the predicted potential

workspace, with the extent of this variation dependent on the magnitude and distribution of the external load. The increased external load induces deviations from the idealised curvature model, resulting in a reduced effective workspace and a less accurate prediction of the robot's workspace. These deviations become particularly pronounced when the external load significantly shifts the robot's centre of mass, further complicating the workspace analysis. To enhance accuracy, future work could consider adopting more adaptable curvature models or explicitly account for dynamic load variations in the workspace analysis.

4.5 Summary

Workspace analysis is an important part in design and control of continuum robots. Therefore, an ETS method based on the forward kinematic and PCC assumption is proposed in this chapter. It is a numerical method for estimation of the workspace of a continuum robot with many segments. Extensive simulations with six different maximum bending angles ($\theta_{\max}$) and seven different number of segments (N) were conducted and verified the efficiency and accuracy of the ETS method. By comparing to the true workspace calculated by an exhaustive approach, the ETS method is demonstrated to be efficient and have adequate accuracy.

Chapter 5

Simultaneous Position and Stiffness Control

Despite efforts at dynamic modelling and control synthesis over the past decade, few studies have incorporated stiffness regulation into their feedback control design. However, this is one of the initial motivations to develop continuum robots. This chapter addresses the crucial challenge of controlling both the position and stiffness of underactuated continuum robots actuated by antagonistic tendons. A rigid-link dynamical model is first presented for analysing the open-loop stiffening of tendon-driven continuum robots. Based on this model, a novel passivity-based position-and-stiffness controller that adheres to the non-negative tension constraint is proposed. Comprehensive experiments on the continuum robot presented in Chapter 3 are conducted to validate the theoretical results and demonstrate the efficacy and precision of this approach. [1]

[1]The results presented in this chapter have previously appeared in the publication: Bowen Yi[†], Yeman Fan[†], Dikai Liu, José Guadalupe Romero. "Simultaneous position-and-stiffness control of underactuated antagonistic tendon-driven continuum robots", *IEEE Transactions on Automation Science and Engineering*, pp.1-17, 2024, Early Access.

[†]Bowen Yi and Yeman Fan contributed equally to this work.

5.1 Introduction

As described in Chapter 2, even continuum robots have many advantages, rigid-body robots still outperform continuum robots in tasks requiring adaptable movement and compliant interactions [32]. Consequently, many efforts have been devoted to addressing the challenges for real-time control of continuum robots that facilitate fast, efficient, and reliable operation [35–37]. The existing control approaches for soft robots can be broadly classified into two categories: data-driven and model-based design. Initially, data-driven approaches dominated the research in this specific field, as obtaining reliable models of a continuum robot was believed to be overwhelmingly complex [35]. Various learning methodologies have been applied to control soft robots, such as Koopman operator [232], Gaussian process temporal difference learning [233, 234], supervised learning via recurrent neural networks [235–238], and feedforward neural networks [239]. However, these approaches have some key limitations, including stringent date set requirements and no guarantee of stability or safety [240–242]. Conversely, the recent resurgence of interest in model-based approaches has made them particularly appealing for soft robots due to their robustness, interpretability, and manageable properties [35].

Elastic deformation of continuum robots theoretically leads to infinite degrees-of-freedom (DoF) motion, which renders them particularly suitable to be modelled by partial differential equations (PDEs) [29]. In particular, there are two prevalent categories of modelling approaches: mechanics-based and geometry-based. The former focuses on studying the elastic behaviour of the constitutive materials and solving the boundary conditions problem, such as the methods using Cosserat rod theory and Euler-Bernoulli beam theory [243, 244]. They need to be solved numerically to obtain a closed formulation for each material subdomain that has proven successful in the design and analysis of continuum robots with high accuracy [245], but, due to the extremely heavy computational burden, they are not adapted to real-time control [246]. In contrast, geometrical models assume that the soft body can be represented by a specific geometric shape, *e.g.*, piecewise constant curvature (PCC). As these modelling approaches often lead to kinematic models rather than dynamical models, they enable the design of kinematic or quasi-static controllers [247, 248]. It has been shown that such types of kinematic controllers are likely to

yield poor closed-loop performance [249].

To address these challenges, recent research has been focused on the dynamic modelling and model-based control of continuum robots.[2] Several dynamical models have been adopted for controller synthesis, including the geometrically exact dynamic Cosserat model [28], port-Hamiltonian Cosserat model [29, 30], rigid-link models [31, 32], and reduced-order Euler-Lagrangian model [33, 34]; see also [251, 252] for stability analysis of equilibria in continuum robots. These works employ model-based control approaches such as passivity-based control (PBC) [253], partial feedback linearisation, proportional derivative (PD) control, and immersion and invariance (I&I) adaptive control. Among these, [32] reports probably the earliest solution in the literature to the design and experimental validation of *dynamic* feedback control for soft robots.

As illustrated above, one of the primary motivations for developing continuum robots is to enhance agility, adaptability, and compliant interactions [254]. Consequently, there is an urgent and rapidly growing need to develop high-performance control algorithms to regulate position and stiffness simultaneously, particularly in certain applications involving human interaction or in complicated environments, such as search and rescue, industrial inspection, medical service, and home living care. The problems of stiffness control and impedance control are well established for *rigid* and *softly-actuated* robotics [255–257]. In contrast, simultaneous position-and-stiffness control of continuum robots remains an open research area. The first stiffness controller for continuum robots in the literature may refer to [258], which extends a simple Cartesian impedance controller using a kinematic model. In [259], the authors tailor the classic hybrid motion/force controller for a static model of multi-backbone continuum robots, requiring estimation of external wrenches. Note that [258, 259] are concerned with static/kinematic models, thus limiting their transient performance. In [32], a Cartesian stiffness controller was proposed for dynamic control of a fully-actuated soft robot, facilitating interaction with the environment. Note that these approaches are not applicable to *underactuated* dynamical models of continuum robots.

[2] In this thesis, the term "dynamic controllers" is used to refer to feedback laws designed from dynamical and kinematic models. This differs from the terminology in control theory, which typically refers to feedback control with dynamics extension (*e.g.* adaptive and observer-based control) [250].

This chapter aims to address the above gap by proposing a novel dynamical model and a real-time control approach that regulates both position and stiffness concurrently for underactuated antagonistic tendon-driven continuum robots. Note that continuum robots have infinite DoF with only finite actuation inputs, the fact that makes them intrinsically underactuated systems [260].

This chapter aims to address the above gap by proposing a novel dynamical model and a real-time control approach that regulates both position and stiffness concurrently for underactuated antagonistic tendon-driven continuum robots.

Notation. All functions and mappings are assumed C^2-continuous. I_n is the $n \times n$ identity matrix, $0_{n\times s}$ is an $n \times s$ matrix of zeros, the vector $\mathbf{0}_n$ represents $\text{col}(0,\dots,0) \in \mathbb{R}^n$, and $\mathbf{1}_n := \text{col}(1,\dots,1) \in \mathbb{R}^n$. Throughout the chapter, bold font is used for variables denoting vectors, while scalars and matrices are represented in normal font. For $\boldsymbol{x} \in \mathbb{R}^n$, $S \in \mathbb{R}^{n\times n}$, $S = S^\top > 0$, the Euclidean norm is $|\boldsymbol{x}|^2 := \boldsymbol{x}^\top \boldsymbol{x}$, and the weighted–norm is $\|\boldsymbol{x}\|_S^2 := \boldsymbol{x}^\top S \boldsymbol{x}$. Given a function $f : \mathbb{R}^n \to \mathbb{R}$. The differential operators is defined as $\nabla f := (\frac{\partial f}{\partial x})^\top$, $\nabla_{x_i} f := (\frac{\partial f}{\partial x_i})^\top$, where $x_i \in \mathbb{R}^p$ is an element of the vector $\boldsymbol{x}$. The set $\mathcal{N}$ is defined as $\mathcal{N} := \{1,\dots,n\}$. When clear from the context, the arguments of the functions may be omitted.

5.2 Model and problem set

5.2.1 Modelling of a class of continuum robots

In this section, a *control-oriented* rigid-link dynamical model specifically designed for a class of underactuated continuum robots driven by tendons is presented. This model class encompasses a wide range of recently reported continuum robots in the literature, including the elephant trunk-inspired robot [261], the deployable soft robotic arm [262], the push puppet-inspired robot [263], the dexterous tip-extending robot [264], and our own developed OctRobot-I [10], alongside other notable examples [31, 265]. By employing this versatile model, a general framework that can effectively describe and analyse a variety

of underactuated continuum robots is provided, enabling a deeper understanding of their stiffening mechanisms and facilitating control design.

In order to visualise the modelling process, the OctRobot-I is taken as an example to introduce the proposed dynamical model but keep its generality in mind that the model is not limited to this specific robotic platform. This robot imitates an octopus tentacle's structure and motion mechanism, as shown in Figure 5.1. The whole continuum manipulator consists of several sections in order to be able to deform in three-dimensional space. Each of them is made of connected spine segments that are driven by a pair of cables. More details of the continuum robot OctRobot-I are given in Section 5.6.1 and Chapter 3, as well as in [10].

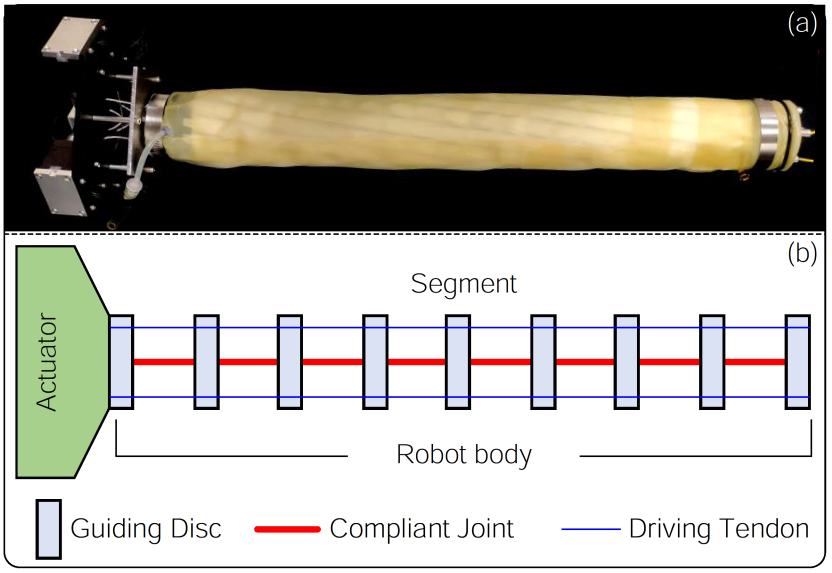

FIGURE 5.1: Diagram of continuum robots. (a) a photo of the OctRobot-I robot. (b) mechanical structure of a class of continuum robots.

In this chapter, a rigid-link model is used to approximate the dynamical behaviours of continuum robots for three reasons: 1) the considered class of continuum robots naturally partitions into spine segments; 2) rigid-link models simplify *control-oriented* tasks; and 3) it is convenient to account for external loading.

To derive the dynamical model, the following assumptions are made:

***Assumption* 5.1.** The continuum robot satisfies the properties:

(**a**) The actuator dynamics is negligible, i.e., the motor is operating in the torque control mode with sufficiently short transient stages.

(**b**) The sections have a PCC, conforming to the segments[3], and the curvatures consistently have the same sign.

(**c**) The continuum robot allows for axial extension, but the axial deformation resulting from antagonistic tensions is negligible compared to the bending. ◁

In order to effectively illustrate the underlying mechanism[4], this chapter specifically concentrates on the two-dimensional case, which only needs to analyse one section of the continuum robot.

The rigid-link dynamical model uses a serial chain of rigid links with n rotational joints to approximate one section of the continuum robot. Then, the configuration variable can be defined as

$$\boldsymbol{q} = [q_1 \dots q_n]^\top \in \mathcal{X} \subset \mathbb{R}^n \tag{5.1}$$

with q_i representing the approximate link angles, where $\mathcal{X}$ is the feasible configuration space; see Figure 5.2 for an illustration. Practically, all angles q_i are within some subsets of $[-\frac{\pi}{2}, \frac{\pi}{2}]$ due to physical constraints.

The continuum robot is modelled as a port-Hamiltonian system in the form of [260, 266]

$$\begin{bmatrix} \dot{\boldsymbol{q}} \\ \dot{\boldsymbol{p}} \end{bmatrix} = \begin{bmatrix} 0_{n\times n} & I_n \\ -I_n & -D(\boldsymbol{q}) \end{bmatrix} \begin{bmatrix} \nabla_{\boldsymbol{q}} H \\ \nabla_{\boldsymbol{p}} H \end{bmatrix} + \begin{bmatrix} \mathbf{0}_n \\ G(\boldsymbol{q})\boldsymbol{u} + \tau_{\text{ext}} \end{bmatrix} \tag{5.2}$$

with the generalised momenta $\boldsymbol{p} \in \mathbb{R}^n$, the damping matrix $D(\boldsymbol{q}) \in \mathbb{R}^{n\times n}_{\succ 0}$, the external torque $\tau_{\text{ext}} \in \mathbb{R}^n$, and the input matrix $G(\boldsymbol{q}) \in \mathbb{R}^{n\times m}$ with $m < n$. The total energy of the robotic system is given by

$$H(\boldsymbol{q}, \boldsymbol{p}) = \frac{1}{2}\boldsymbol{p}^\top M^{-1}(\boldsymbol{q})\boldsymbol{p} + U(\boldsymbol{q}) \tag{5.3}$$

[3]Each spine segment has constant curvatures but is variable in time.

[4]It is promising to extend the main results to the three-dimensional case with multi-sections. This is considered as a valuable avenue for further exploration.

with the inertia matrix $M(\boldsymbol{q}) \succ 0$, and the potential energy $U(\boldsymbol{q})$, which consists of the gravitational part U_{G} and the elastic one $U_{\mathrm{E}}(\boldsymbol{q})$, i.e.,

$$U(\boldsymbol{q}) \;=\; U_{\mathrm{G}}(\boldsymbol{q}) + U_{\mathrm{E}}(\boldsymbol{q}) \tag{5.4}$$

The potential energy function has an isolated local minimum at its open-loop equilibrium of the origin $\boldsymbol{q} = \mathbf{0}_n$.

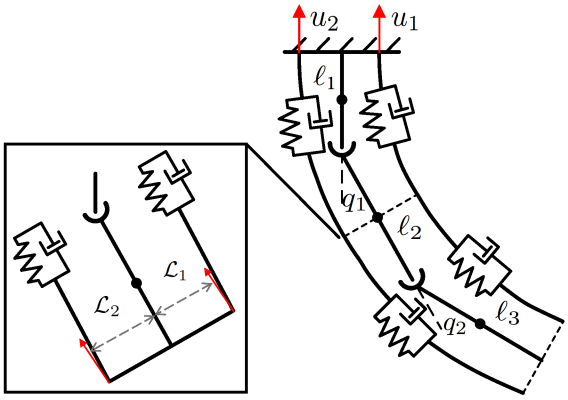

(a) an illustration of configuration variables (the symbol "•" indicates the lumped mass m_i; the angle q_i takes positive values for small counter-clockwise rotation).

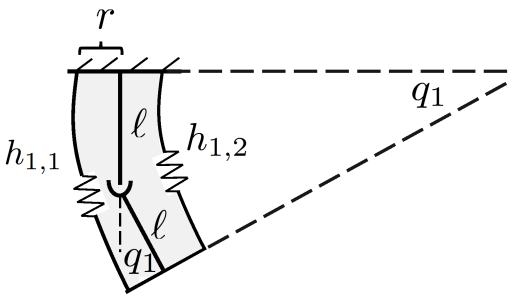

(b) illustration of the elastic potential energy in springs.

FIGURE 5.2: Diagram of the rigid-link approximate model of continuum robots.

Figure 5.2(a) shows the above rigid-link model of continuum robots. Similar to [32], the assumption that a lumped mass with the value m_i ($i \in \mathcal{N}$) is virtually placed in the middle of each link is adopted, and the link lengths are ℓ_i. Additionally, the following assumption on the mass and length is made:

***Assumption* 5.2.** The continuum robot satisfies the uniformity assumptions:

(**a**) The masses verify $m_i = m_j,\ \forall i, j \in \mathcal{N}$.

(**b**) The lengths satisfy the relation: $l_0 = \ell$ and $l_i = 2\ell$ ($i \in \mathcal{N}$) for some $\ell > 0$. The radius of the beam is r. ◁

The gravitational and elastic potential energy functions U_{G} and U_{E} can be derived according to the geometric deformation under the uniformity assumptions of the materials by the following details.

1) Gravitational energy function:

In order to approximate the gravitational potential energy U_{G}, the mass is assumed to be lumped at the centre of each link with the segment lengths $l_i > 0$ and the masses $m_i > 0$ for $i \in \mathcal{N}$. From basic geometric relations, it has

$$U_{\mathrm{G}}(\boldsymbol{q}) = \sum_{i\in\mathcal{N}} \frac{l_i m_i}{2} \left[\cos(q_0 + \ldots + q_{i-1}) - \cos(q_0 + \ldots + q_i)\right] \tag{5.5}$$

with the parameter $q_0 = 0$, which satisfies $U_{\mathrm{G}}(\mathbf{0}_n) = 0$.

In addition, from Assumption 5.2 about the mass and length, under which the potential energy becomes

$$U_{\mathrm{G}}(\boldsymbol{q}) \;=\; \alpha_1(1 - \cos(q_\Sigma)) \tag{5.6}$$

with $q_\Sigma \;:=\; \sum_{i\in\mathcal{N}} \boldsymbol{q}_i$ and some coefficient $\alpha_1 > 0$.

2) Elastic energy function:

In a continuum robot such as the OctRobot-I, each spine segment contains two pairs of helical compression springs. Since the two-dimensional case is considered, only a pair of springs is analysed as illustrated in Figure 5.2(b), and the following assumption is made:

***Assumption* 5.3.** The deformable part of the continuum robot consists of a fixed number of segments with constant curvature and differentiable curves everywhere [32]. ◁

Based on the above assumptions, the boundary lengths in the i-th segment are given by $h_{i,1} = q_i\left[\ell \cot\left(\frac{q_i}{2}\right) + r\right]$, $h_{i,2} = q_i\left[\ell \cot\left(\frac{q_i}{2}\right) - r\right]$. Note that the above functions are well-posed when $q_i \to 0$, i.e., $\lim_{q_i\to 0} h_{i,1} = 2\ell$, $\lim_{q_i\to 0} h_{i,2} = 2\ell$. Hence, the elastic energy can be modelled as

$$U_{\mathrm{E}} = \sum_{i\in\mathcal{N}} k_i \left[q_i^2\left(\ell^2 \cos\left(\frac{q_i}{2}\right)^2 + r^2\right) - \ell^2\right] + k_i' q_i^2 \tag{5.7}$$

in which $k_i > 0$ and $k_i' > 0$ are some elastic coefficients to characterise the elastic energies caused by the elongation and bending of springs.

In the proposed rigid-link model, each configuration variable q_i would generally be small, i.e., $q_i \in [-\frac{\pi}{12}, \frac{\pi}{12}]$, for which the term $\cos(\frac{q_i}{2})^2$ takes values within $[0.983, 1]$. Then, it is

reasonable to make the following quadratic assumption to approximate the highly nonlinear function in (5.7).

***Assumption* 5.4.** The elastic energy function U_{E} has the quadratic form

$$U_{\mathrm{E}}(\boldsymbol{q}) = \frac{1}{2}\boldsymbol{q}^{\top}\Lambda\boldsymbol{q} + U_0 \tag{5.8}$$

with a constant coefficient U_0 and a diagonalisable matrix $\Lambda := \mathrm{diag}(\alpha_2, \dots \alpha_2) \succ 0$. ◁

3) Inertia and kinematic energy function:

The analytic form of the inertia matrix $M(\boldsymbol{q})$ can be obtained following the standard way for rigid-link robotic models. The interested reader may find detailed procedures in [267, Chapter 8.4]. Then, the kinematic energy is given by $\frac{1}{2}\boldsymbol{p}^{\top}M^{-1}(\boldsymbol{q})\boldsymbol{p}$.

Note that the specific formulation of the inertia $M(\boldsymbol{q})$ is not involved in the controller design. This makes the closed loop relatively robust, and it is unnecessary to obtain the analytic formulation of $M(\boldsymbol{q})$ for experimental implementation.

The variable $\boldsymbol{u} \in \mathbb{R}^m$ represents the control input, denoting the tensions along the cables generated by actuators. In the planar case, it has $m = 2$ with two cables. Due to the specific structure, these two tensions are one-directional, i.e.,

$$u_i \geq 0 \quad (i = 1, 2) \tag{5.9}$$

For the studied case, the input matrix $G(\boldsymbol{q}) : \mathbb{R}^n \to \mathbb{R}^{n\times 2}$ can be conformally partitioned as

$$G(\boldsymbol{q}) = \begin{bmatrix} G_1(\boldsymbol{q}) & G_2(\boldsymbol{q}) \end{bmatrix} \tag{5.10}$$

In the following assumption, some key properties of the matrix $G(\boldsymbol{q})$ are underlined when modelling the continuum robot.

***Assumption* 5.5.** The input matrix $G(\boldsymbol{q})$ of the continuum robot model (5.2) – or equivalently in (5.10) – satisfies

(**a**) $G(\boldsymbol{q})$ is state-dependent and C^1-continuous.

(**b**) $G_1(\mathbf{0}_n) = -G_2(\mathbf{0}_n)$.

(**c**) $\|G_1(\boldsymbol{q}) + G_2(\boldsymbol{q})\| \neq 0$ for $\boldsymbol{q} \in \mathcal{X}\backslash\{\mathbf{0}_n\}$. ◁

Among the above three items, the state-dependency of the input matrix is a key feature of the proposed model, which is instrumental in showing the tunability of open-loop stiffness of tendon-driven continuum robots. More details about the input matrix will be given in the subsequent sections of this chapter. The second point (**b**) means that at the open-loop equilibrium (i.e., $\boldsymbol{q} = \mathbf{0}_n$), the tensions in the two cables are equal in magnitude but opposite in direction.

***Remark* 5.1.** For a single link in the zoomed-in subfigure in Figure 5.2(a), if the forces along the cables are assumed lossless, their directions are nonparallel to the centroid of the continuum robot. The torques imposed on the first approximate link are given by $u_1\mathcal{L}_1(q_1)$ and $u_2\mathcal{L}_2(q_1)$ with $\mathcal{L}_1, \mathcal{L}_2$ the lever's fulcrums, which are nonlinear functions of the configuration q_1. From basic geometric relations, it satisfies $\mathcal{L}_1(0) = \mathcal{L}_2(0)$. This illustrates the rationality of Assumption 5.5. ◁

***Remark* 5.2.** In Assumption 5.1(c), the geometry of the continuum robot is assumed to satisfy the PCC condition. Additionally, the assumption that the *curvatures* have an unchanged sign excludes the second type of configuration (S-shape) shown in Figure 5.3(b); see [16] for a comprehensive analysis of this case. This assumption is reasonable, as it covers the majority of scenarios for our platform. In contrast, the S-shape configuration necessitates precise symmetry in both the mechanical design and the wire arrangement.

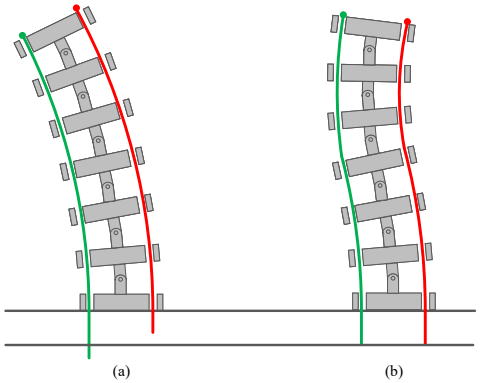

FIGURE 5.3: Illustration of a continuum robot with two bending configurations [16].

5.2.2 Problem set

This chapter studies how to design a feedback controller that is capable of regulating the continuum robot deformation and achieving variable stiffness capability. To be precise, the closed loop complies with the input constraint (5.9) and achieves the following aims:

A1: In the absence of the external torque (i.e., $\tau_{\text{ext}} = \mathbf{0}_n$), it achieves the asymptotically accurate regulation of the position, that is

$$\lim_{t\to\infty} \boldsymbol{q}(t) = \boldsymbol{q}_\star \tag{5.11}$$

with the desired configuration $\boldsymbol{q}_\star \in \mathcal{X}$.

A2: Stiffness control at the closed-loop equilibrium can be controlled concurrently.

5.3 Open-loop stiffening

The antagonism mechanism is a popular method for stiffening tendon-driven continuum robots [262]. By arranging a pair of cables on two sides of the robot and adjusting their tensions simultaneously, the robot body compresses or expands, and generates a reaction that counteracts the tension. As a consequence, the stiffness of the robot changes.

This section will show that there is a redundant degree of freedom of input in the proposed model, which provides the possibility to regulate the stiffness in the open-loop system. This property is instrumental for the controller design to regulate position and stiffness simultaneously.

Now consider the case of the open-loop system with a pair of identical constant inputs

$$u_1 = u_2 = \mu \tag{5.12}$$

This balance will keep the configuration variable $\boldsymbol{q}$ at the open-loop equilibrium $\boldsymbol{q}_\star = \mathbf{0}_n$ for any feasible $\mu \geq 0$. Especially, when $\mu = 0$, the robot is in a slack state where its stiffness corresponds to its inherent properties determined by the materials and mechanical structures. Intuitively, as μ increases, the continuum robot progressively transitions

towards a state of higher rigidity or inflexibility. The proposed dynamical model should be capable of interpreting the above phenomenon – a larger value of $\mu > 0$ implies a larger transverse stiffness.

In order to study the stiffness at the end-effector, the Jacobian $J(\boldsymbol{q}) \in \mathbb{R}^{2\times n}$ from the contact force $\boldsymbol{f}_{\text{ext}} \in \mathbb{R}^2$ should satisfy

$$\tau_{\text{ext}} = J^{\top}(\boldsymbol{q})\boldsymbol{f}_{\text{ext}} \tag{5.13}$$

in which $\tau_{\text{ext}} \in \mathbb{R}^n$ is the external torque vector acting on each link.

The following proposition will demonstrate the property of stiffness tunability by changing the value μ in the proposed dynamical model.

***Proposition* 5.1.** Consider the antagonistic tendon-driven model (5.2) for continuum robots, with the constant inputs (5.12) under Assumption 5.5. If the following assumptions are satisfied:

H1: For $j = 1, 2$

$$\frac{\partial G_{n,j}}{\partial q_n}(\boldsymbol{q}) < 0, \quad \frac{\partial G_{n,j}}{\partial q_k}(\boldsymbol{q}) = 0, \ k \in \mathcal{N}\backslash\{n\} \tag{5.14}$$

in a neighbourhood of the origin.

H2: The forward kinematics (mapping from the configuration $\boldsymbol{q} \in \mathcal{X}$ to the end-effector Cartesian coordinate $\boldsymbol{x} \in \mathbb{R}^2$) is a *locally* injective immersion.

Then, the input (5.12) guarantees the origin $\mathbf{0}_n$ an equilibrium in the absence of the external perturbation, i.e., $\tau_{\text{ext}} = 0$. Furthermore, a large input value $\mu > 0$ implies a larger transverse stiffness K_{T} of the end-effector at this open-loop equilibrium.

Proof. From Assumption 5.5(b), the input term

$$G(\boldsymbol{q})\boldsymbol{u}|_{\boldsymbol{q}=\mathbf{0}_n} = \mathbf{0}_n \tag{5.15}$$

with (5.12) guarantees that the origin $\boldsymbol{q}_\star = \mathbf{0}_n$ is an equilibrium in the case of $\tau_{\text{ext}} = \mathbf{0}$. The Cartesian coordinate $\boldsymbol{x} \in \mathbb{R}^2$ of the end-effector can be uniquely determined by the

configuration $\boldsymbol{q}$ as

$$\boldsymbol{x} = T(\boldsymbol{q}) \tag{5.16}$$

for some smooth function $T : \mathbb{R}^n \to \mathbb{R}^2$, with the open-loop equilibrium $\boldsymbol{x}_\star := T(\boldsymbol{q}_\star)$. Note that the function T depends on the coordinate selection. Without loss of generality, $\boldsymbol{x}_\star = \mathbf{0}_2$ is assumed, and the local coordinate of $\boldsymbol{x} := \mathrm{col}(x_1, x_2)$ is selected as the tangential and the axial directions of the n-th link.

For a non-zero external torque τ_{ext}, the *shifted equilibrium* is denoted as $(\bar{\boldsymbol{q}}, \mathbf{0}_n)$ in the presence of the external perturbation, with the corresponding end-effector coordinate $\bar{\boldsymbol{x}} = T(\bar{\boldsymbol{q}})$.

In order to study the transverse stiffness at the end of the robot, it is assumed that the external force $\boldsymbol{f}_{\mathrm{ext}}$ is only applied to the n-th link [268]. Substituting it into the port-Hamiltonian model (5.2), it satisfies the following equations at the shifted equilibrium

$$\begin{aligned} \nabla U(\bar{\boldsymbol{q}}) &= [G_1(\bar{\boldsymbol{q}}) + G_2(\bar{\boldsymbol{q}})]\mu + J^\top(\bar{\boldsymbol{q}})\boldsymbol{f}_{\mathrm{ext}} \\ \boldsymbol{f}_{\mathrm{ext}} &= K_{\mathrm{C}}(\bar{\boldsymbol{x}} - \boldsymbol{x}_\star) \end{aligned} \tag{5.17}$$

in which $K_{\mathrm{C}} \in \mathbb{R}^{2\times 2}$ is the stiffness matrix with the partition

$$\begin{aligned} K_{\mathrm{C}} &:= \mathrm{diag}(K_{\mathrm{T}}, K_{\mathrm{A}}) \\ J(\boldsymbol{q}) &= \begin{bmatrix} J_1(\boldsymbol{q}) \\ J_2(\boldsymbol{q}) \end{bmatrix} \end{aligned} \tag{5.18}$$

with the axial stiffness K_{A} and the transverse stiffness K_{T}. For the particular coordinate selection as mentioned above, the Jacobian matrix $J_1(\boldsymbol{q})$ is in the form

$$J_1 = \begin{bmatrix} 0 & \dots & 0 & l_n \end{bmatrix} \tag{5.19}$$

in which $l_n > 0$ represents the distance from the contact point to the centre of the n-th link.

Now, it has

$$\nabla U(\bar{\boldsymbol{q}}) = [G_1(\bar{\boldsymbol{q}}) + G_2(\bar{\boldsymbol{q}})]\mu + K_{\mathrm{T}} J_1^\top [\bar{x}_1 - x_{\star 1}] + J_2^\top [\bar{x}_2 - x_{\star 2}] \tag{5.20}$$

For the convenience of presentation and analysis, a function $f_\mu : \mathbb{R}^n \to \mathbb{R}^n$ is defined as

$$f_\mu(\boldsymbol{q}) := \nabla U(\boldsymbol{q}) - [G_1(\boldsymbol{q}) + G_2(\boldsymbol{q})]\mu \tag{5.21}$$

which is parameterised by the constant force $\mu \geq 0$. Invoking the fact that $\boldsymbol{q}_\star = \mathbf{0}_n$ is an open-loop equilibrium, then

$$f_\mu(\boldsymbol{q}_\star) = 0 \tag{5.22}$$

and thus

$$f_\mu(\bar{\boldsymbol{q}}) - f_\mu(\boldsymbol{q}_\star) = K_{\mathrm{T}} J_1^\top(\bar{\boldsymbol{q}})[\bar{x}_1 - x_{\star 1}] + J_2^\top(\bar{\boldsymbol{q}})[\bar{x}_2 - x_{\star 2}] \tag{5.23}$$

Noting the local injectivity assumption **H2**, there exists a left inverse function T^{L} – which is defined *locally* – of the function T such that

$$\boldsymbol{q} = T^{\mathrm{L}}(T(\boldsymbol{q})) \tag{5.24}$$

in a small neighborhood of $\boldsymbol{q}_\star$.

Given that the axial deformation due to antagonistic tensions is negligible compared to the transverse deformation, for sufficiently small $\bar{x}_1 - x_{\star 1}$, it has $\bar{x}_2 - x_{\star 2} = o(\bar{x}_1 - x_{\star 1})$, where $o(\cdot)$ represents terms of higher-order smallnesss. Therefore, when considering $\bar{x}_1 \to x_{\star 1}$, the term $J_2^\top(\bar{\boldsymbol{q}})[\bar{x}_2 - x_{\star 2}]$ can be dropped in the limit analysis. From the equation (5.23), the transverse stiffness K_{T} at the open-loop equilibrium $\boldsymbol{q}_\star$ can be defined by taking the limit $\bar{\boldsymbol{q}} \to \boldsymbol{q}_\star$, i.e.,

$$\begin{aligned} K_{\mathrm{T}} &= \frac{J_1(\boldsymbol{q}_\star)}{\|J_1(\boldsymbol{q}_\star)\|^2} \lim_{\bar{x}_1 \to x_{\star 1}} \frac{f_\mu(\bar{\boldsymbol{q}}) - f_\mu(\boldsymbol{q}_\star)}{\bar{x}_1 - x_{\star 1}} \\ &= \frac{J_1(\boldsymbol{q}_\star)}{\|J_1(\boldsymbol{q}_\star)\|^2} [\nabla f_\mu(\boldsymbol{q}_\star)]^\top \nabla_{x_1} T^{\mathrm{L}}(\boldsymbol{x}_\star) \\ &= \frac{J_1}{\|J_1\|^2} \big[\nabla^2 U - \mu\big(\nabla G_1 + \nabla G_2\big)^\top\big] \nabla_{x_1} T^{\mathrm{L}} \Big|_{\boldsymbol{q}_\star} \end{aligned} \tag{5.25}$$

The assumption **H1** guarantees that the (n,n)-element of $\nabla G_j(\boldsymbol{q}_\star)$ for $j = 1, 2$ is negative. On the other hand, from the local coordinate selection, the variation of x_1 implies that q_n will also change accordingly. As a consequence, the last element of $\nabla_{x_1} T^{\mathrm{L}}$ is non-zero,

and indeed, it is positive. It is straightforward to see that K_{T} is increasing by selecting a larger $\mu > 0$. □

With the proposed dynamical model, the above calculation shows the underlying mechanism of the tunability of open-loop stiffness. The section below will illustrate that the tension difference $(u_1 - u_2)$ provides another degree of freedom to regulate the robot configuration.

***Remark* 5.3.** Assumption **H1** means that $G_{n,j}$ only depends on the state q_n rather than other configuration variables. It is used to simplify the presentation and analysis. Indeed, from the above proof, it may be replaced by a weaker condition $J_1(\nabla G_1 + \nabla G_2)\nabla_{x_1} T^{\mathrm{L}} \neq 0$, for which it is still able to show the ability to tune the open-loop stiffness via changing the tendon force μ. The assumption **H2** means that a unique inverse kinematic solution can be determined in a small neighbourhood of a given configuration $\boldsymbol{q}_\star$. While it is generally not true to ensure the existence of a *global* inverse, achieving it within a local context is feasible.

***Remark* 5.4.** In practice, when the value μ is increased beyond a certain threshold, the continuum robot may be observed to experience the phenomenon of *buckling* [10, Sec. III]. However, the critical values are usually very large, and cannot be generated by actuators in many robotic platforms. Therefore, the buckling behaviour is not taken into account in this thesis. Also note that the unchanged sign of curvature condition in Assumption 5.1 rules out the scenario discussed in [16] where "the manipulator can be moved to various configurations without changing the wire length". As a result, the control input is capable of adjusting the robot's stiffness.

5.4 Control design

This section will study how to design a state feedback law, based on the proposed model in Section 5.2, to regulate position and stiffness simultaneously.

To facilitate the controller design, the following assumption for the input matrix $G(\boldsymbol{q})$ in terms of the geometric constraints is made.

***Assumption* 5.6.** The input matrix $G(\boldsymbol{q})$ given by (5.10) is reparameterised as

$$\begin{aligned} G_1(\boldsymbol{q}) &= \boldsymbol{g}_1(\boldsymbol{q}) + \boldsymbol{g}_0 \\ G_2(\boldsymbol{q}) &= \boldsymbol{g}_1(\boldsymbol{q}) - \boldsymbol{g}_0 \end{aligned} \tag{5.26}$$

with a constant vector $\boldsymbol{g}_0 \in \mathbb{R}^n$ and a C^1-continuous function $\boldsymbol{g}_1 : \mathbb{R}^n \to \mathbb{R}^n$ satisfying the following:

(**a**) $\boldsymbol{g}_1(\boldsymbol{q})$ is a smooth *odd* function;

(**b**) $\boldsymbol{g}_1(\boldsymbol{q})$ is full column rank for $\boldsymbol{q} \in \mathcal{X}/\{\mathbf{0}_n\}$;

(**c**) The constant vector $\boldsymbol{g}_0$ and the vector field $\boldsymbol{g}_1(\boldsymbol{q})$ can be re-parameterised as

$$\boldsymbol{g}_0 = g_0 \mathbf{1}_n, \quad \boldsymbol{g}_1(\boldsymbol{q}) = g_1(\boldsymbol{q}) \mathbf{1}_n \tag{5.27}$$

and $g_0 + g_1(\boldsymbol{q}) \neq 0$ for all $\boldsymbol{q}$. ◁

Clearly, the above is compatible with Assumption 5.5. The vector-valued function $\boldsymbol{g}_1(\boldsymbol{q})$ is related to the open-loop stiffness tunability outlined in Proposition 5.1.

For the input matrix, a single link is taken as an example to discuss the modelling of the input matrix $G(\boldsymbol{q})$. The tension is assumed to be uniformly distributed along the cables and lumped forces are along the tangential directions at the middle points of the constant-curvature outline. Then, the lever's fulcrums $\mathcal{L}_1$ and $\mathcal{L}_2$ in Figure 5.2(a) are given by $\mathcal{L}_1 = r - \frac{\ell}{2}\sin(q_i)$ and $\mathcal{L}_2 = r + \frac{\ell}{2}\sin(q_i)$. According to some basic geometric relations, it can be obtained the i-th row of the input matrix as $\begin{bmatrix} G_{i,1} & G_{i,2} \end{bmatrix} = k_u \begin{bmatrix} r - \frac{\ell}{2}\sin(q_i) & -r - \frac{\ell}{2} \end{bmatrix}$, in which $k_u > 0$ is a coefficient to denote the loss of inputs at the virtual joint, subject to friction and viscoelastic effects [269]. Correspondingly, $g_0 = k_u r$ and $g_1 = -\frac{1}{2}\ell k_u \sin(q_i)$. This model verifies the key assumption (5.14) with $\partial G_{i,j}/\partial q_i(\boldsymbol{q}) < 0$.

5.4.1 Assignable equilibria

For underactuated mechanical systems, it is crucial to identify the set of assignable equilibria, also known as achievable or feasible equilibria. Although extensively explored, tendon-driven robots face a significant *obstacle* in the form of the one-directional input constraint

(5.9). In order to facilitate the control design, the following input transformation is made:

$$\tau = T_{\mathrm{u}}\boldsymbol{u}, \quad T_{\mathrm{u}} := \begin{bmatrix} 1 & -1 \\ 0 & 1 \end{bmatrix} \tag{5.28}$$

with new input control $\tau = \mathrm{col}(\tau_1,\ \tau_2) \in \mathbb{R}^2$. For τ_1, there is no sign constraint; the other input channel verifies $\tau_2 \geq 0$, and thus the admissible input set is defined as

$$\mathcal{E}_\tau := \{\tau \in \mathbb{R}^2 : \tau_1 \in \mathbb{R},\ \tau_2 \geq 0\} \tag{5.29}$$

Invoking the intuitive idea in Section 5.3, these two inputs τ_1, τ_2 may be used to regulate the position and stiffness concurrently. For convenience, the new input matrix is defined as

$$G_\tau(\boldsymbol{q}) = \begin{bmatrix} \rho_1(\boldsymbol{q}) & \rho_2(\boldsymbol{q}) \end{bmatrix} =: G(\boldsymbol{q})T_{\mathrm{u}}^{-1} \tag{5.30}$$

with

$$\begin{aligned} \rho_1(\boldsymbol{q}) &= \boldsymbol{g}_0 + \boldsymbol{g}_1(\boldsymbol{q}) \\ \rho_2(\boldsymbol{q}) &= 2\boldsymbol{g}_1(\boldsymbol{q}) \end{aligned} \tag{5.31}$$

With the above input transformation, the controlled model (5.2) now becomes

$$\begin{bmatrix} \dot{\boldsymbol{q}} \\ \dot{\boldsymbol{p}} \end{bmatrix} = \begin{bmatrix} 0_{n\times n} & I_n \\ -I_n & -D(\boldsymbol{q}) \end{bmatrix} \begin{bmatrix} \nabla_{\boldsymbol{q}} H \\ \nabla_{\boldsymbol{p}} H \end{bmatrix} + \begin{bmatrix} \mathbf{0}_n \\ G_\tau(\boldsymbol{q})\tau \end{bmatrix} \tag{5.32}$$

in the absence of the external perturbation τ_{ext}.

***Remark* 5.5.** Indeed, the real constraint for τ_1 should be $\tau_1 \geq -\tau_2$ rather than $\tau_1 \in \mathbb{R}$ in order to guarantee the constraint $u_1, u_2 \geq 0$. Since the value of τ_2 can be set *arbitrarily*, the admissible input set $\mathcal{E}_\tau$ is defined above for convenience in the subsequent analysis. $\triangleleft$

According to [260] and invoking the full-rankness of T_u, if *there were not* input constraints, the assignable equilibrium set would be given by $\{\boldsymbol{q} \in \mathbb{R}^n : G(\boldsymbol{q})^\perp \nabla U(\boldsymbol{q}) = 0\}$. Clearly, this *does not* hold true for our case, because the feasible solution cannot be guaranteed to live within the set $\mathcal{E}_\tau$ rather than $\tau \in \mathbb{R}^2$. To address this point, in the following proposition, the assignable equilibria set is presented for the studied case with constrained inputs.

***Proposition* 5.2.** (*Assignable Equilibria*) Consider the unperturbed model (5.2) and the input transformation (5.28) with $\tau_{\text{ext}} = \mathbf{0}$ under the input constraint $\mathcal{E}_\tau$ in (5.29). All the assignable equilibria are given by the set $\mathcal{E}_q \cap \mathcal{X}$, with the definition

$$\mathcal{E}_q := \left\{ \boldsymbol{q} \in \mathbb{R}^n \middle| \begin{array}{r} (\boldsymbol{g}_1^\perp \boldsymbol{g}_0)^\perp \boldsymbol{g}_1^\perp \nabla U = 0 \\ \boldsymbol{g}_1^\top \nabla U - \boldsymbol{g}_1^\top (\boldsymbol{g}_0 + \boldsymbol{g}_1)(\boldsymbol{g}_1^\perp \boldsymbol{g}_0)^\dagger \boldsymbol{g}_1^\perp \nabla U \geq 0 \end{array} \right\} \tag{5.33}$$

Proof. In terms of Assumption 5.6(**b**), a full rank left annihilator $\boldsymbol{g}_1^\perp(\boldsymbol{q}) \in \mathbb{R}^{(n-1)\times n}$ for all $\boldsymbol{q} \in \mathcal{X}/\{\mathbf{0}_n\}$ can be always found. For an equilibrium $(\boldsymbol{q}, \mathbf{0})$, there should exist τ_1 and τ_2 satisfying

$$\nabla U(\boldsymbol{q}) \;=\; G_\tau(\boldsymbol{q})\tau = [\boldsymbol{g}_0 + \boldsymbol{g}_1(\boldsymbol{q})]\tau_1 + 2\boldsymbol{g}_1(\boldsymbol{q})\tau_2 \tag{5.34}$$

Considering the full-rankness of the square matrix $\text{col}(\boldsymbol{g}_1^\perp(\boldsymbol{q}), \boldsymbol{g}_1^\top(\boldsymbol{q})) \in \mathbb{R}^{n\times n}$ for $\boldsymbol{q} \in \mathcal{X}/\{\mathbf{0}_n\}$, it has

$$(5.34) \iff \begin{bmatrix} \boldsymbol{g}_1^\perp \\ \boldsymbol{g}_1^\top \end{bmatrix} \nabla U = \begin{bmatrix} \boldsymbol{g}_1^\perp \boldsymbol{g}_0 \tau_1 \\ \boldsymbol{g}_1^\top (\boldsymbol{g}_0 + \boldsymbol{g}_1)\tau + 2\|\boldsymbol{g}_1\|^2 \tau_2 \end{bmatrix} \tag{5.35}$$

Its solvability relies on finding all the points $\boldsymbol{q} \in \mathcal{X} \subset \mathbb{R}^n$ satisfying

$$\boldsymbol{g}_1^\perp \nabla U = \boldsymbol{g}_1^\perp \boldsymbol{g}_0 \tau_1 \tag{5.36}$$

$$\boldsymbol{g}_1^\top \nabla U = \boldsymbol{g}_1^\top (\boldsymbol{g}_0 + \boldsymbol{g}_1)\tau_1 + 2\|\boldsymbol{g}_1\|^2 \tau_2 \tag{5.37}$$

at the same time under the constraint $\tau \in \mathcal{E}_\tau$. Clearly, all the feasible equilibria satisfying (5.36) live in the set $\{\boldsymbol{q} \in \mathbb{R}^n : (\boldsymbol{g}_1^\perp(\boldsymbol{q})\boldsymbol{g}_0)^\perp \boldsymbol{g}_1^\perp(\boldsymbol{q}) \nabla U(\boldsymbol{q}) = 0\}$, and the corresponding input τ_1 is given by

$$\tau_1 = (\boldsymbol{g}_1^\perp \boldsymbol{g}_0)^\dagger \boldsymbol{g}_1^\perp \nabla U \tag{5.38}$$

On the other hand, Assumption 5.6(**b**) imposes the constraint $\|\boldsymbol{g}_1\|^2 > 0$, thus (5.37) admits a positive solution to $\tau_2 \geq 0$ if and only if

$$\boldsymbol{g}_1^\top \nabla U - \boldsymbol{g}_1^\top (\boldsymbol{g}_0 + \boldsymbol{g}_1)\tau_1 \geq 0 \tag{5.39}$$

Inserting (5.38) into the above equation completes the proof. □

After imposing Assumption 5.6(**c**) to the input matrix $G(\boldsymbol{q})$, a class of particular equilibria is interested in analysis. In this chapter, they are called the *homogeneous equilibria* that are characterised by the set

$$\mathcal{E}_\theta := \{\boldsymbol{q} \in \mathbb{R}^n : q_i = \theta,\ \forall i \in \mathcal{N}\} \tag{5.40}$$

for some constant θ. This definition is tailored for the proposed continuum robot model under the assumptions in this thesis.

In the following, all homogeneous equilibria belonging to the assignable equilibrium set $\mathcal{E}_q$ in Proposition 5.2 have been demonstrated.

***Proposition* 5.3.** Consider the model (5.2) of the continuum robot under Assumptions 5.4-5.6. Then, all homogeneous equilibria are assignable, i.e., $\mathcal{E}_\theta \subset \mathcal{E}_q$.

Proof. For the case with $\theta = 0$, since $g_1(\mathbf{0}_n) = 0$, the equilibrium $\boldsymbol{q}_\star = \theta \mathbf{1}_n$ makes the equation (5.34) solvable with $\tau_1 = 0$ and any $\tau_2 \geq 0$. For the case with $\theta \neq 0$ and any *fixed* $\tau_1 \geq 0$, the determination of the set $\mathcal{E}_q$ is equivalent to solving (5.34), which can be written as $\nabla U(\boldsymbol{q}) = [\boldsymbol{g}_0 + \boldsymbol{g}_1(\boldsymbol{q})]\tau_1 + 2\mathbf{g}_1(\boldsymbol{q})\tau_2$. This equation can be compactly formulated as

$$\nabla U(\boldsymbol{q}) = G_{\mathrm{N}} \tau_{\mathrm{N}} \tag{5.41}$$

with the new definitions

$$\begin{aligned} G_{\mathrm{N}} &:= \mathbf{1}_n \\ \tau_{\mathrm{N}}(\tau) &:= [g_0 + g_1(\boldsymbol{q})]\tau_1 + 2g_1(\boldsymbol{q})\tau_2 \end{aligned} \tag{5.42}$$

For any fixed $\tau_2 \geq 0$, invoking (5.27) from Assumption 5.6, the mapping $\tau_1 \to \tau_{\mathrm{N}}$ is a diffeomorphism from $\mathbb{R} \to \mathbb{R}$. It implies that there is no constraint for τ_{N}. As a consequence, the PDE (5.41) becomes

$$G_{\mathrm{N}}^{\perp} \nabla U(\boldsymbol{q}_\star) = 0 \tag{5.43}$$

at the desired equilibrium $\boldsymbol{q}_\star$.

A feasible full-rank annihilator of G_{N} is given by

$$G_{\mathrm{N}}^{\perp} = \begin{bmatrix} 1 & -1 & 0 & \dots & 0 \\ 0 & 1 & -1 & \dots & 0 \\ & & \ddots & \ddots & \\ 0 & \dots & 0 & 1 & -1 \end{bmatrix} \in \mathbb{R}^{(n-1)\times n} \tag{5.44}$$

and the Jacobian ∇U at the desired equilibrium $\boldsymbol{q}_\star$ is in the form

$$\nabla U(\boldsymbol{q}_\star) = \alpha_1 \underbrace{\begin{bmatrix} \sin(q_\Sigma) \\ \vdots \\ \sin(q_\Sigma) \end{bmatrix}}_{\sin(n\theta)\mathbf{1}_n} + \alpha_2 \underbrace{\begin{bmatrix} \boldsymbol{q}_{\star,1} \\ \vdots \\ \boldsymbol{q}_{\star,n} \end{bmatrix}}_{\theta\mathbf{1}_n} \tag{5.45}$$

with $q_\Sigma := \sum_{i\in\mathcal{N}} \boldsymbol{q}_i$. It is straightforward to verify that (5.43) holds true for any $\tau_2 \geq 0$ with a homogeneous equilibrium $\boldsymbol{q}_\star = \theta\mathbf{1}_n$. Since there is no constraint for the input variable τ_1, the equilibrium for this case is also assignable under the constraint (5.29). The proof is now completed. □

The next section will focus on control design which is aimed at regulating certain homogeneous equilibria that have been demonstrated to be assignable within the proposed class of models for continuum robots.

5.4.2 Simultaneous position-and-stiffness control

To stabilise an arbitrary homogeneous equilibrium $\boldsymbol{q}_\star$ in the subset of $\mathcal{E}_\theta$ with a tunable stiffness of the closed loop, the passivity-based control (PBC) method will be employed since it has a clear energy interpretation and simplifies both modelling and controller design. This makes it suitable for continuum robotics to preserve the system compliance [31].

The basic idea is to fix τ_2 at some constant value $\tau_2^\star \geq 0$, and then utilise the input τ_1 to achieve potential energy shaping for the regulation task. Compared to the more general approach of interconnection and damping assignment (IDA) PBC [270], on the one hand, potential energy shaping may provide a simpler controller form, and on the other hand,

as pointed out in [271] changing the inertia is prone to fail in practice – albeit being theoretically sound with additional DoF.

For a given input $\tau_2 = \tau_2^\star \geq 0$, the actuation into the dynamics is given by

$$\begin{aligned} G_\tau(\boldsymbol{q})\tau &= \rho_1(\boldsymbol{q})\tau_1 + \rho_2(\boldsymbol{q})\tau_2^\star \\ &:= G_{\mathrm{N}}\tau_{\mathrm{N}}(\mathrm{col}(\tau_1, \tau_2^\star)) \end{aligned} \tag{5.46}$$

with the function $\tau_{\mathrm{N}} : \mathbb{R}^2 \to \mathbb{R}$ defined in (5.42). From Assumption 5.6, the vector field $\rho_1(\boldsymbol{q}) \neq 0$ for all $\boldsymbol{q} \in \mathcal{X}$. Now the design target becomes using the control input τ_1 (with a fixed $\tau_2^\star$) to shape the potential energy function $U(\boldsymbol{q})$ into a new one – the desired potential energy function $U_{\mathrm{d}}(\boldsymbol{q})$. To this end, the PDE [260] needs to be solved

$$G_{\mathrm{N}}^{\perp}\big[\nabla U(\boldsymbol{q}) - \nabla U_{\mathrm{d}}(\boldsymbol{q})\big] = 0 \tag{5.47}$$

Note that the solution must adhere to the constraints

$$\nabla U_{\mathrm{d}}(\boldsymbol{q}_\star) = 0 \tag{5.48}$$

$$\nabla^2 U_{\mathrm{d}}(\boldsymbol{q}_\star) \succ 0 \tag{5.49}$$

in order to make the desired configuration $\boldsymbol{q}_\star$ an asymptotically stable equilibrium.

The next work is to propose the controller for simultaneous control of position and stiffness.

***Proposition* 5.4.** Consider the continuum robotic model (5.2), (5.28) with the constraint (5.29) satisfying Assumptions 5.3-5.6, and the full-rank damping matrix $D(\boldsymbol{q})$ is uniformly positive definite. The feedback controller

$$u = T_u^{-1}\tau \tag{5.50}$$

with the transformed input

$$\tau = \tau_{\mathrm{es}} + \tau_{\mathrm{da}} + \tau_{\mathrm{st}} \tag{5.51}$$

and the terms

$$\begin{aligned}\tau_{\mathrm{st}} &= \begin{bmatrix} -\frac{2g_1(\boldsymbol{q})}{g_0+g_1(\boldsymbol{q})} \\ 1 \end{bmatrix} \tau_2^\star \\ \tau_{\mathrm{es}} &= \begin{bmatrix} \frac{1}{g_0+g_1(\boldsymbol{q})} G_{\mathrm{N}}^\dagger (\nabla U_{\mathrm{d}} - \nabla U) \\ 0 \end{bmatrix} \\ \tau_{\mathrm{da}} &= \begin{bmatrix} -\frac{1}{g_0+g_1(\boldsymbol{q})} G_{\mathrm{N}}^\top K_{\mathrm{d}} M^{-1}(\boldsymbol{q}) \boldsymbol{p} \\ 0 \end{bmatrix}\end{aligned} \tag{5.52}$$

where $G_{\mathrm{N}} = \mathbf{1}_n$, $\tau_2^\star > 0$, $K_{\mathrm{d}} \succ 0$ is the gain matrix, and the desired potential energy function is given by

$$\begin{aligned} U_{\mathrm{d}}(\boldsymbol{q}) &= -\gamma \cos(q_\Sigma - q_\Sigma^\star) + \frac{\alpha_2}{2} \|\boldsymbol{q} - \boldsymbol{q}_\star\|^2 \\ q_\Sigma^\star &= \sum_{i \in \mathcal{N}} \boldsymbol{q}_{\star,i} \end{aligned} \tag{5.53}$$

the gain $\gamma > 0$, and some desired regulation configuration $\boldsymbol{q}_\star \in \mathcal{E}_\theta$, achieves the following closed-loop properties:

P1: (*Position regulation in free motion*) If the external force $\tau_{\mathrm{ext}} = 0$ and $\gamma < \alpha_2$, then the desired equilibrium point $\boldsymbol{q}_\star$ is globally asymptotically stable (GAS) with

$$\lim_{t \to +\infty} \boldsymbol{q}(t) = \boldsymbol{q}_\star \tag{5.54}$$

P2: (*Compliant behaviour*) The overall closed-loop stiffness (i.e., from the external torque $\tau_{\mathrm{ext}} \in \mathbb{R}^n$ to the configuration $\boldsymbol{q} \in \mathbb{R}^n$) is

$$K_{\mathrm{o}} = \gamma \mathbf{1}_{n \times n} + \alpha_2 I_n \tag{5.55}$$

where $\mathbf{1}_{n \times n}$ is an $n \times n$ matrix of ones. ◁

Proof. First, it is straightforward to verify that the vector τ_{st} in (5.52) is in the null space of $\tau_{\mathrm{N}}(\tau)$ for any $\tau_2^\star$, i.e.,

$$\tau_{\mathrm{N}}(\tau_{\mathrm{st}}) = 0, \quad \forall \tau_2^\star \in \mathbb{R}_{\geq 0} \tag{5.56}$$

It means that the first term τ_{st} does not change the closed-loop dynamics.

For the effect of the potential energy shaping term τ_{es}, the Jacobian of the desired potential energy function U_{d} is given by

$$\nabla U_{\text{d}}(\boldsymbol{q}) = \gamma \sin(q_\Sigma - q_\Sigma^\star)\mathbf{1}_n + \alpha_2(\boldsymbol{q} - \boldsymbol{q}_\star) \tag{5.57}$$

It satisfies the following:

$$\nabla U_{\text{d}}(\boldsymbol{q}_\star) = 0 \tag{5.58}$$

$$\nabla^2 U_{\text{d}}(\boldsymbol{q}) = \gamma \cos(q_\Sigma - q_\Sigma^\star)\mathbf{1}_{n\times n} + \alpha_2 I_n \succ 0 \tag{5.59}$$

where the second line holds true for all $\boldsymbol{q} \in \mathbb{R}^n$ by noting that the eigenvalues of the symmetric matrix $\nabla^2 U_{\text{d}}$ are given by

$$\{\underbrace{\alpha_2, \ldots, \alpha_2}_{n-1}, \alpha_2 + \gamma|\cos(q_\Sigma - q_\Sigma^\star)|\}$$

with all elements positive from the condition $\gamma < \alpha_2$ in **P1**. This implies that the desired potential energy function U_{d} is convex and achieves its global minimum at $\boldsymbol{q}_\star$.

For the function U_{d}, it has

$$\begin{aligned}
&G_{\text{N}}^{\perp}[\nabla U - \nabla U_{\text{d}}] \\
=&G_{\text{N}}^{\perp}[\alpha_1 \sin(q_\Sigma)\mathbf{1}_n + \alpha_2 \boldsymbol{q} - \gamma \sin(\boldsymbol{q}_\Sigma - \boldsymbol{q}_\Sigma^\star)\mathbf{1}_n - \alpha_2(\boldsymbol{q} - \boldsymbol{q}_\star)] \\
=&G_{\text{N}}^{\perp}[\alpha_1 \sin(q_\Sigma)\mathbf{1}_n - \gamma \sin(q_\Sigma - q_\Sigma^\star)\mathbf{1}_n + \alpha_2 \boldsymbol{q}_\star] \\
=&0
\end{aligned} \tag{5.60}$$

where in the last equation the fact $\boldsymbol{q}_\star \in \mathcal{E}_\theta$ is used, so that the PDE (5.47) is verified. Together with (5.56), the controller (5.51) makes the closed-loop dynamics have the form

$$\begin{bmatrix} \dot{\boldsymbol{q}} \\ \dot{\boldsymbol{p}} \end{bmatrix} = \begin{bmatrix} 0_{n\times n} & I_n \\ -I_n & -\mathsf{D} \end{bmatrix} \begin{bmatrix} \nabla_{\boldsymbol{q}} H_{\text{d}} \\ \nabla_{\boldsymbol{p}} H_{\text{d}} \end{bmatrix} + \begin{bmatrix} \mathbf{0}_n \\ \tau_{\text{ext}} \end{bmatrix} \tag{5.61}$$

with

$$\begin{aligned}
H_{\text{d}}(\boldsymbol{q}, \boldsymbol{p}) &:= \frac{1}{2}\boldsymbol{p}^\top M^{-1}(\boldsymbol{q})\boldsymbol{p} + U_{\text{d}}(\boldsymbol{q}) \\
\mathsf{D}(\boldsymbol{q}) &:= D(\boldsymbol{q}) + G_{\text{N}} K_{\text{d}} G_{\text{N}}^\top \succ 0
\end{aligned} \tag{5.62}$$

The function $\mathsf{D}(\boldsymbol{q})$ is used to represent the closed-loop damping. For free motion (i.e., $\tau_{\text{ext}} = 0$), following the standard Lyapunov analysis, it has

$$\dot{H}_{\text{d}} \leq -(\nabla H_{\text{d}})^{\top} \mathsf{D}(\boldsymbol{q}) \nabla H_{\text{d}} \leq 0 \tag{5.63}$$

For the closed-loop system (5.61), the set $\{(\boldsymbol{q}, \boldsymbol{p}) : (\nabla H_{\text{d}})^{\top} \mathsf{D}(\boldsymbol{q}) \nabla H_{\text{d}} = 0\}$ contains only a single point $(\boldsymbol{q}_{\star}, \mathbf{0}_n)$. From the LaSalle's invariance principle [272, Sec 4.2], the global asymptotic stability of the desired equilibrium $(\boldsymbol{q}_{\star}, \mathbf{0}_n)$ is able to show. Hence, the property **P1** is proven.

The next step is to verify the stiffness property **P2** in a small neighbourhood $B_{\varepsilon(\boldsymbol{q}_{\star})}$ of $\boldsymbol{q}_{\star}$ with a sufficiently small $\varepsilon > 0$. For a constant external force τ_{ext}, the shifted equilibrium point $(\bar{\boldsymbol{q}}, \mathbf{0}_n)$ should satisfy

$$-\nabla_{\boldsymbol{q}} U_{\text{d}} + \tau_{\text{ext}} = 0 \tag{5.64}$$

or equivalently

$$\phi(\bar{\boldsymbol{q}}) := \gamma \sin(\bar{q_{\Sigma}} - q_{\Sigma^{\star}}) \mathbf{1}_n + \alpha_2 (\bar{\boldsymbol{q}} - \boldsymbol{q}_{\star}) = \tau_{\text{ext}} \tag{5.65}$$

with the definition $\bar{q}_{\Sigma} := \sum_{i \in \mathcal{N}} \bar{\boldsymbol{q}}_i$. Note that $\nabla \phi = \nabla^2 U_{\text{d}} \succ 0$, which means that $\phi : \boldsymbol{q} \mapsto \tau_{\text{ext}}$ is a (locally) injective immersion. Hence, in the small neighborhood $B_{\varepsilon}(\boldsymbol{q}_{\star})$ of $\boldsymbol{q}_{\star}$, there is a *unique* solution $\bar{\boldsymbol{q}}$ to (5.65) for a given τ_{ext}.

The shifted equilibrium $(\bar{\boldsymbol{q}}, \mathbf{0}_n)$ is shown that asymptotically stable by considering the Lyapunov function

$$V(\boldsymbol{q}, \boldsymbol{p}) = H_{\text{d}}(\boldsymbol{q}, \boldsymbol{p}) - \boldsymbol{q}^{\top} \tau_{\text{ext}} \tag{5.66}$$

From the above analysis, it is clear that

$$\begin{aligned} \nabla V(\bar{\boldsymbol{q}}, \mathbf{0}) &= \begin{bmatrix} \phi(\bar{\boldsymbol{q}}) - \tau_{\text{ext}} \\ \mathbf{0} \end{bmatrix} = \mathbf{0} \\ \nabla^2 V(\bar{\boldsymbol{q}}, \mathbf{0}) &\succ 0 \end{aligned} \tag{5.67}$$

Hence, V qualifies as a Lyapunov function. Its time derivative along the system trajectory is given by

$$\begin{aligned} \dot{V} &= -\|\nabla_{\boldsymbol{p}} H_{\mathrm{d}}\|_{\mathsf{D}}^2 - (\nabla_{\boldsymbol{p}} H_{\mathrm{d}})^\top \tau_{\mathrm{ext}} - \dot{\boldsymbol{q}}^\top \tau_{\mathrm{ext}} \\ &= -\|\nabla_{\boldsymbol{p}} H_{\mathrm{d}}\|_{\mathsf{D}}^2 \\ &\leq 0 \end{aligned} \tag{5.68}$$

It yields the Lyapunov stability of the closed-loop dynamics (5.61) in the presence of a constant external torque τ_{ext}, and all the system states are bounded. On the other hand, the set $\mathcal{E}_u := \{(\boldsymbol{q}, \boldsymbol{p}) : \|\nabla_{\boldsymbol{p}} H_{\mathrm{d}}(\boldsymbol{q})\| = 0\}$ only contains a single isolated equilibrium $(\bar{\boldsymbol{q}}, \boldsymbol{0})$. According to LaSalle's invariance principle, $(\bar{\boldsymbol{q}}, \boldsymbol{0})$ is an asymptotically stable equilibrium, in which $\bar{\boldsymbol{q}}$ depends on the (arbitrary) constant torque τ_{ext} – in terms of the unique solution of the algebraic equation (5.65).

The overall stiffness K_{o} is defined by $\tau_{\mathrm{ext}} = K_{\mathrm{o}}(\bar{\boldsymbol{q}} - \boldsymbol{q}_\star)$. Substituting it into (5.65), it has

$$\gamma \sin(\mathbf{1}_n^\top \bar{\boldsymbol{q}} - q_{\Sigma^\star}) \mathbf{1}_n + \alpha_2 (\bar{\boldsymbol{q}} - \boldsymbol{q}_\star) = K_{\mathrm{o}} (\bar{\boldsymbol{q}} - \boldsymbol{q}_\star) \tag{5.69}$$

The stiffenss at the desired equilibrium $\boldsymbol{q}_\star$ is calculated from any direction of the limit $\bar{\boldsymbol{q}} \to \boldsymbol{q}_\star$, thus obtaining

$$\begin{aligned} K_{\mathrm{o}}\Big|_{\boldsymbol{q}_\star} &= \frac{\partial \phi}{\partial \boldsymbol{q}}(\boldsymbol{q}_\star) \\ &= \lim_{\bar{\boldsymbol{q}} \to \boldsymbol{q}_\star} \gamma \cos(\mathbf{1}_n^\top \bar{\boldsymbol{q}} - q_\Sigma^\star) \mathbf{1}_{n \times n} + \alpha_2 I_n \\ &= \gamma \mathbf{1}_{n \times n} + \alpha_2 I_n \end{aligned} \tag{5.70}$$

This verifies the stiffness property **P2**, and the proof is completed. □

The above shows that the proposed controller (5.50)-(5.52) can achieve the position regulation with the closed-loop stiffness K_{o} given by (5.55). It implies that a prescribed stiffness can be set by selecting the control gain $\gamma > 0$ properly. More discussions about the control law will be provided in the next section.

5.5 Discussions

The following remarks about the proposed controller are given in order.

1) In **P2**, the *overall* stiffness is studied – from the external torque vector τ_{ext} to the configuration $\boldsymbol{q} \in \mathcal{X}$, rather than the transverse stiffness at the end-effector. Consider the external force $f_{\text{ext}} \in \mathbb{R}$ at the end-effector along the transverse direction of the n-link with the Jacobian $J = [0, \ldots, 0, \ell]$. With a *small* force f_{ext}, the coordinate of the end-effector would shift from $\left(\ell\left(\sum_{k\in\mathcal{N}} \sin(k\theta_\star)\right), \ell\left(\sum_{k\in\mathcal{N}} \cos(k\theta_\star)\right)\right)$ to $(F_x(f_{\text{ext}}), F_y(f_{\text{ext}}))$ with

$$\begin{pmatrix} F_x \\ F_y \end{pmatrix} = \begin{pmatrix} \ell\sin(\beta) + \ell\sum_{k\in\mathcal{N}\backslash\{n\}} \sin(k\theta_\star + \gamma\ell f_{\text{ext}}) \\ \ell\cos(\beta) + \ell\sum_{k\in\mathcal{N}\backslash\{n\}} \cos(k\theta_\star + \gamma\ell f_{\text{ext}}) \end{pmatrix}$$

and $\beta := n\theta_\star + (\gamma + \alpha_2)\ell f_{\text{ext}}$. Hence, the transverse stiffness is given by

$$K_{\text{T}} = \lim_{f_{\text{ext}}\to 0} \frac{\sqrt{[F_x(f_{\text{ext}}) - F_x(0)]^2 + [F_y(f_{\text{ext}}) - F_y(0)]^2}}{f_{\text{ext}}}$$

As a result, it has

$$\boxed{K_{\text{T}} \;\propto\; \kappa_1\gamma + \kappa_2} \tag{5.71}$$

with some non-zero constants κ_1, κ_2 for $\theta_\star \neq 0$. This important affine relationship will be experimentally verified in the next section. It means that for a given desired equilibrium $\boldsymbol{q}_\star \in \mathcal{X}\backslash\{\boldsymbol{0}\}$, the transverse stiffness is affine in the gain γ, thus providing a way to tune the closed-loop stiffness *linearly*.

2) The proposed controller can be roughly viewed as a nonlinear proportional-derivative (PD) controller. The first term τ_{st} is used to compensate the "anisotropy" in the input matrix $G(\boldsymbol{q})$ due to its state-dependency property; the potential energy shaping term τ_{es} and the damping injection term τ_{da}, indeed, play the role of nonlinear PD control. To be precise, the term τ_{es} is the error between the nonlinear functions of the position $\boldsymbol{q}$ and its desired value $\boldsymbol{q}_\star$; and the term τ_{da} can be viewed as the negative feedback of velocity errors. This is not surprising, since the original idea of energy shaping has its roots in the pioneering work of Takegaki and Arimoto in

robot manipulator control [273], in which they proposed a very well-known "PD + gravity compensation" feedback [250].

3) To ensure that $\nabla^2 U_{\mathrm{d}}(\boldsymbol{q}_\star) \succ 0$, it is necessary to impose the condition $\gamma < \alpha_2$ on the control gains. However, this condition may restrict the range of closed-loop stiffness values within an interval. If this condition is not imposed, it is only possible to guarantee the positive definiteness of ∇U_{d} in the vicinity of $\boldsymbol{q}_\star$, which would result in *local* asymptotic stability. Some experimental evidence regarding this point in the next section will be provided.

4) For the proposed controller (5.50)-(5.51), note that the term $M^{-1}(\boldsymbol{q})\boldsymbol{p}$ corresponds to the generalised velocity of $\boldsymbol{p}$. Thus, the controller depends on only three *plant parameters* (α_1, α_2 and g_0) and a nonlinear function g_1 – which need to be identified beforehand – and two adaptation gains (i.e., K_{d} and γ). This means that it is unnecessary to identify all parameters and functions in the plant model. This makes the resulting controller robust *vis-à-vis* different types of uncertainties.

5) Continuum robots inherently admit infinite DoF, and thus increasing the link number $n \in \mathbb{N}_+$ in the rigid-link model will enhance precision. On the other hand, a higher dimension n will bring computational challenges to obtaining the real-time detection/estimation of the configuration $\mathbf{q}$. Consequently, it is necessary to make a tradeoff between accuracy and computational burden, for the selection of the link number n.

5.6 Experimental results

5.6.1 Experimental setup

The proposed approach was tested using the OctRobot-I, a continuum robot developed in our lab at the University of Technology Sydney [10]. The planar case with six segments (i.e., $n = 6$) is considered with an overall length of 252 mm, and a diameter of approximately 50 mm, which meets the critical assumptions outlined in this chapter. Notably, the

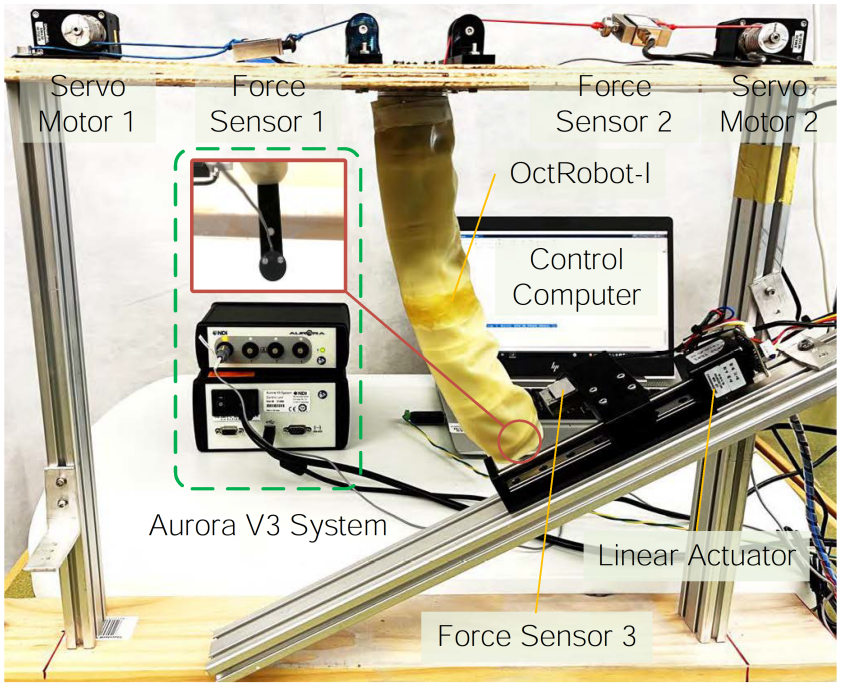

FIGURE 5.4: Photo of the entire experimental platform.

OctRobot-I has a jamming sheath that can provide an extra degree of freedom for stiffening, though the present research does not delve into this feature's stiffening capabilities. Additional details of the OctRobot-I can be found in Chapter 3 and [10].

As shown in Figure 5.4, the test platform used in the experiments consists of the one-section robot (OctRobot-I), two servo motors (XM430-W350, DYNAMIXEL) with customised aluminium spools, three force sensors (JLBS-M2-10kg), a linear actuator, and an electromagnetic tracking system (Aurora V3, NDI). The control experiments and data collections were conducted using the software MATLAB™. The Aurora sensor is installed at the distal point of the robot to provide its real-time coordinate z_e. In the position regulation tasks, no external load was applied to the robot, and the phenomenon is observed that it nearly satisfied the constant curvature condition with the approximation $q_i = q_j \ (i, j \in \mathcal{N})$ available.[5] Together with the coordinate z_e and some basic geometric relations, it is able to estimate the configuration vector $\boldsymbol{q}$ in real time. In the experimental setup, where $q_i = q_j$ is assumed, and $\theta(t)$ is used to represent the estimated value q_i in the sequel of this section.

[5]Note that in the theoretical analysis, it does not assume $q_i = q_j \ (i, j \in \mathcal{N})$.

The servo motors in the platform can provide accurate position information with high accuracy, making it easier to control cable lengths between the servo motors and the actuator unit. Using Hooke's law, it is possible to consider the cable length proportional to the force for each cable, with a few coefficients to be identified off-line using collected data sets. To verify the linear relationship between the cable length and the tension force, as well as to obtain the coefficients, a group of experiments with different configurations is conducted and the cable lengths and the corresponding forces are recorded. Each configuration is repeatedly conducted three times under identical conditions, and all the data are utilised for identification. In Figure 5.5, the relation between the right cable length L_2 and the corresponding force, and the one between the length difference $\Delta L := L_1 - L_2$ and the force difference $\tau_1 := u_1 - u_2$ of these two cables are plotted. The correlation coefficients are 0.9977 and 0.9987, which imply the strong linearity between cable lengths and forces. Thus, it is reasonable to use the cable lengths – driven by motors – as the "real" input signals. Note that the above-mentioned linearity only holds in static or low-speed conditions. To satisfy this, a high gain is used for the cable length control loop to yield a very short transient stage.

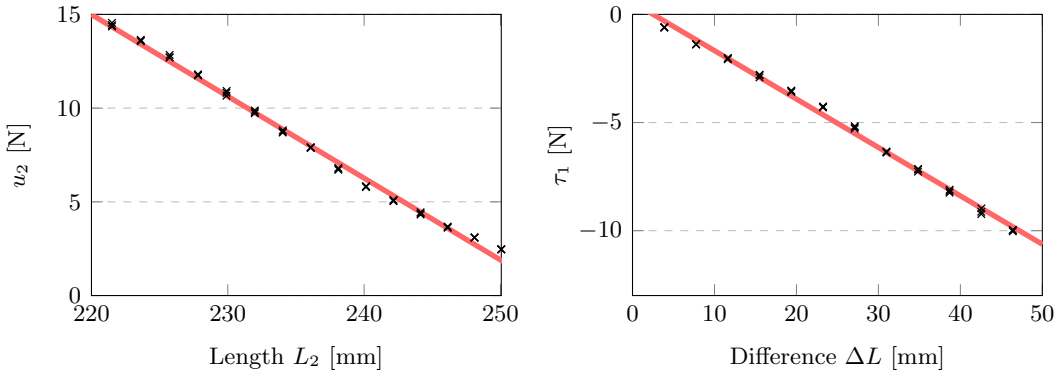

FIGURE 5.5: The linearity between forces and lengths: the length L_1 vs the force u_1 of the right cable; and the length difference $\Delta L := L_1 - L_2$ vs the force difference $\tau_1 := u_1 - u_2$. ("×" represents test data, and the dash lines are the fitted functions.)

The force sensors are used in the open-loop stiffening experiments to provide real-time force signals, and then the relation between the value μ and the open-loop stiffness can be studied. Additionally, these sensors have proven important for examining the relation between cable lengths and applied forces as mentioned above. However, in closed-loop

control, force sensors on the platform are removed and the cable lengths are directly regulated. Note that these sensors may cause significant inertial disturbances to the loop.

5.6.2 Open-loop stiffening experiments

This subsection will validate the results regarding open-loop stiffening presented in Section 5.3. For this purpose, a linear actuator placed at the end-effector is utilised to generate a small displacement $\delta x > 0$, as illustrated in Figure 5.6(a). The actuator is connected to the force sensors for measuring the external force, denoted as f_{ext}, in relation to the displacement. By calculating the ratio of the measured force to the applied displacement, i.e., $\frac{f_{\text{ext}}}{\delta x}$, the transverse stiffness can be estimated, given that δx is sufficiently small. This procedure is to verify the findings related to open-loop stiffening as outlined in Section 5.3.

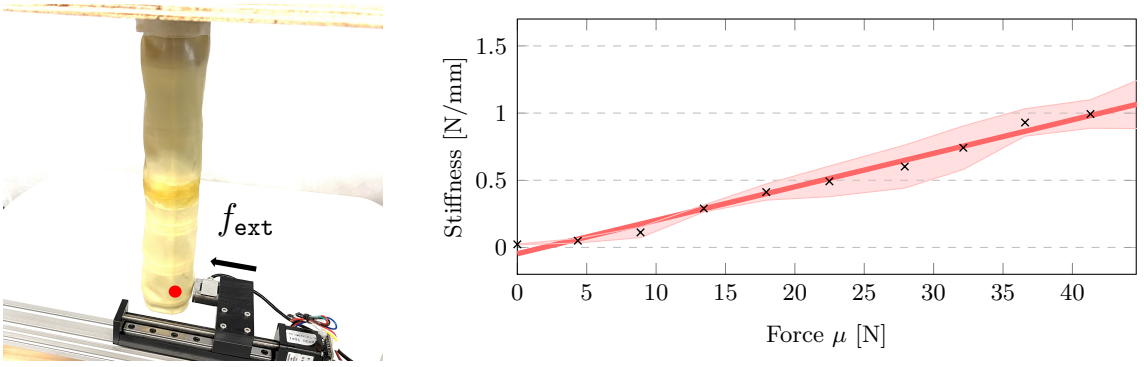

(a) experimental setup.

(b) experimental results of transverse stiffness.

FIGURE 5.6: Experiments for open-loop stiffening.

The stiffness values under different open-loop tendon forces $\mu > 0$ in the interval $[0, 45]$ N are measured. Each experiment is repeatedly conducted three times under the same conditions in order to improve reliability. The experimental results are shown in Figure 5.6(b), where "$\times$" represents the mean values of the calculated stiffness for all μ, and the error bars are ± 1 standard deviation. This clearly verifies the theoretical results in Proposition 5.1. The correlation coefficient between μ and the stiffness is 0.9890, which illustrates the strong linearity – exactly coinciding with the equation (5.25).

5.6.3 Closed-loop experiments

In order to apply the proposed real-time control algorithm to the experimental platform, the identification procedure to estimate the parameters outlined in the fourth discussing point in Section 5.5 is first conducted. It relies on the fact that at any *static* configuration $\boldsymbol{q}$ (i.e., with $\boldsymbol{p} = 0$) the identity $\nabla_{\boldsymbol{q}} U(\boldsymbol{q}) = G(\boldsymbol{q})\boldsymbol{u}$ holds true, and thus $J(\theta) = 0$ with the cost function

$$J(\theta, u_1, u_2) := \left|\alpha_1 \sin(n\theta) + \alpha_2\theta - [g_0 + g_1(\theta)]u_1 + [g_0 - g_1(\theta)]u_2\right|^2 \tag{5.72}$$

that contains all the quantities to be identified. According to the modelling procedure in Section 5.3, it can be simply parameterised $g_0 + g_1(\theta) = c_1 + c_2 \sin(\theta)$ with two constants $c_1 > 0$ and $c_2 < 0$, complying with the assumptions on the input matrix. The continuum robot to different equilibria θ^j ($j = 1, \ldots, w$ with some $w \in \mathbb{N}_+$) can be regulated by driving the cables, and recorded the corresponding forces (u_1^j, u_2^j).

The identification procedure boils down to solving the optimisation

$$\underset{c_1,\alpha_1,\alpha_2>0,c_2<0}{\arg\min} \sum_{j\in\{1,\ldots,w\}} J(\theta^j, u_1^j, u_2^j) \tag{5.73}$$

The identification experiments are run to collect data at 15 equilibria points (i.e., $w = 15$) and repeated six times at each equilibria point. Using this data set, the identified parameters are $c_1 = 1.2143$, $c_2 = -2.9015$, $\alpha_1 = 8.6114$, $\alpha_2 = 0.001$.

To evaluate the performance of position control, a desired configuration $\mathbf{q}_\star = [\theta_\star, \ldots, \theta_\star]^\top$ with $\theta_\star = 5$ deg is first considered for the proposed control scheme. Experiments for the cases without external forces under various values of the gains γ and K_d are conducted, as shown in Figures 5.8-5.9, respectively. The second row of these figures depicts the configuration variable at the steady-state stage during $[2, 8]$ s. It is worth noting that the control inputs u_i ($i = 1, 2$) are mapped to the cable length L_i ($i = 1, 2$), as explained in Section 5.6.1. In all these scenarios, the transient stage lasted for less than 1.5 seconds, and the configuration variable quickly converged to small neighbourhoods of the desired angle, demonstrating the high accuracy of the proposed control approach. There are no

apparent overshootings in configuration variables. The results indicate that selecting either a sufficiently small or large K_{d} can negatively affect the control performance during the transient stage. On the other hand, setting a large $\gamma > 0$ may lead to chattering due to measurement noise at the steady-state stage, which is well understood as the deleterious effect of high-gain design in the control literature [250].

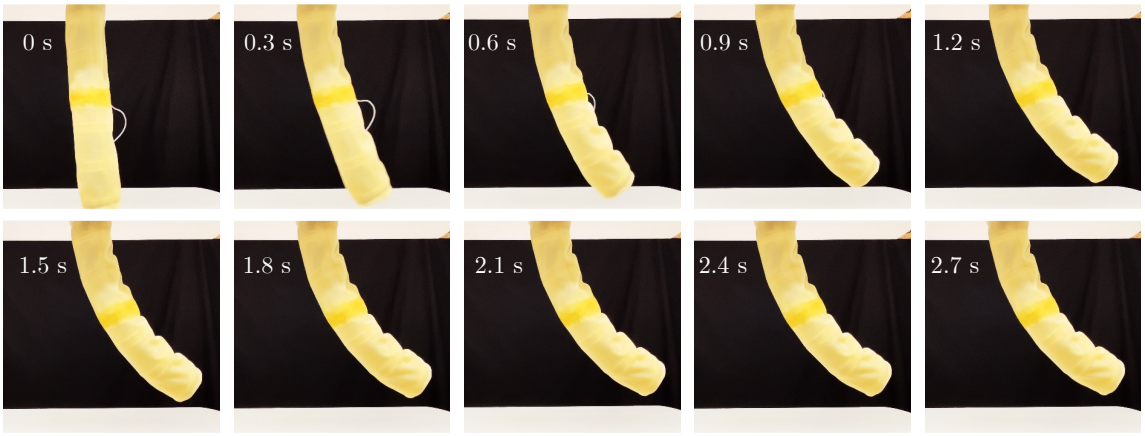

FIGURE 5.7: Photo sequence of the position control with $\theta_\star = 10$ deg and $\gamma = 1, K_{\mathrm{d}} = 0.1$.

Additional experiments are conducted to test the proposed control approach in different scenarios, including the desired configurations of $\theta_\star = 10$ deg and 15 deg, which are shown in Figure 5.10. These results demonstrate that the algorithm is capable of achieving high accuracy and performance for position control. To quantify the steady performance, the configuration trajectories during $\mathcal{I}_{\mathrm{s}} := [4, 8]$ s are studied because the system states arrive at the steady-state stage for all these scenarios. For these two desired equilibria, the proposed design achieved high accuracy, verifying the property **P1** in Proposition 5.4.

The accuracy achieved in these experiments is summarised with different equilibria (5 deg, 10 deg and 15 deg) and gains of γ and K_{d} in Table 5.1, where $[\theta_{\mathtt{min}}, \theta_{\mathtt{max}}]$ represents the minimal and the maximal values during the interval $\mathcal{I}_{\mathrm{s}}$. The root mean square (RMS) and the mean absolute error (MAE) for each scenario are also given in the same table. For $\theta_\star = 5$ deg, it achieved the highest accuracy among the three equilibria, for which the selections of γ as 1 and 5 degraded the steady-state accuracy a little bit. In Figure 5.7, a photo sequence of one of the scenarios is presented with the desired configuration $\theta_\star = 10$ deg, and the gains $K_{\mathrm{d}} = 0.1$ and $\gamma = 1$. This sequence serves as an intuitive illustration of the dynamic behaviour of the closed loop.

In addition, the result with a *large* $\gamma = 10$ is reported. However, as explained in the discussion point 3) in Section 5.5, a large $\gamma > 0$ may make the desired potential energy function U_{d} *non-convex*, resulting in instability. This is consistent with the experimental results, as the neutral stability with oscillating behaviours at the steady-state stage for $\gamma = 10$ are observed; see Figure 5.11. Evaluating the closed-loop performance in Figure 5.8, it is observed that a smaller gain K_{d} was likely to cause poor *transient* performance with longer time. Whereas, the experimental results in Table 5.1 show that the value of K_{d} within the interval $[0.1, 10]$ has limited effects on the *steady-state* performance for position control.

Experimental results demonstrate closed-loop stiffness regulation around the desired equilibria, which is related to **P2** in Proposition 5.4. While measuring the overall stiffness is generally not manageable, the transverse stiffness can be tested as outlined in Item 1) of Section 5.5. To this end, a linear actuator is equipped perpendicularly to the tangential direction of the continuum robot at the end-effector, as shown in Figure 5.4. The experiments are repeated for two different desired equilibria, namely 8 deg and 10 deg. Stiffness data is collected using different gains γ and results are plotted in Figure 5.12. The results match the equation (5.71) in Section 5.5 that the closed-loop stiffness is affine in the control gain γ. This implied that the parameters κ_1 and κ_2 can be identified and used to tune the controller for a prescribed stiffness around the desired configuration.

Finally, in order to investigate the robustness of the proposed approach, the experiments are conducted for two supplementary scenarios: one for examining the robot response in the presence of external disturbances, and the other for studying passive environmental interaction via encountering a semi-rigid foam obstruction. These setups are shown in Figure 5.13, and the corresponding experimental results are presented in Figure 5.14. Specifically, Figure 5.14(Left) provides evidence of the remarkable robustness of the proposed controller *vis-à-vis* external disturbances, as it effectively made the system back to its desired configuration after the vanishing of disturbances. It is also noted that a larger gain $\gamma > 0$ yielded a shorter recovery response. In the encounter experiments, as shown in Figures 5.13(b) and 5.14(Right), a larger value of $\gamma = 5$ ensured that the robot passed the foam obstruction, resulting in a recorded trajectory that was approximately *monotonic* over time – indicating the robot's stiff behaviour. In contrast, using the smaller value

TABLE 5.1: The steady-state errors in the time interval $[4, 8]$s of different scenarios (Unit: deg)

	γ	$K_\mathrm{d} = 10$			$K_\mathrm{d} = 1$			$K_\mathrm{d} = 0.1$		
		$[\theta_{\mathtt{min}}, \theta_{\mathtt{max}}]$	RMS	MAE	$[\theta_{\mathtt{min}}, \theta_{\mathtt{max}}]$	RMS	MAE	$[\theta_{\mathtt{min}}, \theta_{\mathtt{max}}]$	RMS	MAE
5 deg	0.01	[4.8876, 4.9403]	4.9336	0.0664	[4.9492, 4.9532]	4.9506	0.0494	[4.9236, 4.9515]	4.9413	0.0587
	0.1	[4.9538, 4.9687]	4.9605	0.0395	[4.9387, 4.9556]	4.9505	0.0495	[4.9480, 4.9528]	4.9503	0.0497
	1	[4.9148, 4.9265]	4.9570	0.0430	[4.9148, 4.9265]	4.9219	0.0781	[4.9156, 4.9195]	4.9179	0.0821
	5	[4.9325, 4.9367]	4.9351	0.0649	[4.9333, 4.9425]	4.9383	0.0617	[4.9316, 4.9473]	4.9408	0.0592
10 deg	0.01	[9.5437, 10.2709]	9.8684	0.1460	[9.8328, 9.9597]	9.8824	0.1176	[9.8458, 9.9596]	9.8902	0.1098
	0.1	[9.8320, 9.9048]	9.8803	0.1197	[9.8328, 9.9597]	9.8810	0.1190	[9.8440, 9.9758]	9.8991	0.1009
	1	[9.9074, 9.9295]	9.9216	0.0784	[9.7814, 9.9044]	9.8455	0.1546	[9.8204, 9.8457]	9.8324	0.1676
	5	[9.8706, 9.8857]	9.8756	0.1244	[9.8955, 9.8701]	9.8884	0.1116	[9.8942, 9.8442]	9.8812	0.1188
15 deg	0.01	[12.0252, 14.9968]	14.5881	0.4266	[14.7067, 14.7753]	14.7651	0.2350	[14.7333, 14.7798]	14.7711	0.2289
	0.1	[14.3324, 14.9968]	14.7970	0.2044	[14.5142, 14.7350]	14.6812	0.3190	[14.7174, 17.7939]	14.7710	0.2290
	1	[14.6276, 14.9968]	14.8059	0.1942	[14.7499, 14.7794]	14.7632	0.2368	[14.7228, 14.7597]	14.7482	0.2519
	5	[14.6863, 14.7590]	14.7209	0.2792	[14.7061, 14.7307]	14.7236	0.2764	[14.7051, 14.7301]	14.7186	0.2814

of $\gamma = 0.1$ did not yield this effect, causing the robot to exhibit some deformation when encountering the foam and displaying real-time position fluctuations in the transient stage due to its softness.

It is important to note that although various control approaches have been proposed for continuum robotics, their suitability for achieving simultaneous control of position and stiffness in underactuated robots is limited, particularly considering the variations in actuation mechanisms across different continuum robotic platforms. Given the absence of applicable control strategies in the existing literature, this study did not provide experimental comparisons to previous works. However, the objective is to lay the groundwork for future exploration and development of experimental studies in this topic area.

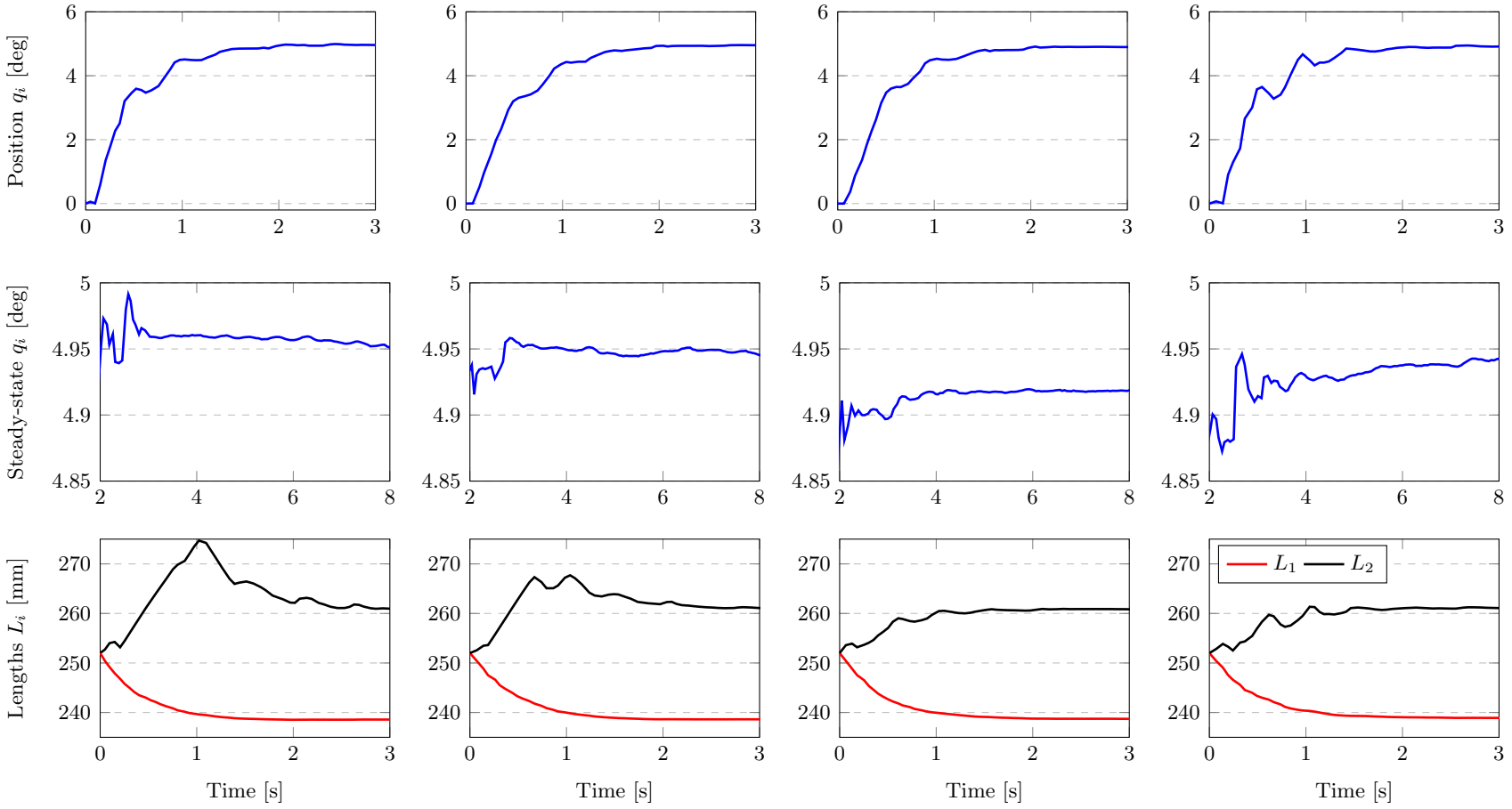

(a) $K_\mathrm{d} = 10$ (b) $K_\mathrm{d} = 5$ (c) $K_\mathrm{d} = 0.1$ (d) $K_\mathrm{d} = 0.01$

FIGURE 5.8: Position control performance for the desired configuration $\theta_\star = 5$ deg with $\gamma = 1$ and different K_d.

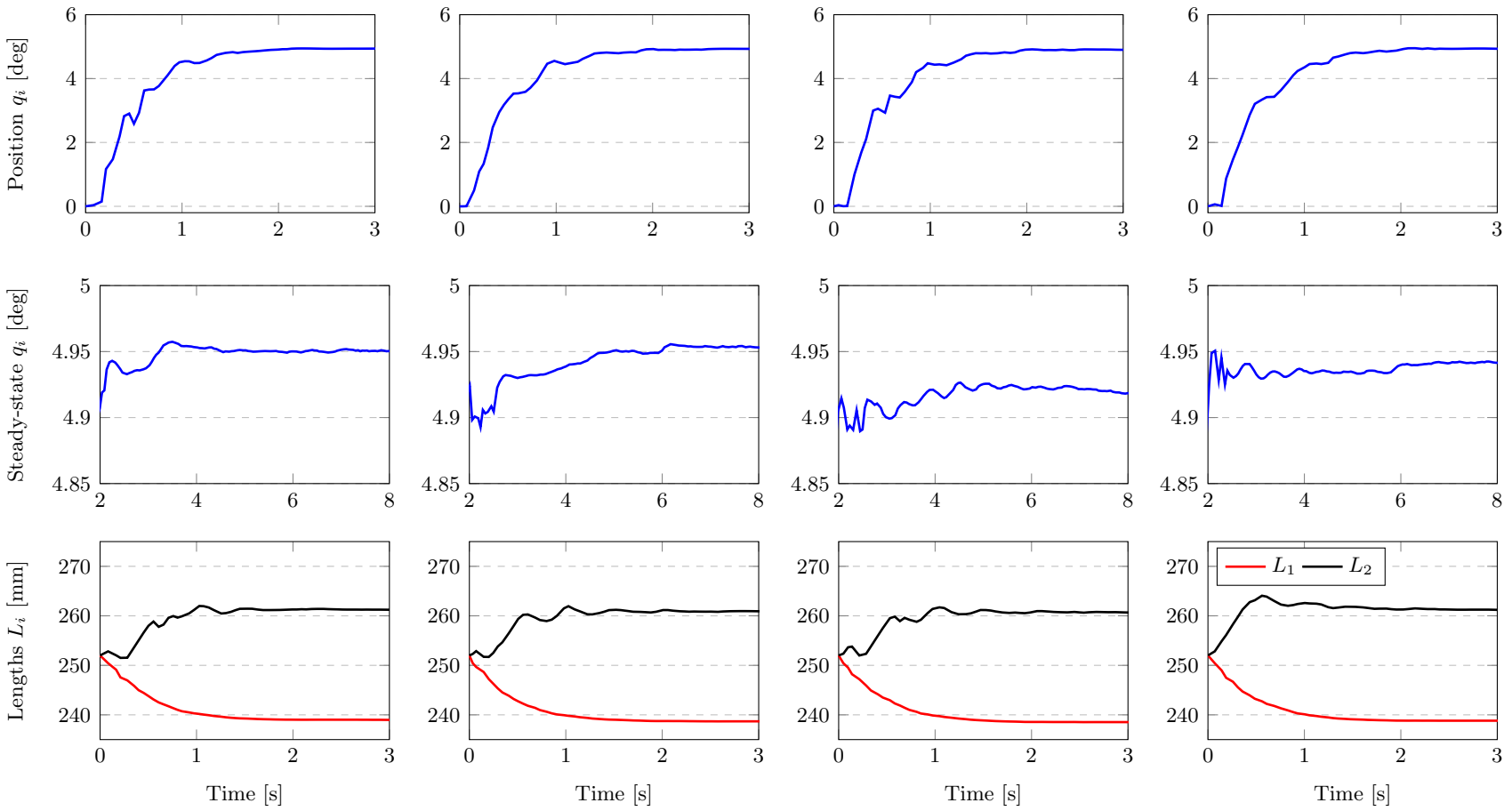

(a) $\gamma = 0.01$ (b) $\gamma = 0.1$ (c) $\gamma = 1$ (d) $\gamma = 5$

FIGURE 5.9: Position control performance for the desired configuration $\theta_\star = 5$ deg with $K_\mathrm{d} = 1$ and different γ.

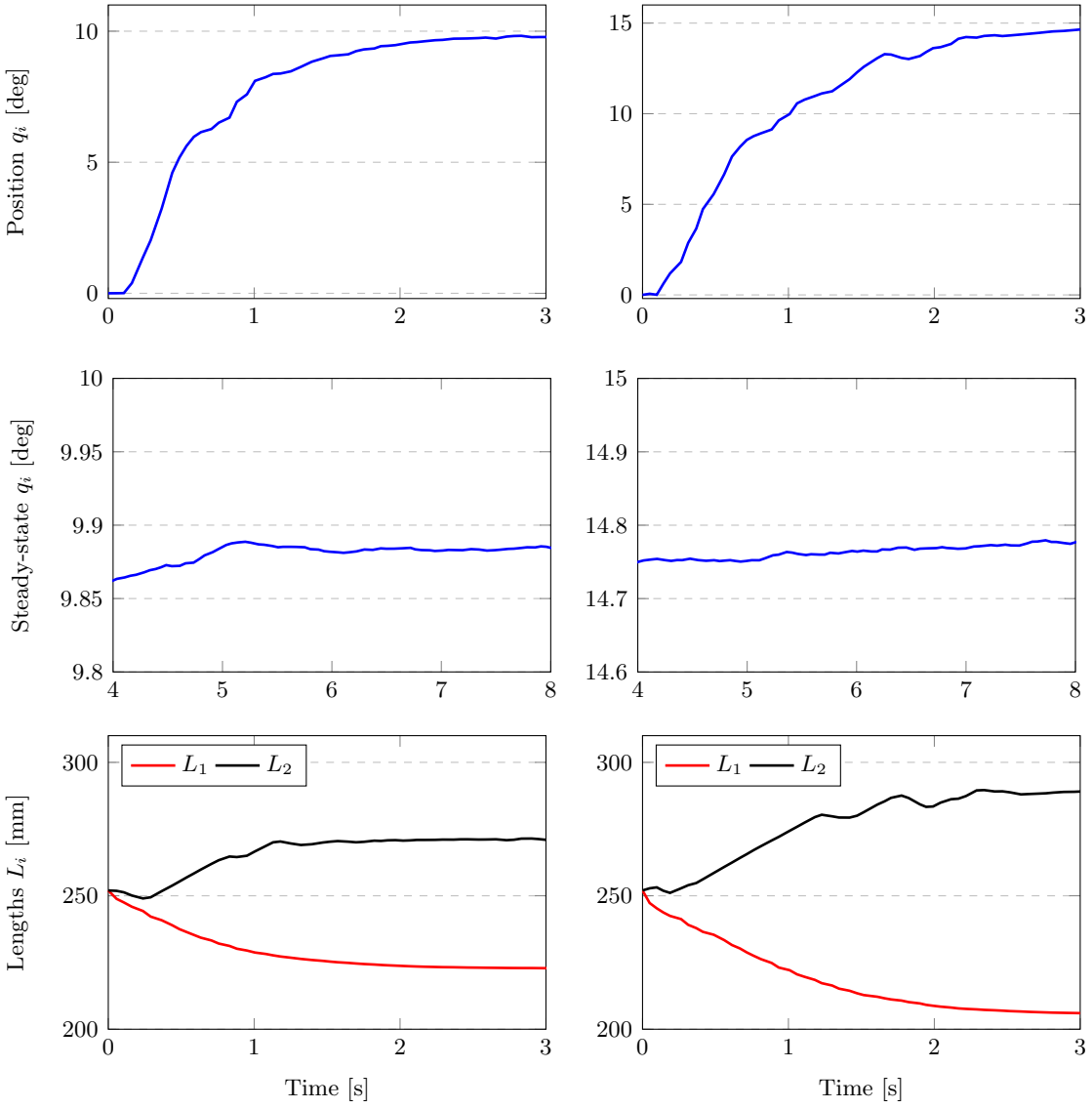

(a) $\theta_\star = 10$ deg (b) $\theta_\star = 15$ deg

FIGURE 5.10: Position control performance for the desired configurations $\theta_\star = 10$ deg and 15 deg with $K_\mathtt{d} = 1$ and $\gamma = 0.1$.

5.7 Summary

In this chapter, the modelling and control of underactuated antagonistic tendon-driven continuum robots are studied. The proposed model possesses a configuration-dependent input matrix, which effectively captures the mechanism for open-loop stiffening through

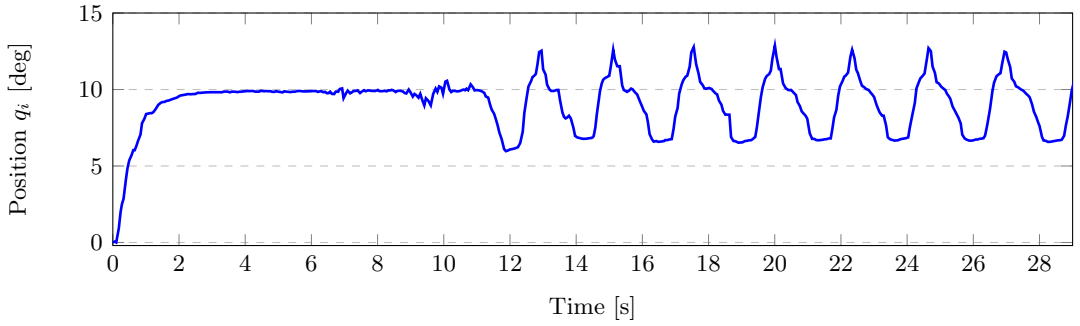

FIGURE 5.11: A large $\gamma = 10$ leads to unstable performance.

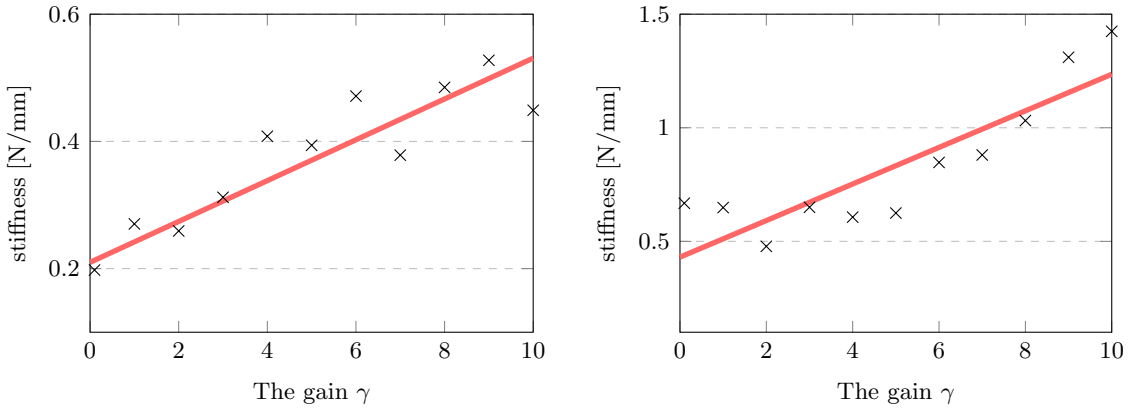

(a) desired configuration $\theta_\star = 8$ deg ($\kappa_1 = 0.0288$ and $\kappa_2 = 0.2332$)

(b) desired configuration $\theta_\star = 10$ deg ($\kappa_1 = 0.0805$ and $\kappa_2 = 0.4305$)

FIGURE 5.12: Stiffness regulation with the different configurations.

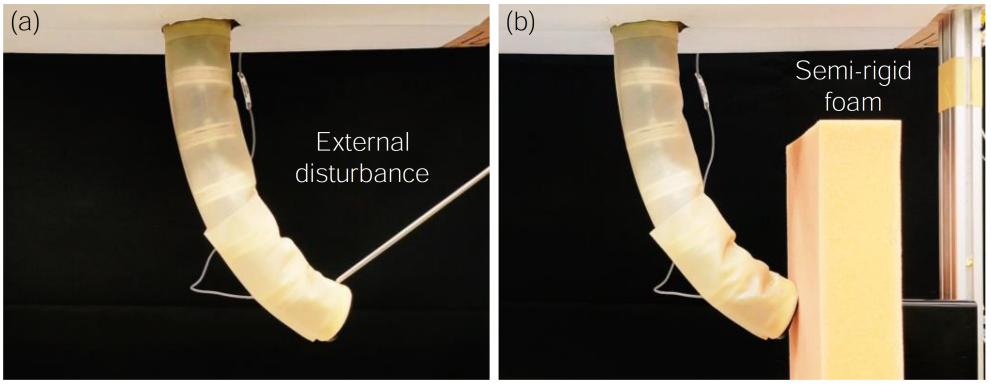

FIGURE 5.13: Experiments to evaluate the robustness of the closed-loop robotic system: (a) an external disturbance was added to the distal point of the robot. (b) the robot was controlled to encounter a semi-rigid foam obstruction.

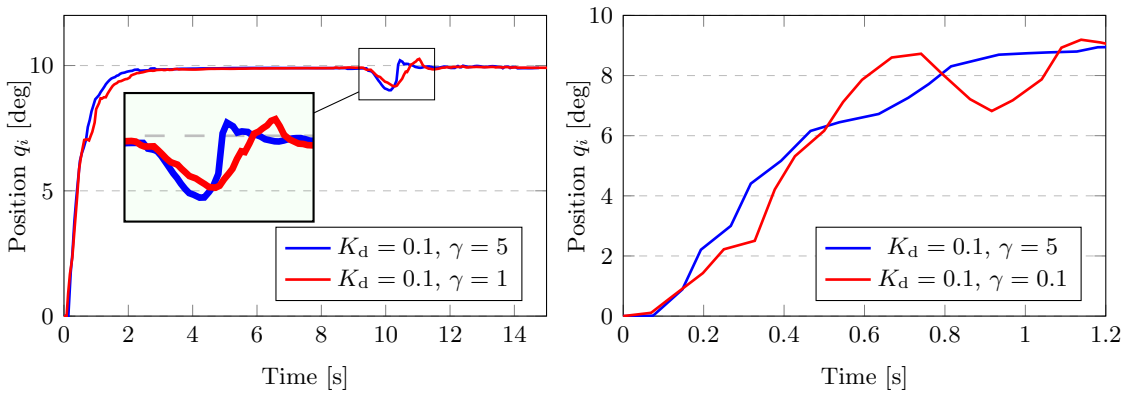

FIGURE 5.14: Results of the robustness evaluation experiments: (Left) Applying external disturbances; (Right) Encountering a semi-rigid foam obstruction.

cable tension regulation. The assignable equilibria set and devised a potential shaping feedback controller have been thoroughly analysed, which enables simultaneous position-and-stiffness regulation while adhering to the non-negative input constraint. The experimental results on the robotic platform OctRobot-I demonstrate the effectiveness and reliability of the proposed approach. This approach relies on only a few intrinsic parameters of the model, rather than depending on the complete dynamical model. This grants it remarkable robustness against modelling errors.

Along the research line, the following problems are considered as potential future works:

1) As per Proposition 5.4, the condition $\gamma < \alpha_2$ is imposed to guarantee the convexity of the desired potential energy function U_d. It should be noted that the parameter α_2 is an intrinsic characteristic of the continuum robot, and consequently the range of choices for the adaptation gain γ is limited, which restricts the ability to control the stiffness in a relatively narrow interval. The experimental results support this assertion. To enlarge the closed-loop stiffness range, a potential way is to make full use of *jamming* in the continuum robot via changing the compression level of jamming flaps [189].

2) Exploring alternative desired potential energy functions may offer a promising approach to enhance closed-loop performance. In addition, applying state-of-the-art energy shaping methodologies, such as those demonstrated in e.g., [274, 275], could

prove valuable for solving more complex tasks for continuum robots, such as path following and robust simultaneous position-and-stiffness control.

3) Similar to the recent works [31, 32], the approach in this chapter is developed for the robot with one section used in planar case, which is quite simple for continuum robots being utilised in the real word. It is underway to extend to multiple sections in the spatial case. A promising approach is to change the mechanical structure and actuate the overall robot in a sagittal plane for each section to prevent sections from twisting about their neutral axis [276]. Then, the proposed approach may be used to control sections separately in different planes, and the manipulator would be capable of three-dimensional Cartesian positioning.

4) The proposed approach does not consider the *actuation dynamics*, opting instead to utilise a high-gain design to enforce time-scale separation and disregard these dynamics. It would be advantageous to take the actuation dynamics into the controller synthesis by incorporating advanced robustification techniques [277].

5) In this thesis, the proposed method is applicable only to cases where the signs of curvatures in the PCC structure remain unchanged. Extending this approach to more complex configurations, such as the S-shape illustrated in Figure 5.3(b), would be a valuable direction for future work.

Chapter 6

Dynamic Model for Continuum Robots with Layer Jamming

Layer jamming (LJ) has emerged as a simple and efficient technique to achieve tunable stiffness for continuum robots. The development of a control-oriented dynamical model tailored for continuum robots with layer jamming remains an open problem in the literature. This chapter presents possibly the first solution to close the gap. An energy-based model that is integrated with the LuGre frictional model for LJ-based continuum robots is proposed. Then, a comprehensive theoretical analysis of this model is conducted, which focuses on two fundamental characteristics of LJ-based continuum robots: shape locking and adjustable stiffness. To validate the model and the theoretical results, a series of experiments are conducted using the OctRobot-I robotic platform. [1]

6.1 Introduction

Continuum robots have integrated variable stiffness techniques within their design, allowing for soft flexible motion or rigid resistance and greatly expanding their application

[1]The results presented in this chapter have previously appeared in the publication: Bowen Yi[†], Yeman Fan[†], Dikai Liu, "A novel model of layer jamming-based continuum robots", *2024 IEEE International Conference on Robotics and Automation (ICRA)*, Yokohama, Japan, pp.12727-12733, 2024.

[†]Bowen Yi and Yeman Fan contributed equally to this work.

range [278, 279]. As described in Chapter 2, jamming approaches have shown great success in adjustable stiffness for continuum robots with rapid reversible responses [5, 280, 281] among various stiffness tuning techniques. Notably, LJ, the concept of which was originally proposed in [156, 256], has received particular attention due to the advantages of being lighter weights and taking less space. It utilises thin plastic or paper layers as its jamming flaps. For continuum robots with LJ, there is an airtight pneumatic chamber in which a series of overlapping layers are installed to cover the robot spine or wrapped as the robot body. This mechanism exploits the friction between layers that can be controlled by external pressure via a vacuum and provides a large range of controllable stiffness.

Feedback control is one of the important topics of research in continuum robotics. Over the past few years, *model-based* approaches have gained resurgence since more experimental evidence has shown that feedback control approaches are robust to approximations for continuum robot dynamics [31, 282]. However, as figured out by one of the leading groups in the field, the modelling of LJ-based continuum robots with variable stiffness has not been well addressed yet [283]. There are recent works on analytical or computational models to characterise the mechanism of stiffness variation in LJ-based continuum robots [256, 283, 284]. However, to the best of the author's knowledge, there is no *control-oriented* model in the literature to approximate the dynamical behaviours of continuum robots.

This chapter aims to close the above-mentioned gap by updating the control model described in Chapter 5 for a class of LJ-based tendon-driven continuum robots, which integrates the energy-based modelling technique and the LuGre frictional model [285]. This model is in the port-Hamiltonian form with the vacuum pressure gradient as an additional control input. The proposed updated model has been theoretically proven its ability to illustrate the important phenomena of shape locking and adjustable stiffness. Additionally, an analytical relation between stiffness and negative pressure is also presented.

Notation. All functions and mappings are assumed to be C^2-continuous. I_n is the $n \times n$ identity matrix, $0_{n\times s}$ is an $n \times s$ matrix of zeros, the vector $\mathbf{0}_n := \text{col}(0, \dots, 0) \in \mathbb{R}^n$, and $\mathbf{1}_n := \text{col}(1, \dots, 1) \in \mathbb{R}^n$. Throughout the chapter, the bold font is for variables denoting vectors, while scalars and matrices are represented in normal font. For $\boldsymbol{x} \in \mathbb{R}^n$, $S \in \mathbb{R}^{n\times n}$, $S = S^\top > 0$, the Euclidean norm is $|\boldsymbol{x}|^2 := x^\top x$, and the weighted–norm is

$\|\boldsymbol{x}\|_S^2 := \boldsymbol{x}^\top S\boldsymbol{x}$. Given a function $f : \mathbb{R}^n \to \mathbb{R}$, the differential operators is defined as $\nabla f := (\frac{\partial f}{\partial x})^\top$, $\nabla_{x_i} f := (\frac{\partial f}{\partial x_i})^\top$, where $x_i \in \mathbb{R}^p$ is an element of the vector $\boldsymbol{x}$. The set $\bar{n}$ is defined as $\bar{n} := \{1, \ldots, n\}$. The $\mathrm{diag}\{x_i\}$ $(i \in \bar{n})$ is used to represent the diagonal matrix $\mathrm{diag}\{x_1, \ldots, x_n\}$, and the set $B_\varepsilon(\mathcal{X}) := \{x \in \mathbb{R}^n : \inf_{y\in\mathcal{X}} |x - y| \leq \varepsilon\}$ is defined for a given set $\mathcal{X} \in \mathbb{R}^n$. When clear from the context, the arguments of the functions may be omitted.

6.2 Dynamic modelling

6.2.1 Preliminary of jamming-free model

As described in Chapter 5 and the previous work [200], the control-oriented modelling of a class of underactuated tendon-driven continuum robots is considered. A rigid-link model is used to approximate the dynamical behaviour of continuum robots without layer jamming as follows:

$$\begin{bmatrix} \dot{\boldsymbol{q}} \\ \dot{\boldsymbol{p}} \end{bmatrix} = \begin{bmatrix} 0_{n\times n} & I_n \\ -I_n & -D(\boldsymbol{q}) \end{bmatrix} \begin{bmatrix} \nabla_{\boldsymbol{q}} H \\ \nabla_{\boldsymbol{p}} H \end{bmatrix} + \begin{bmatrix} \mathbf{0}_n \\ G(\boldsymbol{q})\boldsymbol{u} \end{bmatrix} \tag{6.1}$$

with the configuration variable $\boldsymbol{q} \in \mathcal{X} \subset \mathbb{R}^n$, the generalized momentum $\boldsymbol{p} \in \mathbb{R}^n$, the input matrix $G : \mathbb{R}^n \to \mathbb{R}^{n\times m}$, the damping matrix $D(\boldsymbol{q}) \in \mathbb{R}^{n\times n}_{\succeq 0}$, and the tension input $\boldsymbol{u} \in \mathbb{R}^m$. The total energy is characterised by the Hamiltonian as

$$H(\boldsymbol{q}, \boldsymbol{p}) = \frac{1}{2}\boldsymbol{p}^\top M^{-1}(\boldsymbol{q})\boldsymbol{p} + U(\boldsymbol{q}) \tag{6.2}$$

where $M : \mathbb{R}^n \to \mathbb{R}^{n\times n}_{\succ 0}$ is the positive definite inertial matrix satisfying $m_1 I \preceq M(\boldsymbol{q}) \preceq m_2 I$ for $m_2 \geq m_1 > 0$, and the potential energy function $U(\boldsymbol{q})$ contains the gravitational part U_{G} and the elastic part U_{E} that are functions of $\boldsymbol{q}$, i.e.,

$$U(\boldsymbol{q}) = U_{\mathrm{G}}(\boldsymbol{q}) + U_{\mathrm{E}}(\boldsymbol{q}) \tag{6.3}$$

As shown in Chapter 5 and [200], these functions can be modelled as

$$\begin{aligned} U_{\mathrm{G}}(\boldsymbol{q}) &= \alpha_1(1-\cos(q_\Sigma)) \\ U_{\mathrm{E}}(\boldsymbol{q}) &= \frac{1}{2}\boldsymbol{q}^\top \Lambda \boldsymbol{q} + U_0 \end{aligned} \tag{6.4}$$

with the diagonal matrix $\Lambda := \mathrm{diag}\{\alpha_2, \ldots, \alpha_2\}$, positive scalar U_0 and $q_\Sigma := \sum_{i\in\bar{n}} \boldsymbol{q}_i$. Note that α_1 and α_2 are elastic and gravitational coefficients, respectively. More details about the robotic structure and the modelling procedure can be found in Chapter 3, Chapter 5, and [200].

6.2.2 Assumptions and frictional model with layer jamming

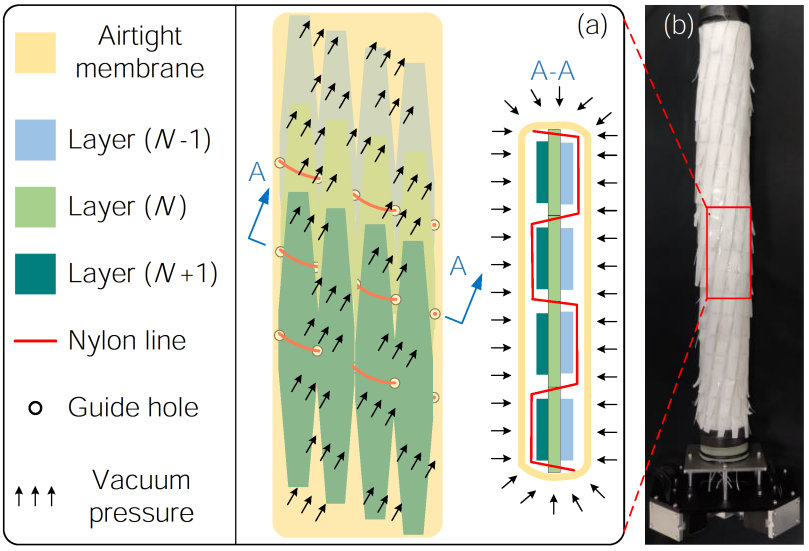

FIGURE 6.1: Schematic of a layer-jamming structure in continuum robots.

For continuum robots with layer jamming, the layer jamming technique provides a lightweight and rapid response approach to adjust the robots' stiffness [283, 286, 287]. In these robots, layer jamming – consisting of a laminate of flexible strips or sheets – is installed throughout the continuum robot's body, and winded up into a tube sheath, as illustrated in Figure 6.1. In Chapter 5 and [200], the robot is operated in its default state that behaves highly compliant. Meanwhile, the jamming sheath forms an enclosed structure in which a negative pressure $-u_{\mathrm{p}} \leq 0$ (relative to the atmospheric pressure) may be applied [240].

As a result, friction between strips or sheets would increase dramatically, thus changing the robot stiffness and dissipating energy [283].

As described above, the pressure value $u_{\mathrm{p}} \in \mathbb{R}_{\geq 0}$ can be adjusted online and viewed as an additional input that changes the robotic dynamics. One of the main objectives of this chapter is to develop a control-oriented dynamical model for LJ-based continuum robots. For control purposes, it is useful to have simple models that describe the essential properties of continuum robots with layer jamming. When the pressure $u_{\mathrm{p}} = 0$, the modelshould degrade into the LJ-free model in Section 6.2.1.

First, the dependence of the plant parameters α_i $(i = 1, 2)$ and the function $D(\boldsymbol{q})$ on u_{p} are discussed. The following assumptions are made:

***Assumption* 6.1.** During the variation process of u_{p}, the continuum robot satisfies

(a) The mass change of air in the airtight membrane is negligible. Hence, the gravitational parameter α_1 is constant and thus *independent* of the pressure u_{p}.

(b) The elastic coefficient $\alpha_2 > 0$ is a function of the pressure u_{p}. For simplicity, it is written as $\alpha_2(u_{\mathrm{p}})$. ◁

***Assumption* 6.2.** The energy dissipation of the robot with layer jamming is only derived from the lumped friction torque with $D(\boldsymbol{q}) = 0$. ◁

***Remark* 6.1.** In Assumption 6.1, it is reasonable to consider constant mass during inflation and deflation. Next, the underlying reason for considering a pressure-dependent function $\alpha_2(u_{\mathrm{p}})$ in the point (**b**) is briefly illustrated. In [283], the *elastic modulus* of the jamming structure has been quantitatively demonstrated to exhibit distinct values in the vacuum-on and vacuum-off states, with a factor of k_n^2 (where k_n denotes the number of layers). This implies that U_{E} is determined by the pressure u_{p} for a given configuration. Consequently, the elastic coefficient α_2 in the proposed model should be a function of u_{p}. This point is also experimentally validated, and the identification of the nonlinear function $\alpha_2(u_{\mathrm{p}})$ will be studied in the subsequent sections. ◁

Under the above assumptions, the dynamical model (6.1) of the LJ-based continuum robot can be compactly written as

$$\Sigma_r : \quad \begin{cases} \dot{\boldsymbol{x}} = J\nabla H(\boldsymbol{x}) + G_r(\boldsymbol{x})\boldsymbol{u} - G_f\tau_f \\ \boldsymbol{v} = G_f^\top \nabla H(\boldsymbol{x}) \end{cases} \tag{6.5}$$

with the new variable $\boldsymbol{x} := \mathrm{col}(\boldsymbol{q}, \boldsymbol{p})$ and

$$\begin{aligned} G_r &:= \begin{bmatrix} 0_{n\times m} \\ G(\boldsymbol{q}) \end{bmatrix} \\ G_f &:= \begin{bmatrix} 0_{n\times n} \\ I_n \end{bmatrix} \\ J &:= \begin{bmatrix} 0_{n\times n} & I_n \\ -I_n & 0_{n\times n} \end{bmatrix} \end{aligned} \tag{6.6}$$

where $\tau_f \in \mathbb{R}^n$ is the lumped frictional torque acting in the links. If the friction τ_f is reviewed as the "input", then the *passive output* $\boldsymbol{v} \in \mathbb{R}^n$ is the generalised velocity [288, 289], i.e.,

$$\boldsymbol{v} = M^{-1}(\boldsymbol{q})\boldsymbol{p} \tag{6.7}$$

The jamming phenomenon is due to the distributed friction along the layers, and the remaining task boils down to studying the modelling of the frictional effects from τ_f and its interconnection to the system Σ_r.

To take this behaviour into account in the model, the LuGre friction model proposed in [290] is considered. It is a *dynamical* model capable of describing many frictional properties, such as zero slip displacement (a.k.a. micromotion), slick-slip motion, invariance, state boundedness, and passivity [285]. Before presenting the LuGre model, the following assumption about the (lumped) normal force $F_n > 0$ between the surfaces is made:

***Assumption* 6.3.** The pressure along the layer is uniformly distributed with a value $(-u_\mathrm{p})$ and is proportional to a function of the lumped normal force, i.e., $F_n \propto \phi(u_\mathrm{p})$, where $\phi(\cdot) : \mathbb{R}^n \to \mathbb{R}^n$ is yet to be determined. ◁

To facilitate the analysis in the subsequent sections, the port-Hamiltonian form of the LuGre model is adopted, as introduced in [291]:

$$\Sigma_z : \quad \begin{cases} \dot{\boldsymbol{z}} = -R_z(\boldsymbol{v})\nabla H_z(\boldsymbol{z}) + [\mathcal{N}(\boldsymbol{v}) - \mathcal{P}(\boldsymbol{v})]\boldsymbol{v} \\ \boldsymbol{\tau}_f = [\mathcal{N}(\boldsymbol{v}) + \mathcal{P}(\boldsymbol{v})]^\top \nabla H_z(\boldsymbol{z}) + S\boldsymbol{v} \end{cases} \tag{6.8}$$

where $\boldsymbol{z} \in \mathbb{R}^n$ represents the virtual bristle deflection at each joint, $\boldsymbol{v} \in \mathbb{R}^n$ is the input – the relative generalised velocity of the surfaces in contact given by (6.7), and the output $\boldsymbol{\tau}_f \in \mathbb{R}^n$ is the frictional torque. The mappings in Σ_z include the virtual bristle potential energy

$$H_z(\boldsymbol{z}) = \frac{1}{2}\sigma_0 \phi(u_\mathrm{p})|\boldsymbol{z}|^2 \tag{6.9}$$

the damping matrix

$$\begin{aligned} R_z(\boldsymbol{v}) &= \mathrm{diag}(\beta_1(\boldsymbol{v}), \ldots, \beta_n(\boldsymbol{v})) \\ \beta_i(\boldsymbol{v}) &:= \frac{|\boldsymbol{v}_i|}{\phi(u_\mathrm{p})}\rho(\boldsymbol{v}_i), \quad i \in \bar{n} \end{aligned} \tag{6.10}$$

the state-modulation matrices

$$\begin{aligned} \mathcal{N}(\boldsymbol{v}) &:= I_n - \frac{1}{2}\sigma_1 \phi(u_\mathrm{p}) R_z(\boldsymbol{v}) \\ \mathcal{P}(\boldsymbol{v}) &:= -\frac{1}{2}\sigma_1 \phi(u_\mathrm{p}) R_z(\boldsymbol{v}) \\ S &:= (\sigma_1 + \sigma_2)\phi(u_\mathrm{p}) I_n \end{aligned} \tag{6.11}$$

and the function

$$\rho(\boldsymbol{v}_i) = \mu_C + (\mu_S - \mu_C)\exp\left(-\left|\frac{\boldsymbol{v}_i}{\boldsymbol{v}_s}\right|^{\sigma_3}\right) \tag{6.12}$$

Physical meanings of coefficients in the above model are summarised in Table 6.1. Interested readers may refer to [290–292] for additional details.

TABLE 6.1: List of coefficients in the LuGre model

μ_S	Stiction friction coefficient
μ_C	Coulomb friction
$\boldsymbol{v}_s$	Stribeck velocity
σ_0	Bristle stiffness coefficient
σ_1	Bristle damping coefficient
σ_2	Viscous friction coefficient
σ_3	Curve parameter (further tuning of the Stribeck effects)

Note that in the model presented above, there is a need to identify the unknown function $\phi(\cdot)$. From physical considerations and prior knowledge of the following properties of the function $\phi(\cdot)$, the following assumption is made:

***Assumption* 6.4.** The function $\phi(\cdot)$ is smooth and satisfies:

(a) It is positive definite, i.e., $\phi(u_{\mathrm{p}}) \geq 0$ for all $u_{\mathrm{p}} \geq 0$.

(b) The function is monotonically increasing with respect to u_{p}. ◁

The function can be obtained either from mechanisms or data-driven methods. This will be investigated in the Section 6.5.

***Remark* 6.2.** The model Σ_z is well-posed for all $\phi(u_{\mathrm{p}}) \geq 0$ even though $\phi(u_{\mathrm{p}})$ appears in the denominator of the function β_i in (6.10). This is due to the product $R_z(\boldsymbol{v})\nabla H_z$ in the dynamics and ∇H_z being linear in $\phi(u_{\mathrm{p}})$. If the function $\phi(u_{\mathrm{p}}) = 0$, it has $\boldsymbol{\tau}_f = 0$ for which zero friction injected to the robotic mechanical dynamics Σ_r. The friction torque $\boldsymbol{\tau}_f$ at the steady-state stage becomes $\boldsymbol{\tau}_f^{\mathrm{ss}} = [\mathrm{diag}\{\rho(\boldsymbol{v}_i)\}\mathrm{sign}(\boldsymbol{v}) + \sigma_2\boldsymbol{v}]u_{\mathrm{p}}$, with $\mathrm{sign}(\boldsymbol{v}) := \mathrm{col}(\mathrm{sign}(\boldsymbol{v}_1), \ldots, \mathrm{sign}(\boldsymbol{v}_n))$ collecting the signs of $\boldsymbol{v}_i$. ◁

***Remark* 6.3.** The LuGre model has the boundedness property for the internal state, i.e., the set $\mathcal{E}_z := \{\boldsymbol{z} \in \mathbb{R}^n : |\boldsymbol{z}| \leq \frac{\mu_S}{\sigma_0}\}$ [285]. The input-output pair $(\boldsymbol{v}, \boldsymbol{\tau}_f)$ satisfies the passivity property

$$\int_0^t \boldsymbol{v}^\top(s)\boldsymbol{\tau}_f(s)ds \geq H_z(\boldsymbol{z}(t)) - H_z(\boldsymbol{z}(0)), \quad \forall t \geq 0$$

if the coefficients satisfy the inequality constraints [292]: ◁

$$\sigma_2 > \sigma_1 \frac{\mu_S - \mu_C}{\mu_C} \tag{6.13}$$

6.2.3 Variable stiffness model using jamming layers

The dynamical model for the LJ-based continuum robots is the negative interconnection of Σ_r and Σ_z. For convenience, the full systems state is defined as

$$\chi := \mathrm{col}(\boldsymbol{q}, \boldsymbol{p}, \boldsymbol{z}) \in \mathbb{R}^{3n}. \tag{6.14}$$

Its dynamics can be compactly written in the port-Hamiltonian form as [291]

$$\dot{\chi} = [\mathcal{J} - \mathcal{R}]\nabla\mathcal{H} + \mathcal{G}(\chi)\boldsymbol{u} \tag{6.15}$$

with the total Hamiltonian

$$\begin{aligned} \mathcal{H}(\chi, u_{\mathrm{p}}) &:= H(\boldsymbol{q}, \boldsymbol{p}) + H_z(\boldsymbol{z}, u_{\mathrm{p}}) \\ &= \underbrace{\frac{1}{2}\boldsymbol{p}^\top M^{-1}(\boldsymbol{q})\boldsymbol{p}}_{\text{kinematic energy}} + \underbrace{\frac{1}{2}\sigma_0 u_{\mathrm{p}}|\boldsymbol{z}|^2 + U(\boldsymbol{q})}_{\text{potential energy}} \end{aligned} \tag{6.16}$$

and the matrices

$$\begin{aligned} \mathcal{J}(\chi, u_{\mathrm{p}}) &:= \begin{bmatrix} J & -G_f\mathcal{N}^\top \\ \mathcal{N}G_f^\top & 0_{n\times n} \end{bmatrix} \\ \mathcal{R}(\chi, u_{\mathrm{p}}) &:= \begin{bmatrix} G_f S(\boldsymbol{v})G_f^\top & G_f\mathcal{P}^\top \\ \mathcal{P}^\top G_f^\top & R_z \end{bmatrix} \\ \mathcal{G}(\chi) &:= \begin{bmatrix} G_r^\top & 0_{n\times m}^\top \end{bmatrix}^\top \end{aligned} \tag{6.17}$$

Note that $\mathcal{N}, \mathcal{P}$ and S are linear functions of the pressure u_{p}. The overall model has an $(m+1)$-dimensional input

$$u_\chi = \begin{bmatrix} \boldsymbol{u} \\ u_{\mathrm{p}} \end{bmatrix} \tag{6.18}$$

with all the elements non-negative.

***Remark* 6.4.** The damping matrix $\mathcal{R}$ can be expanded as $\mathcal{R} = \mathrm{diag}(0_{n\times n}, \mathcal{R}_{22})$ with

$$\mathcal{R}_{22} := \begin{bmatrix} (\sigma_1 + \sigma_2)\phi(u_{\mathrm{p}})I_n & -\frac{1}{2}\sigma_1\phi(u_{\mathrm{p}})R_z(\boldsymbol{v}) \\ -\frac{1}{2}\sigma_1\phi(u_{\mathrm{p}})R_z^\top(\boldsymbol{v}) & R_z(\boldsymbol{v}) \end{bmatrix} \tag{6.19}$$

It is shown in [291, Sec. 4] that positive semi-definitenss of $\mathcal{R}$ can be guaranteed under the coefficient constraint (6.13). This can make $\mathcal{R}$ qualified as a *damping* matrix. ◁

6.3 Interpretation to key phenomena

In this section, the model proposed in Section 6.2.3 is used to theoretically prove the two phenomena in LJ-based continuum robots – shape locking and adjustable stiffness.

6.3.1 Shape locking

Shape locking is one of the important capabilities of LJ structures when applied to continuum robots [281, 283, 284]. Tensions along the cables can change the robot's configuration from its undeformed shape. When a vacuum with negative pressure ($-u_{\mathrm{p}}$) is applied before the release of tension actuation, the continuum robot is able to preserve its current shape. This phenomenon is known as shape locking. This subsection aims to illustrate that shape locking can be characterised by the proposed model. First, its mathematical definition is formulated as follows.

***Definition* 6.1.** (*Shape Locking*) Consider the dynamical model for LJ-based continuum robots with zero input $\boldsymbol{u}$, if the deformed configuration $\bar{\boldsymbol{q}} \neq \mathbf{0}_3$ guarantees the set $\mathcal{E}_{\mathrm{SL}} := \{(\boldsymbol{q}, \boldsymbol{p}, \boldsymbol{z}) \in \mathbb{R}^{3n} : \boldsymbol{q} = \bar{\boldsymbol{q}},\ \boldsymbol{p} = \mathbf{0}_3\}$ under $u_{\mathrm{p}} > 0$ forward invariant, i.e.,

$$\chi(0) \in \mathcal{E}_{\mathrm{SL}} \implies [\ \dot{\boldsymbol{q}}(t) = 0,\ \dot{\boldsymbol{p}}(t) = 0,\ \forall t \geq 0\ ] \tag{6.20}$$

then this invariance is called shape locking. ◁

The following proposition gives a theoretical analysis of the shape-locking phenomenon using the proposed model, and an intuitive illustration is shown immediately after its proof.

***Proposition* 6.1.** Consider the dynamical model (6.15) for LJ-based continuum robots without external input, i.e., $\boldsymbol{u} = \mathbf{0}_m$. For arbitrary configuration $\boldsymbol{q}_a \in \mathbb{R}^n$ and a *constant* pressure $u_{\mathrm{p}} > 0$,

(a) There exists a vector $\boldsymbol{z}_a \in \mathbb{R}^n$ such that $(\boldsymbol{q}_a, \mathbf{0}_n, \boldsymbol{z}_a)$ is an equilibrium;

(b) The equilibria manifold $\mathcal{M} := \{(\boldsymbol{q}, \boldsymbol{p}, \boldsymbol{z}) \in \mathbb{R}^{3n} : \boldsymbol{p} = \mathbf{0},\ \nabla U(\boldsymbol{q}) = \sigma_0 \phi(u_{\mathrm{p}}) \boldsymbol{z}\}$ is locally asymptotically stable.

Proof. First, the existence of $\boldsymbol{z}_a$ such that $(\boldsymbol{q}_a, \mathbf{0}_n, \boldsymbol{z}_a)$ is an equilibrium is verified. From (6.7), $\boldsymbol{p} = \mathbf{0}$ implies the velocity $\boldsymbol{v} = \mathbf{0}$, thus

$$\dot{\boldsymbol{q}} = \nabla_{\boldsymbol{p}} H = M^{-1}(\boldsymbol{q})\boldsymbol{p} = 0 \tag{6.21}$$

The dynamics of $\boldsymbol{z}$ is given by

$$\dot{\boldsymbol{z}} = -R_z(0)\nabla H_z + [\mathcal{N} - \mathcal{P}]v\Big|_{v=0} = 0 \tag{6.22}$$

where the fact $R_z(0) = 0$ from (6.10) is used. For the momentum, it has the following:

$$\begin{aligned}
\dot{\boldsymbol{p}} &= -\frac{\partial}{\partial q}\left\{\frac{1}{2}\boldsymbol{p}^\top M^{-1}(\boldsymbol{p})\boldsymbol{q}\right\} - \nabla U(\boldsymbol{q}_a) + S\boldsymbol{v} + [\mathcal{N} + \mathcal{P}]\nabla H_z\Big|_{\boldsymbol{p}=0} \\
&= -\nabla U(\boldsymbol{q}_a) + [I_n - \sigma_1\phi(u_\mathrm{p})R_z(\boldsymbol{v})]\sigma_0\phi(u_\mathrm{p})\boldsymbol{z} \\
&= -\nabla U(\boldsymbol{q}_a) + \left(I_n - \sigma_1 \mathrm{diag}\left\{\frac{|v_i|}{\rho(v_i)}\right\}\right)\Big|_{\boldsymbol{v}=0} \sigma_0\phi(u_\mathrm{p})\boldsymbol{z} \\
&= -\nabla U(\boldsymbol{q}_a) + \sigma_0\phi(u_\mathrm{p})\boldsymbol{z}
\end{aligned} \tag{6.23}$$

Invoking Assumption 6.4, for any non-zero u_p, the point $\chi_\star := \mathrm{col}(\boldsymbol{q}_a, \mathbf{0}_n, \boldsymbol{z}_a)$ with

$$\boldsymbol{z}_a := \frac{1}{\sigma_0\phi(u_\mathrm{p})}\nabla U(\boldsymbol{q}_a) \tag{6.24}$$

is an equilibrium.

The next step of the proof is to show the local asymptotic stability of the manifold $\mathcal{M}$. Calculating the time derivative of the overall Hamiltonian, it yields for $\chi \in B_\varepsilon(\mathcal{M})$ with a small $\varepsilon > 0$,

$$\begin{aligned}
\dot{\mathcal{H}} &= -[\nabla\mathcal{H}(\chi, u_\mathrm{p})]^\top \mathcal{R}(\chi, u_\mathrm{p})\nabla\mathcal{H}(\chi, u_\mathrm{p}) \\
&\leq -\left\|\begin{bmatrix}\nabla_p\mathcal{H} \\ \nabla_z\mathcal{H}\end{bmatrix}\right\|^2_{\mathcal{R}_{22}} \\
&\leq 0
\end{aligned} \tag{6.25}$$

in which the fact is used that in $B_\varepsilon(\mathcal{M})$ the matrix $\mathcal{R}$ is positive semidefinite from Remark 6.4. Thus, in the neighbourhood of the manifold $\mathcal{M}$, the system is Lyapunov stable.

In the set

$$\{\chi \in \mathbb{R}^{3n} : \|\mathrm{col}(\nabla_p \mathcal{H}, \nabla_z \mathcal{H})\|_{\mathcal{R}_{22}} = 0\} \tag{6.26}$$

it should verify

$$(\sigma_1 + \sigma_2) M^{-1}(\boldsymbol{q})\boldsymbol{p} - \frac{1}{2}\sigma_0\sigma_1\phi(u_\mathrm{p})R_z(\boldsymbol{v})\boldsymbol{z} = 0 \tag{6.27}$$

$$-\frac{1}{2}\sigma_1 R_z(\boldsymbol{v})M^{-1}(\boldsymbol{q})\boldsymbol{p} + \sigma_0 R_z(\boldsymbol{v})\boldsymbol{z} = 0 \tag{6.28}$$

For (6.28), there are two possible cases:

- case (i): $R_z(\boldsymbol{v}) = 0$ (or equivalently $\boldsymbol{p} = 0$).
- case (ii): For some $j \in \bar{n}$, $\beta_j(\boldsymbol{v}) \neq 0$, and thus

$$M^{-1}(\boldsymbol{q})\boldsymbol{p} = 2\frac{\sigma_0}{\sigma_1}\boldsymbol{z} \tag{6.29}$$

For case (i), the trajectory verifies $p(t) \equiv 0$, thus

$$\dot{\boldsymbol{p}} = -\nabla U(\boldsymbol{q}) + \sigma_0\phi(u_\mathrm{p})\boldsymbol{z} = 0$$

which is exactly the manifold $\mathcal{M}$.

For case (ii), by substituting (6.29) into (6.27), resulting in

$$4(\sigma_1 + \sigma_2)\boldsymbol{z} = \sigma_1^2\beta_j(\boldsymbol{v})\phi(u_\mathrm{p})\boldsymbol{z} \tag{6.30}$$

There are two sub-cases: case (ii-1) $\boldsymbol{z} = 0$ and case (ii-2) $\boldsymbol{z} \neq 0$. For case (ii-1), the trajectory should guarantee $\boldsymbol{z} \equiv 0$ and thus

$$\begin{aligned}\dot{\boldsymbol{z}} &= -\mathcal{R}_z(\boldsymbol{v})\nabla H_z(0) + [\mathcal{N} - \mathcal{P}]\boldsymbol{v}\Big|_{\boldsymbol{v}\neq 0} \\ &= [\mathcal{N} - \mathcal{P}]\boldsymbol{v}\Big|_{\boldsymbol{v}\neq 0} = 0\end{aligned}$$

Since $\mathcal{N} - \mathcal{P} = I_n$, it contradicts with $\boldsymbol{v} \neq 0$ in case (ii). Thus, there is no feasible trajectory. For case (ii-2), the equation (6.30) can be rewritten as

$$\sigma_1 + \sigma_2 = \sigma_1^2 \frac{|v_j|}{4\rho(v_j)} \tag{6.31}$$

Note that $\lim_{|v|\to 0} \rho(v_j) = \mu_C$. For given coefficients σ_1, σ_2, the (6.31) does not admit any feasible solution for a sufficiently small $\varepsilon > 0$. Therefore, the only feasible solutions in $B_\varepsilon(\mathcal{M})$ are all on the equilibria manifold $\mathcal{M}$.

As shown above, $\mathcal{M}$ is the largest invariant set in the neighborhood $B_\varepsilon(\mathcal{M}) \subset \mathbb{R}^{3n}$. Applying the LaSalle's invariance principle [293, Sec. 3], the manifold $\mathcal{M}$ is locally asymptotically stable. □

***Remark* 6.5.** The above proposition shows that

(i) If the initial condition $\chi(0)$ starts from any configuration $\boldsymbol{q}_a$ and zero momentum $p(0) = 0$, a virtual bristle vector $\boldsymbol{z}_a$ may always be found such that the system trajectory maintains at the initial values over time, and $\mathcal{M} \subset \mathcal{E}_{\text{SL}}$ is also noted. In this way, it achieves shape locking.

(ii) A more realistic scenario is that the continuum robot achieves deformation with the tension input $\boldsymbol{u} \in \mathbb{R}^m$; then a vacuum is applied, and the actuator is released. Once completing the tension release, the initial condition is given by $\chi(0) = (\boldsymbol{q}(0), \mathbf{0}_3, \mathbf{0}_3)$ instead of $(\boldsymbol{q}_a, \mathbf{0}_3, \boldsymbol{z}_a)$. Proposition 6.1(**b**) shows the *local* asymptotic stability of the manifold $\mathcal{M}$, which means if the initial distance

$$d(\chi(0), \mathcal{M}) := \inf_{\chi' \in \mathcal{M}} |\chi' - \chi(0)| < \varepsilon_0 \tag{6.32}$$

is sufficiently small, the trajectory ultimately converges to equilibrium $(\boldsymbol{q}_a, \mathbf{0}_3, \boldsymbol{z}_a) \in \mathcal{M}$.

(iii) From (ii), the convergence only happens when $\varepsilon_0 > 0$ is sufficiently small. Note that the vector $\boldsymbol{z}_a$ is parameterised as $\boldsymbol{z}_a = \frac{1}{\sigma_0 \phi(u_{\text{p}})} \nabla U(\boldsymbol{q}_a)$. Thus, a large value of $\phi(u_{\text{p}})$ can impose the initial condition $(\boldsymbol{q}(0), \mathbf{0}_3, \mathbf{0}_3)$ in a small neighborhood of $\mathcal{M}$;

see Figure 6.2 for an intuitive illustration. *Physically, it means that a large pressure value u_{p} is capable of achieving shape locking.*

(iv) The above item(iii) shows that after releasing the actuation, the system will change from the initial configuration $(\boldsymbol{q}(0), \mathbf{0}_3, \mathbf{0}_3)$ to the new equilibrium $(\boldsymbol{q}_a, \mathbf{0}_3, \boldsymbol{z}_a)$, and it will be closed to each other with a high pressure u_{p}. It means when the continuum robot changes from flexible to stiff, a tiny positional change will be observed, and it has been experimentally verified in [279, Sec. III-B]. ◁

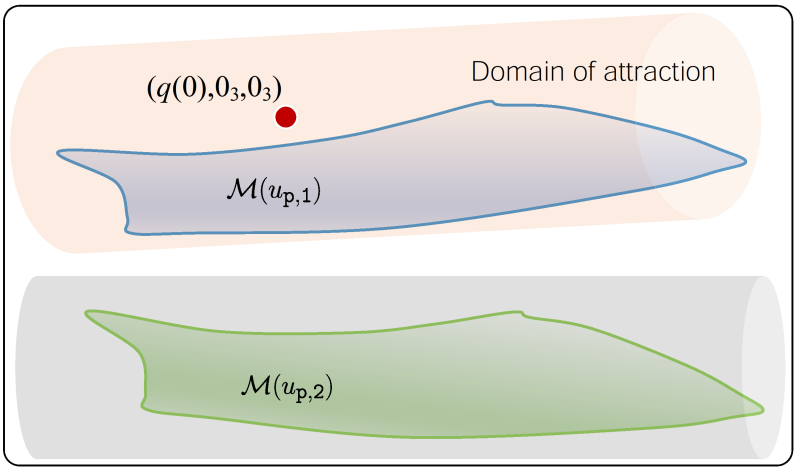

FIGURE 6.2: An illustration of the initial condition and the equilibria manifold $\mathcal{M}$. For a given initial condition $(\boldsymbol{q}(0), \mathbf{0}_3, \mathbf{0}_3)$, a larger $u_{\mathrm{p},1}$ implies a smaller distance from $\chi(0)$ to $\mathcal{M}$, thus $\chi(0)$ located in its domain of attraction; a smaller $u_{\mathrm{p},2}$ may cause the initial condition outside the domain of attraction, failing to achieve shape locking.

6.3.2 Adjustable stiffness

The open-loop equilibrium $\chi_\star := (\boldsymbol{q}_\star, \boldsymbol{p}_\star, \boldsymbol{z}_\star)$ is the origin. The stiffness analysis assumes that there is an external torque τ_{ext} acting on the dynamics of $\boldsymbol{p}$, i.e., the dynamics with $\boldsymbol{u} = 0$ becomes

$$\dot{\tilde{\chi}} = [\mathcal{J} - \mathcal{R}]\nabla\mathcal{H} + G_0\tau_{\mathrm{ext}} \tag{6.33}$$

with $G_0 = \mathrm{col}(0_{3\times3}, I_3, 0_{3\times3})$, under which there is a shifted equilibrium $\bar{\chi} := \mathrm{col}(\bar{\boldsymbol{q}}, \mathbf{0}, \bar{\boldsymbol{z}})$.

***Definition* 6.2.** (*Adjustable Stiffness*) Assume that a positive semidefinite $K \in \mathbb{R}^{3\times3}$ can be found such that

$$\tau_{\mathrm{ext}} := K(\bar{\boldsymbol{q}} - \boldsymbol{q}_\star) \tag{6.34}$$

solves (6.33)-(6.34). When taking $\bar{\boldsymbol{q}} \to \boldsymbol{q}_\star$ and $\bar{\boldsymbol{z}} \to \boldsymbol{z}_\star$, if the limit of K exists, K is the overall stiffness. ◁

***Proposition* 6.2.** Consider the dynamical model (6.15) for LJ-based continuum robots. Its overall stiffness in the sense of Definition 6.2 at the open-loop equilibrium $\chi_\star$ is given by

$$K = \alpha_1 \mathbf{1}_{n\times n} + [\alpha_2 + \sigma_0 \phi(u_{\mathrm{p}})] I_n \tag{6.35}$$

with $\mathbf{1}_{n\times n} \in \mathbb{R}^{n\times n}$ an all elements ones.

Proof. When consider a tiny displacement $(\delta q, \delta z) \in \mathbb{R}^n \times \mathbb{R}^n$ around $(q_\star, z_\star)$, i.e.,

$$q = q_\star + \delta q, \quad z = z_\star + \delta z \tag{6.36}$$

For ease of analysis, the model is rewritten in an Euler-Lagrangian form

$$\begin{aligned} \dot{M}(q)\ddot{q} + C(q,\dot{q})\dot{q} + \nabla U(q) &= \tau_{\mathrm{ext}} - \tau_f \\ \dot{z} &= -\sigma_0 \mathrm{diag}\left\{ \frac{|\dot{q}_i|}{\rho(\dot{q}_i)} \right\} z + \dot{q} \\ \tau_f &= (\sigma_0 z + \sigma_1 \dot{z} + \sigma_2 \dot{q})\phi(u_{\mathrm{p}}) \end{aligned} \tag{6.37}$$

with zero initial condition, in which $C(q,\dot{q})$ is the Coriolis and Centrifugal term [288].

Linearising the dynamics (6.37) around $q_\star = 0, \dot{q}_\star = 0$ and $z_\star = 0$ and invoking (6.36), the model is obtained

$$M_\star \delta\ddot{q} + [\sigma_1 \phi(u_{\mathrm{p}})]\delta\dot{q} + [\nabla^2 U(q_\star) + \sigma_0 \phi(u_{\mathrm{p}}) I_3]\delta q = \tau_{\mathrm{ext}} + \mathcal{O}(\delta q^2) \tag{6.38}$$

with $M_\star := M(q_\star)$ and high-order remainder term $\mathcal{O}(\delta q^2)$, in which the facts are used

$$C(q_\star, 0) = 0, \quad \nabla U(q_\star) = 0$$

Since $\sigma_1 \phi(u_{\mathrm{p}}) > 0$ and $\nabla^2 U(q_\star) + \sigma_0 \phi(u_{\mathrm{p}}) I_3 \succ 0$, the linearised dynamics (6.38) is exponentially stable at equilibrium

$$\delta q = [\nabla^2 U(q_\star) + \sigma_0 \phi(u_{\mathrm{p}}) I_3]^{-1} \tau_{\mathrm{ext}} + \mathcal{O}(\delta q^2)$$

By taking $|\delta q| \to 0$, the algebraic equation (6.34) is obtained with K given by

$$K = \nabla^2 U(q_\star) + \sigma_0 \phi(u_\mathrm{p}) I_3$$

Substituting the function U in (6.3) into the above, equation (6.35) is obtained and the proof is completed. □

6.4 Experiments

In this section, the theoretical analysis in Section 6.3 is verified on the continuum robotic platform OctRobot-I. Although the overall stiffness matrix $K \succ 0$ cannot be measured directly, it isable to detect the transverse stiffness $K_\mathrm{T} \in \mathbb{R}_{\geq 0}$ in the end-effector around the open-loop equilibrium $\boldsymbol{q}_\star$ of the continuum robot. The same testing setup and approach are used as in Chapter 5 and [200, Sec. VI-B]. In the experiments, each test is repeated three times under the same conditions.

6.4.1 Shape locking

The first experiment is designed to verify shape-locking phenomenon of continuum robots with LJ. The robot was initialised from the open-loop configuration $\boldsymbol{q}_\star = \mathbf{0}$ (Phase 1), and then driven to the bending angle of 60° via tendon (Phase 2). When the robot was kept at the steady-state stage, the vacuum process was applied and kept the jamming layer sheath to a negative pressure of -30 kPa (Phase 3) and then the tendons is released (Phase 4). The sequence photos are presented in Figure 6.3 to show this process. The tendon force u_1 is shown in Figure 6.4. Note that $[-4, 0]$ s is used to denote the initial status before starting the motor drive. As illustrated in Figures 6.3(c)-(d), it achieved shape locking after applying negative pressures. To clearly show the shape-locking phenomenon, the photos of Phases 3 and 4 with two different u_p (30 and 80 kPa) were overlapped and presented in Figure 6.5. It illustrates the tiny positional changes as theoretically predicted in Remark 6.5(iv) – a larger u_p yields a smaller displacement (3.8 mm of 80 kPa, 6.7 mm of 60 kPa, and 9.2 mm of 30 kPa).

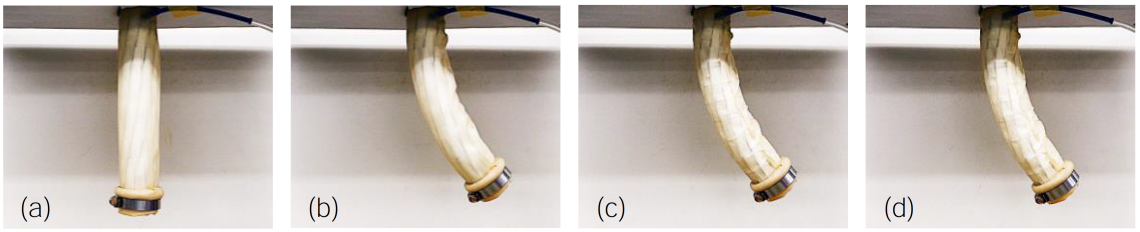

FIGURE 6.3: Photo sequence of the shape-locking experiments: (a) Phase 1: initial configuration without u; (b) Phase 2: drive to the bending configuration 60° via tendon force u; (c) Phase 3: vacuum to $u_{\mathrm{P}} = 30$ kPa with motor-driven retained; (d) Phase 4: vacuum retained and tendon released $u = 0$. (Photos were taken in the steady state of each phase.)

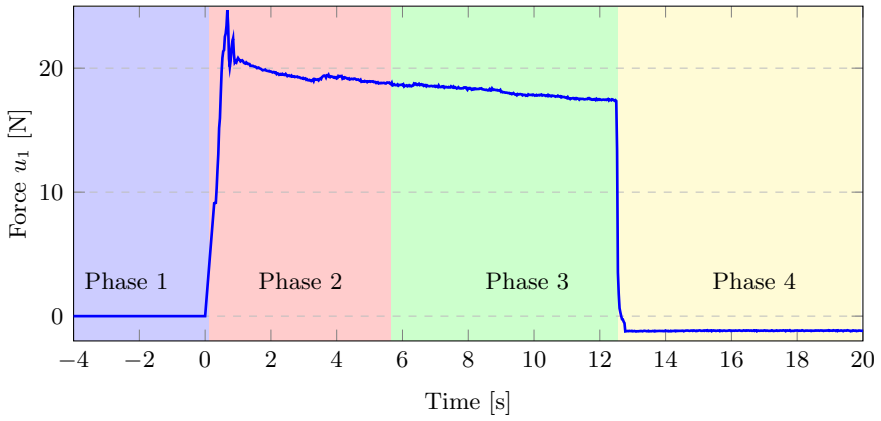

FIGURE 6.4: Trajectory of the tendon force u_1 in the shape-locking experiment.

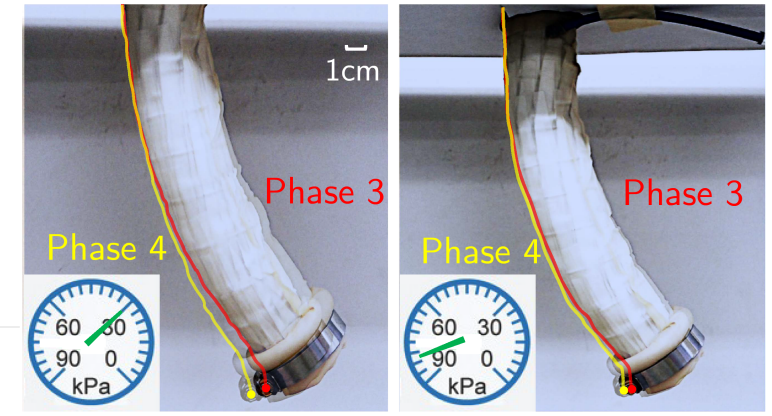

FIGURE 6.5: Overlay photos of the shape-locking phenomenon. Left: displacement of 9.2 mm with $u_{\mathrm{p}} = 30$ kPa; Right: displacement of 3.8 mm with $u_{\mathrm{p}} = 80$ kPa. ("•" and "•" are used to mark a fixed point on the robot body; one-side contours are also highlighted in the figure.)

6.4.2 Adjustable stiffness

The open-loop transverse stiffness under different negative pressures ($-u_{\mathrm{p}}$) is plotted in Figure 6.6, which shows the stiffness can be adjusted by changing the negative pressures ($-u_{\mathrm{p}}$) in the LJ sheath. The coefficient of determination R_s^2 is 0.9216 and 0.9547 for jamming sheaths with different number of layers $k_n = 2$ and $k_n = 5$, respectively. Note that these fitting features show good results with respect to the value u_{p}, and this verifies the equation (6.35).

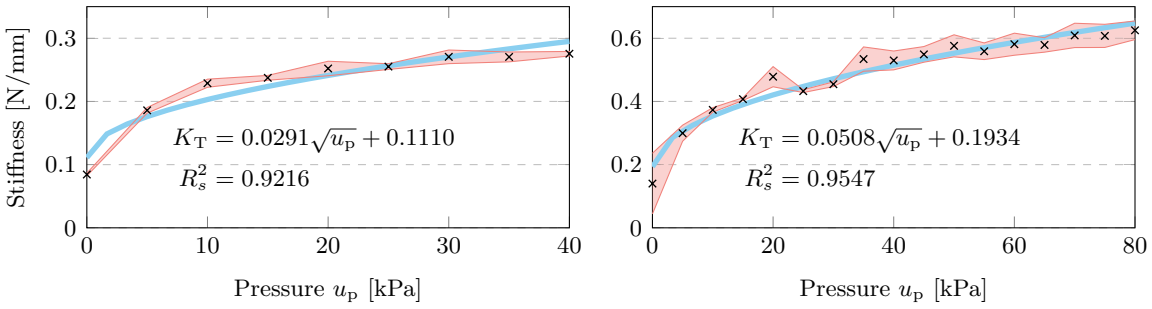

(a) number of layers $k_n = 2$

(b) number of layers $k_n = 5$

FIGURE 6.6: Experimental results showing the relationship between u_{p} and the transverse stiffness under jamming sheaths with different layers. ("×" shows the mean values; color band represents the ±1 standard deviation.)

6.5 Discussions

This chapter presented the updated energy-based model to interpret the two important phenomena of LJ-based continuum robots by integrating the LuGre frictional model. To further improve the performance of LJ-based continuum robots, it is essential to design a feedback controller based on the proposed model to realise almost decoupling control of position and stiffness for LJ-based continuum robots, which is a future work of this chapter.

To facilitate the design of the controller, the approaches to identify the functions $\alpha_2(\cdot)$ and $\phi(\cdot)$ are discussed in this section.

1) Selection of $\alpha_2(u_\mathrm{p})$

As described in Assumption 6.1 and Remark 6.1, the pressure-dependent function $\alpha_2(u_\mathrm{p})$ is more appropriate than a constant coefficient. In order to obtain the function form, experiments were conducted to obtain the input force u_1 under different u_p. Experimental results in Figure 6.7 shows the nonlinearity of $\alpha_2(u_\mathrm{p})$. Since α_1 is constant, it can be concluded that $\alpha_2(\cdot)$ is a monotonically increasing function. In terms of the shape of the curve, the following equation is suggested to use:

$$\alpha_2(u_\mathrm{p}) = c_1 \exp(c_2 u_\mathrm{p}) - c_3 \exp(-c_4 u_\mathrm{p}) \tag{6.39}$$

where $c_i > 0$ $(i = 1, 2, 3, 4)$ are platform-related coefficients that need to be determined with experiments.

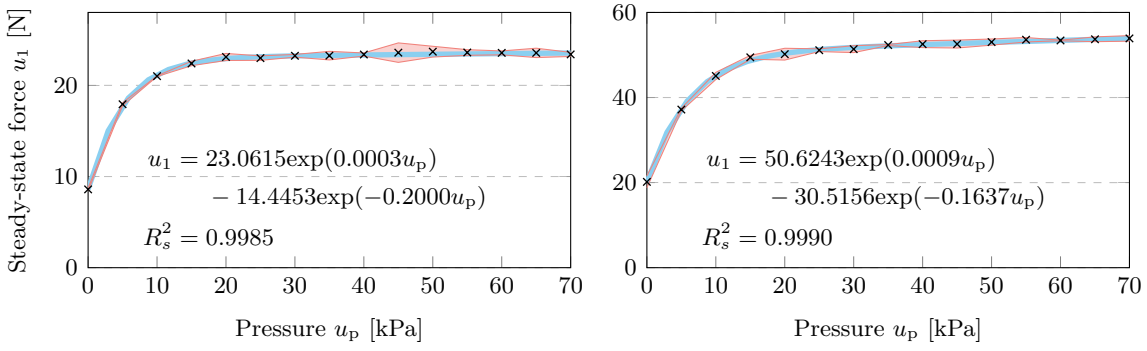

(a) total bending angle 30 deg

(b) total bending angle 60 deg

FIGURE 6.7: Experimental results showing the relationship between pressure u_p and the steady-state input force u_1 ("×" shows the mean values; color band represents the ±1 standard deviation).

2) Modelling of $\phi(u_\mathrm{p})$

$\phi(\cdot)$ is another unknown function in the LuGre frictional model. Instead of a data-driven approach to identify this non-linear function, it is noted that this nonlinearity from friction present between layers of thin material has been studied via underlying mechanisms in LJ-based continuum robots. In particular, it is shown in [256, Eq. (21)] that the resisting torque caused by membrane elongation and shear τ_m satisfies $\tau_m \propto \sqrt{u_\mathrm{p}}$. Based on the research in [256] and the results shown in Figure 6.6, the following equation is considered

to be used for $\phi(u_\mathrm{p})$:

$$\phi(u_\mathrm{p}) = c_5 + c_6\sqrt{u_\mathrm{p}} \tag{6.40}$$

with yet-to-be-determined parameters $c_i > 0$ $(i = 5, 6)$ to fit the nonlinear function $\phi(\cdot)$. The experimental results in Figure 6.6 showing the stiffness under different negative pressures have good fitting results with the coefficient of determination $R_s^2 = 0.9216$ and $R_s^2 = 0.9547$ for jamming sheaths with a number of layers $k_n = 2$ and $k_n = 5$, respectively.

3) Identification of coefficients

With the above parameterisation to $\alpha_2(\cdot)$ and $\phi(\cdot)$, it is able to identify the six coefficients c_i using experimental data. By regulating the continuum robot to different equilibria $q_\star$ under different pressures u_p, the recorded data are denoted as $(u_\star^j, u_\mathrm{p}^j, q_\star^j)$ with j the j-th experiment and $j \in W := \{1, \ldots, w\}$, $w \in \mathbb{N}_+$. The parameters c_i $(i = 1, 2, 3, 4)$ can be estimated by solving the optimisation problem

$$\begin{aligned} \underset{c_1,c_2,c_3,c_4}{\arg\min} \quad & \sum_{j\in W} J(q_\star^j, u_\star^j, u_\mathrm{p}^j) \\ \text{s.t.} \quad & c_i > 0 \end{aligned} \tag{6.41}$$

where $J(q_\star^j, u_\star^j, u_\mathrm{p}^j) := \left| T_u g(q_\star^j) u_\star^j - [\alpha_1 \sin(q_\Sigma^{\star,j}) + (c_1 e^{c_2 u_\mathrm{p}^j} - c_3 e^{c_4 u_\mathrm{p}^j}) q_{1,\star}^j] \right|^2$ is the regulating result.

It requires a sufficient number of experiments, i.e., a relatively large value for w, to ensure that the identified parameters are more accurate. The identification of c_5 and c_6 can be done in a similar way using the parameterisation (6.40) and the stiffness relation (6.35), which contains the unknown function $\phi(\cdot)$ [2].

[2] Indeed, compared to other actuation inputs such as cable tensions, it is challenging to regulate the pressure u_p to given value *with high precision*. As a result, this limitation hinders the generation of a dataset with sufficient samples for data-driven approaches to identify the nonlinear function $\phi(\cdot)$. This is the underlying reason why a model for the function $\phi(\cdot)$ via mechanisms is suggested in this research.

6.6 Summary

This chapter has presented a novel dynamical model for layer jamming-based continuum robots, which integrates the energy-based modelling approach and the LuGre frictional model. Based on this model, two important phenomena, i.e., shape locking and adjustable stiffness, are theoretically analysed and proved, and experimentally verified. A future work will focus on feedback controller design by using the proposed model.

Chapter 7

Conclusions and Future Work

7.1 Conclusions

The first part of this research provided a comprehensive review of the state-of-the-art research on stiffness tuning techniques for continuum robots over the last two decades. This review on different stiffness tuning techniques that have been investigated for diverse application scenarios gives a guideline for the researcher who needs to select proper stiffness techniques when designing continuum robots.

Following this, a continuum robot (OctRobot-I) was designed and developed. This prototype demonstrated adjustable stiffness in both transverse and axial directions through a layer jamming technique. In order to analyse the variable stiffness and its changing tendency of the continuum robot, a stiffness model based on the Euler-Bernoulli beam theory was developed, and four static deflection cases were studied. Experimental results with different pressures and different numbers of jamming sheaths demonstrated the robot's performance in adjusting its stiffness.

For analysing the robot's workspace, this research then proposed the equivalent two section (ETS) method for calculating the workspace of multi-segment continuum robots. Applying forward kinematics and a piecewise constant curvature assumption, this method can

effectively determine the boundary of the workspace, providing an accurate and efficient approach to calculating the workspace size and volume of continuum robots with a high number of segments.

A rigid-link dynamical model was developed to analyse the open-loop stiffening of a class of tendon-driven continuum robots. Based on this model, a new passivity-based controller that adheres to non-negative tension constraints was developed to realise simultaneously position and stiffness control. This model and controller have been verified with efficacy and precision by a series of experiments conducted on the OctRobot-I robotic platform.

Furthermore, a control-oriented dynamical model for layer jamming (LJ) based continuum robots was presented. The integration of the LuGre frictional model into an energy-based framework allowed for the theoretical analysis of two of the fundamental properties of LJ-based continuum robots, namely shape locking and adjustable stiffness. The model and the theoretical analysis were validated on the OctRobot-I robots through experiments.

In conclusion, this thesis has advanced the understanding of continuum robots, particularly in design, workspace analysis, modelling and control methodologies. The outcomes could potentially be applied in practical applications ranging from healthcare to industry.

7.2 Future work

Based on the discussions on future work in Chapter 3-6, three other topics of future work are discussed below:

- **Optimal design of continuum robots**

  In the design of continuum robots, parameters of segment length, maximum bending angle, maximum rotation angle, and the number of segments need to be optimised. This can be modelled as a multi-objective optimisation problem. Therefore, research may include modelling, mathematical analysis, and optimisation algorithms of the multi-objective optimisation design problem.

- **Fine workspace analysis**

  For workspace analysis of multi-segment continuum robots, the research in Chapter 4

assumed each segment is identical, which resulted in a relatively simple analysis of the workspace. However, a continuum robot may need to have many different types of segments to meet specific task requirements. Therefore, further research is needed to improve the model for calculating the workspace of continuum robots with more complex structures. In the meanwhile, as the workspace is an essential parameter for the optimisation design of continuum robots, the improved model will also help the robot design process.

- **Position and stiffness control in 3D space**

  In this thesis, the research on simultaneous position and stiffness control focused on the 2D scenario. Therefore, potential future research can be further analysis of the dynamical model and controller for 3D scenarios for continuum robots to further improve their performance in different applications.

Bibliography

[1] Xin Dong, Mark Raffles, Salvador Cobos-Guzman, Dragos Axinte, and James Kell. A novel continuum robot using twin-pivot compliant joints: design, modeling, and validation. *J. Mech. Robot.*, 8(2), 2016.

[2] Yeongjin Kim, Shing Shin Cheng, and Jaydev P Desai. Active stiffness tuning of a spring-based continuum robot for mri-guided neurosurgery. *IEEE Trans. Robot.*, 34 (1):18–28, 2018.

[3] Jongwoo Kim, Woo-Young Choi, Sungchul Kang, Chunwoo Kim, and Kyu-Jin Cho. Continuously variable stiffness mechanism using nonuniform patterns on coaxial tubes for continuum microsurgical robot. *IEEE Trans. Robot.*, 35(6):1475–1487, 2019.

[4] Yong-Jae Kim, Shanbao Cheng, Sangbae Kim, and Karl Iagnemma. A novel layer jamming mechanism with tunable stiffness capability for minimally invasive surgery. *IEEE Trans. Robot.*, 29(4):1031–1042, 2013.

[5] Marlene Langer, Ernar Amanov, and Jessica Burgner-Kahrs. Stiffening sheaths for continuum robots. *Soft Robot.*, 5(3):291–303, 2018.

[6] Tommaso Ranzani, Matteo Cianchetti, Giada Gerboni, Iris De Falco, and Arianna Menciassi. A soft modular manipulator for minimally invasive surgery: design and characterization of a single module. *IEEE Trans. Robot.*, 32(1):187–200, 2016.

[7] Ali Shiva, Agostino Stilli, Yohan Noh, Angela Faragasso, Iris De Falco, Giada Gerboni, Matteo Cianchetti, Arianna Menciassi, Kaspar Althoefer, and Helge A Wurdemann. Tendon-based stiffening for a pneumatically actuated soft manipulator. *IEEE Robot. Autom. Lett.*, 1(2):632–637, 2016.

[8] Xin An, Yafeng Cui, Hao Sun, Qi Shao, and Huichan Zhao. Active-cooling-in-the-loop controller design and implementation for an sma-driven soft robotic tentacle. *IEEE Trans. Robot.*, 739(3):2325–2341, 2023.

[9] Angus Benedict Clark and Nicolas Rojas. Malleable robots: Reconfigurable robotic arms with continuum links of variable stiffness. *IEEE Trans. Robot.*, 38(6):3832–3849, 2022.

[10] Yeman Fan, Dikai Liu, and Lin Ye. A novel continuum robot with stiffness variation capability using layer jamming: Design, modeling, and validation. *IEEE Access*, 10: 130253–130263, 2022.

[11] Yuchen Zhao and Yifan Wang. A palm-shape variable-stiffness gripper based on 3d-printed fabric jamming. *IEEE Robot. Autom. Lett.*, 8(6):3238 – 3245, 2023.

[12] Mingfeng Wang, Xin Dong, Weiming Ba, Abdelkhalick Mohammad, Dragos Axinte, and Andy Norton. Design, modelling and validation of a novel extra slender continuum robot for in-situ inspection and repair in aeroengine. *Robot. Comput.-Integr. Manuf.*, 67:102054, 2021.

[13] Yang Zheng, Baibo Wu, Yuyang Chen, Lingyun Zeng, Guoying Gu, Xiangyang Zhu, and Kai Xu. Design and validation of cable-driven hyper-redundant manipulator with a closed-loop puller-follower controller. *Mechatronics*, 78:102605, 2021.

[14] Guodong Qin, Aihong Ji, Yong Cheng, Wenlong Zhao, Hongtao Pan, Shanshuang Shi, and Yuntao Song. A snake-inspired layer-driven continuum robot. *Soft Robot.*, 9(4):788–797, 2022.

[15] Yuanqian Gao, Kiyoshi Takagi, Takahisa Kato, Naoyuki Shono, and Nobuhiko Hata. Continuum robot with follow-the-leader motion for endoscopic third ventriculostomy and tumor biopsy. *IEEE Trans. Biomed. Eng.*, 67(2):379–390, 2020.

[16] Yong-Jae Kim, Shanbao Cheng, Sangbae Kim, and Karl Iagnemma. A stiffness-adjustable hyperredundant manipulator using a variable neutral-line mechanism for minimally invasive surgery. *IEEE Trans. Robot.*, 30(2):382–395, 2014.

[17] Daniela Rus and Michael T Tolley. Design, fabrication and control of soft robots. *Nature*, 521(7553):467–475, 2015.

[18] Oncay Yasa, Yasunori Toshimitsu, Mike Y Michelis, Lewis S Jones, Miriam Filippi, Thomas Buchner, and Robert K Katzschmann. An overview of soft robotics. *Annu. Rev. Control Robot. Auton. Syst.*, 6:1–29, 2023.

[19] Srikanth Kolachalama and Sridhar Lakshmanan. Continuum robots for manipulation applications: A survey. *J. Robot.*, 2020, 2020.

[20] Jessica Burgner-Kahrs, D Caleb Rucker, and Howie Choset. Continuum robots for medical applications: A survey. *IEEE Trans. Robot.*, 31(6):1261–1280, 2015.

[21] Pierre E Dupont, Bradley J Nelson, Michael Goldfarb, Blake Hannaford, Arianna Menciassi, Marcia K O'Malley, Nabil Simaan, Pietro Valdastri, and Guang-Zhong Yang. A decade retrospective of medical robotics research from 2010 to 2020. *Sci. Robot.*, 6(60):eabi8017, 2021.

[22] Sangbae Kim, Cecilia Laschi, and Barry Trimmer. Soft robotics: a bioinspired evolution in robotics. *Trends Biotechnol.*, 31(5):287–294, 2013.

[23] Matteo Russo, Seyed Mohammad Hadi Sadati, Xin Dong, Abdelkhalick Mohammad, Ian D Walker, Christos Bergeles, Kai Xu, and Dragos A Axinte. Continuum robots: An overview. *Adv. Intell. Syst.*, 5(5):2200367, 2023.

[24] Pierre E Dupont, Nabil Simaan, Howie Choset, and Caleb Rucker. Continuum robots for medical interventions. *Proc. IEEE*, 110(7):847–870, 2022.

[25] Mariangela Manti, Vito Cacucciolo, and Matteo Cianchetti. Stiffening in soft robotics: A review of the state of the art. *IEEE Robot. Autom. Mag.*, 23(3):93–106, 2016.

[26] Yang Yang, Yingtian Li, and Yonghua Chen. Principles and methods for stiffness modulation in soft robot design and development. *Bio-Des. Manuf.*, 1(1):14–25, 2018.

[27] Loïc Blanc, Alain Delchambre, and Pierre Lambert. Flexible medical devices: Review of controllable stiffness solutions. *Actuators*, 6(3):23, 2017.

[28] Federico Renda, Michele Giorelli, Marcello Calisti, Matteo Cianchetti, and Cecilia Laschi. Dynamic model of a multibending soft robot arm driven by cables. *IEEE Trans. Robot.*, 30(5):1109–1122, 2014.

[29] Brandon Caasenbrood, Alexander Pogromsky, and Henk Nijmeijer. Energy-shaping controllers for soft robot manipulators through port-Hamiltonian Cosserat models. *SN Comput. Sci.*, 3(6):494, 2022.

[30] Heng-Sheng Chang, Udit Halder, Chia-Hsien Shih, Noel Naughton, Mattia Gazzola, and Prashant G Mehta. Energy-shaping control of a muscular octopus arm moving in three dimensions. *Proc. R. Soc. A*, 479(2270), 2023. Art. no. 20220593.

[31] Enrico Franco and Arnau Garriga-Casanovas. Energy-shaping control of soft continuum manipulators with in-plane disturbances. *Int. J. Robot. Res.*, 40(1):236–255, 2021.

[32] Cosimo Della Santina, Robert K Katzschmann, Antonio Bicchi, and Daniela Rus. Model-based dynamic feedback control of a planar soft robot: Trajectory tracking and interaction with the environment. *Int. J. Robot. Res.*, 39(4):490–513, 2020.

[33] Valentin Falkenhahn, Alexander Hildebrandt, Rüdiger Neumann, and Oliver Sawodny. Dynamic control of the bionic handling assistant. *IEEE/ASME Trans. Mechatron.*, 22(1):6–17, 2016.

[34] Bastian Deutschmann, Alexander Dietrich, and Christian Ott. Position control of an underactuated continuum mechanism using a reduced nonlinear model. In *Proc. IEEE Conf. Decis. Control*, pages 5223–5230. IEEE, 2017.

[35] Cosimo Della Santina, Christian Duriez, and Daniela Rus. Model-based control of soft robots: A survey of the state of the art and open challenges. *IEEE Control Syst. Mag.*, 43(3):30–65, 2023.

[36] Jue Wang and Alex Chortos. Control strategies for soft robot systems. *Adv. Intell. Syst*, 4(5), 2022. Art. no. 2100165.

[37] Thomas George Thuruthel, Yasmin Ansari, Egidio Falotico, and Cecilia Laschi. Control strategies for soft robotic manipulators: A survey. *Soft Robot.*, 5(2):149–163, 2018.

[38] Izadyar Tamadon, Yu Huan, Antonius G de Groot, Arianna Menciassi, and Edoardo Sinibaldi. Positioning and stiffening of an articulated/continuum manipulator for implant delivery in minimally invasive surgery. *Int. J. Med. Robot. Comput. Assist. Surg.*, 16(2):e2072, 2020.

[39] Xiaolong Zhu and Haiyan Hu. A controllable stiffness robotics for natural orifice transluminal endoscopic surgery. In *World Conf. Mechan. Eng. Intell. Manuf.*, pages 45–48, 2021.

[40] Mingjun Guan, Yadong Yan, and Yu Wang. A bio-inspired variable-stiffness method based on antagonism. In *Int. Conf. Robot. Control Autom. Eng.*, pages 372–375, 2021.

[41] Tianliang Liu, Zonggao Mu, Haomiao Wang, Wenfu Xu, and Yangmin Li. A cable-driven redundant spatial manipulator with improved stiffness and load capacity. In *Proc. IEEE/RSJ Int. Conf. Intell. Robot. Syst.*, pages 6628–6633, 2018.

[42] Ali Sadeghi, Alessio Mondini, Emanuela Del Dottore, Anand Kumar Mishra, and Barbara Mazzolai. soft-legged wheel-based robot with terrestrial locomotion abilities. *Front. Robot. AI*, 3:73, 2016.

[43] Costanza Culmone, Iris De Falco, A Menciassi, Jenny Dankelman, and John van den Dobbelsteen. A variable stiffness mechanism for minimally invasive surgical needles. In *Proc. Hamlyn Symp. Med. Robot.*, pages 7–8, 2017.

[44] James M Bern, Leonardo Zamora Yañez, Emily Sologuren, and Daniela Rus. Contact-rich soft-rigid robots inspired by push puppets. In *Proc. IEEE Int. Conf. Soft Robot.*, pages 607–613, 2022.

[45] M Cianchetti, A Arienti, M Follador, B Mazzolai, P Dario, and C Laschi. Design concept and validation of a robotic arm inspired by the octopus. *Mater. Sci. Eng. C*, 31(6):1230–1239, 2011.

[46] Wei-Hsi Chen, Shivangi Misra, Yuchong Gao, Young-Joo Lee, Daniel E Koditschek, Shu Yang, and Cynthia R Sung. A programmably compliant origami mechanism for dynamically dexterous robots. *IEEE Robot. Autom. Lett.*, 5(2):2131–2137, 2020.

[47] Alok Ranjan Sahoo and Pavan Chakraborty. Development and analysis of a bio-inspired wire-driven variable stiffness double spring based tapered multi-section flexible robot. *Ind. Robot*, 49(2):187–199, 2022.

[48] Cihat Bora Yigit and Pinar Boyraz. Design and modelling of a cable-driven parallel-series hybrid variable stiffness joint mechanism for robotics. *Mech. Sci.*, 8(1):65–77, 2017.

[49] Daan L Bakker, Daisuke Matsuura, Yukio Takeda, and Just L Herder. Design of an environmentally interactive continuum manipulator. In *Proc. World Congr. Mech. Mach. Sci.*, pages 327–336, 2015.

[50] Revanth Konda, David Bombara, Steven Swanbeck, and Jun Zhang. Anthropomorphic twisted string-actuated soft robotic gripper with tendon-based stiffening. *IEEE Trans. Robot.*, 39(2):1178 – 1195, 2023.

[51] Mingyuan Wang, Jianjun Yuan, Sheng Bao, Liang Du, and Shugen Ma. Research on self-stiffness adjustment of growth-controllable continuum robot (gccr) based on elastic force transmission. *Biomimetics*, 8(5), 2023.

[52] Ibrahim A. Seleem, Mohamed A. Naeem, and Hiroyuki Ishii. Design and analysis of extensible cable-driven continuum robot with variable stiffness. In *Int. Conf. Robot. Biomimetics*, pages 1–8. IEEE, 2023.

[53] Yunong Li, Hailin Huang, and Bing Li. Design of a deployable continuum robot using elastic kirigami-origami. *IEEE Robot. Autom. Lett.*, 8(12):8382 – 8389, 2023.

[54] Ying Zhang, Wenlin Chen, Jie Chen, Qiang Cheng, Haikuan Zhang, Chaoqun Xiang, and Lina Hao. Stiffness analysis of a pneumatic soft manipulator based on bending shape prediction. *IEEE Access*, 8:82227–82241, 2020.

[55] Lina Hao, Chaoqun Xiang, Maria Elena Giannaccini, Hongtai Cheng, Ying Zhang, Samia Nefti-Meziani, and Steven Davis. Design and control of a novel variable stiffness soft arm. *Adv. Robot.*, 32(11):605–622, 2018.

[56] Xifeng Gao, Xingchen Li, Changsheng Zhao, Lina Hao, and Chaoqun Xiang. Variable stiffness structural design of a dual-segment continuum manipulator with independent stiffness and angular position. *Robot. Comput.-Integr. Manuf.*, 67:102000, 2021.

[57] Loai AT Al Abeach, Samia Nefti-Meziani, and Steve Davis. Design of a variable stiffness soft dexterous gripper. *Soft Robot.*, 4(3):274–284, 2017.

[58] GiannacciniMaria Elena et al. Novel design of a soft lightweight pneumatic continuum robot arm with decoupled variable stiffness and positioning. *Soft Robot.*, 5: 54–70, 2018.

[59] Jianhui Liu, Xiaocheng Wang, Sicong Liu, Juan Yi, Xueqian Wang, and Zheng Wang. Vertebraic soft robotic joint design with twisting and antagonism. *IEEE Robot. Autom. Lett.*, 7(2):658–665, 2022.

[60] SP Murali Babu, Ali Sadeghi, Alessio Mondini, and Barbara Mazzolai. Antagonistic pneumatic actuators with variable stiffness for soft robotic applications. In *Proc. IEEE Int. Conf. Soft Robot.*, pages 283–288. IEEE, 2019.

[61] Zhonggui Fang, Chaoyi Huang, Yaxi Wang, Jiahao Xu, Jiyong Tan, Bin Li, Zichen Wang, Yige Wu, Anlun Huang, Juan Yi, et al. Multi-dimensional proprioception and stiffness tuning for soft robotic joints. In *Proc. IEEE Int. Conf. Robot. Autom.*, pages 10973–10979. IEEE, 2022.

[62] Jae Hyuck Jang, Babar Jamil, Youngjin Moon, Altair Coutinho, Gijun Park, and Hugo Rodrigue. Design of gusseted pouch motors for improved soft pneumatic actuation. *IEEE/ASME Trans. Mechatron.*, 28(6):3053 – 3063, 2023.

[63] Yasmin Ansari, Mariangela Manti, Egidio Falotico, Yoan Mollard, Matteo Cianchetti, and Cecilia Laschi. Towards the development of a soft manipulator as an assistive robot for personal care of elderly people. *Int. J. Adv. Robot. Syst.*, 14(2):1–17, 2017.

[64] Yasmin Ansari, Mariangela Manti, Egidio Falotico, Matteo Cianchetti, and Cecilia Laschi. Multiobjective optimization for stiffness and position control in a soft robot arm module. *IEEE Robot. Autom. Lett.*, 3(1):108–115, 2017.

[65] Mariangela Manti, Andrea Pratesi, Egidio Falotico, Matteo Cianchetti, and Cecilia Laschi. Soft assistive robot for personal care of elderly people. In *Proc. IEEE Int. Conf. Biomed. Robot. Biomechatron.*, pages 833–838, 2016.

[66] Edward Harsono, Jun Yang, Shounak Bhattacharya, and Haoyong Yu. Design and analysis of a novel hybrid-driven continuum robot with variable stiffness. *Mech. Mach. Theory*, 177:105067, 2022.

[67] Agostino Stilli, Helge A Wurdemann, and Kaspar Althoefer. Shrinkable, stiffness-controllable soft manipulator based on a bio-inspired antagonistic actuation principle. In *Proc. IEEE Int. Conf. Intell. Robots Syst.*, pages 2476–2481, 2014.

[68] Farahnaz Maghooa, Agostino Stilli, Yohan Noh, Kaspar Althoefer, and Helge A Wurdemann. Tendon and pressure actuation for a bio-inspired manipulator based on an antagonistic principle. In *Proc. IEEE Int. Conf. Robot. Autom.*, pages 2556–2561, 2015.

[69] Maria Elena Giannaccini, Ioannis Georgilas, Ian Horsfield, BHPM Peiris, Alexander Lenz, Anthony G Pipe, and Sanja Dogramadzi. A variable compliance, soft gripper. *Auton. Robot.*, 36(1):93–107, 2014.

[70] Sicheng Wang, Ruotong Zhang, David A Haggerty, Nicholas D Naclerio, and Elliot W Hawkes. A dexterous tip-extending robot with variable-length shape-locking. In *Proc. IEEE Int. Conf. Robot. Autom.*, pages 9035–9041, 2020.

[71] Zhuang Zhang, Shujie Tang, Weicheng Fan, Yuanhao Xun, Hao Wang, and Genliang Chen. Design and analysis of hybrid-driven origami continuum robots with extensible and stiffness-tunable sections. *Mech. Mach. Theory.*, 169, 2022. Art. no. 104607.

[72] Jahanshah Fathi, Timo JC Oude Vrielink, Mark S Runciman, and George P Mylonas. A deployable soft robotic arm with stiffness modulation for assistive living applications. In *Proc. IEEE Int. Conf. Robot. Autom.*, pages 1479–1485. IEEE, 2019.

[73] Ugo Chouinard, Sofiane Achiche, Thor Bieze, Luc Baron, and Christian Duriez. Analyzing design modification effects on the compliance of deformable hybrid serial-parallel manipulators. In *CCToMM Symp. Mech. Mach. Mechatron.*, pages 1–12, 2017.

[74] Xiaojiao Chen, Juan Yi, Jing Li, Jianshu Zhou, and Zheng Wang. Soft-actuator-based robotic joint for safe and forceful interaction with controllable impact response. *IEEE Robot. Autom. Lett.*, 3(4):3505–3512, 2018.

[75] Jianshu Zhou, Wei Chen, Shing Shin Cheng, Lingbin Xue, Michael CF Tong, and Yunhui Liu. Bio-inspired soft (bis) hand for tele-operated covid-19 oropharyngeal (op) swab sampling. In *Prof. IEEE Int. Conf. Robot. Biomim.*, pages 80–86. IEEE, 2021.

[76] Jun-Young Lee, Eun-Yeong Go, Woo-Young Choi, Woong-Bae Kim, and Kyu-Jin Cho. Development of soft continuum manipulator with pneumatic and tendon driven actuations. In *Proc. Int. Conf. Ubiquitous Robot. Ambient Intell.*, pages 377–379, 2016.

[77] Guohua Gao, Han Ren, Yunsong Du, and Hao Wang. Research and development of stiffness regulator by 3d printing. In *IEEE Adv. Inf. Manag. Commun. Electron. Autom. Control Conf.*, pages 785–789. IEEE, 2018.

[78] Luigi Manfredi, Lei Yue, and Alfred Cuschieri. A 3 dofs mini variable stiffness soft pneumatic actuator. In *Proc. Int. Conf. New Actuators*, pages 1–4. VDE, 2018.

[79] Luigi Manfredi, Lei Yue, Jiajia Zhang, and Alfred Cuschieri. A 4 dofs variable stiffness soft module. In *Proc. IEEE Int. Conf. Soft Robot.*, pages 94–99. IEEE, 2018.

[80] Nan Lin, Peichen Wu, Menghao Wang, Fan Yang, Jizhou Wei, and Xiaoping Chen. Design and control of a soft combined actuator. In *WRC Symp. Adv. Robot. Autom.*, pages 255–260. IEEE, 2018.

[81] Jian Tao, Qiqiang Hu, Tianzhi Luo, and Erbao Dong. A soft hybrid-actuated continuum robot based on dual origami structures. In *Proc. IEEE Int. Conf. Robot. Autom.*, volume 2023-May, page 524 – 529, 2023.

[82] Safeh Clinton Mawah and Yong-Jai Park. Tendon-driven variable-stiffness pneumatic soft gripper robot. *Robotics*, 12(5), 2023.

[83] Xiangyu Luo, Dezhi Song, Zhiqiang Zhang, Shuxin Wang, and Chaoyang Shi. A novel distal hybrid pneumatic/cable-driven continuum joint with variable stiffness capacity for flexible gastrointestinal endoscopy. *Adv. Intell. Syst.*, 5(6), 2023.

[84] Jie Zhang, Bo Wang, Haohan Chen, Jianing Bai, Zhigang Wu, Ji Liu, Haijun Peng, and Jianing Wu. Bioinspired continuum robots with programmable stiffness by harnessing phase change materials. *Adv. Mater. Technol.*, 8(6):2201616, 2023.

[85] MinJo Park, Woongbae Kim, Sung-Yol Yu, Jungmin Cho, Wonkyeong Kang, Junghwan Byun, Useok Jeong, and Kyu-Jin Cho. Deployable soft origami modular robotic arm with variable stiffness using facet buckling. *IEEE Robot. Autom. Lett.*, 8(2):864 – 871, 2023.

[86] Matteo Cianchetti, Maurizio Follador, Barbara Mazzolai, Paolo Dario, and Cecilia Laschi. Design and development of a soft robotic octopus arm exploiting embodied intelligence. In *Proc. IEEE Int. Conf. Robot. Autom.*, pages 5271–5276, 2012.

[87] Cecilia Laschi, Matteo Cianchetti, Barbara Mazzolai, Laura Margheri, Maurizio Follador, and Paolo Dario. Soft robot arm inspired by the octopus. *Adv. robot.*, 26 (7):709–727, 2012.

[88] Yanfei Cao, Feng Ju, Lei Zhang, Dongming Bai, Fei Qi, and Bai Chen. A novel variable-stiffness flexible manipulator actuated by shape memory alloy for minimally invasive surgery. *Proc. Inst. Mech. Eng., Part H: J. Eng. Med.*, 232(11):1098–1110, 2018.

[89] Surong Jiang, Bai Chen, Fei Qi, Yanfei Cao, Feng Ju, Dongming Bai, and Yaoyao Wang. A variable-stiffness continuum manipulators by an sma-based sheath in minimally invasive surgery. *Int. J. Med. Robot. Comput. Assist. Surg.*, 16(2):e2081, 2020.

[90] Kim Yan, Wanquan Yan, Wenhui Zeng, Qingpeng Ding, Jianghua Chen, Junyan Yan, Chun Ping Lam, Song Wan, and Shing Shin Cheng. Towards a wristed percutaneous robot with variable stiffness for pericardiocentesis. *IEEE Robot. Autom. Lett.*, 6(2):2993–3000, 2021.

[91] Chenghao Yang, Shineng Geng, Ian Walker, David T Branson, Jinguo Liu, Jian S Dai, and Rongjie Kang. Geometric constraint-based modeling and analysis of a novel continuum robot with shape memory alloy initiated variable stiffness. *Int. J. Robot. Res.*, 39(14):1620–1634, 2020.

[92] Tianjiang Zheng, Yawei Yang, David T Branson, Rongjie Kang, Emanuele Guglielmino, Matteo Cianchetti, Darwin G Caldwell, and Guilin Yang. Control design of shape memory alloy based multi-arm continuum robot inspired by octopus. In *Proc. IEEE Conf. Ind. Electr. Appl.*, pages 1108–1113, 2014.

[93] Aman Arora, Yuichi Ambe, Tae Hyon Kim, Ryo Ariizumi, and Fumitoshi Matsuno. Development of a maneuverable flexible manipulator for minimally invasive surgery with varied stiffness. *Artif. Life Robot.*, 19(4):340–346, 2014.

[94] Kyujin Hyeon, Chongyoung Chung, Jihyeong Ma, and Ki-Uk Kyung. Lightweight and flexible prosthetic wrist with shape memory alloy (sma)-based artificial muscle and elliptic rolling joint. *IEEE Robot. Autom. Lett.*, 8(11):7849 – 7856, 2023.

[95] Phuoc Thien Do, Quang Ngoc Le, Quoc Viet Luong, Hyun-Ho Kim, Hyeong-Mo Park, and Yeong-Jin Kim. Tendon-driven gripper with variable stiffness joint and water-cooled sma springs. *Actuators*, 12(4), 2023.

[96] Joonmyeong Choi, Se Hyeok Ahn, Chunwoo Kim, Jung-Hoon Park, Ho-Young Song, and Kyu-Jin Cho. Design of continuum robot with variable stiffness for gastrointestinal stenting using conformability factor. *IEEE Trans. Med. Robot. Bionics*, 2 (4):529–532, 2020.

[97] Jianbin Liu, Junbo Wei, Guokai Zhang, Shuxin Wang, and Siyang Zuo. Pneumatic soft arm based on spiral balloon weaving and shape memory polymer backbone. *J. Mech. Des.*, 141(8), 2019.

[98] Yang Yang, Yonghua Chen, Yingtian Li, Zheng Wang, and Yunquan Li. Novel variable-stiffness robotic fingers with built-in position feedback. *Soft Robot.*, 4(4): 338–352, 2017.

[99] Yang Yang, Yonghua Chen, Yingtian Li, Michael ZQ Chen, and Ying Wei. Bioinspired robotic fingers based on pneumatic actuator and 3d printing of smart material. *Soft Robot.*, 4(2):147–162, 2017.

[100] Junius Santoso, Erik H Skorina, Marco Salerno, Sébastien de Rivaz, Jamie Paik, and Cagdas D Onal. Single chamber multiple degree-of-freedom soft pneumatic actuator enabled by adjustable stiffness layers. *Smart Mater. Struct.*, 28(3):035012, 2019.

[101] Tingchen Liao, Manivannan Sivaperuman Kalairaj, Catherine Jiayi Cai, Zion Tsz Ho Tse, and Hongliang Ren. Fully-printable soft actuator with variable stiffness by phase transition and hydraulic regulations. *Actuators*, 10(10):269, 2021.

[102] Xiaoyong Wei, Feng Ju, Bai Chen, Hao Guo, Dan Wang, Yaoyao Wang, and Hongtao Wu. Analysis of a novel manipulator with low melting point alloy initiated stiffness variation and shape detection for minimally invasive surgery. *Ind. Robot*, 48(2): 247–258, 2021.

[103] Zhiguang Xing, Fengxu Wang, Yiming Ji, David McCoul, Xinbo Wang, and Jianwen Zhao. A structure for fast stiffness-variation and omnidirectional-steering continuum manipulator. *IEEE Robot. Autom. Lett.*, 6(2):755–762, 2021.

[104] Jinhua Li, Xuejie Li, Jianchen Wang, Yuan Xing, Shuxin Wang, and Xiangyun Ren. Design and evaluation of a variable stiffness manual operating platform for laparoendoscopic single site surgery (less). *Int. J. Med. Robot. Comput. Assist. Surg.*, 13(4):e1797, 2017.

[105] Jianchen Wang, Shuxin Wang, Jinhua Li, Xiangyun Ren, and Randall Miller Briggs. Development of a novel robotic platform with controllable stiffness manipulation

arms for laparoendoscopic single-site surgery (LESS). *Int. J. Med. Robot. Comput. Assist. Surg.*, 14(1):e1838, 2018.

[106] Farshid Alambeigi, Reza Seifabadi, and Mehran Armand. A continuum manipulator with phase changing alloy. In *Proc. IEEE Int. Conf. Robot. Autom.*, pages 758–764, 2016.

[107] Haibo Wang, Zhiwei Chen, and Siyang Zuo. Flexible manipulator with low-melting-point alloy actuation and variable stiffness. *Soft Robot.*, 9(3):577–590, 2022.

[108] Shotaro Yoshida, Yuya Morimoto, Lanying Zheng, Hiroaki Onoe, and Shoji Takeuchi. Multipoint bending and shape retention of a pneumatic bending actuator by a variable stiffness endoskeleton. *Soft Robot.*, 5(6):718–725, 2018.

[109] Yufei Hao, Tianmiao Wang, Zhexin Xie, Wenguang Sun, Zemin Liu, Xi Fang, Minxuan Yang, and Li Wen. A eutectic-alloy-infused soft actuator with sensing, tunable degrees of freedom, and stiffness properties. *J. Micromech. Microeng.*, 28(2), 2018. Art. no. 024004.

[110] Chaoqun Xiang, Wenyi Li, and Yisheng Guan. A variable stiffness electroadhesive gripper based on low melting point alloys. *Polymers*, 14(21):4469, 2022.

[111] Yahao Liu, Yuansheng Wang, Xue Yang, Jian Zheng, Wei Huang, Yu Zhang, Xiao Zhang, and Xuan Wang. 3d-architected low melting point alloys foam microstructure-reinforced polymer composite with superior stiffness-switchable for soft actuator. *Polymer Composites*, 44(12):8805 – 8818, 2023.

[112] Chengquan Hu, Jiayuan Liu, Jiaqi Chen, Shangqi Dai, Jie Wang, Boyu Zhang, and Hongen Liao. A miniaturized variable stiffness soft manipulator with a customizable lmpa pattern. *IEEE Robot. Autom. Lett.*, 8(9):5704 – 5711, 2023.

[113] Niccolò Pagliarani, Luca Arleo, Stefano Albini, and Matteo Cianchetti. Variable stiffness technologies for soft robotics: A comparative approach for the stiff-flop manipulator. *Actuators*, 12(3), 2023.

[114] Fengxu Wang, Zhiguang Xing, Xinbo Wang, and Jianwen Zhao. A method to fabricate complex structure for variable stiffness manipulators based on low-melting-point alloy. In *Proc. IEEE Int. Conf. Soft Robot.*, pages 491–495. IEEE, 2019.

[115] Ruzhen Zhao, Yao Yao, and Yun Luo. Development of a variable stiffness over tube based on low-melting-point-alloy for endoscopic surgery. *J. Med. Devices.*, 10(2): 021002, 2016.

[116] Huu Minh Le, Lin Cao, Thanh Nho Do, and Soo Jay Phee. Design and modelling of a variable stiffness manipulator for surgical robots. *Mechatronics*, 53:109–123, 2018.

[117] Huu Minh Le, Phuoc Thien Phan, Cao Lin, Liu Jiajun, and Soo Jay Phee. A temperature-dependent, variable-stiffness endoscopic robotic manipulator with active heating and cooling. *Ann. Biomed. Eng.*, 48(6):1837–1849, 2020.

[118] Yihua Fang, Christopher Bishop, Weiming Ba, Jorge Barrientos Díez, Abd Mohammad, and Xin Dong. A universal stiffening sleeve designed for all types of continuum robot systems. In *Annu. Conf. Auton. Robot. Syst.*, pages 15–24, 2020.

[119] Qian Gao and Zhenglong Sun. A novel design of water-activated variable stiffness endoscopic manipulator with safe thermal insulation. *Actuators*, 10(6):130, 2021.

[120] Quang Ngoc Le, Hyunho Kim, Sanghun Jeong, Handdeut Chang, Hardik J Pandya, and Yeongjin Kim. Development of a variable stiffness modulating mechanism based on phase-change material and a temperature control system. *Int. J. Precis. Eng. Manuf.*, 23(5):517–531, 2022.

[121] Jinhua Li, Lan Zhang, Yuan Xing, and Rui Liu. A continuum over tube with variable stiffness for transrectal NOTES. *J. Med. Device.*, 16(3):1–8, 2022. Art. no. 031007.

[122] Junfeng Li, Jiahao Li, Zuqi Wu, and YongAn Huang. Designing a soft variable stiffness hand with an integrated actuating–cooling system. *IEEE Trans. Ind. Electron.*, pages 1–9, 2022.

[123] Jihong Yan, Zhidong Xu, Peipei Shi, and Jie Zhao. A human-inspired soft finger with dual-mode morphing enabled by variable stiffness mechanism. *Soft Robot.*, 9 (2):399–411, 2022.

[124] Jihong Yan, Peipei Shi, Zhidong Xu, and Jie Zhao. A wide-range stiffness-tunable soft actuator inspired by deep-sea glass sponges. *Soft Robot.*, 9(3):625–637, 2022.

[125] Shangqi Dai, Chengquan Hu, Longfei Ma, Xinran Zhang, Hui Zhang, and Hongen Liao. A stiffness-tunable soft actuator inspired by helix for medical applications. *Int. J. Comput. Assist. Radiol. Surg.*, 18(9):1625 – 1638, 2023.

[126] Matthew S Moses, Michael DM Kutzer, Hans Ma, and Mehran Armand. A continuum manipulator made of interlocking fibers. In *Proc. IEEE Int. Conf. Robot. Autom.*, pages 4008–4015. IEEE, 2013.

[127] Joonwon Kang, Sudong Lee, and Yong-Lae Park. Soft bending actuator with fiber-jamming variable stiffness and fiber-optic proprioception. *IEEE Robot. Autom. Lett.*, 8(11):7344 – 7351, 2023.

[128] Junfeng Hu, Chengkun Xiao, and Tao Wen. A novel tunable stiffness mechanism using filament jamming. *J. Mech. Robot.*, 13(6):1–12, 2021. Art. no. 061015.

[129] Saurabh Jadhav, Mohamad Ramzi Abdul Majit, Benjamin Shih, Jürgen P Schulze, and Michael T Tolley. Variable stiffness devices using fiber jamming for application in soft robotics and wearable haptics. *Soft Robot.*, 9(1):173–186, 2022.

[130] Ayush Giri, Robert Bloom, and Tania K. Morimoto. Hapstick: A soft flexible joystick for stiffness rendering via fiber jamming. *IEEE Robot. Autom. Lett.*, 8(7): 4163 – 4170, 2023.

[131] Nadia G Cheng, Maxim B Lobovsky, Steven J Keating, Adam M Setapen, Katy I Gero, Anette E Hosoi, and Karl D Iagnemma. Design and analysis of a robust, low-cost, highly articulated manipulator enabled by jamming of granular media. In *Proc. IEEE Int. Conf. Robot. Autom.*, pages 4328–4333. IEEE, 2012.

[132] E Amanov, Thien-Dang Nguyen, Florian Imkamp, and J Burgner-Kahrs. First results on a flexible variable stiffness endoport for single-site partial nephrectomy. In *Hamlyn Symp. Med. Robot.*, pages 91–92, 2017.

[133] Wilhelm R Wockenfuß, Viktor Brandt, Linda Weisheit, and Welf-Guntram Drossel. Design, modeling and validation of a tendon-driven soft continuum robot for planar

motion based on variable stiffness structures. *IEEE Robot. Autom. Lett.*, 7(2):3985–3991, 2022.

[134] Ernar Amanov, Florian Imkamp, and Jessica Burgner-Kahrs. Initial investigations towards a flexible variable stiffness single port system for partial nephrectomy. In *CURAC*, pages 93–98, 2016.

[135] Jianshu Zhou, Hanwen Cao, Wei Chen, Shing Shin Cheng, and Yun-Hui Liu. Bioinspired soft wrist based on multicable jamming with hybrid motion and stiffness control for dexterous manipulation. *IEEE/ASME Trans. Mechatron.*, pages 1–12, 2022.

[136] Yujia Li, Tao Ren, Yonghua Chen, and Michael ZQ Chen. A variable stiffness soft continuum robot based on pre-charged air, particle jamming, and origami. In *Proc. IEEE Int. Conf. Robot. Autom.*, pages 5869–5875, 2020.

[137] Ji Luo, Pei Jiang, Xiaobin Li, Long Bai, Fuqiang Liu, and Rui Chen. A soft self-stable actuator and its energy-efficient grasping. *Actuators*, 11(4), 2022.

[138] S Mohammad Z Sayyadan, Faezeh Gharib, and Alireza Garakan. Granular jamming manipulator filled with new organic materials. In *Proc. Int. Conf. Methods Models Autom. Robot.*, pages 396–401. IEEE, 2017.

[139] Yanzhi Zhao, Yu Shan, Jie Zhang, Kaida Guo, Lizhe Qi, Longguang Han, and Hongnian Yu. A soft continuum robot, with a large variable-stiffness range, based on jamming. *Bioinspir. Biomim.*, 14(6):066007, 2019.

[140] Matteo Cianchetti, Tommaso Ranzani, Giada Gerboni, Iris De Falco, Cecilia Laschi, and Arianna Menciassi. Stiff-flop surgical manipulator: Mechanical design and experimental characterization of the single module. In *Proc. IEEE/RSJ Int. Conf. on Intell. Rob. Syst.*, pages 3576–3581. IEEE, 2013.

[141] Matteo Cianchetti, Tommaso Ranzani, Giada Gerboni, Thrishantha Nanayakkara, Kaspar Althoefer, Prokar Dasgupta, and Arianna Menciassi. Soft robotics technologies to address shortcomings in today's minimally invasive surgery: The STIFF-FLOP approach. *Soft Robot.*, 1(2):122–131, 2014.

[142] Iris De Falco, Matteo Cianchetti, and Arianna Menciassi. STIFF-FLOP surgical manipulator: Design and preliminary motion evaluation. In *Workshop Proc. Comput./Robot. Assist. Surg.*, pages 131–134, 2014.

[143] J Fraś, Jan Czarnowski, M Maciaś, J Główka, Matteo Cianchetti, and Arianna Menciassi. New STIFF-FLOP module construction idea for improved actuation and sensing. In *Proc. IEEE Int. Conf. Robot. Autom.*, pages 2901–2906, 2015.

[144] Tommaso Ranzani, Giada Gerboni, Matteo Cianchetti, and A Menciassi. A bioinspired soft manipulator for minimally invasive surgery. *Bioinspir. Biomim.*, 10(3), 2015. Art. no. 035008.

[145] Iris De Falco, Matteo Cianchetti, and Arianna Menciassi. A soft multi-module manipulator with variable stiffness for minimally invasive surgery. *Bioinspir. Biomim.*, 12(5), 2017.

[146] Ying Wei, Yonghua Chen, Tao Ren, Qiao Chen, Changxin Yan, Yang Yang, and Yingtian Li. A novel, variable stiffness robotic gripper based on integrated soft actuating and particle jamming. *Soft Robot.*, 3(3):134–143, 2016.

[147] Pei Jiang, Yandong Yang, Michael ZQ Chen, and Yonghua Chen. A variable stiffness gripper based on differential drive particle jamming. *Bioinspir. Biomim.*, 14(3), 2019. Art. no. 036009.

[148] Junfeng Hu, Long Liang, and Bin Zeng. Design, modeling, and testing of a soft actuator with variable stiffness using granular jamming. *Robotica*, pages 1–17, 2022.

[149] Yongkang Jiang, Diansheng Chen, Che Liu, and Jian Li. Chain-like granular jamming: A novel stiffness-programmable mechanism for soft robotics. *Soft Robot.*, 6 (1):118–132, 2019.

[150] Hang Wei, Yu Shan, Yanzhi Zhao, Lizhe Qi, and Xilu Zhao. A soft robot with variable stiffness multidirectional grasping based on a folded plate mechanism and particle jamming. *IEEE Trans. Robot.*, 38(6):3821–3831, 2022.

[151] Allen Jiang, Georgios Xynogalas, Prokar Dasgupta, Kaspar Althoefer, and Thrishantha Nanayakkara. Design of a variable stiffness flexible manipulator with composite

granular jamming and membrane coupling. In *2012 IEEE/RSJ International Conference on Intelligent Robots and Systems*, pages 2922–2927, 2012.

[152] Angus B Clark and Nicolas Rojas. Stiffness-tuneable limb segment with flexible spine for malleable robots. In *Proc. IEEE Int. Conf. Robot. Autom.*, pages 3969–3975, 2019.

[153] Angus B Clark and Nicolas Rojas. Assessing the performance of variable stiffness continuum structures of large diameter. *IEEE Robot. Autom. Lett.*, 4(3):2455–2462, 2019.

[154] Allen Jiang, Asghar Ataollahi, Kaspar Althoefer, Prokar Dasgupta, and Thrishantha Nanayakkara. A variable stiffness joint by granular jamming. In *Proc. Int. Des. Eng. Tech. Conf. Comput. Inf. Eng. Conf.*, volume 45035, pages 267–275. American Society of Mechanical Engineers, 2012.

[155] Jessie Lee C Santiago, Isuru S Godage, Phanideep Gonthina, and Ian D Walker. Soft robots and kangaroo tails: Modulating compliance in continuum structures through mechanical layer jamming. *Soft Robot.*, 3(2):54–63, 2016.

[156] Yong-Jae Kim, Shanbao Cheng, Sangbae Kim, and Karl Iagnemma. Design of a tubular snake-like manipulator with stiffening capability by layer jamming. In *Proc. IEEE/RSJ Int. Conf. Intell. Robot. Syst.*, pages 4251–4256, 2012.

[157] Bin Fang, Fuchun Sun, Linyuan Wu, Fukang Liu, Xiangxiang Wang, Haiming Huang, Wenbing Huang, Huaping Liu, and Li Wen. Multimode grasping soft gripper achieved by layer jamming structure and tendon-driven mechanism. *Soft Robot.*, 9 (2):233–249, 2022.

[158] Dickson Chun Fung Li, Zerui Wang, Jianshu Zhou, and Yun-Hui Liu. Honeycomb jamming: An enabling technology of variable stiffness reconfiguration. *Soft Robot.*, 8(6):720–734, 2021.

[159] Xiangli Li, Yufei Hao, Jianhua Zhang, Chang Wang, Dai Li, and Jianjun Zhang. Design, modeling and experiments of a variable stiffness soft robotic glove for stroke patients with clenched fist deformity. *IEEE Robot. Autom. Lett.*, 8(7):4044 – 4051, 2023.

[160] Xianpai Zeng and Hai-Jun Su. A high performance pneumatically actuated soft gripper based on layer jamming. *J. Mech. Robot.*, 15(1):014501, 2023.

[161] Zhipeng Liu, Linsen Xu, Xingcan Liang, and Jinfu Liu. Stiffness-tuneable segment for continuum soft robots with vertebrae. *Machines*, 10(7):581, 2022.

[162] Zhexin Xie, Muralidharan Mohanakrishnan, Peiyi Wang, Jiaqi Liu, Wenci Xin, Zhiqiang Tang, Li Wen, and Cecilia Laschi. Soft robotic arm with extensible stiffening layer. *IEEE Robot. Autom. Lett.*, 8(6):3597 – 3604, 2023.

[163] E Amanov, T-D Nguyen, S Markmann, F Imkamp, and J Burgner-Kahrs. Toward a flexible variable stiffness endoport for single-site partial nephrectomy. *Ann. Biomed. Eng.*, 46(10):1498–1510, 2018.

[164] Yang Yang, Yazhan Zhang, Zicheng Kan, Jielin Zeng, and Michael Yu Wang. Hybrid jamming for bioinspired soft robotic fingers. *Soft Robot.*, 7(3):292–308, 2020.

[165] Botao Lin, Jiaole Wang, Shuang Song, Bing Li, and Max Q-H Meng. A modular lockable mechanism for tendon-driven robots: Design, modeling and characterization. *IEEE Robot. Autom. Lett.*, 7(2):2023–2030, 2022.

[166] Hao Wang, Zhengxue Zhou, Xingyu Yang, and Xuping Zhang. A switchable rigid-continuum robot arm: Design and testing. In *Proc. IEEE Int. Conf. Robot. Autom.*, pages 5162–5169. IEEE, 2022.

[167] Christopher Bishop, Matteo Russo, Xin Dong, and Dragos Axinte. A novel underactuated continuum robot with shape memory alloy clutches. *IEEE/ASME Trans. Mechatron.*, 27(6):5339–5350, 2022.

[168] Zhiguang Xing, David McCoul, Fengxu Wang, Tao Jin, and Jianwen Zhao. Principle of stiffness variation based on matching composite structures with fibers. *Smart Mater. Struct.*, 29(9):095017, 2020.

[169] Hyerim Jeon, Quang Ngoc Le, Sanghun Jeong, Sujin Jang, Hoeryong Jung, Handeut Chang, Hardik J Pandya, and Yeongjin Kim. Towards a snake-like flexible robot with variable stiffness using an sma spring-based friction change mechanism. *IEEE Robot. Autom. Lett.*, 7(3):6582–6589, 2022.

[170] Peiyi Wang, Sheng Guo, Xiangyang Wang, and Yifan Wu. Design and analysis of a novel variable stiffness continuum robot with built-in winding-styled ropes. *IEEE Robot. Autom. Lett.*, 7(3):6375–6382, 2022.

[171] Qi Ruan, Fei Yang, Honghao Yue, Qiancheng Li, Jinsui Xu, and Rongqiang Liu. An accurate position acquisition method of a hyper-redundant arm with load. *IEEE Sens. J.*, 22(9):8986–8995, 2022.

[172] Jin Guo, Jin-Huat Low, Jun Liu, Yangfan Li, Zhuangjian Liu, and Chen-Hua Yeow. Three-dimensional printable ball joints with variable stiffness for robotic applications based on soft pneumatic elastomer actuators. *Polymers*, 14(17):3542, 2022.

[173] Yingtian Li and Yonghua Chen. The ultimate hyper redundant robotic arm based on omnidirectional joints. In *Proc. IEEE Int. Conf. Mechatron. Autom.*, pages 1840–1845. IEEE, 2015.

[174] Zheng Li, Hongliang Ren, Philip Wai Yan Chiu, Ruxu Du, and Haoyong Yu. A novel constrained wire-driven flexible mechanism and its kinematic analysis. *Mech. Mach. Theory*, 95:59–75, 2016.

[175] Changsheng Li, Xiaoyi Gu, Xiao Xiao, Chwee Ming Lim, and Hongliang Ren. Flexible robot with variable stiffness in transoral surgery. *IEEE/ASME Trans. Mechatron.*, 25(1):1–10, 2020.

[176] Muhammad Umar Farooq and Seong Young Ko. A stiffness-changing continuum robotic manipulator for possible use in mri-guided neurosurgical interventions. In *Proc. IEEE Int. Conf. Biomed. Robot. Biomechatron.*, pages 1260–1265. IEEE, 2018.

[177] Bin Zhao, Weihao Zhang, Zhaoyu Zhang, Xiangyang Zhu, and Kai Xu. Continuum manipulator with redundant backbones and constrained bending curvature for continuously variable stiffness. In *Proc. IEEE/RSJ Int. Conf. Intell. Robot. Syst.*, pages 7492–7499. IEEE, 2018.

[178] Bin Zhao, Lingyun Zeng, Zhonghao Wu, and Kai Xu. A continuum manipulator for continuously variable stiffness and its stiffness control formulation. *Mech. Mach. Theory*, 149, 2020. Art. no. 103746.

[179] Bin Zhao, Lingyun Zeng, Baibo Wu, and Kai Xu. A continuum manipulator with closed-form inverse kinematics and independently tunable stiffness. In *Proc. IEEE Int. Conf. Robot. Autom.*, pages 1847–1853, 2020.

[180] Naveen Kumar Uppalapati and Girish Krishnan. Valens: Design of a novel variable length nested soft arm. *IEEE Robot. Autom. Lett.*, 5(2):1135–1142, 2020.

[181] J S Kim, C. K. Kim, S. Kang, and Kyu-Jin Cho. A novel variable stiffness mechanism for minimally invasive surgery using concentric anisotropic tube structure. In *Proc. Hamlyn Symp. Med. Robot.*, pages 43–44, 2017.

[182] Soyeon Park, Jongwoo Kim, Chunwoo Kim, Kyu-Jin Cho, and Gunwoo Noh. Design optimization of asymmetric patterns for variable stiffness of continuum tubular robots. *IEEE Trans. Ind. Electron.*, 69(8):8190–8200, 2022.

[183] Taimoor Hassan, Matteo Cianchetti, Barbara Mazzolai, Cecilia Laschi, and Paolo Dario. Active-braid, a bioinspired continuum manipulator. *IEEE Robot. Autom. Lett.*, 2(4):2104–2110, 2017.

[184] Joowon Park, Hyoryong Lee, Hyeonwoo Kee, and Sukho Park. Magnetically steerable manipulator with variable stiffness using graphene polylactic acid for minimally invasive surgery. *Sensors and Actuators A: Physical*, 309:112032, 2020.

[185] Hugo Rodrigue, Wei Wang, Min-Woo Han, Thomas JY Kim, and Sung-Hoon Ahn. An overview of shape memory alloy-coupled actuators and robots. *Soft Robot.*, 4(1): 3–15, 2017.

[186] Buse Aktaş, Yashraj S Narang, Nikolaos Vasios, Katia Bertoldi, and Robert D Howe. A modeling framework for jamming structures. *Adv. Funct. Mater.*, 31(16), 2021. Art. no. 2007554.

[187] Seth G Fitzgerald, Gary W Delaney, and David Howard. A review of jamming actuation in soft robotics. *Actuators*, 9(4):104, 2020.

[188] Yashraj S Narang, Joost J Vlassak, and Robert D Howe. Mechanically versatile soft machines through laminar jamming. *Adv. Intell. Syst.*, 28(17):1707136, 2018.

[189] Bowen Yi, Yeman Fan, and Dikai Liu. A novel model for layer jamming-based continuum robots. In *Proc. IEEE Int. Conf. Robot. Autom.*, pages 12727–12733. IEEE, 2024.

[190] Ling-Jie Gai, Jie Huang, and Xiaofeng Zong. Stiffness-tunable soft bellows actuators by cross-fiber jamming effect for robust grasping. *IEEE/ASME Trans. Mechatron.*, 28(5):2897 – 2907, 2023.

[191] Miaohang Wei, Fengyu Xu, Changyu Xu, and Yurong Su. Design and experiment of soft grasping robot with variable stiffness based on jamming principles of layer and particle. In *Chin. Control Conf.*, volume 2023-July, page 4524 – 4529, 2023.

[192] Fenglin Han, Lei Fei, Run Zou, Weijian Li, Jinghao Zhou, and Haiming Zhao. A restorable, variable stiffness pneumatic soft gripper based on jamming of strings of beads. *IEEE Trans. Robot.*, 39(5):4065 – 4077, 2023.

[193] Si-Qi An, Wen-Hao Li, Ji-Hui Li, Hai-Lin Zou, and Zi-Chen Deng. Tuning stiffness with granular chain structures for versatile soft robots. *Soft Robot.*, 10(3):493 – 503, 2023.

[194] Yifan Wang, Liuchi Li, Douglas Hofmann, José E Andrade, and Chiara Daraio. Structured fabrics with tunable mechanical properties. *Nature*, 596(7871):238–243, 2021.

[195] Rianna Jitosho, Sofia Simon-Trench, Allison M. Okamura, and Brian H. Do. Passive shape locking for multi-bend growing inflated beam robots. In *Proc. IEEE Int. Conf. Soft Robot.*, pages 1–6, 2023.

[196] Priyanka Rao, Chloe Pogue, Quentin Peyron, Eric Diller, and Jessica Burgner-Kahrs. Modeling and analysis of tendon-driven continuum robots for rod-based locking. *IEEE Robot. Autom. Lett.*, 8(6):3126 – 3133, 2023.

[197] Donghua Shen, Qi Zhang, Yali Han, Chunlei Tu, and Xingsong Wang. Design and development of a continuum robot with switching-stiffness. *Soft Robot.*, 10(5):1015 – 1027, 2023.

[198] Charles M Best, Levi Rupert, and Marc D Killpack. Comparing model-based control methods for simultaneous stiffness and position control of inflatable soft robots. *Int. J. Robot. Res.*, 40(1):470–493, 2021.

[199] Riccardo Mengacci, Franco Angelini, Manuel G Catalano, Giorgio Grioli, Antonio Bicchi, and Manolo Garabini. On the motion/stiffness decoupling property of articulated soft robots with application to model-free torque iterative learning control. *Int. J. Robot. Res.*, 40(1):348–374, 2021.

[200] Bowen Yi, Yeman Fan, Dikai Liu, and Jose Guadalupe Romero. Simultaneous position-and-stiffness control of underactuated antagonistic tendon-driven continuum robots. *IEEE Trans. Autom. Sci. Eng.*, 2023. Conditionally Accept.

[201] Costanza Armanini, Frédéric Boyer, Anup Teejo Mathew, Christian Duriez, and Federico Renda. Soft robots modeling: A structured overview. *IEEE Trans. Robot.*, 39(3):1728–1748, 2023.

[202] Cosimo Della Santina, Christian Duriez, and Daniela Rus. Model-based control of soft robots: A survey of the state of the art and open challenges. *IEEE Control Syst. Mag.*, 43(3):30–65, 2023.

[203] Mohsen Mahvash and Pierre E Dupont. Stiffness control of surgical continuum manipulators. *IEEE Trans. Robot.*, 27(2):334–345, 2011.

[204] Mahmood Mazare, Silvia Tolu, and Mostafa Taghizadeh. Adaptive variable impedance control for a modular soft robot manipulator in configuration space. *Meccanica*, 57(1):1–15, 2022.

[205] Seri M Mustaza, Chakravarthini M Saaj, Francisco J Comin, Wissam A Albukhanajer, Duale Mahdi, and Constantina Lekakou. Stiffness control for soft surgical manipulators. *Int. J. Humanoid Rob.*, 15(05):1850021, 2018.

[206] Jiewen Lai, Bo Lu, and Henry K Chu. Variable-stiffness control of a dual-segment soft robot using depth vision. *IEEE/ASME Trans. Mechatron.*, 27(2):1034–1045, 2022.

[207] Junwen Huang, Yu Liu, Yuxin Yang, Zhijun Zhou, Jie Mao, Tong Wu, Jun Liu, Qipeng Cai, Chaohua Peng, Yiting Xu, et al. Electrically programmable adhesive hydrogels for climbing robots. *Sci. Robot.*, 6(53):eabe1858, 2021.

[208] Yusen Zhao, Chen Xuan, Xiaoshi Qian, Yousif Alsaid, Mutian Hua, Lihua Jin, and Ximin He. Soft phototactic swimmer based on self-sustained hydrogel oscillator. *Sci. Robot.*, 4(33):eaax7112, 2019.

[209] Jongkuk Ko, Changhwan Kim, Dongjin Kim, Yongkwon Song, Seokmin Lee, Bongjun Yeom, June Huh, Seungyong Han, Daeshik Kang, Je-Sung Koh, et al. High-performance electrified hydrogel actuators based on wrinkled nanomembrane electrodes for untethered insect-scale soft aquabots. *Sci. Robot.*, 7(71):eabo6463, 2022.

[210] Dylan S Shah, Ellen J Yang, Michelle C Yuen, Evelyn C Huang, and Rebecca Kramer-Bottiglio. Jamming skins that control system rigidity from the surface. *Adv. Funct. Mater.*, 31(1):2006915, 2021.

[211] Matthew Shen, Angus B Clark, and Nicolas Rojas. A scalable variable stiffness revolute joint based on layer jamming for robotic exoskeletons. In *Annual Conference Towards Autonomous Robotic Systems*, pages 3–14. Springer, 2020.

[212] Kaitlin Oliver-Butler, John Till, and Caleb Rucker. Continuum robot stiffness under external loads and prescribed tendon displacements. *IEEE Trans. Robot.*, 35(2):403–419, 2019.

[213] Mohsen Moradi Dalvand, Saeid Nahavandi, and Robert D Howe. An analytical loading model for n-tendon continuum robots. *IEEE Trans. Robot.*, 34(5):1215–1225, 2018.

[214] CM Wang, Junuthula Narasimha Reddy, and KH Lee. *Shear deformable beams and plates: Relationships with classical solutions*. Elsevier, 2000.

[215] David B Camarillo, Christopher F Milne, Christopher R Carlson, Michael R Zinn, and J Kenneth Salisbury. Mechanics modeling of tendon-driven continuum manipulators. *IEEE Trans. Robot.*, 24(6):1262–1273, 2008.

[216] Igor A Karnovsky and Olga Lebed. *Advanced methods of structural analysis*. Springer Nature, 2021.

[217] Ya-guang Zhu, Bo Jin, Wei Li, and Shi-tong Li. Optimal design of hexapod walking robot leg structure based on energy consumption and workspace. *Trans. Can. Soc. Mech. Eng.*, 38(3):305–317, 2014.

[218] Mir Amin Hosseini and HM Daniali. Cartesian workspace optimization of tricept parallel manipulator with machining application. *Robotica*, 33(9):1948–1957, 2015.

[219] Bin He, Shuangchao Hou, Zhongqiang Deng, Jintao Cao, and Wenzhen Liu. Workspace analysis of a novel underactuated robot wrist based on virtual prototyping. *Int. J. Adv. Manuf. Tech*, 72:531–541, 2014.

[220] Karim Abdel-Malek, Harn-Jou Yeh, and Saib Othman. Interior and exterior boundaries to the workspace of mechanical manipulators. *Robot. Com-Int Manuf,.*, 16(5): 365–376, 2000.

[221] Jessica Burgner-Kahrs, Hunter B Gilbert, Josephine Granna, Philip J Swaney, and Robert J Webster. Workspace characterization for concentric tube continuum robots. In *2014 IEEE/RSJ International Conference on Intelligent Robots and Systems*, pages 1269–1275. IEEE, 2014.

[222] Yi Cao, Ke Lu, Xiujuan Li, and Yi Zang. Accurate numerical methods for computing 2d and 3d robot workspace. *Int. J. Adv. Robot. Syst.*, 8(6):76, 2011.

[223] Bin He, Xuanren Zhu, and Dong Zhang. Boundary encryption-based monte carlo learning method for workspace modeling. *J. Comput. Inf. Sci. Eng*, 20(3):034502, 2020.

[224] Yiqun Zhou, Junchuan Niu, Zhihui Liu, and Fuliang Zhang. A novel numerical approach for workspace determination of parallel mechanisms. *J. Mech. Sci. Technol.*, 31:3005–3015, 2017.

[225] Adrián Peidró, Óscar Reinoso, Arturo Gil, José María Marín, and Luis Payá. An improved monte carlo method based on gaussian growth to calculate the workspace of robots. *Eng. Appl. Artif. Intell.*, 64:197–207, 2017.

[226] Carlo Canali, Alessandro Pistone, Daniele Ludovico, Paolo Guardiani, Roberto Gagliardi, Lorenzo De Mari Casareto Dal Verme, Giuseppe Sofia, and Darwin G Caldwell. Design of a novel long-reach cable-driven hyper-redundant snake-like manipulator for inspection and maintenance. *Appl. Sci.*, 12(7):3348, 2022.

[227] Nan Ma, Stephen Monk, and David Cheneler. Modelling and analysis of the spital branched flexure-hinge adjustable-stiffness continuum robot. *Robotics*, 11(5):97, 2022.

[228] Xishuang Jing, Jiayu Jiang, Fubao Xie, Chengyang Zhang, Siyu Chen, and Lesheng Yang. Continuum manipulator with rigid-flexible coupling structure. *IEEE Robot. Autom. Lett.*, 7(4):11386–11393, 2022.

[229] Bryan A Jones and Ian D Walker. Kinematics for multisection continuum robots. *IEEE Trans. Robot.*, 22(1):43–55, 2006.

[230] Cosimo Della Santina, Antonio Bicchi, and Daniela Rus. On an improved state parametrization for soft robots with piecewise constant curvature and its use in model based control. *IEEE Robot. Autom. Lett.*, 5(2):1001–1008, 2020.

[231] Thomas George Thuruthel, Yasmin Ansari, Egidio Falotico, and Cecilia Laschi. Control strategies for soft robotic manipulators: A survey. *Soft robot.*, 5(2):149–163, 2018.

[232] Daniel Bruder, Xun Fu, R Brent Gillespie, C David Remy, and Ram Vasudevan. Data-driven control of soft robots using Koopman operator theory. *IEEE Trans. Robot.*, 37(3):948–961, 2020.

[233] Yaakov Engel, Peter Szabo, and Dmitry Volkinshtein. Learning to control an octopus arm with Gaussian process temporal difference methods. In *Adv. Neural. Inf. Process. Syst.*, volume 18, 2005.

[234] Hangjie Mo et al. Data-efficient learning control of continuum robots in constrained environments. *IEEE Trans. Autom. Sci. Eng.*, pages 1–12, 2024.

[235] Thomas George Thuruthel, Egidio Falotico, Federico Renda, and Cecilia Laschi. Model-based reinforcement learning for closed-loop dynamic control of soft robotic manipulators. *IEEE Trans. Robot.*, 35(1):124–134, 2018.

[236] Pingyu Xiang et al. Learning-based high-precision force estimation and compliant control for small-scale continuum robot. *IEEE Trans. Autom. Sci. Eng.*, 2023.

[237] Ning Tan, Peng Yu, Zhaohui Zhong, and Yunong Zhang. Data-driven control for continuum robots based on discrete zeroing neural networks. *IEEE Trans. Ind. Inform.*, 19(5):7088–7098, 2023.

[238] Ning Tan et al. Discrete quad neural dynamics for inverse-free control of model-unavailable continuum robots. *IEEE Trans. Ind. Inform.*, pages 1–11, 2024.

[239] David Braganza, Darren M Dawson, Ian D Walker, and Nitendra Nath. A neural network controller for continuum robots. *IEEE Trans. Robot.*, 23(6):1270–1277, 2007.

[240] Fletcher Fan, Bowen Yi, David Rye, Guodong Shi, and Ian R Manchester. Learning stable Koopman embeddings. In *Proc. Amer. Control Conf.*, pages 2742–2747, 2022.

[241] Bowen Yi and Ian R Manchester. On the equivalence of contraction and Koopman approaches for nonlinear stability and control. *IEEE Trans. Autom. Control*, pages 1–16, 2023. Early access.

[242] Hiroyasu Tsukamoto, Soon-Jo Chung, and Jean-Jaques E Slotine. Contraction theory for nonlinear stability analysis and learning-based control: A tutorial overview. *Annu. Rev. Control*, 52:135–169, 2021.

[243] Matthias Tummers, Vincent Lebastard, Frédéric Boyer, Jocelyne Troccaz, Benoit Rosa, and M Taha Chikhaoui. Cosserat rod modeling of continuum robots from Newtonian and Lagrangian perspectives. *IEEE Trans. Robot.*, 39(3):2360–2378, 2023.

[244] Yuhan Chen, Shilong Yao, Max Q-H Meng, and Li Liu. Chained spatial beam constraint model: A general kinetostatic model for tendon-driven continuum robots. *IEEE/ASME Trans. Mechatron.*, 2024.

[245] Costanza Armanini, Frédéric Boyer, Anup Teejo Mathew, Christian Duriez, and Federico Renda. Soft robots modeling: A structured overview. *IEEE Trans. Robot.*, 39(3):1728–1748, 2023.

[246] Thor Morales Bieze, Frederick Largilliere, Alexandre Kruszewski, Zhongkai Zhang, Rochdi Merzouki, and Christian Duriez. Finite element method-based kinematics and closed-loop control of soft, continuum manipulators. *Soft Robot.*, 5(3):348–364, 2018.

[247] Bryan A Jones and Ian D Walker. Kinematics for multisection continuum robots. *IEEE Trans. Robot.*, 22(1):43–55, 2006.

[248] Qingxiang Zhao, Shuai Wang, Jian Hu, Hongbin Liu, and Henry K Chu. Controller design for a soft continuum robot with concurrent continuous rotation. *IEEE/ASME Trans. Mechatron.*, 2024.

[249] Apoorva D Kapadia, Katelyn E Fry, and Ian D Walker. Empirical investigation of closed-loop control of extensible continuum manipulators. In *Proc. IEEE/RSJ Int. Conf. Intell. Robots Syst.*, pages 329–335. IEEE, 2014.

[250] Romeo Ortega, Arjan J Van Der Schaft, Iven Mareels, and Bernhard Maschke. Putting energy back in control. *IEEE Control Syst. Mag.*, 21(2):18–33, 2001.

[251] Timothy Bretl and Zoe McCarthy. Quasi-static manipulation of a Kirchhoff elastic rod based on a geometric analysis of equilibrium configurations. *Int. J. Robot. Res.*, 33(1):48–68, 2014.

[252] John Till and D Caleb Rucker. Elastic stability of Cosserat rods and parallel continuum robots. *IEEE Trans. Robot.*, 33(3):718–733, 2017.

[253] Heng-Sheng Chang, Udit Halder, Chia-Hsien Shih, Arman Tekinalp, Tejaswin Parthasarathy, Ekaterina Gribkova, Girish Chowdhary, Rhanor Gillette, Mattia Gazzola, and Prashant G Mehta. Energy shaping control of a CyberOctopus soft arm. In *IEEE Conf. Decis. Control*, pages 3913–3920. IEEE, 2020.

[254] Yeman Fan, Bowen Yi, and Dikai Liu. An overview of stiffening approaches for continuum robots. *Robot. Comput. Integr. Manuf.*, 90, 2024. Art. no. 102811.

[255] Charles M Best, Levi Rupert, and Marc D Killpack. Comparing model-based control methods for simultaneous stiffness and position control of inflatable soft robots. *Int. J. Robot. Res.*, 40(1):470–493, 2021.

[256] Min Jun Kim, Alexander Werner, Florian Loeffl, and Christian Ott. Passive impedance control of robots with viscoelastic joints via inner-loop torque control. *IEEE Trans. Robot.*, 38(1):584–598, 2021.

[257] Riccardo Mengacci, Franco Angelini, Manuel G Catalano, Giorgio Grioli, Antonio Bicchi, and Manolo Garabini. On the motion/stiffness decoupling property of articulated soft robots with application to model-free torque iterative learning control. *Int. J. Robot. Res.*, 40(1):348–374, 2021.

[258] Mohsen Mahvash and Pierre E Dupont. Stiffness control of surgical continuum manipulators. *IEEE Trans. Robot.*, 27(2):334–345, 2011.

[259] Andrea Bajo and Nabil Simaan. Hybrid motion/force control of multi-backbone continuum robots. *Int. J. Robot. Res.*, 35(4):422–434, 2016.

[260] Romeo Ortega, Mark W Spong, Fabio Gómez-Estern, and Guido Blankenstein. Stabilization of a class of underactuated mechanical systems via interconnection and damping assignment. *IEEE Trans. Autom. Control*, 47(8):1218–1233, 2002.

[261] Jie Zhang, You Li, Ziyun Kan, Qiufeng Yuan, Hamed Rajabi, Zhigang Wu, Haijun Peng, and Wu Jianing. A preprogrammable continuum robot inspired by elephant trunk for dexterous manipulation. *Soft Robot.*, 10(3):636–646, 2023.

[262] Jahanshah Fathi, Timo JC Oude Vrielink, Mark S Runciman, and George P Mylonas. A deployable soft robotic arm with stiffness modulation for assistive living applications. In *Proc. IEEE Int. Conf. Robot. Autom.*, pages 1479–1485. IEEE, 2019.

[263] James M Bern, Leonardo Zamora Yañez, Emily Sologuren, and Daniela Rus. Contact-rich soft-rigid robots inspired by push puppets. In *Proc. IEEE Int. Conf. Soft Robot.*, pages 607–613. IEEE, 2022.

[264] Sicheng Wang, Ruotong Zhang, David A Haggerty, Nicholas D Naclerio, and Elliot W Hawkes. A dexterous tip-extending robot with variable-length shape-locking. In *Proc. IEEE Int. Conf. Robot. Autom.*, pages 9035–9041. IEEE, 2020.

[265] Wei-Hsi Chen, Shivangi Misra, Yuchong Gao, Young-Joo Lee, Daniel E Koditschek, Shu Yang, and Cynthia R Sung. A programmably compliant origami mechanism for dynamically dexterous robots. *IEEE Robot. Autom. Lett.*, 5(2):2131–2137, 2020.

[266] Arjan van der Schaft. *L_2-Gain and Passivity Techniques in Nonlinear Control*. Springer, 2000.

[267] Kevin M Lynch and Frank C Park. *Modern Robotics*. Cambridge University Press, 2nd edition, 2019.

[268] J Kenneth Salisbury. Active stiffness control of a manipulator in Cartesian coordinates. In *Proc. IEEE Conf. Decis. Control*, pages 95–100. IEEE, 1980.

[269] Gianluca Palli, Gianni Borghesan, and Claudio Melchiorri. Modeling, identification, and control of tendon-based actuation systems. *IEEE Trans. Robot.*, 28(2):277–290, 2011.

[270] Romeo Ortega, Arjan van der Schaft, Bernhard Maschke, and Gerardo Escobar. Interconnection and damping assignment passivity-based control of port-controlled hamiltonian systems. *Automatica*, 38(4):585–596, 2002.

[271] Manuel Keppler, Dominic Lakatos, Christian Ott, and Alin Albu-Schäffer. Elastic structure preserving (ESP) control for compliantly actuated robots. *IEEE Trans. Robot.*, 34(2):317–335, 2018.

[272] Hassan K Khalil. *Nonlinear Systems*. Patience Hall, 3 edition, 2002.

[273] Morikazu Takegaki and Suguru Arimoto. A new feedback method for dynamic control of manipulators. *ASME J. Dyn. Syst. Meas. Control*, 102:119–125, 1981.

[274] Bowen Yi, Romeo Ortega, Dongjun Wu, and Weidong Zhang. Orbital stabilization of nonlinear systems via mexican sombrero energy shaping and pumping-and-damping injection. *Automatica*, 112, 2020. Art. no. 108661.

[275] José Guadalupe Romero, Alejandro Donaire, and Romeo Ortega. Robust energy shaping control of mechanical systems. *Syst. Control Lett.*, 62(9):770–780, 2013.

[276] Andrew D Marchese and Daniela Rus. Design, kinematics, and control of a soft spatial fluidic elastomer manipulator. *Int. J. Robot. Res.*, 35(7):840–869, 2016.

[277] Romeo Ortega, Bowen Yi, and Jose Guadalupe Romero. Robustification of nonlinear control systems vis-à-vis actuator dynamics: An immersion and invariance approach. *Syst. Control Lett.*, 146, 2020. Art. no. 104811.

[278] Yashraj S Narang, Alperen Degirmenci, Joost J Vlassak, and Robert D Howe. Transforming the dynamic response of robotic structures and systems through laminar jamming. *IEEE Robot. Autom. Lett.*, 3(2):688–695, 2017.

[279] Angus B Clark and Nicolas Rojas. Assessing the performance of variable stiffness continuum structures of large diameter. *IEEE Robot. Autom. Lett.*, 4(3):2455–2462, 2019.

[280] Angus Benedict Clark and Nicolas Rojas. Malleable robots: Reconfigurable robotic arms with continuum links of variable stiffness. *IEEE Trans. Robot.*, 38(6):3832–3849, 2022.

[281] Jessie Lee C Santiago, Isuru S Godage, Phanideep Gonthina, and Ian D Walker. Soft robots and kangaroo tails: Modulating compliance in continuum structures through mechanical layer jamming. *Soft Robot.*, 3(2):54–63, 2016.

[282] Cosimo Della Santina, Christian Duriez, and Daniela Rus. Model-based control of soft robots: A survey of the state of the art and open challenges. *IEEE Control Syst. Mag.*, 43(3):30–65, 2023.

[283] Yashraj S Narang, Joost J Vlassak, and Robert D Howe. Mechanically versatile soft machines through laminar jamming. *Adv. Funct. Mater.*, 28(17):1–9, 2018. Art. no. 1707136.

[284] Y Zhao *et al.* A soft continuum robot, with a large variable-stiffness range, based on jamming. *Bioinspir. Biomim.*, 14(6), 2019. Art. no. 066007.

[285] Karl Johanastrom and Carlos Canudas-De-Wit. Revisiting the lugre friction model. *IEEE Control Syst. Mag.*, 28(6):101–114, 2008.

[286] Won Ho Choi, Sunghwan Kim, Dongun Lee, and Dongjun Shin. Soft, multi-DoF, variable stiffness mechanism using layer jamming for wearable robots. *IEEE Robot. Autom. Lett.*, 4(3):2539–2546, 2019.

[287] Saurabh Jadhav, Mohamad Ramzi Abdul Majit, Benjamin Shih, Jürgen P Schulze, and Michael T Tolley. Variable stiffness devices using fiber jamming for application in soft robotics and wearable haptics. *Soft Robot.*, 9(1):173–186, 2022.

[288] Romeo Ortega, Antonio Loria, Per Johan Nicklasson, and Hebertt Sira-Ramirez. *Passivity-based Control of Euler-Lagrange Systems: Mechanical, Electrical and Electromechanical Applications*. Springer, 1998.

[289] Arjan van der Schaft. *L_2-Gain and Passivity Techniques in Nonlinear Control*. Springer, 3rd edition, 2017.

[290] C Canudas De Wit, Henrik Olsson, Karl Johan Astrom, and Pablo Lischinsky. A new model for control of systems with friction. *IEEE Trans. Autom. Control*, 40(3): 419–425, 1995.

[291] Johan Koopman, Dimitri Jeltsema, and Michel Verhaegen. Port-Hamiltonian description and analysis of the LuGre friction model. *Simul. Model. Pract. Theory.*, 19(3):959–968, 2011.

[292] N Barahanov and Romeo Ortega. Necessary and sufficient conditions for passivity of the LuGre friction model. *IEEE Trans. Autom. Control*, 45(4):830–832, 2000.

[293] Hassan K Khalil. *Nonlinear Systems*. Prentice Hall, 3 edition, 2001.